November 2017

Environmentally Driven Galaxy Evolution and Quenching: Insights from the Low-redshift Circumgalactic Medium

Joseph Burchett

ENVIRONMENTALLY DRIVEN GALAXY EVOLUTION AND QUENCHING: INSIGHTS FROM THE LOW-REDSHIFT CIRCUMGALACTIC MEDIUM

A Dissertation Presented

by

JOSEPH N. BURCHETT

Submitted to the Graduate School of the
University of Massachusetts Amherst in partial fulfillment
of the requirements for the degree of

DOCTOR OF PHILOSOPHY

September 2017

Astronomy

ENVIRONMENTALLY DRIVEN GALAXY EVOLUTION AND QUENCHING: INSIGHTS FROM THE LOW-REDSHIFT CIRCUMGALACTIC MEDIUM

A Dissertation Presented

by

JOSEPH N. BURCHETT

Approved as to style and content by:

Todd M. Tripp, Chair

Erin M. Conlon, Member

Neal Katz, Member

James D. Lowenthal, Member

John M. O'Meara, Member

Stephen Schneider, Department Chair
Astronomy

DEDICATION

To Amanda Houpt, an unwavering partner;

my parents, Stan and Mary;

and my brother, nieces, and nephew, Corey, Maia, Autumn and Aidan

ACKNOWLEDGMENTS

The work herein was made possible thanks to so many insightful and talented people, many of whom are coauthors of these papers but also many who are not. The guidance and fastidious mentorship of my advisor, Todd Tripp, has certainly helped shape the direction of our efforts, but his cultivating a welcoming environment to explore my own curiosity has transformed me into a scientist. Others from beyond our UMass group, including but not limited to Jess Werk, Xavier Prochaska, John O'Meara, Jason Tumlinson, and Nicolas Lehner, took an interest in my work early on in my graduate career and sparked a sense of community and collaborative relationships I hope will last a lifetime. Furthermore, engaging scientific discussions at various conferences along the way such as those with Rongmon Bordoloi, Nicolas Tejos, Kristen McQuinn, and Ben Oppenheimer have turned into simultaneous fruitful collaboration and friendship. Bill Irvine, through the Mary Dailey Irvine travel grant, has been vital to enabling these opportunities. Kate Rubin and Kate Whitaker have likewise been extremely generous with patient advice and valuable criticism of fellowship applications, CVs, etc. Daniel Wang has impeccably modeled positivity and creativity all while serving as a brilliant collaborator. Lively discussions with Ron Snell and Neal Katz continually provided important new perspectives at morning coffee and beyond. As graduate program director, Daniela Calzetti has averted many self-inflicted administrative near-crises for all of us graduate students and, as a gifted educator and scientist, inspired us as well. Denise Parent, Connie Milne, and Pam Poissant have made all of our lives so much easier and perhaps demonstrated how well they do what they do through all the things we never have to think about or

see them do. The UMass astronomy family is thriving, and I have been and always will be proud to be a part of that family.

From the pre-UMass days, I am indebted to Joe Meiring, who patiently guided me through my first encounters with spectroscopy and astronomical data analysis, and Jim Lauroesch, my Masters thesis advisor. Christopher Davis, graduate program director at the University of Louisville, in many ways got this whole wild ride started by encouraging me to begin graduate studies and offering me a teaching assistantship. Sheila Kannappan imparted myriad skills and knowledge in observational techniques and educational methods and philosophy as well as career guidance.

Lastly, too many friends, musicians, and loved ones to name have enriched my life in Louisville, Chapel Hill, and Western Massachusetts by providing inspiration, support, encouragement, diversion, and community just when I have needed it. The Pioneer Valley has been an amazing place to call home for the past five years and I will continue to reflect fondly upon the kindness and passion of the people and the natural beauty of the landscape that I encountered here.

I offer my highest gratitude to all these people and those that I may have neglected to mention here. Thank you!

ABSTRACT

ENVIRONMENTALLY DRIVEN GALAXY EVOLUTION AND QUENCHING: INSIGHTS FROM THE LOW-REDSHIFT CIRCUMGALACTIC MEDIUM

SEPTEMBER 2017

JOSEPH N. BURCHETT

B.Sc., UNIVERSITY OF LOUISVILLE

M.Sc., UNIVERSITY OF LOUISVILLE

Ph.D., UNIVERSITY OF MASSACHUSETTS AMHERST

Directed by: Professor Todd M. Tripp

The gaseous halos of galaxies – the circumgalactic medium (CGM) – serve as interfaces playing host to the fueling and feedback processes that sustain and regulate star formation. Furthermore, interactions between galaxies one with another and with larger scale structure, such as galaxy cluster halos, must necessarily act through the CGM. This dissertation examines the CGM as traced by H I, C IV, and O VI absorption lines across wide range of halo environments, from isolated dwarf galaxies with $M_* \lesssim 10^8\ M_\odot$ to galaxy clusters with $M_{\rm halo} > 10^{14}\ M_\odot$. By first conducting a blind survey of C IV absorption systems in Hubble Space Telescope spectra of quasi-stellar objects, we measure the incidence and cosmic density of triply ionized carbon in the $z < 0.16$ Universe, showing that both have increased since $z \sim 1$. We then characterize the associations between C IV absorbers and galaxies leveraging the C IV absorber sample and spectroscopic galaxy surveys with sensitivity down to

$L \sim 0.01\ L*$ to show a strong dependence of C IV absorption and host galaxy mass, with $M_* < 10^{9.5}\ M_\odot$galaxies showing a deficiency of C IV absorption to our detection limits relative to galaxies more massive. However, $M_* > 10^{9.5}\ M_\odot$ galaxies in rich group environments show a suppression in C IV absorption. H I, which is largely ubiquitous in all halos across these scales, is suppressed in the CGM of cluster galaxies. The transformations that occur in the CGM moving from very low-mass halos to very high-mass halos (in dense environments) are consistent with an increasingly hotter CGM as halo mass increases (individual, group, and cluster), where star formation may be quenched by a lack of gas reservoir in the halo or a deprivation of fuel by the hot virialized medium.

TABLE OF CONTENTS

LIST OF TABLES

LIST OF FIGURES

Figure **Page**

INTRODUCTION

The term 'island universes' as coined by Kant (1755) to describe the nature of the 'spiral nebulae' observed by Herschel and others may now seem quite endearing, if anachronistic. While the debate over the origin of these nebulae, Galactic or extragalactic, spanned centuries, 'island Universe' nicely encapsulates what ended up as the correct side of the debate: that these spiral nebulae were in fact systems of stars themselves, external to the system comprising our Sun. Galaxies, we now know, are essentially the largest building blocks of the Universe. However, much of the effort in extragalactic astrophysics over the last century has shown us just how island-like galaxies are *not*.

Once such key discovery was that galaxies do not evolve as simple closed boxes. In the closed-box scenario, stars form out of their nascent gas clouds, fuse heavy elements (or 'metals'), return the material back into the gaseous environment, and the process repeats with the next generation of stars forming out of this metal-enriched material all without gas flowing into or out of the system (Tinsley, 1974; Pagel & Patchett, 1975). Such models are inconsistent with empirical data and lead to, for example, the 'G-dwarf problem', the accounting of too few metal-poor G dwarf stars in the solar neighborhood (van den Bergh, 1962; Schmidt, 1963). This tension arises from closed-box models predicting gas that is underenriched at the time intermediate aged stars formed. However, scenarios where the gas reservoir for star formation is replenished and more stars are able to form than suggested by the gas reservoir mass at a given instant ('infall models'; Larson, 1972; Lynden-Bell, 1975; Rocha-Pinto & Maciel, 1996) resolve the tension by enabling the formation of stars at an increased

rate that will sufficiently enrich the medium. Thus, these star forming systems must be fed from somewhere and cannot have evolved in isolation.

Furthermore, the heavy elements forged by stars do not solely enrich the local medium where star formation occurs but are propelled into the surrounding regions and with sufficient momentum, may escape the potential well of the galaxy altogether. Star forming galaxies and those with active nuclei often show signatures of material outflowing at high speeds that may exceed the escape velocity of the host galaxy (e.g. Cecil et al., 2001; Martin, 2005; Rupke et al., 2005; Tremonti et al., 2007; Tripp et al., 2011; Rubin et al., 2014). Spectroscopic surveys of the intergalactic medium (IGM) in the high-redshift Universe show that the IGM gas is already already quite enriched at early times, even a billion years after the Big Bang (Cowie & Songaila, 1998; Songaila, 2001; Pettini et al., 2003), and increases rapidly during this period (Simcoe et al., 2011). Hence, the flow of matter out of galaxies has been central to the chemical evolution of the Universe throughout cosmic time.

On scales more local to galaxies themselves, it is now well accepted that whether a galaxy forms stars (and the rate of star formation) depends critically on the interplay of these fueling and outflow processes as well as the transport of energy provided by stellar winds, supernovae, active galactic nuclei, gravitational processes, and radiation. Models of galaxy formation and evolution, as they have become more sophisticated, have reinforced this picture (e.g., White & Frenk, 1991; Katz et al., 1996; Kereš et al., 2005; Hopkins et al., 2006; Oppenheimer & Davé, 2008; Hopkins et al., 2014; Vogelsberger et al., 2014) to the point where the their differences now lie in their treatment of these 'feedback' processes much more so than differences in numerical techniques. While simulators can track the behavior of gas parcels or diagnose the physical conditions of galactic regions, such as gas temperature and density and the radiation field intensity, where feedback and accretion occur in their data, observers do not have this luxury.

If one were to persist with an island analogy for galaxies even still, he/she would at least have to concede that these islands are quite gregarious and the oceans separating them are not often not so vast. Galaxies typically reside in associations on some scale, with galaxy clusters (Abell, 1965) serving as the most densely populated end of the spectrum and possibly comprising hundreds or thousands of galaxies. On considerably less dense scales, sparsely populated groups may contain a Milky Way-mass galaxy and a system of dwarf satellites. On any scale, galaxies interact quite readily with one other and their environment whether through, for example, tidal disruption of stellar or gas morphology (Martínez-Delgado et al., 2010; Chung et al., 2007) or ram-pressure stripping Gunn & Gott (1972); Weinberg (2014). As with gas fueling and feedback, galaxy environment critically impacts star formation activity and gas content (Dressler, 1980; Sandage et al., 1985), with galaxies in dense environments exhibiting suppressed star formation and lower cold gas content (Stark et al., 2016). Of course, these characteristics (e.g., star formation rate and gas density) that we typically measure are consequences of processes about which we must infer or speculate due to anecdotal evidence, e.g., residing within a galaxy cluster. At the risk of overplaying the foreshadowing, the work herein represents an important step towards a physical understanding of the mechanisms at play *in the locations where they operate*.

Since the much-celebrated assertion by Bahcall & Spitzer (1969) that the multiple absorption line systems at varying redshifts in the spectra of quasars arise from gaseous halos of intervening galaxies, much work has ensued to further connect the properties of these galaxy halos to those of the absorption and, ultimately, what these systems may reveal about the host galaxy itself. Progress in this field has been hard-won in the nearly five decades since, partly because of the fact that conducting such investigations requires not only spectra of background quasi-stellar objects (QSOs) but also galaxy surveys in the fields around the QSOs to identify foreground

associated galaxies. It took almost a decade before Boksenberg & Sargent (1978) found perhaps the first truly convincing evidence of a galaxy halo-absorption line association. Bergeron (1986) ushered in a new era of studying the halo gas around galaxies with the discovery of a Mg II doublet associated with a galaxy at $z \sim 0.4$, as Mg II is a very strong spectral feature observable by ground-based telescopes at redshifts down to $z \sim 0.2$ and galaxy surveys are much more feasible at these redshifts than where other strong lines such as the C IV doublet shift into the optical bands at $z \sim 1.5$. The 1990s saw this field truly gain traction, starting with a survey by Bergeron & Boissé (1991) producing an actual sample of Mg II absorber-galaxy associations then the scientific revolution (for many fields) accompanying the launch of the Hubble Space Telescope (HST). Now, far-ultraviolet lines such as the ubiquitous H I Lyα and metal-line transitions such as C IV and O VI were observable at low redshift. Several seminal papers both observational and theoretical (Lanzetta et al., 1995a; Bowen et al., 1996; Mo & Miralda-Escude, 1996; Tripp et al., 1998, e.g.) put a circumgalactic origin for QSO absorption lines on firm footing and questions turned to the nature of the circumgalactic medium (CGM) and its role in the host galaxy's evolution. Many studies from the last decade and a half will be reviewed in the following chapters due to their particular relevance, and I will defer to later in this dissertation for such information. Suffice it to say, little doubt remains that deep connections lie between the characteristics of the CGM gas and the star formation and mass of the host galaxy (Chen et al., 2010; Tumlinson et al., 2011; Prochaska et al., 2011; Kacprzak et al., 2012a, e.g.).

As I have advocated at the beginning of this introduction, galaxies form ecosystems, where interactions with their surroundings and each other drive their sustained star formation, morphological transformation, and mass assembly. Just as an icthyologist must consider the conditions of the water in which fish reside, physical understanding of galaxy evolution necessitates investigating the conditions in the CGM, the

point of contact for any galaxy interaction mechanism (feedback, accretion, mergers). I argue that the CGM science should take an ecosystem-oriented perspective, and the lion's share of the work presented in this dissertation will hopefully have done so and present some of the some insight such an approach can yield.

Chapters 1, 2, and 3 present a large survey of the C IV-traced CGM down to $z \sim 0$, where publicly available galaxy survey data provide highly complete samples of even faint dwarf galaxies whose CGM are probed by QSO spectra from HST. Each chapter includes, as published in the Astrophysical Journal, the corresponding article for Papers I, II, and III of this survey; the only difference from their published versions is that I have moved the respective Appendices to appear as Appendices of the dissertation. Bergeron & Stasińska (1986) ended their abstract with the following: "...to definitively link the absorption line systems with galaxies, the authors plead for a survey of C IV absorption systems at low-z." These papers should answer this plea. While the first three chapters largely analyze galaxies in environments ranging from individual dwarf halos through massive groups, Chapter 4 moves towards higher environmental densities and examines the behavior of the CGM in galaxy clusters as well as the physical conditions of the ambient intracluster medium. The material presented in Chapter 4 has been submitted to Monthly Notices of the Royal Astronomy and received a favorable referee review; included here is the manuscript as submitted. Taken together, these works paint a coherent picture that the CGM is transformed quite dramatically as the galaxy halo environment, the galaxy's ecosystem, changes.

CHAPTER 1

A DEEP SEARCH FOR FAINT GALAXIES ASSOCIATED WITH VERY LOW-REDSHIFT C IV ABSORBERS: A CASE WITH COLD-ACCRETION CHARACTERISTICS

Joseph N. Burchett[1], Todd M. Tripp[1], Jessica K. Werk[2], J. Christopher Howk[3], J. Xavier Prochaska[2], Amanda Brady Ford[4], and Romeel Davé[5,6,7]

Studies of QSO absorber-galaxy connections are often hindered by inadequate information on whether faint/dwarf galaxies are located near the QSO sight lines. To investigate the contribution of faint galaxies to QSO absorber populations, we are conducting a deep galaxy redshift survey near low$-z$ C IVabsorbers. Here we report a blindly-detected C IV absorption system ($z_{\rm abs} = 0.00348$) in the spectrum of PG1148+549 that appears to be associated either with an edge-on dwarf galaxy with an obvious disk (UGC 6894, $z_{\rm gal} = 0.00283$) at an impact parameter of $\rho = 190$ kpc or with a very faint dwarf irregular galaxy at $\rho = 23$ kpc, which is closer to the sightline but has a larger redshift difference ($z_{\rm gal} = 0.00107$, i.e., δv =724 km/s).

[1]Department of Astronomy, University of Massachusetts, 710 North Pleasant Street, Amherst, MA 01003-9305

[2]UCO/Lick Observatory, University of California, Santa Cruz, CA

[3]Department of Physics, University of Notre Dame, Notre Dame, IN 46556

[4]Astronomy Department, University of Arizona, Tucson, AZ 85721, USA

[5]University of the Western Cape, Bellville, Cape Town 7535, South Africa

[6]South African Astronomical Observatories, Observatory, Cape Town 7925, South Africa

[7]African Institute for Mathematical Sciences, Muizenberg, Cape Town 7945, South Africa

We consider various gas/galaxy associations, including infall and outflows. Based on current theoretical models, we conclude that the absorber is most likely tracing (1) the remnants of an outflow from a previous epoch, a so-called 'ancient outflow' or (2) intergalactic gas accreting onto UGC 6894, "cold mode" accretion. The latter scenario is supported by H I synthesis imaging data that shows the rotation curve of the disk being codirectional with the velocity offset between UGC6894 and the absorber, which is located almost directly along the major axis of the edge-on disk.

1.1 Introduction

The interactions of galaxies with their ambient surrounding media and with one another have come into sharp focus as crucial components of galaxy evolution. These interactions include the continuing accretion of material required to fuel on-going star formation and, conversely, the feedback mechanisms that regulate galactic physical conditions and transport metal-enriched gas to galactic halos/circumgalactic media (CGM) and beyond (e.g., Fumagalli et al., 2011; Hopkins et al., 2006; Veilleux et al., 2005a; Heckman et al., 2011). Although inflow and outflow processes are challenging to observe, QSO absorption spectroscopy provides a sensitive tool for doing so.

However, discerning the origin of the gas detected in QSO absorption spectra is greatly complicated by the incompleteness of galaxy redshift surveys in the fields of the absorbers. For instance, the Sloan Digital Sky Survey's 95% spectroscopic completeness down to $m_r = 17.7$ (Strauss et al., 2002) includes only $L > L_*$ galaxies at z$\geq$0.15. Thus, while the local Universe provides the most suitable laboratory for studying the galaxy environments of intervening gaseous systems, the possibility remains of attributing the detected gas to a more luminous galaxy when a fainter, undetected dwarf galaxy is present. These concerns have important implications because while an absorber might appear to arise in some type of inflow or outflow

connected to a luminous galaxy, it could in fact be bound to a faint satellite or nearby dwarf galaxy that was overlooked in the incomplete redshift survey.

Table 1.1 Absorption line properties

Ion	λ_0 (Å)	W_r (mÅ)[a]	log N (cm^{-2})[b]	b (km/s)	v (km/s)[c]
H I	1215.67	375.7 ± 5.55	>14.41	30 ± 1	0
H I	1215.67	134.51 ± 5.52	13.51 ± 0.02	29 ± 1	134
C IV	1548.2	89.84 ± 7.19	13.64 ± 0.03	9 ± 1	-9
C IV	1550.77	58.39 ± 7.27	13.64 ± 0.03	9 ± 1	-9
C II	1334.53	<71.14	<13.59	-	-
Si IV	1393.75	<68.45	<12.92	-	-
Si IV	1402.77	<86.12	<13.33	-	-
Si III[d]	1206.5	-	-	-	-
Si II	1260.42	<53.94	<12.54	-	-

[a] Nondetections are reported as 3σ upper limits.
[b] Column density upper limits are calculated from the W_r limits assuming a linear curve-of-growth relationship.
[c] Velocity offsets are measured relative to the strong Lyα feature.
[d] We report a nondetection of Si III because, if present, this line is blended with an O VI feature at another redshift.

At very low redshifts, the C IV $\lambda\lambda$ 1548.2, 1550.8 doublet provides an easily identifiable signature of metal-enriched gas in QSO spectra. Space-based observations are required at these wavelengths in the nearby universe, and the Cosmic Origin Spectrograph (COS) aboard the Hubble Space Telescope (Green et al., 2012) is the most sensitive space-based instrument to-date for this work. As part of a larger, blind survey of C IV absorbers at low redshift, we have discovered a z=0.003 C IV absorption system whose location and/or kinematics, in light of previous observations, suggest two interesting galaxy associations: the absorber is (1) at a similar redshift but at

1.4 virial radii from a normal star-forming galaxy or (2) at an impact parameter of 23 kpc from a faint dwarf galaxy but with a velocity separation of $\delta v \sim 700$ km/s. In this letter, we report our analysis of this absorber, and throughout we assume a cosmology of $H_0 = 72$ km/s Mpc^{-1}, $\Omega_M = 0.27$, and $\Omega_\Lambda = 0.73$.

1.2 Observations

The absorber of interest is a C IV absorption system detected in high signal-to-noise (S/N) HST/COS spectra, and the corresponding galaxy survey employs publicly available data from the SDSS, imaging with the Large Binocular Telescope (LBT), and spectroscopy with the MMT+Hectospec (Fabricant et al., 1998), Keck+DEIMOS (Faber et al., 2003) and Shane 3m+Kast (Miller & Stone, 1992).

1.2.1 HST/COS Spectroscopy

The system appears at redshift $z_{\rm abs} = 0.00348$ in the spectrum of PG1148+549 ($z_{\rm QSO} = 0.9754$), which was observed as part of the HST program 11741 using the Cosmic Origins Spectrograph. The observations and data reduction are described by Meiring et al. (2013, 2011). At the absorber redshift, the spectrum has signal-to-noise per resolution element S/N = 30 at the wavelength of the Lyα line and S/N = 28 near the C IV doublet, which enable us to detect C IV lines with rest-frame equivalent width $W_r \gtrsim 10$ mÅ. The Lyα and C IV lines detected in the COS spectrum at $z_{\rm abs} = 0.00348$ are shown in Figure 1.1.

1.2.2 Optical Imaging and Spectroscopy

To seek associated faint or low-surface brightness galaxies with greater depth than SDSS, we obtained deep broadband imaging of the field using the Large Binocular Telescope (LBT) with a limiting magnitude of $B_{AB} \sim 25.5$ (Meiring et al., 2013).

We also obtained follow-up multi-object spectroscopy using Hectospec to measure fainter galaxy redshifts. Two low-surface brightness objects were visible in the LBT

imaging but were not measured with Hectospec, and we obtained their slit spectra from Keck/DEIMOS and the Kast Double Spectrograph on the Lick 3.0-m telescope.

1.3 Analysis

The UV spectrum of PG1148+549 was visually inspected for absorption systems by two members of our team independently, and we unambiguously identify the C IV doublet and Lyα absorption at z=0.00348. Si III absorption cannot be measured due to blending. We fit Voigt profiles to the lines to determine column densities, Doppler parameters, and velocity centroids; the C IV doublet and Ly-α line are shown in Figure 1.1 along with the superimposed apparent column density profiles (Savage & Sembach, 1991) of the doublet, and the corresponding measurements are listed in Table 1. Although Lyα appears to be unsaturated in Figure 1.1, we report the H I column density measurements as lower limits because the line spread function of COS is known to have large wings that can fill in the cores of deep lines (Ghavamian et al., 2009). Because we do not have wavelength coverage for the higher Lyman series lines, we opt for this conservative estimate. With only a lower limit on the H I column density and a precise measurement of a single metal (C IV), we cannot determine the absorber metallicity. Even if we constrain n_H [based on our limit on N(C IV)/N(C II)] and then use n_H to estimate N(H I) by assuming hydrostatic equilibrium (Schaye, 2001), we still find that a very large range of metallicities is allowed.

To search for associated galaxies, we used data from the SDSS along with the follow-up observations described in Section 2. For galaxies brighter than $m_b = 18.2$, our survey is 86% complete out to impact parameter $\rho = 180$ kpc (corresponding to the 1° field of view of Hectospec at the absorber redshift). This magnitude limit corresponds to $L = 0.0008\ L_*$ at the absorber redshift. Table 2 lists the galaxies with measured redshifts within 400 kpc of the absorber with $|\delta v| \leq 900$ km/s of the C IV doublet heliocentric velocity. Verheijen & Sancisi (2001) report a mean distance of

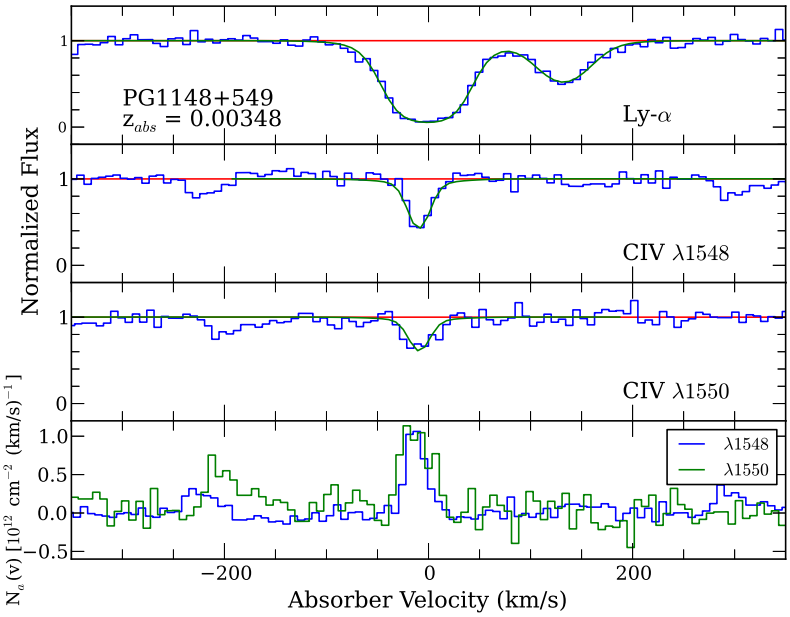

Figure 1.1 Normalized spectrum showing the C IV doublet along with the Lyα line for the z=0.00348 absorber. The bottom pane shows the superimposed apparent column density profiles of the C IV λ 1548 (blue) and λ 1550 (green) lines.

18.6 Mpc for UGC 6894 and galaxies in this vicinity; therefore, the galaxy impact parameters and luminosity (as a fraction of L_*) corresponding to this distance are listed, with the exception of LBT J115205.6+544732.2, which was calculated at the Hubble flow luminosity distance corrected for the Local Group (LG) velocity, Virgo infall, the Great Attractor, and the Shapley Supercluster (Mould et al., 2000).

Figure 1.2 shows the galaxies with measured redshifts within 400 kpc of the absorber and with $|\delta v| \leq 900$ km/s. Here, we call attention to the two closest galaxies to the sightline: UGC 6894 lying almost directly to the east of the sightline and LBT J115205.6+544732.2, which we refer to as "the Grapes" hereafter, lying just northeast of the sightline. UGC 6894 is separated in velocity by -196.9 $\pm$ 15.1 km/s and by 190 kpc in impact parameter; the Grapes is only 23 kpc away but has a velocity difference of -724 $\pm$ 210 km/s. We consider these two galaxies the most likely candidates for association with the absorber because there are no other galaxies brighter than 0.001

L_* closer in impact parameter (kpc). However, we note that a group of luminous and actively star-forming galaxies is found at somewhat larger projected distances northeast of the QSO (see Figure 1.2), two of which are at similar impact parameter in virial radius units as UGC 6894 but are nearly 100 kpc further from the sightline.

We wish to place these potential galaxy/absorber associations into a physical context related to the properties of the galaxies themselves, including their stellar masses (M_*) and halo masses ($M_{\rm halo}$). Therefore, we employ the stellar/halo mass relation of Moster et al. (2013) combined with a stellar mass calculation from the KCORRECT software (Blanton & Roweis, 2007, estimated errors for low mass galaxies: $\pm$50%), which fits stellar population synthesis models to broadband photometry (we use SDSS+2MASS photometry). KCORRECT assumes a Chabrier IMF and H_0 = 100 km/s Mpc^{-1}, and the Moster et al. (2013) formalism also assumes a Chabrier IMF but with H_0 = 70.4 km/s Mpc^{-1}. We use the stellar mass calculation of McIntosh et al. (2008), which simply uses broadband colors, to calculate the ratio of the masses when the absolute magnitudes are scaled using these differing cosmologies. Finally, we scale the stellar mass from KCORRECT and solve the stellar mass/halo mass ratio model derived by Moster et al. (2013) for the halo mass:

$$\frac{M_*}{M_{\rm halo}} = 2\left(\frac{m}{M}\right)_0 \left[\left(\frac{M_{\rm halo}}{M_1}\right)^{-\beta} + \left(\frac{M_{\rm halo}}{M_1}\right)^{\gamma}\right]^{-1} \tag{1.1}$$

where we use their fitted values of log M_1 = 11.594, $(m/M)_0$ = 0.0350, β = 1.3735, and γ = 0.6090, corresponding to z=0.003. The virial radius, defined by a factor of 200 overdensity, is then

$$r_{vir} = \left(\frac{M_{\rm halo}}{200\ (4\pi/3)\ \rho_{\rm crit}}\right)^{\frac{1}{3}} \tag{1.2}$$

Using this formulation, we calculate $log\ M_*$ = 8.62 $M_\odot$, $log\ M_{\rm halo}$ = 10.83 $M_\odot$, and r_{vir}= 133 kpc for UGC 6894. For comparison, we also calculated the virial radius using three other methods (Prochaska et al., 2011; Werk et al., 2012; Stocke et al., 2013) to find r_{vir}= 116 kpc, 160 kpc, and 70 kpc.

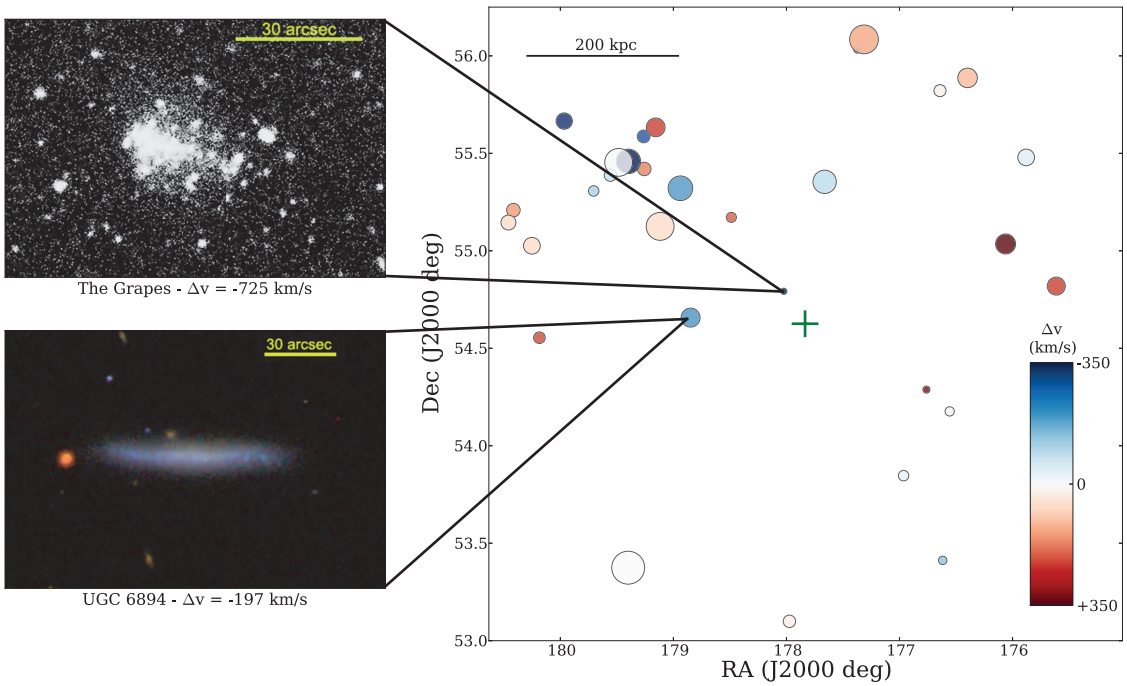

Figure 1.2 The field of PG1148+547 showing all galaxies with measured redshifts within 400 kpc impact parameter to the sightline and 900 km/s of the absorber. The marker colors indicate the recession velocity difference between the galaxy and absorber, and marker sizes indicate the luminosity of the galaxy. For reference, the lower-leftmost galaxy (M109) plotted has luminosity L $\sim$ 2 L*. The two galaxies primarily discussed in this analysis are the Grapes (top image on the left) and UGC 6894 (bottom image on the left).

1.4 Discussion

1.4.1 The Grapes

The Grapes is a dwarf irregular galaxy located at z=0.00107 $\pm$ 0.0007 with an impact parameter of 23 kpc. The redshift was measured from the Hα emission line found in the Lick/Kast spectrum, and we measure a minimum star formation rate (SFR) of 5.9×10^{-6} $M_{\odot}/yr$ from this line (Kennicutt, 1998). This is a minimum SFR for two reasons: first, we do not measure the Hβ emission and therefore cannot correct for dust reddening; second, the Grapes is very clumpy, and our long-slit spectrum did not cover all star clusters in the galaxy. SDSS (DR10) detected the Grapes in its imaging, but resolved it into three individual clumps, two of which are

labeled as faint galaxies. From the SDSS photometry, we estimate stellar masses of M_*= $4.8 \times 10^5 M_\odot$, $9.1 \times 10^3 M_\odot$, and $2.3 \times 10^4 M_\odot$ for these three clumps. This third clump, which SDSS classified as an interloping star, differs in u-g color from the other two, which could indicate that this clump is not associated with the galaxy; also, it is a much fainter object with large photometric uncertainties.

While the Grapes has by far the smallest projected distance and therefore is a prime candidate for the absorbing gas source, the galaxy is separated in velocity by $\delta v = 724 \pm 210$ km/s, where uncertainties of 15 km/s and 210 km/s arise from the COS wavelength calibration and the Kast Hα measurement, respectively. This large δv would seem to suggest that the absorber and galaxy are unrelated, but both models and observations indicate that galaxies can drive outflows with velocities of hundreds of km/s (Tremonti et al., 2007; Murray et al., 2011; Rupke & Veilleux, 2013; Rubin et al., 2014). Of course, the velocity observed is only the radial component, and this δv is a lower limit to the total velocity offset. For a plausible association, one must invoke some sort of feedback process, such as a galactic superwind in which the gas might be entrained. We implemented the formalism of Murray et al. (2010, 2011) to test the plausibility of this galaxy driving a $>$ 500 km/s wind. Even while allowing strong contributions from protostellar jets, overestimating the typical cluster mass (using the mass of the largest clump) and supernova rate, and using a likely gross overestimate of the total galaxy luminosity, we find that we must neglect any resistance from the galaxy ISM, such as turbulence, to accelerate a wind to 200 km/s at comparable impact parameters. On this basis, we conclude that it is unlikely that the Grapes could drive an outflow to sufficient speed to explain the large redshift difference between the absorber and the galaxy.

1.4.2 UGC 6894

UGC 6894 is located on the very outer perimeter of the Ursa Major Cluster (Tully, 1987), which raises some concerns. For example, the halo mass/virial radius calculation could be invalid if the galaxy is actually within the much larger halo of a cluster. However, Tully (1987) define this cluster based purely on spatial overdensity and the members' similar recession velocities, not because the members possess the typical cluster environment characteristics in morphology and velocity dispersion. This region of the sky is dominated by gas-rich, late-type spiral galaxies unlike true clusters, which are dominated by early-type members. Furthermore, using the quoted cluster virial radius from Tully (1987), UGC 6894 is located $> 2\,r_{vir}$ from the apparent spatial center.

We assume an 18.6 Mpc distance (Verheijen & Sancisi, 2001) for UGC 6894, and we note that this distance is much greater than that indicated by a pure Hubble flow from the heliocentric redshift (12.0 Mpc) but is similar to that obtained when correcting for the LG velocity, etc. (17.1 Mpc). At a distance of 18.6 Mpc, the corresponding angular scale is 5.41 kpc/arcmin, and the galaxy's 35.210 arcmin angular distance from the sightline then corresponds to an impact parameter of 190.5 kpc. The recession velocities of the absorber and galaxy differ by 196.9 ± 15.1 km/s, where the uncertainty is dominated by the COS wavelength calibration uncertainty of 15 km/s (Holland, 2012); Verheijen & Sancisi (2001) report a redshift uncertainty of 2 km/s for UGC 6894. As shown in Figure 1.2, the QSO sightline passes almost directly to the east, lying along a direction oriented just 2° south of east from the edge-on major axis of UGC 6894. Based on the four virial radii calculated in Section 3, the absorber appears to be located 1.2-2.7 r_{vir} from the center of UGC 6894.

By using Eqs. 1 & 2 of Davé et al. (2010), we calculate the threshold virial overdensity relative to the critical density at the absorber redshift $\delta_{\rm th} \sim 120$. From our lower limit on N(H I) and Eq. 3 of Davé et al. (2010), we find that log N(H I) =

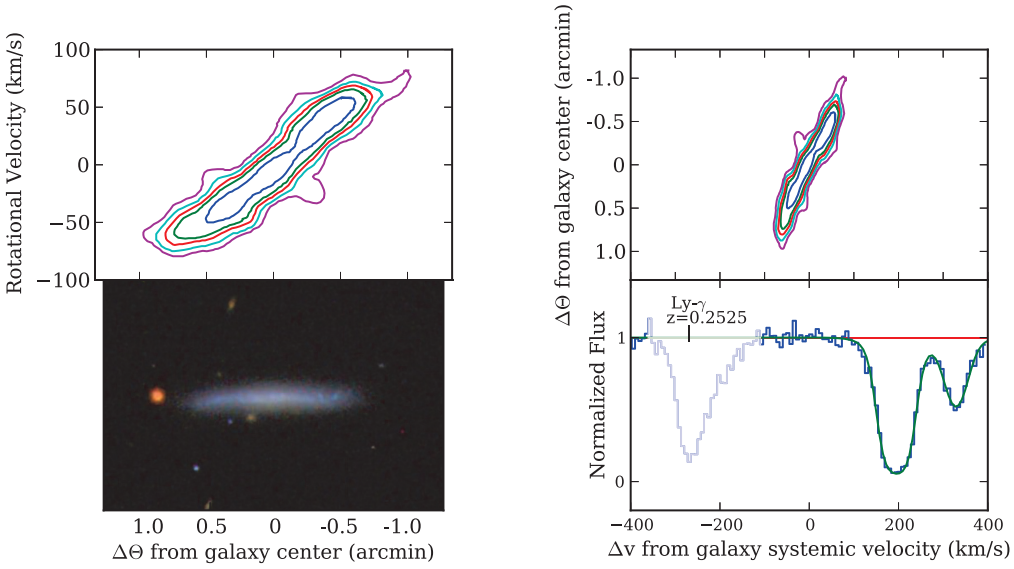

Figure 1.3 (Left) A color composite image of UGC 6894 from the SDSS along with the H I rotation curve from the WSRT. The QSO sightline is off the panel to the right. The galaxy's rotation in this spatial direction is receding (into the plane of the sky), in the same direction as the absorber/galaxy velocity offset. Note that the detected H I emission extends only slightly beyond the optical disk. (Right) The rotation curve from H I line emission along with the absorber Lyα line in the frame of the galaxy systemic velocity. The galaxy's gaseous rotation curve rises through the last point measured, at 63 $\pm$ 5 km/s, and the velocity offset of the absorber is in the same direction as the galaxy's rotation. One arcmin corresponds to $\sim$5.4 kpc, and the outer contours on the H I maps correspond to $\sim 2 \times 10^{20}$ atoms cm^{-2}. Position-velocity data adapted from Verheijen & Sancisi (2001).

14.4 corresponds to an overdensity $\rho/\bar{\rho} \sim 94$, which is consistent with association at a distance just outside the virial radius of a galaxy halo. If the absorber is associated with UGC 6894, one can consider three possible scenarios: (1) the absorber traces gas that is currently neither inflowing nor outflowing, e.g., residing in a gaseous halo, possibly a result of much earlier outflows, (2) the gas is being ejected from the galaxy, or (3) the absorber is tracing accretion from the IGM onto the galaxy.

In considering scenario (1), we question whether $\sim$190 kpc is a reasonable extent for the gaseous disk. Sheth et al. (2010) measure the diameter of the 25th magnitude isophote in the B-band (D_{25}) to be 1.66 arcmin, which corresponds to $\sim$9 kpc. Therefore, 42x this isophotal radius is well beyond a reasonably expected extent of

the disk. This absorber/galaxy pair features a somewhat large extent for a C IV absorber compared to other studies (Bordoloi et al. 2013, in preparation; Chen et al., 2001; Chen & Mulchaey, 2009; Stocke et al., 2013). Tripp et al. (2006) suggested that O VI/C IV systems they detected far away from galaxies may be metal-enriched gas from outflows that occurred in previous epochs. This claim is supported by recent simulations from Ford et al. (2013, submitted). For example, these simulations show a mean column density of N(C IV)=10^{13} cm^{-2} at $\sim$190 kpc for gas attributed to 'ancient outflows' in an $M_{\rm halo} = 10^{11} M_{\odot}$ galaxy, similar to the halo mass of UGC 6894. This material could also be residual gas from dynamical processes such as tidal stripping.

Scenario (2) suffers from several problems. First, the orientation of the galaxy is such that the sightline falls nearly 90° from the polar axis of the galaxy, where biconical outflows are most likely to propagate perpendicular to the disk (Rubin et al., 2014; Bordoloi et al., 2011; Bouché et al., 2012; Kacprzak et al., 2012a). Also, if the gas is outflowing coplanarly with the UGC 6894 disk and was expelled from the more stellar-dense visible disk, the gas would have had to travel directly through the relatively dense medium of the gaseous/stellar disk for billions of years at 100s of km/s all while gaining angular momentum. However, it is possible that this C IV absorber is the detritus from a galactic-fountain flow or from tidal interactions that has settled into the disk and is now returning to the galaxy.

Scenario (3) provides perhaps the most compelling comparison with theory. Figure 1.3 shows the H I rotation curve of UGC 6894 obtained using aperture synthesis (Verheijen & Sancisi, 2001), and the side of the disk closest to the absorber is receding (into the plane of the sky). Consequently, the absorber velocity is roughly consistent with an extension of the rotation curve to a larger angular separation. Such a configuration was predicted by Stewart et al. (2011b) as an observational signature of cool gas accreting into a galaxy via a long, warped disk stream that adds angular

momentum and mass to the galaxy. Absorber velocity separations consistent with the rotation of a disk galaxy have been observed at z=0.4-0.6 by Steidel et al. (2002), but at smaller impact parameters ($\rho \lesssim$75 kpc). Stewart et al. (2011b) predict this accretion signature to be observed at $\rho \sim r_{vir}/3$ at z=0 for L_* galaxies because the transition to hot mode accretion is believed to have occurred (Stewart et al., 2011a) by z=0, as enough mass will have accreted onto the galaxy to exceed the cold/hot mode threshold mass ($M_{\rm halo} \sim 10^{12}$). Therefore, the gas in the outer halo will have been virialized and shock-heated, removing the cool gas signature from the regions near the virial radius. However, UGC 6894 is well below this threshold mass, and we suggest that the absorber could be cool gas accreting onto the galaxy; at low redshifts, cold accretion could occur predominantly in lower mass halos reflecting the shift of star-formation activity to lower mass galaxies at the present epoch (the so-called downsizing trend). To probe this topic with a larger, statistically significant sample, we are now conducting a follow-up survey of the redshifts and properties of galaxies in the vicinity of low-z C IV absorbers blindly identified in COS spectra. The larger survey results will be reported in a forthcoming paper once the follow-up observations are completed.

We thank Neal Katz, John O'Meara, and the referee for helpful discussions and Scott Lange for assistance with the Keck observations. The authors wish to recognize and acknowledge the very significant cultural role and reverence that the summit of Mauna Kea has always had within the indigenous Hawaiian community. We are most fortunate to have the opportunity to conduct observations from this mountain. This research was supported by NASA grant HST-GO-11741 from the STScI and by NSF grant AST-0908334 and AST-1212012.

CHAPTER 2

A DEEP SEARCH FOR FAINT GALAXIES ASSOCIATED WITH VERY LOW-REDSHIFT C IV ABSORBERS: II. PROGRAM DESIGN, ABSORPTION-LINE MEASUREMENTS, AND ABSORBER STATISTICS

Joseph N. Burchett[1], Todd M. Tripp[1], J. Xavier Prochaska[2], Jessica K. Werk[2], Jason Tumlinson[3], John M. O'Meara[4], Rongmon Bordoloi[3], Neal Katz[1], and C. N. A. Willmer[5]

To investigate the evolution of metal-enriched gas over recent cosmic epochs as well as to characterize the diffuse, ionized, metal-enriched circumgalactic medium (CGM), we have conducted a blind survey for C IV absorption systems in 89 QSO sightlines observed with the Hubble Space Telescope (HST) Cosmic Origins Spectrograph (COS). We have identified 42 absorbers at z < 0.16, comprising the largest uniform blind sample size to date in this redshift range. Our measurements indicate an increasing C IV absorber number density per comoving path length ($d\mathcal{N}/dX = 7.5 \pm 1.1$) and modestly increasing mass density relative to the critical density of the Universe ($\Omega_{\rm C\ IV} = 10.0 \pm 1.5 \times 10^{-8}$) from $z \sim 1.5$ to the present epoch, consistent with predictions from cosmological hydrodynamical simulations. Furthermore,

[1]Department of Astronomy, University of Massachusetts, 710 North Pleasant Street, Amherst, MA 01003-9305

[2]UCO/Lick Observatory, University of California, Santa Cruz, CA

[3]Space Telescope Science Institute, Baltimore, MD 21218

[4]Department of Chemistry and Physics, Saint Michaels College, One Winooski Park, Colchester, VT 05439

[5]Steward Observatory, University of Arizona, Tucson, AZ, 85721

the data support a functional form for the column density distribution function that deviates from a single power-law, also consistent with independent theoretical predictions. As the data also probe heavy element ions in addition to C IV at the same redshifts, we identify, measure, and search for correlations between column densities of these species where components appear aligned in velocity. Among these ion-ion correlations, we find evidence for tight correlations between C II and Si II, C II and Si III, and C IV and Si IV, suggesting that these pairs of species arise in similar ionization conditions. However, the evidence for correlations decreases as the difference in ionization potential increases. Finally, when controlling for observational bias, we find only marginal evidence for a correlation (86.8% likelihood) between the Doppler line width b(C IV) and column density N(C IV).

2.1 Introduction

Within the first spectra of quasars (Burbidge et al., 1966; Lynds et al., 1966), astronomers detected absorption lines from intervening, enriched gas with properties distinct from the dense, neutral gas characteristic of the interstellar medium (ISM). This gas contains neutral hydrogen column densities $N(H\ \mathrm{I})$ that are several orders-of-magnitude lower than galactic disks and have associated high-ion absorption (e.g., C IV, Si IV) that is suggestive of a diffuse, ionized medium. Together, these data inspired predictions that the absorption arises in a 'halo gas' that surrounds distant galaxies (Bahcall & Spitzer, 1969). Decades of subsequent research has confirmed this basic interpretation (e.g., Bergeron et al., 1987; Morris et al., 1993; Bowen et al., 1995; Lanzetta et al., 1995b; Bowen et al., 1996; Chen et al., 2001; Prochaska et al., 2011), and dedicated surveys of metal-line transitions have yielded statistical constraints on the cosmic distribution and mass density of heavy elements (e.g., Sargent et al., 1979, 1988).

Ironically, the most rapid progress occurred first for the high-z universe owing to the construction of 10 m-class, ground-based telescopes. These facilities could access redshifted far-UV transitions of, e.g., Mg II and C IV in the spectra of $z > 2$ quasars. Indeed, the first such spectra recorded with Keck/HIRES revealed a remarkably high incidence of C IV absorbers from gas with N(H I)$\lesssim 10^{15}$ cm^{-2} (Cowie et al., 1995), and statistical techniques indicated significant C IV enrichment also for gas with N(H I)$\lesssim 10^{14}$ cm^{-2} (Cowie & Songaila, 1998; Ellison et al., 2000). Specifically, the cosmic incidence of C IV systems, $d\mathcal{N}/dX$ (with dX the differential absorption path length; Bahcall & Peebles, 1969), at column densities $12 \leq \log N(\text{C IV}) \leq 15$ cm^{-2} was ~ 14 at $z \approx 3$ (D'Odorico et al., 2010), exceeding theoretical predictions (Cen & Chisari, 2011) in the ΛCDM cosmology. Also, cosmological simulations (Booth et al., 2012) reproducing the observed C IV optical depth relative to H I (Schaye et al., 2003) require that the gas between galaxies, the intergalactic medium (IGM), was enriched by ejecta from low-mass haloes at early times.

A simple integration of the observed C IV column densities N(C IV) normalized by the total survey path ΔX yields the cosmic mass density in C IV, $\Omega_{\text{C IV}}$. In principle, this quantity assesses the enrichment of intergalactic gas, and researchers have measured $\Omega_{\text{C IV}}$ across cosmic time to track chemical evolution (e.g, Songaila, 2001; Cooksey et al., 2010; D'Odorico et al., 2010). In practice, however, $\Omega_{\text{C IV}}$ may be dominated by metals from gas surrounding galaxies (the so-called circumgalactic medium or CGM) and may have little correspondence to the enrichment of the IGM. Furthermore, the C IV ion may not be the dominant ionization state of C in diffuse gas at any epoch, and the C IV/C ratio likely evolves with redshift in a complex fashion (Oppenheimer et al., 2012; Cen & Chisari, 2011). Nevertheless, an evaluation of $\Omega_{\text{C IV}}$ with cosmic time does offer a unique constraint on the enrichment history of the universe (Oppenheimer & Davé, 2006). Analysis at $z > 2$ yields a relatively constant $\Omega_{\text{C IV}}$ value from $z \sim 2 - 5$ (Songaila, 2001; Pettini et al., 2003), although

Cooksey et al. (2013) and D'Odorico et al. (2010) show a modest smooth decrease in $\Omega_{\rm C\ IV}$ with increasing z, and then a steep decline at higher z (Ryan-Weber et al., 2009; Simcoe et al., 2011). The latter may suggest a decline in enrichment at early times (although D'Odorico et al. (2013) do not find a sharp decline at $z > 5$) while the former has been interpreted as evidence for ongoing enrichment (Simcoe, 2011).

Progress on such research at $z \ll 2$ has been stymied by technical limitations. At these redshifts, the key (far-UV) transitions for diffuse gas shift to observed wavelengths $\lambda_{\rm obs} < 3000$ Å, requiring space-borne UV spectrometers. Furthermore, the expansion of the universe alone implies fewer detections per Å of spectrum. Indeed, a statistical survey at low-z requires nearly an order-of-magnitude more sightlines than at $z \approx 3$. This has resulted in relatively slow progress at $z < 1$ despite the many years of observations with UV spectrometers on *HST*.

Over time, however, the well-maintained *HST* archive has eventually enabled such analysis. Drawing on the GHRS and STIS high-dispersion datasets, Cooksey et al. (2010) and Cooksey et al. (2011) examined the incidence and mass density of C IV and Si IV, respectively, at $z < 1$. Furthermore, the $z \lesssim 0.15$ regime has been studied by Tilton et al. (2012) and Shull et al. (2014). These four studies all agree that the frequency of strong C IV absorption and, therefore, the related mass density have increased since early cosmic time ($z \sim 5$), suggesting that the diffuse gas surrounding and between galaxies has been continuously enriched. However, some discrepancy remains in the very-low-z regime whether the C IV mass density as traced by $\Omega_{\rm C\ IV}$ has experienced a sudden upturn (Tilton et al., 2012).

The installation of COS has lead to a resurgence of quasar spectroscopy with *HST* and, subsequently, a statistically powerful archival dataset covering $\lambda \approx 1150 - 1700$ Å. We therefore recognized the potential for two major advances as regards C IV:

1. improved statistics in the present-day universe ($z < 0.1$);

2. the opportunity to examine the physical association of this enriched gas to galaxies at unprecedented levels.

As stated above, additional motivation for conducting an absorber survey at low redshift comes from the feasible opportunity to conduct deep, high spatial resolution, multiwavelength studies of the galaxy environments near the absorbers with high *spectroscopic* completeness; indeed, rich publicly available data already exist. The papers in this series present the results of our survey that combines HST/COS UV QSO spectroscopy covering the $\lambda\lambda$ 1548.2, 1550.8 Å C IV doublet and many other heavy element ion transitions down to $z \sim 0$ with corresponding deep galaxy spectroscopy and imaging in these QSO fields. Our survey aims for unprecedented spectroscopic completeness to faint galaxies on the order of 0.01 $L*$ in the environments along the QSO lines of sight, once again enabled by the low-redshift nature of the absorber sample. The first paper in this series (Paper I, Burchett et al., 2013) focused on one such absorber environment. The current paper (Paper II) presents the parent C IV absorber sample and focuses on analyses of the UV absorption data, including the integrated cosmic enrichment in the most recent epoch as traced by the cosmic mass density mentioned above. Subsequent papers will present analyses of galaxy-absorber CGM relationships leveraging the galaxy survey data from public sources (Paper III) and our own ongoing ground-based observational campaign (Paper IV).

This paper is organized as follows: In Sections 2 and 3, we describe our data sources and measurements, respectively. Section 4 presents our calculated C IV evolutionary statistics and discusses them in context with previous work. Section 5 examines relationships between the various metal ions measured in our QSO spectroscopy, and Section 6 focuses on the possible relationship between C IV column density and Doppler line width. We summarize our results in Section 7. Throughout, we assume a cosmology of $H_0 = 70$ km/s Mpc^{-1}, $\Omega_M = 0.3$, and $\Omega_\Lambda = 0.7$.

2.2 Data

2.2.1 HST/COS Spectroscopy

Our C IV sample is composed of systems detected in 89 sightlines targeted by three Hubble Space Telescope (HST) programs using the Cosmic Origins Spectrograph (COS; Green et al., 2012): COS-Halos (Tumlinson et al., 2013; Werk et al., 2012), COS-Dwarfs (Bordoloi et al., 2014), and the COS Absorption Survey of Baryon Harbors (CASBaH, Tripp et al., 2011; Meiring et al., 2013). Information about the QSOs included in this study is presented in Table 2.1, and we will generally refer to them with abbreviated versions of their names in this table. All of these data use the G130M and G160M gratings, covering the wavelength range 1100-1800 Å, and were reduced as descrbed by Meiring et al. (2011). Due to the differing goals of each survey, the spectra possess various signal-to-noise ratios (S/N), and the S/N varies greatly across the wavelength range of each spectrum (see Section 2.3.3); the COS-Halos and COS-Dwarfs data have typical S/N values of ∼11 per ∼18 km/s resolution element, while CASBaH spectra have S/N ∼30 per resolution element (also ∼18 km/s). The COS-Halos survey targeted 42 QSO sightlines that pass within 150 kpc of $L \sim L*$ galaxies with various stellar masses, star-formation rates, and impact parameters at redshifts $z = 0.15 - 0.35$ that bring the O VI $\lambda\lambda$ 1031.7, 1037.8 Å doublet and Lyα 1215.7 Å lines into the G130M/G160M bandpasses. The COS-Dwarfs survey similarly targeted sightlines that pass near known galaxies with selected star-formation properties and masses, but the 43 galaxies selected were specifically $L < 0.1\ L*$ galaxies. Also, the galaxies selected for COS-Dwarfs are at a lower redshift range, z_{gal} = 0.02-0.08, ideal for detecting the C IV doublet with COS. Lastly, the highest S/N spectra in our dataset comes from the CASBaH survey (PI: Tripp), which targeted higher-redshift QSOs to measure transitions from high ions such as Ne VIII, Mg X, and Si XII. These 9 sightlines were not targeted based on pres-

elected proximal galaxies, but deep follow-up galaxy environment data is currently being obtained around them (Meiring et al., 2011).

Table 2.1. QSO Sample for C IV survey.

QSO Name	α (J2000 deg)	δ (J2000 deg)	$z_{\rm qso}$
SDSS J001224.01-102226.5	3.1001	−10.3740	0.228
SDSS J004222.29-103743.8	10.5929	−10.6288	0.424
SDSS J015530.02-085704.0	28.8751	−8.9511	0.165
SDSS J021218.32-073719.8	33.0764	−7.6222	0.174
SDSS J022614.46+001529.7	36.5603	0.2583	0.615
PHL 1337	38.7808	−4.0349	1.437
SDSS J024250.85-075914.2	40.7119	−7.9873	0.377
SDSS J025937.46+003736.3	44.9061	0.6268	0.534
SDSS J031027.82-004950.7	47.6159	−0.8308	0.080
SDSS J040148.98-054056.5	60.4541	−5.6824	0.570
FBQS 0751+2919	117.8013	29.3273	0.915
SDSS J080359.23+433258.4	120.9968	43.5496	0.449
SDSS J080908.13+461925.6	122.2839	46.3238	0.657
SDSS J082024.21+233450.4	125.1009	23.5807	0.470
SDSS J082633.51+074248.3	126.6396	7.7134	0.311
SDSS J084349.49+411741.6	130.9562	41.2949	0.990
SDSS J091029.75+101413.6	137.6240	10.2371	0.463
SDSS J091235.42+295725.4	138.1476	29.9571	0.305
SDSS J091440.38+282330.6	138.6683	28.3918	0.735
SDSS J092554.43+453544.4	141.4768	45.5957	0.329
SDSS J092554.70+400414.1	141.4779	40.0706	0.471
SDSS J092837.98+602521.0	142.1583	60.4225	0.296
SDSS J092909.79+464424.0	142.2908	46.7400	0.240
SDSS J093518.19+020415.5	143.8258	2.0710	0.649
SDSS J094331.61+053131.4	145.8817	5.5254	0.564
SDSS J094621.26+471131.3	146.5886	47.1920	0.230
SDSS J094733.21+100508.7	146.8884	10.0858	0.139
SDSS J094952.91+390203.9	147.4705	39.0344	0.365
SDSS J095000.73+483129.3	147.5031	48.5248	0.589
SDSS J095915.65+050355.1	149.8152	5.0653	0.162
SDSS J100102.55+594414.3	150.2606	59.7373	0.746
SDSS J100902.06+071343.8	152.2586	7.2289	0.456
SDSS J101622.60+470643.3	154.0942	47.1120	0.822
SDSS J102218.99+013218.8	155.5791	1.5386	0.789
PG1049-005	162.9643	−0.8549	0.359
SDSS J105945.23+144142.9	164.9385	14.6953	0.631
SDSS J105958.82+251708.8	164.9951	25.2858	0.662
SDSS J110312.93+414154.9	165.8039	41.6986	0.402
SDSS J110406.94+314111.4	166.0289	31.6865	0.434
SDSS J111239.11+353928.2	168.1630	35.6578	0.636
SDSS J111754.31+263416.6	169.4763	26.5713	0.421
SDSS J112114.22+032546.7	170.3092	3.4297	0.152
SDSS J112244.89+575543.0	170.6870	57.9286	0.906
SDSS J113327.78+032719.1	173.3658	3.4553	0.525
SDSS J113457.62+255527.9	173.7401	25.9244	0.710
PG1148+549	177.8353	54.6259	0.975
SDSS J115758.72-002220.8	179.4947	−0.3725	0.260
PG1202+281	181.1754	27.9033	0.165
SDSS J120720.99+262429.1	181.8375	26.4081	0.324
PG1206+459	182.2417	45.6765	1.163
SDSS J121037.56+315706.0	182.6565	31.9517	0.389
SDSS J121114.56+365739.5	182.8107	36.9610	0.171
SDSS J122035.10+385316.4	185.1463	38.8879	0.376
SDSS J123304.05-003134.1	188.2669	−0.5262	0.471
SDSS J123335.07+475800.4	188.3962	47.9668	0.382
SDSS J123604.02+264135.9	189.0168	26.6933	0.209
SDSS J124154.02+572107.3	190.4751	57.3520	0.583
SDSS J124511.25+335610.1	191.2969	33.9361	0.711

Table 2.1 (cont'd)

QSO Name	α (J2000 deg)	δ (J2000 deg)	$z_{\rm qso}$
SDSS J132222.68+464535.2	200.5945	46.7598	0.375
SDSS J132704.13+443505.0	201.7672	44.5847	0.331
SDSS J133045.15+281321.4	202.6881	28.2226	0.417
SDSS J133053.27+311930.5	202.7220	31.3252	0.242
PG1338+416	205.2533	41.3872	1.214
SDSS J134206.56+050523.8	205.5274	5.0900	0.266
SDSS J134231.22+382903.4	205.6301	38.4843	0.172
SDSS J134246.89+184443.6	205.6954	18.7455	0.383
SDSS J134251.60-005345.3	205.7150	−0.8959	0.326
SDSS J135625.55+251523.7	209.1065	25.2566	0.164
SDSS J135712.61+170444.1	209.3026	17.0789	0.150
PG1407+265	212.3496	26.3059	0.940
SDSS J141910.20+420746.9	214.7925	42.1297	0.873
SDSS J143511.53+360437.2	218.7980	36.0770	0.429
SDSS J143726.14+504555.8	219.3589	50.7655	0.783
LBQS 1435-0134	219.4512	−1.7863	1.308
SDSS J144511.28+342825.4	221.2970	34.4737	0.697
SDSS J145108.76+270926.9	222.7865	27.1575	0.064
SDSS J151428.64+361957.9	228.6194	36.3328	0.695
SDSS J152139.66+033729.2	230.4153	3.6248	0.126
PG1522+101	231.1022	9.9748	1.328
SDSS J154553.48+093620.5	236.4729	9.6057	0.665
SDSS J155048.29+400144.9	237.7012	40.0291	0.497
SDSS J155304.92+354828.6	238.2705	35.8079	0.722
SDSS J155504.39+362848.0	238.7683	36.4800	0.714
SDSS J161649.42+415416.3	244.2059	41.9046	0.440
SDSS J161711.42+063833.4	244.2976	6.6426	0.229
SDSS J161916.54+334238.4	244.8189	33.7107	0.471
PG1630+377	248.0047	37.6306	1.476
SDSS J225738.20+134045.4	344.4092	13.6793	0.594
SDSS J234500.43-005936.0	356.2518	−0.9933	0.789

2.3 Measurements

2.3.1 Line Identification

We used a multi-step visual identification process to search for C IV systems within our 89 spectra observed with the G130M and G160M gratings, which enable coverage of the C IV doublet at $z \lesssim 0.16$. To aid in the search for the C IV doublet, we created a user interface to scroll through a spectrum, select a candidate λ 1548 feature, and view the alignment of the 1548 and 1550 features in velocity space and in their apparent column density profiles (Sembach & Savage, 1992; Savage & Sembach, 1991). The apparent column density (as a function of velocity) is defined as follows:

$$N(v) = \frac{m_e c}{\pi e^2 f \lambda} \tau(v) \tag{2.1}$$

where m_e is the electron mass, c is the speed of light, λ is the wavelength, and f is the line oscillator strength. $\tau(v)$ is the apparent optical depth at a given velocity and is defined as

$$\tau(v) = \ln \frac{I_c(v)}{I(v)} \tag{2.2}$$

where $I_c(v)$ is the continuum intensity and $I(v)$ is the observed intensity.

If neither of the lines is blended with interloping absorption from another species and if the lines are not saturated, the apparent column density profiles should align. However, if the apparent column density corresponding to the 1550 line appears greater over a portion of the profile, the 1548 line may be saturated. If the 1548 line apparent column density appears greater than that of the 1550 line, the 1548 line may be blended with an interloper; otherwise, the candidate absorber may be rejected because $f_{1548}\lambda_{1548}/f_{1550}\lambda_{1550} \sim 2$, and a greater apparent column density for the 1548 line is unphysical. In cases of possible blending, we accepted the candidate as a detection if the two apparent column density profiles were aligned in regions of the profile unaffected by a conspicuous interloper.

To further scrutinize the candidate systems, we searched for other common lines, such as Lyα , C II, and Si III, within $\pm$400 km/s of the 'systemic redshift' determined by the C IV absorption. However, we emphasize that the presence of these other lines *was not a necessary criterion* for inclusion in our sample; the purpose was merely to offset some doubt initially held about the system, such as the apparent column density profiles being imprecisely aligned, which could occur merely due to known errors in the COS wavelength calibration (up to $\pm$40 km/s according to Wakker et al., 2015). Then, each system was checked for significance of detection, where we required 3σ detections for both the 1548 and 1550 lines. If a suspected C IV doublet was possibly blended with an interloping line, we used Voigt profile fitting to first fit the contaminant and then assess whether enough optical depth remained in the line profile to account for the presence of C IV. The candidates passing these tests were

then checked for common misidentifications, notably interloping Lyman series lines and higher-z O I 1302, Si II 1304 pairs, which have a similar wavelength separation to the C IV doublet.

Once we had established our independent sample of C IV candidates, we flagged those systems that were at the redshifts of the galaxies targeted in the original COS-Halos and COS-Dwarfs surveys, as those targeted systems would not compose a blind sample and were thus not included in the analyses presented here. Although none were detected, the survey design also called for omitting absorbers within 5000 km/s of the QSO redshifts, based on the Tripp et al. (2008) finding of a proximate O VI absorber overabundance within 5000 km/s of observed QSO redshifts. Lastly, we compared our identifications with those from the COS-Halos and COS-Dwarfs studies for verification. A previous detection by those studies was not required because their analysis was primarily focused on absorption associated with their targeted galaxies. Finally, we were left with a 42-absorber sample (see Figure 2.1).

2.3.2 Absorption Line Measurements

For our equivalent width (EW) and column density measurements, we fit local continua within $\pm$ 500 km/s of each line center using Legendre polynomials whose order was determined by an F-test (Sembach & Savage, 1992), typically 3rd or 4th order. We then measured the equivalent width of each line and calculated the integrated apparent column density, assuming the line was unsaturated and, therefore, on the linear part of the curve of growth.

We then normalized the spectrum flux by the fitted continuum and fit Voigt profiles to the absorption lines to measure column densities, Doppler parameters, and velocity centroids using our own software based on a Levenberg-Marquardt optimization algorithm. COS possesses a unique line spread function (Ghavamian et al., 2009) with large wings, and we accounted for this in the profile fitting process. In several

cases, multiple absorption components were evident for a given species, and we attempted to fit the minimum number of components to account for the optical depth in each profile, including any apparent asymmetry, upon visual inspection. Doublet components were fit simultaneously as were interloping lines where blending from other species was evident. This blending could be observed, for example, by odd features in the (mostly) aligned apparent column density profiles of the doublet or by large asymmetries in the line profiles. In certain cases, line profiles were partially or completely obscured by the geocoronal O I λ 1302 Å emission lines, preventing their measurement.

The resulting Voigt profile fitting measurements are presented in Table 1, and plots of the absorber sample spectra along with our profile fits are presented in the Appendix. Likely due in part to the resolution of our data, certain lines yield invalid Doppler b-value measurements, and these these values are omitted from the table. However, measurements of b(C IV)$<$ 10 km/s may also be unreliable. For components of species with no unsaturated lines that would yield reliable Voigt profile fitting measurements, we report the integrated apparent column density profiles as lower limits.

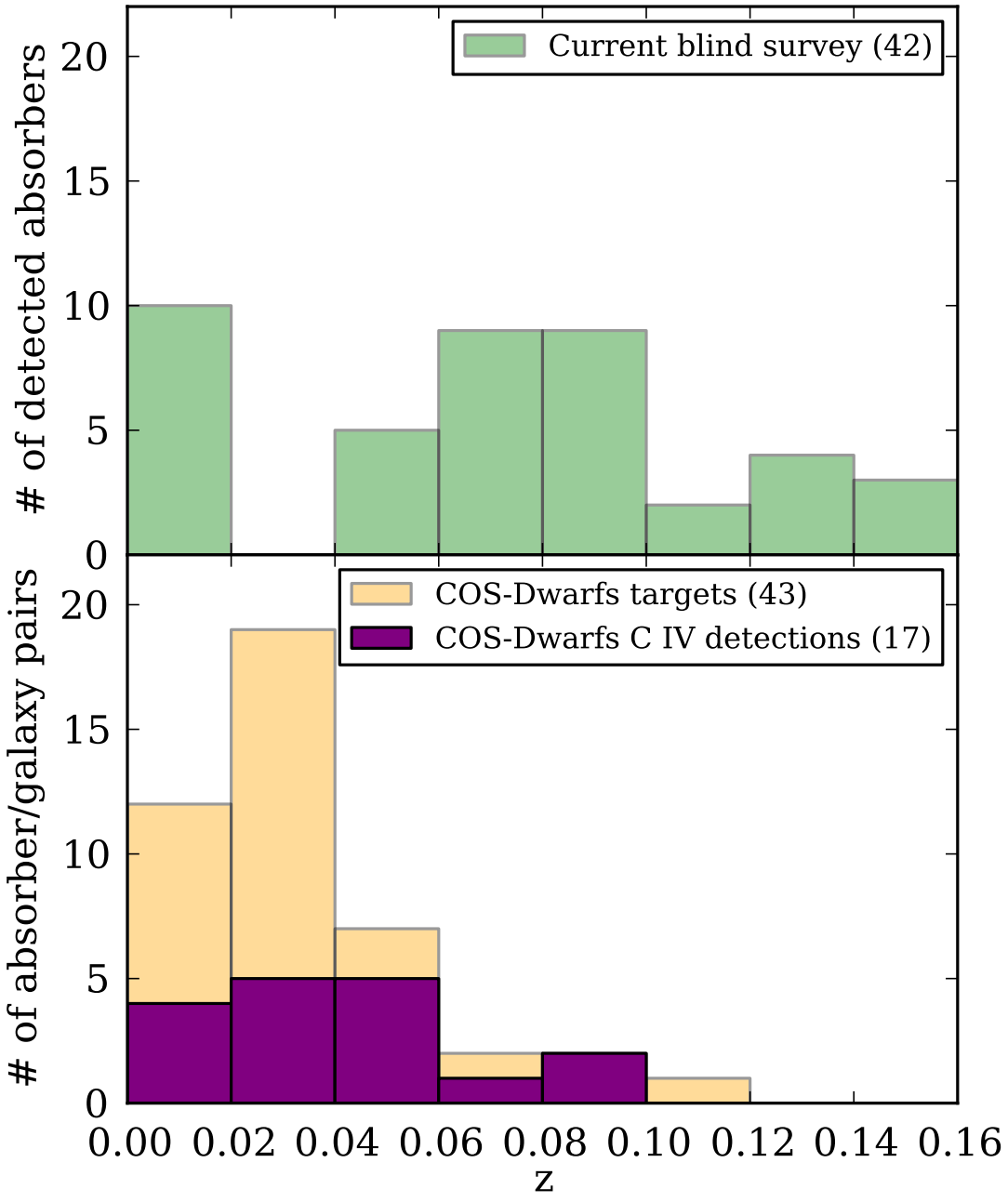

Figure 2.1 (Top) Our blind survey sample of 42 C IV absorbers distributed by redshift. (Bottom) Galaxy-selected targets from the COS-Dwarfs survey (Bordoloi et al., 2014) and the subset for which they detected C IV. To achieve a purely blind sample, absorbers associated with the COS-Dwarfs target galaxies were excluded from the analyses in this paper and are thus not counted in the top panel.

Table 2.2. Voigt profile fitting measurements by absorber component

QSO	z_{abs}	Ion	Lines in profile fit	log N[c](cm^{-2})	b (km/s)	v (km/s)
J0155-0857	0.00547	C IV	1548.2, 1550.8	13.78 ± 0.07	34 ± 9	-38 ± 6
		C IV	1548.2, 1550.8	13.02 ± 0.32	16 ± 19	27 ± 11
		H I		>14.35	-	-
	0.05416	C IV	1548.2, 1550.8	13.75 ± 0.29	7 ± 5	40 ± 2
		H I		>14.15	-	-
J0242-0759	0.00477	C IV	1548.2, 1550.8	13.81 ± 0.08	39 ± 10	-23 ± 6
		H I		>14.42	-	-
		H I	1215.7	13.79 ± 0.12	22 ± 7	-148 ± 5
		Si IV	1393.8, 1402.8	13.04 ± 0.07	30 ± 8	-6 ± 5
J0925+4004	0.00261	C IV	1548.2, 1550.8	14.19 ± 0.07	34 ± 6	9 ± 4
		H I		>14.13	-	-
J0928+6025	0.01494	C IV	1548.2, 1550.8	13.77 ± 0.03	25 ± 3	-23 ± 2
		H I		<14.19	-	-
J0950+4831	0.08049	C IV	1548.2, 1550.8	14.08 ± 0.12	22 ± 6	-8 ± 4
		H I	1215.7	13.84 ± 0.06	26 ± 4	-26 ± 3
J1001+5944	0.15037	C II	1334.5	13.41 ± 0.12	29 ± 13	-29 ± 8
		C IV[a]	1548.2, 1550.8	14.25 ± 0.40	9 ± 3	-16 ± 2
		H I		>14.30	-	-
		N V	1238.8, 1242.8	13.59 ± 0.16	6 ± 3	-6 ± 1
		Si III	1206.5	12.47 ± 0.08	22 ± 7	6 ± 4
J1009+0713	0.05860	C II	1334.5	13.79 ± 0.09	13 ± 5	7 ± 3
		C IV	1548.2, 1550.8	14.08 ± 0.10	29 ± 7	-1 ± 5
		H I		>14.61	-	-
		Si II	1304.4	13.59 ± 0.21	16 ± 14	-14 ± 8
		Si III[a]	1206.5	13.37 ± 0.29	18 ± 7	4 ± 4
		Si IV	1393.8, 1402.8	13.09 ± 0.09	16 ± 6	9 ± 4
	0.11401	C II		>14.61	-	-
		C IV	1548.2, 1550.8	13.57 ± 0.29	9 ± 10	37 ± 5
		C IV	1548.2, 1550.8	13.86 ± 0.17	52 ± 26	-32 ± 18
		Fe II[a]	1608.5	14.82 ± 0.46	23 ± 12	-6 ± 7
		H I[a]	1215.7	20.71 ± 0.01	-	-23 ± 14
		N I		>14.24	-	-
		Si II		>14.22	-	-
		Si III		>13.42	-	-
J1059+1441	0.00242	C II	1334.5	13.46 ± 0.11	10 ± 6	-18 ± 3
		C IV	1548.2, 1550.8	14.06 ± 0.04	20 ± 2	-6 ± 1
		H I		>14.15	-	-
	0.13291	C IV	1548.2, 1550.8	13.57 ± 0.11	42 ± 14	10 ± 10
		H I		>14.93	-	-
		O VI	1031.9, 1037.6	14.26 ± 0.04	72 ± 9	36 ± 7
J1059+2517	0.07884	C II	1334.5	13.97 ± 0.05	51 ± 7	5 ± 5
		C IV	1548.2, 1550.8	13.48 ± 0.22	9 ± 8	-21 ± 4
		C IV	1548.2, 1550.8	13.87 ± 0.14	35 ± 16	32 ± 9
		H I		>14.55	-	-
		Si IV	1393.8, 1402.8	13.38 ± 0.05	53 ± 8	11 ± 5
	0.11884	C II	1334.5	13.59 ± 0.10	22 ± 9	-3 ± 5
		C IV	1548.2, 1550.8	14.16 ± 0.06	25 ± 3	-8 ± 2
		H I[a]	1215.7, 1025.7	14.43 ± 0.13	38 ± 4	-33 ± 3
		O VI	1031.9, 1037.6	13.95 ± 0.11	37 ± 13	-10 ± 9
		Si III	1206.5	12.91 ± 0.06	23 ± 4	-28 ± 3
J1104+3141	0.06223	C IV	1548.2, 1550.8	14.28 ± 0.09	18 ± 2	-24 ± 2
		H I		>14.25	-	-
		H I	1215.7	13.53 ± 0.09	36 ± 9	-137 ± 7
J1112+3539	0.01726	C IV	1548.2, 1550.8	14.05 ± 0.10	44 ± 11	-
		C IV	1548.2, 1550.8	13.68 ± 0.50	-	-34 ± 7
		H I	1215.7	13.48 ± 0.27	10 ± 6	-49 ± 3
		H I	1215.7	13.36 ± 0.13	16 ± 8	13 ± 5
		H I	1215.7	13.15 ± 0.18	35 ± 21	144 ± 14

Table 2.2 (cont'd)

QSO	z_{abs}	Ion	Lines in profile fit	log N[c](cm^{-2})	b (km/s)	v (km/s)
J1117+2634	0.04758	C II	1334.5	14.05 ± 0.08	20 ± 5	-71 ± 4
		C II	1334.5	14.51 ± 0.19	15 ± 4	-25 ± 2
		C IV	1548.2, 1550.8	13.91 ± 0.08	18 ± 5	-65 ± 4
		C IV	1548.2, 1550.8	14.12 ± 0.08	19 ± 4	-8 ± 3
		H I		>14.52	-	-
		Si II	1193.3, 1190.4	13.44 ± 0.04	22 ± 3	-19 ± 3
		Si III	1206.5	13.30 ± 0.23	16 ± 6	-14 ± 6
		Si III	1206.5	12.99 ± 0.24	24 ± 11	-57 ± 13
		Si IV	1393.8, 1402.8	13.43 ± 0.04	19 ± 2	-16 ± 2
J1122+5755	0.00640	C IV[a]	1548.2, 1550.8	14.33 ± 0.07	24 ± 3	21 ± 2
		H I		>14.03	-	-
		H I	1215.7	12.97 ± 0.22	-	-77 ± 4
		H I	1215.7	13.86 ± 0.15	24 ± 6	-162 ± 4
	0.05316	C IV	1548.2, 1550.8	13.73 ± 0.11	30 ± 10	0 ± 7
		H I[a]	1215.7	15.32 ± 2.33	19 ± 12	-10 ± 3
		Si III	1206.5	12.72 ± 0.10	16 ± 6	16 ± 4
J1210+3157	0.05991	C II	1334.5	14.10 ± 0.06	19 ± 3	-42 ± 2
		C IV[a]	1548.2, 1550.8	14.38 ± 0.08	21 ± 2	-30 ± 2
		H I		>14.15	-	-
		Si II	1260.4, 1190.4	13.21 ± 0.07	43 ± 8	-59 ± 6
		Si III	1206.5	13.09 ± 0.13	20 ± 7	-48 ± 4
		Si IV	1402.8, 1393.8	13.29 ± 0.05	19 ± 4	-37 ± 5
	0.07374	C IV	1548.2, 1550.8	13.75 ± 0.05	25 ± 4	-10 ± 3
		H I[b]	-	-	-	-
	0.07818	C IV	1548.2, 1550.8	13.66 ± 0.07	9 ± 2	-12 ± 2
		H I	1215.7	13.89 ± 0.12	20 ± 5	-23 ± 3
		H I	1215.7	13.84 ± 0.11	22 ± 5	-119 ± 4
	0.14959	C II	1036.3, 1334.5	14.19 ± 0.05	41 ± 6	10 ± 4
		C IV[a]	1548.2, 1550.8	14.33 ± 0.12	37 ± 9	-8 ± 7
		H I		>14.90	-	-
		O VI	1031.9, 1037.6	14.65 ± 0.06	45 ± 6	-16 ± 4
		Si II	1190.4, 1193.3, 1260.4	13.04 ± 0.04	40 ± 5	-4 ± 21
		Si III[a]	1206.5	13.68 ± 0.07	38 ± 3	4 ± 2
		Si IV	1393.8, 1402.8	13.49 ± 0.07	42 ± 10	-2 ± 7
J1211+3657	0.07777	C IV	1548.2, 1550.8	14.11 ± 0.07	24 ± 4	-5 ± 2
		H I		>14.16	-	-
J1233-0031	0.00392	C IV	1548.2, 1550.8	13.59 ± 0.09	13 ± 4	-22 ± 3
		H I		>14.18	-	-
J1241+5721	0.14728	C II	1334.5	13.96 ± 0.06	40 ± 7	-47 ± 5
		C IV[a]	1548.2, 1550.8	13.64 ± 0.20	29 ± 19	-13 ± 12
		H I		>17.86	-	-
		O VI	1031.9, 1037.6	14.45 ± 0.04	67 ± 7	-14 ± 5
		Si II	1260.4	12.79 ± 0.06	28 ± 7	-33 ± 4
		Si III	1206.5	13.21 ± 0.04	44 ± 5	-45 ± 4
		Si III	1206.5	12.65 ± 0.10	33 ± 11	75 ± 7
J1342+0505	0.13993	C II	1036.3, 1334.5	14.26 ± 0.02	32 ± 2	-148 ± 1
		C II	1036.3, 1334.5	13.85 ± 0.04	30 ± 5	42 ± 3
		C IV	1548.2, 1550.8	13.85 ± 0.15	19 ± 8	-177 ± 6
		C IV[a]	1548.2, 1550.8	14.30 ± 0.08	65 ± 13	-9 ± 9
		H I		>14.67	-	-
		O VI	1031.9, 1037.6	14.60 ± 0.03	-	-1 ± 6
		O VI	1031.9, 1037.6	14.43 ± 0.04	-	-156 ± 9
		Si II	1190.4, 1193.3	13.41 ± 0.08	43 ± 8	-164 ± 6
		Si III		>13.05	-	-
		Si III	1206.5	13.03 ± 0.07	18 ± 3	37 ± 2
		Si IV	1393.8, 1402.8	13.22 ± 0.07	31 ± 7	32 ± 5
		Si IV	1393.8, 1402.8	13.52 ± 0.04	57 ± 7	-173 ± 5
J1342+1844	0.08474	C IV	1548.2, 1550.8	13.35 ± 0.05	24 ± 5	24 ± 3

Table 2.2 (cont'd)

QSO	z_{abs}	Ion	Lines in profile fit	log N[c](cm^{-2})	b (km/s)	v (km/s)
		H I[a]	1215.7	17.91 ± 0.27	15 ± 9	46 ± 16
		H I[a]	1215.7	17.50 ± 0.50	22 ± 2	214 ± 2
J1342-0053	0.07174	C II	1334.5	14.43 ± 0.11	18 ± 3	-114 ± 1
		C II	1334.5	13.85 ± 0.28	-	-39 ± 2
		C II	1334.5	13.87 ± 0.11	34 ± 9	-11 ± 9
		C IV	1548.2, 1550.8	14.09 ± 0.04	39 ± 5	-17 ± 3
		C IV	1548.2, 1550.8	13.54 ± 0.10	16 ± 6	-114 ± 4
		H I		>14.40	-	-
		N II	1084.0	14.24 ± 0.14	19 ± 8	-113 ± 5
		N II	1084.0	13.41 ± 0.62	-	-49 ± 15
		N II	1084.0	13.96 ± 0.20	25 ± 21	5 ± 13
		O I	1302.2	14.25 ± 0.08	13 ± 4	-110 ± 2
		Si II	1190.4, 1193.3, 1260.4, 1304.4, 1526.7	13.97 ± 0.09	10 ± 1	-124 ± 1
		Si II	1190.4, 1193.3, 1260.4, 1304.4, 1526.7	13.28 ± 0.08	-	-43 ± 3
		Si II	1260.4	12.77 ± 0.11	-	8 ± 2
		Si III	1206.5	12.79 ± 0.09	11 ± 4	-35 ± 2
		Si III	1206.5	13.29 ± 0.07	21 ± 2	-113 ± 1
		Si III	1206.5	12.90 ± 0.15	9 ± 4	0 ± 2
	0.08795	C IV	1548.2, 1550.8	13.86 ± 0.08	22 ± 6	17 ± 4
		H I		>14.29	-	-
		Si III	1206.5	12.86 ± 0.12	13 ± 5	6 ± 3
J1357+1704	0.09779	C II	1334.5	13.99 ± 0.04	27 ± 3	25 ± 2
		C IV	1548.2, 1550.8	13.61 ± 0.17	18 ± 8	-37 ± 5
		C IV	1548.2, 1550.8	13.60 ± 0.19	39 ± 22	21 ± 16
		H I		>14.59	-	-
		Si II	1260.4	12.78 ± 0.04	22 ± 4	25 ± 2
		Si III[a]	1206.5	13.58 ± 0.13	21 ± 3	25 ± 1
		Si III	1206.5	12.90 ± 0.05	17 ± 3	-44 ± 2
		Si IV	1402.8, 1393.8	13.16 ± 0.09	33 ± 9	-36 ± 6
		Si IV	1393.8, 1402.8	13.23 ± 0.07	23 ± 5	29 ± 4
	0.08366	C II	1334.5	13.70 ± 0.05	33 ± 5	-2 ± 4
		C IV	1548.2, 1550.8	13.95 ± 0.07	20 ± 4	0 ± 3
		C IV	1548.2, 1550.8	13.60 ± 0.11	32 ± 12	-71 ± 8
		H I		>14.67	-	-
		Si III	1206.5	13.22 ± 0.17	15 ± 4	-1 ± 2
		Si III	1206.5	12.85 ± 0.07	37 ± 8	-170 ± 5
		Si IV	1402.8, 1393.8	13.20 ± 0.04	18 ± 3	6 ± 2
J1437+5045	0.12971	C II	1334.5	14.21 ± 0.15	71 ± 27	-13 ± 19
		C IV		>14.62	-	-
		H I		>14.46	-	-
		N V[a]	1238.8, 1242.8	14.13 ± 0.20	36 ± 21	15 ± 16
		O VI[a]	1031.9, 1037.6	14.61 ± 0.20	37 ± 14	10 ± 10
		Si III		>13.06	-	-
J1445+3428	0.00549	C IV[a]	1548.2, 1550.8	14.15 ± 0.13	17 ± 4	13 ± 3
		H I[b]	-	-	-	-
		N V	1242.8, 1238.8	13.94 ± 0.09	29 ± 8	17 ± 5
J1521+0337	0.09674	C IV[a]	1548.2, 1550.8	14.21 ± 0.12	40 ± 11	-4 ± 8
		H I		>14.56	-	-
J1553+3548	0.08291	C II	1334.5	14.52 ± 0.05	27 ± 2	-13 ± 1
		C IV	1548.2, 1550.8	14.01 ± 0.07	41 ± 8	-7 ± 7
		Fe II	1144.9, 1143.2	14.08 ± 0.15	9 ± 4	-5 ± 2
		H I[a]	1215.7	18.67 ± 0.55	25 ± 25	157 ± 68
		H I[a]	1215.7	19.53 ± 0.10	-	-42 ± 21
		N II	1084.0	14.28 ± 0.06	32 ± 6	-8 ± 4
		O I	1302.2	14.72 ± 0.08	21 ± 3	-13 ± 2
		Si II	1190.4, 1193.3, 1260.4, 1526.7	14.14 ± 0.08	19 ± 1	-19 ± 3
		Si III[a]	1206.5	13.42 ± 0.09	28 ± 6	4 ± 4
		Si IV	1393.8, 1402.8	13.30 ± 0.07	30 ± 7	-5 ± 4

Table 2.2 (cont'd)

QSO	z_{abs}	Ion	Lines in profile fit	log N[c](cm^{-2})	b (km/s)	v (km/s)
J1619+3342	0.09637	C II	1334.5	14.06 ± 0.02	24 ± 2	-104 ± 1
		C II	1334.5	14.35 ± 0.06	15 ± 1	6 ± 1
		C IV	1548.2, 1550.8	13.82 ± 0.05	15 ± 2	-114 ± 1
		C IV	1548.2, 1550.8	13.70 ± 0.07	74 ± 16	-7 ± 11
		Fe II	1144.9	13.94 ± 0.05	14 ± 3	-4 ± 2
		Fe III	1122.5	13.82 ± 0.10	40 ± 13	5 ± 8
		H I[a]	1215.7	20.53 ± 0.01	126 ± 11	10 ± 6
		N I	1199.5, 1200.2, 1200.7	13.99 ± 0.08	8 ± 1	-8 ± 1
		N II	1084.0	15.94 ± 0.30	-	-16 ± 1
		O I	1039.2, 1302.2	14.55 ± 0.03	17 ± 2	-1 ± 1
		O VI	1037.6	14.80 ± 0.07	42 ± 8	-154 ± 6
		P II	1152.8	13.03 ± 0.19	12 ± 12	-7 ± 7
		S II	1250.6, 1259.5	14.93 ± 0.07	-	-10 ± 2
		Si II	1193.3, 1260.4, 1526.7	14.04 ± 0.08	13 ± 1	-13 ± 2
		Si III	1206.5	13.22 ± 0.04	27 ± 3	7 ± 2
		Si IV	1393.8, 1402.8	13.22 ± 0.03	13 ± 2	0 ± 1
PG1202+281	0.08026	C IV	1548.2, 1550.8	13.73 ± 0.30	-	0 ± 5
		H I[b]	-	-	-	-
FBQS 0751+2919	0.06029	C IV	1548.2, 1550.8	13.62 ± 0.03	15 ± 2	-30 ± 1
		C IV	1548.2, 1550.8	13.21 ± 0.06	15 ± 4	17 ± 2
		H I		>14.70	-	-
LBQS 1435-0134	0.13849	C IV	1548.2, 1550.8	13.40 ± 0.04	20 ± 3	-6 ± 2
		H I	1025.7, 1215.7	14.70 ± 0.02	27 ± 0	2 ± 1
		O VI	1031.9, 1037.6	13.79 ± 0.03	21 ± 3	9 ± 2
PG1148+549	0.00349	C IV	1548.2, 1550.8	13.66 ± 0.03	11 ± 1	-10 ± 1
		H I		>14.17	-	-
		H I	1215.7	13.50 ± 0.02	29 ± 2	132 ± 1
PG1407+265	0.07227	C IV	1550.8, 1548.2	13.47 ± 0.04	22 ± 3	-17 ± 2
		H I[b]	-	-	-	-
PG1522+101	0.07523	C IV	1548.2, 1550.8	13.56 ± 0.05	9 ± 2	-6 ± 1
		H I	1215.7	13.87 ± 0.02	26 ± 1	-24 ± 1
		N V	1238.8, 1242.8	13.19 ± 0.08	10 ± 4	-4 ± 2

[a]Measurements shown with errors from Voigt profile fitting but may suffer from saturation.

[b]The presence of the line is apparent but either telluric emission or bad pixels prevent a measurement.

[c]Column densities expressed as lower limits were measured using the apparent optical method (Savage & Sembach, 1991).

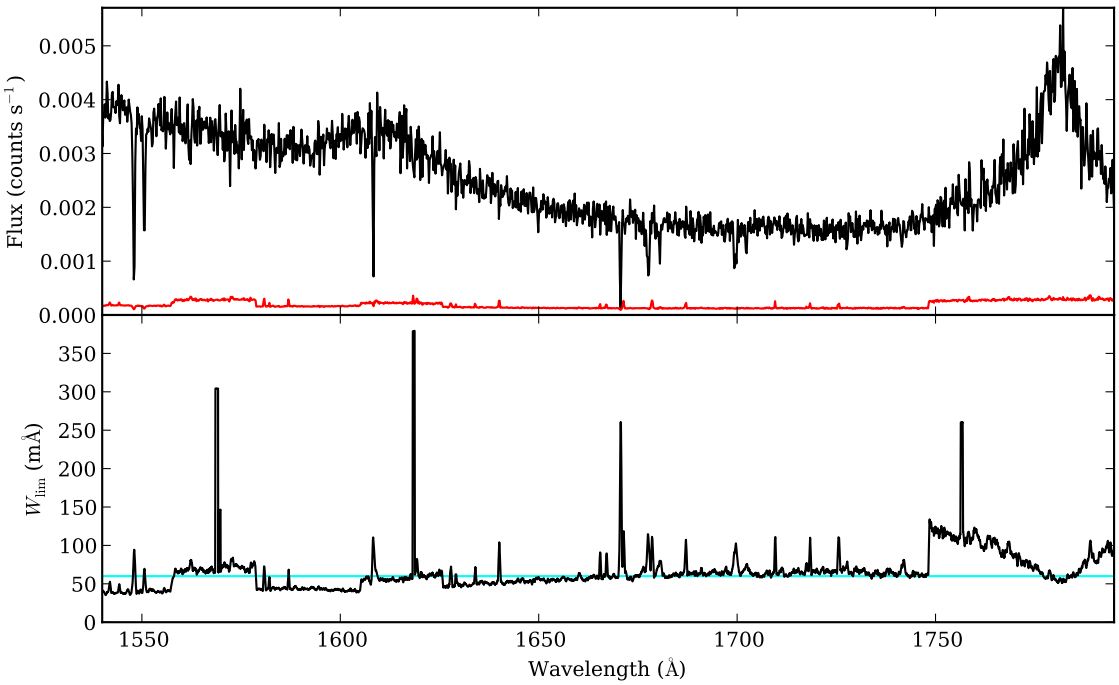

Figure 2.2 The spectral region of one sightline, QSO J1342+1844, over which the COS bandpass covers the C IV doublet. (Top) The QSO spectrum and errors are plotted in black and red, respectively. (Bottom) The limiting equivalent width for a 3-σ detection of a given line. The cyan line marks a fiducial 60 mÅ threshold; if chosen as a limiting equivalent width for Δz or ΔX, all regions of the spectrum with $\mathrm{W_{lim}}$ above this value are rejected from the Δz and ΔX measurement. Spikes in the $\mathrm{W_{lim}}$ panel that do not coincide with absorption features in the spectra primarily occur due to pixel-scale noise fluctuations. The discontinuous periods of increased $W_{\rm lim}$ near, e.g., 1560 Å correspond to detector gaps at the individual central wavelength settings of the COS G160M grating.

2.3.3 Path Length Calculation

Our statistics calculations require measuring the total path over which we may detect the C IV doublet. We express the total path in terms of two quantities: the redshift path length Δz and the comoving path length ΔX(Bahcall & Peebles, 1969). The redshift path is simply the sum of the redshift ranges over which the doublet is detectable in each spectrum to a limiting equivalent width or column density, but this calculation must account for varying S/N across the spectrum and absorption

lines from systems at other redshifts, especially strong Lyα lines. Therefore, we must ignore those segments where the S/N is insufficient to reveal lines of a given strength.

To account for the decreasing sensitivity to lower column densities, authors using automatic line identification methods may also assume a constant path length across all column densities and employ Monte Carlo completeness corrections (e.g., Simcoe et al., 2011) in the derived statistics. Our survey comprises a visually identified absorber sample, and the method presented here alternatively measures a variable path length from the data S/N; the two methods should produce consistent results.

Because a varying redshift describes a varying comoving volume, we also employ the comoving path length X(z), which is defined as follows:

$$\mathrm{X}(z) = \frac{2}{3\Omega_M}\sqrt{\Omega_M \times (1+z)^3 + \Omega_\Lambda} - \frac{2\sqrt{\Omega_\Lambda}}{3\Omega_M} \tag{2.3}$$

For the Δz and ΔX calculation, we first convert the wavelength at each pixel to z and X, respectively, assuming the C IV λ1550 line were to fall at each location (i.e., $z = 1550.77/\lambda - 1$). We then sum over the regions in each spectrum (in terms of z or X) where the λ1550 would be detectable and finally sum the detectable regions in all spectra.

A line's detectability is a function of the line strength and of the S/N of the data at the line's location. Therefore, we calculate at each wavelength position the limiting rest equivalent width ($\mathrm{W_{lim}}$), a threshold above which lines may be detected. The $\mathrm{W_{lim}}$ is defined as follows:

$$\mathrm{W_{lim}}(\lambda) = \frac{3\sigma_{W(\lambda)}}{1+z_{abs}} \tag{2.4}$$

where $\sigma_{W(\lambda)}$ is the uncertainty of the observed equivalent width summed in quadrature over a number of pixels. The number of integrated pixels is taken as a typical width (in pixels) of a line with equivalent width $\mathrm{W_{lim}}$, between 8 and 18 pixels for the absorbers

in our sample and wider than the full width at half maximum of the spectra. The following expression defines $\sigma_{W(\lambda)}$:

$$\sigma^2_{W(\lambda)} = \sum_i \left(\Delta\lambda(i) \left[\frac{\sigma_{I(\lambda_i)}}{I(\lambda_i)} \right] \right)^2 \tag{2.5}$$

where $\Delta\lambda(i)$ is the pixel width (in Å), $I(\lambda_i)$ is the continuum flux at pixel i, and $\sigma_{I(\lambda_i)}$ is the flux uncertainty at pixel i. We chose the number of integrated pixels based on typical widths of lines from our data with measured equivalent widths similar to the threshold $W_{\rm lim}$, e.g., the average profile of an $\sim$80 mÅ line was 12 pixels wide. An example $W_{\rm lim}$ calculation for the spectrum of J1342+1844 is shown in Figure 2.2.

The $W_{\rm lim}$ was measured using these equations centered at each pixel of every spectrum in our dataset in multiple passes using the number of pixels as described above for $W_{\rm lim}$ values commensurate with the column density bins used to compute the column density distribution function (see Section 4.1). The absorber column density range we are probing ($13 \lesssim \log N(\text{C IV}) \lesssim 15$ cm^{-2}) falls in the region of the curve of growth where the lines of the doublet begin to saturate. Therefore, we mapped equivalent width to column density by creating 1000 synthetic C IV doublets with S/N $\sim$ 12 (a typical S/N for our QSO spectra), measuring the resulting equivalent width, and fitting the resulting W_r-log N(C IV) relation from the simulated data with a 4th-order polynomial. We then measured the path length at each $13 \lesssim \log N(\text{C IV}) \lesssim 15$ cm^{-2} at intervals of $\Delta(\log N(\text{C IV})) = 0.05$ cm^{-2}. In accordance with our blind survey criteria, we did not include regions of the spectra within $\pm$ 500 km/s of the COS-Halos and COS-Dwarfs target galaxy redshifts (the CASBaH survey is intrinsically blind) or $\pm$ 5000 km/s of the QSO redshift in our path lengths. The path lengths measured for our dataset and employed for the following statistics calculations are shown in Figure 2.3 and tabulated in Table 2.3; the limiting equivalent width values corresponding to these column density bins are listed in Table 2.3. We also list

Table 2.3 Limiting equivalent widths and path lengths calculated as functions of column density.

log N(C IV) [cm^{-2}]	W_{1550}[a] [mÅ]	Δz	ΔX	$d\mathcal{N}/dz$ [b]
13.0	19	0.1	0.1	-
13.1	24	0.5	0.5	-
13.2	29	0.8	0.8	-
13.3	35	1.1	1.3	$7.80^{+2.4}_{-1.4}$
13.4	43	1.7	1.9	$6.79^{+2.1}_{-1.2}$
13.5	54	1.8	2.0	$6.79^{+2.1}_{-1.2}$
13.6	67	2.8	3.1	$5.51^{+1.6}_{-1.0}$
13.7	83	4.0	4.4	$4.59^{+1.4}_{-0.8}$
13.8	102	4.3	4.7	$3.22^{+1.1}_{-0.6}$
13.9	124	5.5	6.1	$2.59^{+0.9}_{-0.5}$
14.0	150	7.1	7.9	$2.43^{+0.8}_{-0.5}$
14.1	178	8.7	9.6	$1.56^{+0.7}_{-0.4}$
14.2	208	9.9	11.1	$0.91^{+0.6}_{-0.3}$
14.3	241	10.9	12.1	$0.52^{+0.5}_{-0.2}$
14.4	275	11.6	12.9	$0.17^{+0.4}_{-0.1}$
14.5	310	12.0	13.4	$0.08^{+0.3}_{-0.1}$
14.6	345	12.3	13.8	$0.08^{+0.3}_{-0.1}$
14.7	379	12.5	14.0	-
14.8	412	12.7	14.2	-
14.9	442	12.8	14.3	-
15.0	468	12.9	14.4	-

[a] Equivalent width corresponding to N(C IV) in Column 1

[b] Cumulative number of detected absorbers per redshift path length (see Eq. 2.6)

in Table 2.3 the cumulative number of absorbers per unit redshift path length as a function of N(C IV), $d\mathcal{N}/dz$, defined as follows:

$$\frac{d\mathcal{N}}{dz}(N(\text{C IV})) = \sum_i \frac{\mathcal{N}(N_i(\text{C IV}))}{\Delta z(N_i(\text{C IV}))} \tag{2.6}$$

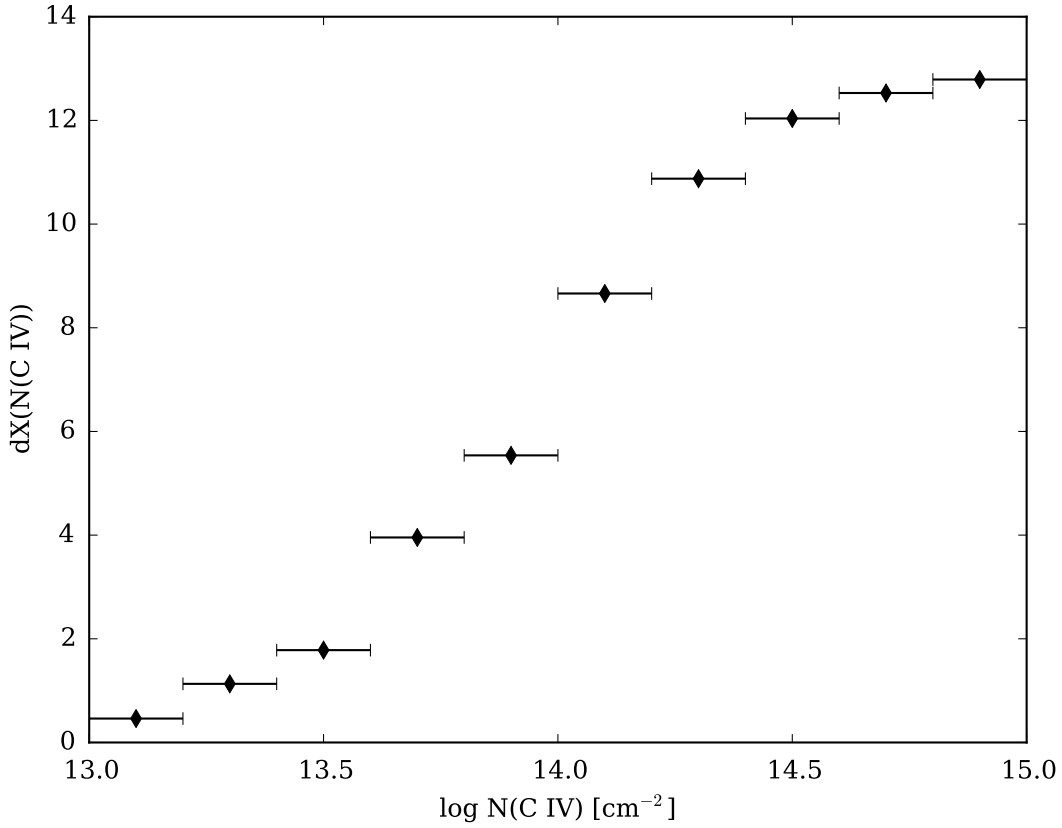

Figure 2.3 The path length as measured from our QSO spectra as a function of column density in the same bins used to calculate the observed column density distribution function, f(N).

where $\mathcal{N}(N_i(\text{C IV}))$ is the number of C IV absorbers in the i-th column density bin, $\Delta z(N_i(\text{C IV}))$ is the redshift path length for detecting absorbers with $N_i(\text{C IV})$, and the summation is carried out for column density bins with $N_i(\text{C IV}) \geq N(\text{C IV})$.

2.4 Absorber Statistics

2.4.1 Column density distribution function $f(N)$

We begin our analysis by deriving the column density distribution function, or $f(N)$, of the C IV absorber sample. A fundamental observable measured for a sample of absorption systems, $f(N)$ is useful for comparisons to theoretical predictions and

describing the incidence and mass density of an absorber sample. One may evaluate $f(N)$ in discrete column density bins $\Delta N(\mathrm{C\ IV})$ as follows:

$$f(N) = \frac{\mathcal{N}_{\mathrm{abs}}(N(\mathrm{C\ IV}))}{\Delta N(\mathrm{C\ IV})\ \Delta X(N(\mathrm{C\ IV}))} \tag{2.7}$$

where $\Delta X(N(C\ \mathrm{IV}))$ is the comoving path length corresponding to the threshold set by the individual column density bin, and $\mathcal{N}_{\mathrm{abs}}(C\ \mathrm{IV})$ is the number of absorbers within the specified column density bin.

Our binned evaluation of $f(N(\mathrm{C\ IV}))$ is presented in Figure 2.4, assuming Poisson uncertainties in $\mathcal{N}_{\mathrm{abs}}(C\ \mathrm{IV})$ for error estimation. Similar to previous work, we observe a steep decline in $f(N)$ with increasing $N(\mathrm{C\ IV})$. Earlier studies have frequently modeled $f(N)$ as a single power-law,

$$f(N) = k_P \left(\frac{N(\mathrm{C\ IV})}{10^{14}\,\mathrm{cm}^{-2}} \right)^{\alpha_P} \tag{2.8}$$

where α_P is the power law index, and k_P is the normalization constant. For small samples, this functional form has offered a good description for the limited data. Following Cooksey et al. (2010), we used a maximum likelihood analysis to find the best-fit parameters for this model: $\log k_P = -13.76 \pm 0.07$ and $\alpha_P = -2.07 \pm 0.15$ (68% c.l.). For this likelihood analysis, we adopted a saturation limit $N_{\mathrm{sat}} = 10^{14.3}\,\mathrm{cm}^{-2}$ and have analyzed the dataset from $N_{\mathrm{min}} = 10^{13.3}\,\mathrm{cm}^{-2}$ to $N_{\mathrm{max}} = 10^{15}\,\mathrm{cm}^{-2}$. This model is overplotted on Figure 2.4 and offers a fair description of the data.

However, Cooksey et al. (2013) found a steep (approximately exponential) turnover in the equivalent width distribution of strong C IV systems. Furthermore, Danforth et al. (2014), whose sample contains more $13.0 \leq \log N(\mathrm{C\ IV}) \leq 13.5$ absorbers than that presented here, argue that a broken power law better fits their measured $f(N(\mathrm{C\ IV}))$ than a single power law. We were thus inspired to consider an alternative model, specifically, fitting $f(N(\mathrm{C\ IV}))$ with a Γ-function

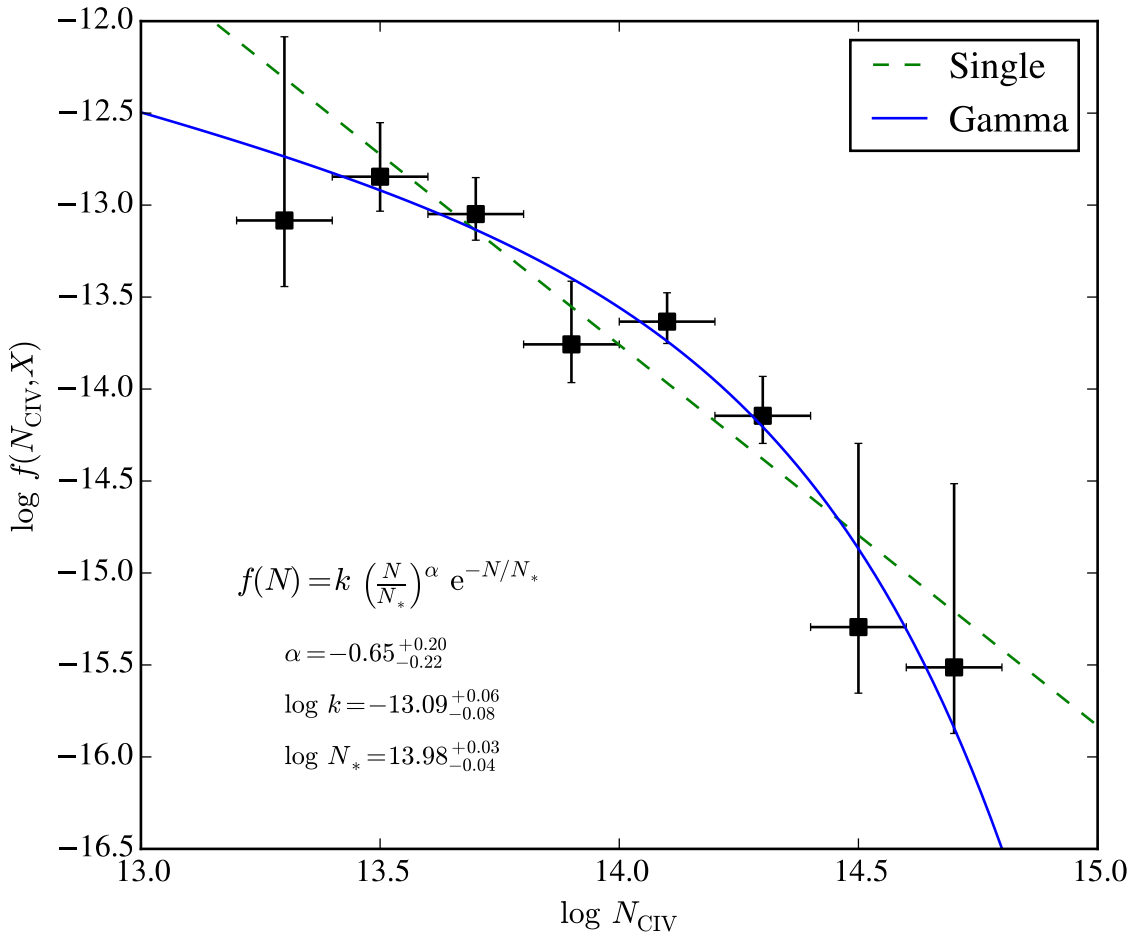

Figure 2.4 The column density distribution function for our 42-absorber C IV sample. Data points indicate binned evaluations with vertical error bars corresponding to 1-σ Poisson errors of the absorber counts in each bin, and the horizontal bars denote the column density bin width, $\Delta(\log N(\mathrm{C\ IV})) = 0.2$. The overplotted models assume a single power law (green, dashed) and Γ function (blue, solid) distributions for $f(N(\mathrm{C\ IV}))$. The latter model offers an excellent description of the observations; the best-fit parameters are labeled in the figure.

$$f(N) = k_\Gamma \left(\frac{N(\mathrm{C\ IV})}{N_*}\right)^{\alpha_\Gamma} \exp\left[\frac{-N(\mathrm{C\ IV})}{N_*}\right] \quad , \tag{2.9}$$

parameterized by a normalization constant[6] k_Γ, a power-law exponent α_Γ, and a 'break' column density N_*. Once again, we perform a maximum likelihood analysis

[6]Note that this normalization constant is at least partially degenerate with $N_*^{-\alpha_\Gamma}$.

with $N_{\rm min}$, $N_{\rm max}$, and $N_{\rm sat}$ as above on a 3-dimenstional grid of k_Γ, α_Γ, and N_* values. The best-fit Γ-function is overplotted on the binned evaluations in Figure 2.4 and provides an excellent description of the observations. The correlation in these parameters is illustrated in Figure 2.5; as expected, we find significant degeneracy between k_Γ and N_* although the latter is rather tightly constrained. The power-law exponent is shallow and constrained at the 99.7% c.l. to be greater than $\alpha_\Gamma = -1.5$.

The best-fit Γ-function is overplotted on the binned evaluations in Figure 2.4 and provides an excellent description of the observed $f(N(\text{C IV}))$. To statistically assess the goodness-of-fit between these models, we conducted one-sample Anderson-Darling comparison tests between our absorber sample and each model. The traditional, but often-employed, implementation of the Kolmogorov-Smirnoff (K-S) and/or Anderson-Darling tests, wherein the so-called 'D statistic' follows the K-S distribution (the integrals of which yield p-values for the null hypothesis) do not apply in this situation because the parameters of the models to be tested are derived from the sample distribution to be compared. Therefore, we produced distributions of the D statistics calculated between the normalized empirical cumulative distribution function of 10^5 bootstrap resamples of our C IV absorber sample and the continuous cumulative distribution function of each model. Potentially due to the small numbers of absorbers we have at the lowest and highest column densities, the Anderson-Darling test does not yield a small enough p-value to reject the power-law model for $f(N(\text{C IV}))$ with strong statistical confidence. However, we call attention to Figure 2.6, which shows the cumulative distribution of our C IV absorber sample as a function of $N(\text{C IV})$ alongside the cumulative distributions following from the Γ-function and power-law models. Due to its superior reproduction of our absorber sample, we adopt the Γ functional form for $f(N(\text{C IV}))$ in the following statistics calculations.

From any $f(N)$ model, it is trivial to integrate from any $N_{\rm min}$ value to estimate the incidence of absorption systems

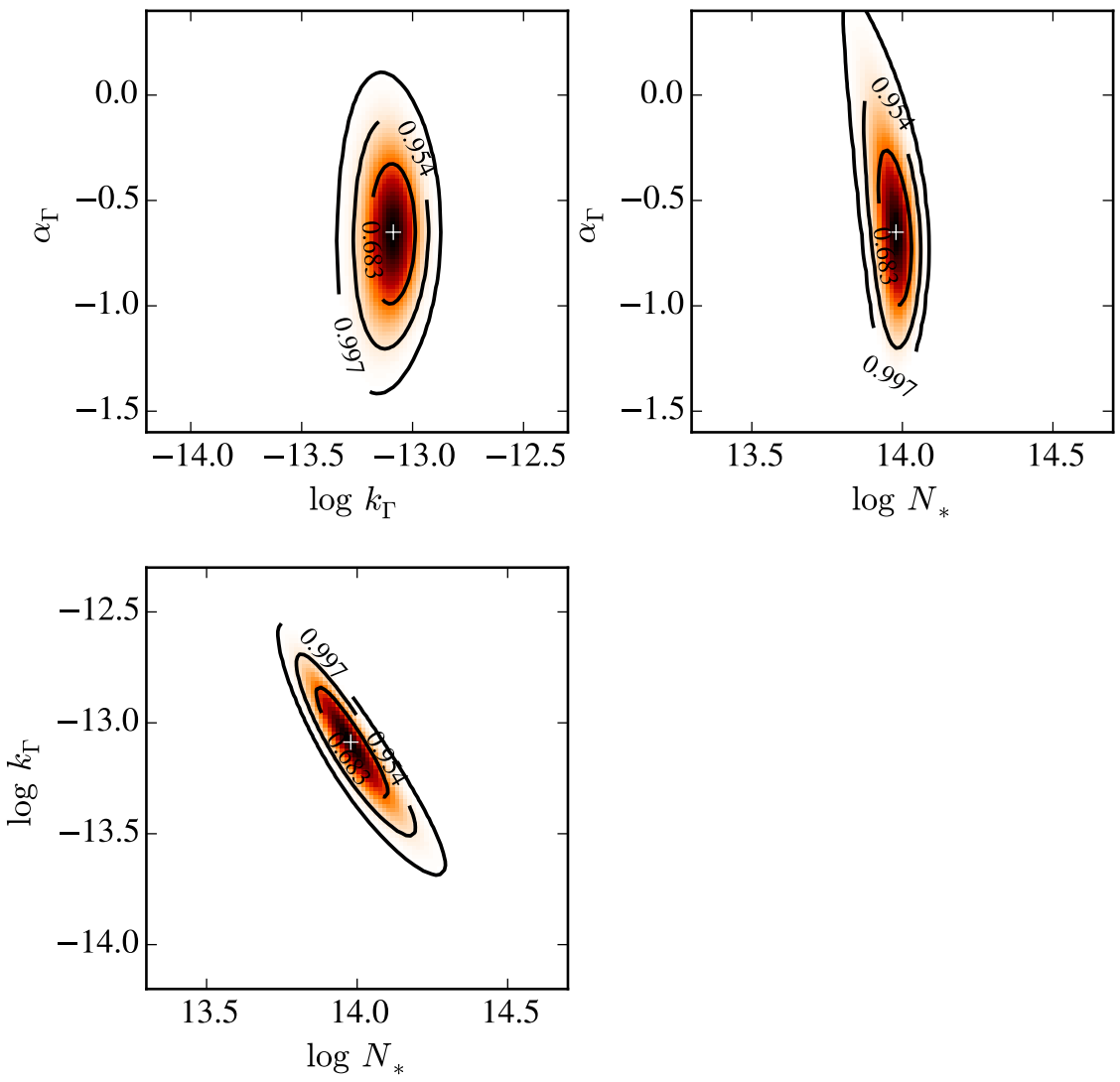

Figure 2.5 Correlation contours for the three parameters describing the Γ-function model for $f(N)$ at 68.4, 95.4, and 99.7% confidence (inner to outer). As expected, k_Γ and N_* are highly correlated. The power-law exponent is more poorly constrained but indicates a shallower slope than $\alpha_\Gamma = -1.5$ at 99.7% c.l.

$$d\mathcal{N}/dX = \int_{N_{\rm min}}^{\infty} f(N, X) dN \tag{2.10}$$

For $N_{\rm min} = 10^{13.3}\,{\rm cm}^{-2}$, we calculate $dN/dX = 7.5$ for our preferred model. Evaluating the likelihood function of this model to a 68% confidence limit, we find the RMS in the resultant dN/dX values to be 1.1 ($\approx 15\%$) which is consistent with the Poisson uncertainty of an $N = 42$ sample.

2.4.2 $\Omega_{C\ \mathrm{IV}}$

The mass density of triply ionized carbon is quantified by the $\Omega_{\mathrm{C\ IV}}$ statistic, which is the ratio of the mass density of C IV to the critical density of the Universe. Formally, $\Omega_{\mathrm{C\ IV}}$ may be calculated from $f(N)$ as follows:

$$\Omega_{\mathrm{C\ IV}} = \frac{H_0 m_C}{c\rho_{c,0}} \int_0^\infty f(N(\mathrm{C\ IV}))N(\mathrm{C\ IV})\, dN(\mathrm{C\ IV}) \quad , \tag{2.11}$$

where H_0 is the Hubble constant, $\rho_{c,0} = 3H_0^2(8\pi G)^{-1}$ is the critical density, m_C is the mass of the carbon atom, and the other symbols have their typical meanings. In practice, $\Omega_{\mathrm{C\ IV}}$ is typically estimated over a finite column density interval $N(\mathrm{C\ IV}) = [N_{\mathrm{min}}, N_{\mathrm{max}}]$. This is required for simple power-law models which will diverge at either high or low $N(\mathrm{C\ IV})$. Furthermore, $f(N)$ is generally only constrained over a finite $N(\mathrm{C\ IV})$ interval.

In Figure 2.7, we present two evaluations of $\Omega_{\mathrm{C\ IV}}$: (1) the integration of our Γ-model for $f(N)$ with $N_{\mathrm{min}} = 10^{13.3}\,\mathrm{cm}^{-2}$ and $N_{\mathrm{max}} = 10^{15}\,\mathrm{cm}^{-2}$; and (2) the summed evaluation of all C IV systems in our statistical analysis (which spans from $10^{13.3}\,\mathrm{cm}^{-2}$ to $10^{14.6}\,\mathrm{cm}^{-2}$):

$$\Omega_{\mathrm{C\ IV}} = \frac{H_0 m_C}{c\rho_{c,0}} \sum_i \frac{N(\mathrm{C\ IV})_i}{\Delta X(N(\mathrm{C\ IV})_i)} \quad . \tag{2.12}$$

These two evaluations are in excellent agreement and yield central values of 10.0×10^{-8} and 9.7×10^{-8}, respectively. We further emphasize that the shallow power-law α_Γ derived from the Γ-model and its exponential decrease at high $N(\mathrm{C\ IV})$ imply that our estimation is rather insensitive to the choice of N_{min} and N_{max}.

We have assessed the uncertainty in $\Omega_{\mathrm{C\ IV}}$ from sample variance through a bootstrap estimation of the summed evaluation (Eq. 2.12). Specifically, we have randomly sampled the observed distribution of $N(\mathrm{C\ IV})$ values with 10,000 trials (allowing for duplications) and evaluated Eq. 2.12 for each trial. Remarkably, the RMS of the resultant distribution of $\Omega_{\mathrm{C\ IV}}$ values is small: $\sigma(\Omega_{\mathrm{C\ IV}}) = 0.35 \times 10^{-8}$. A set of 500

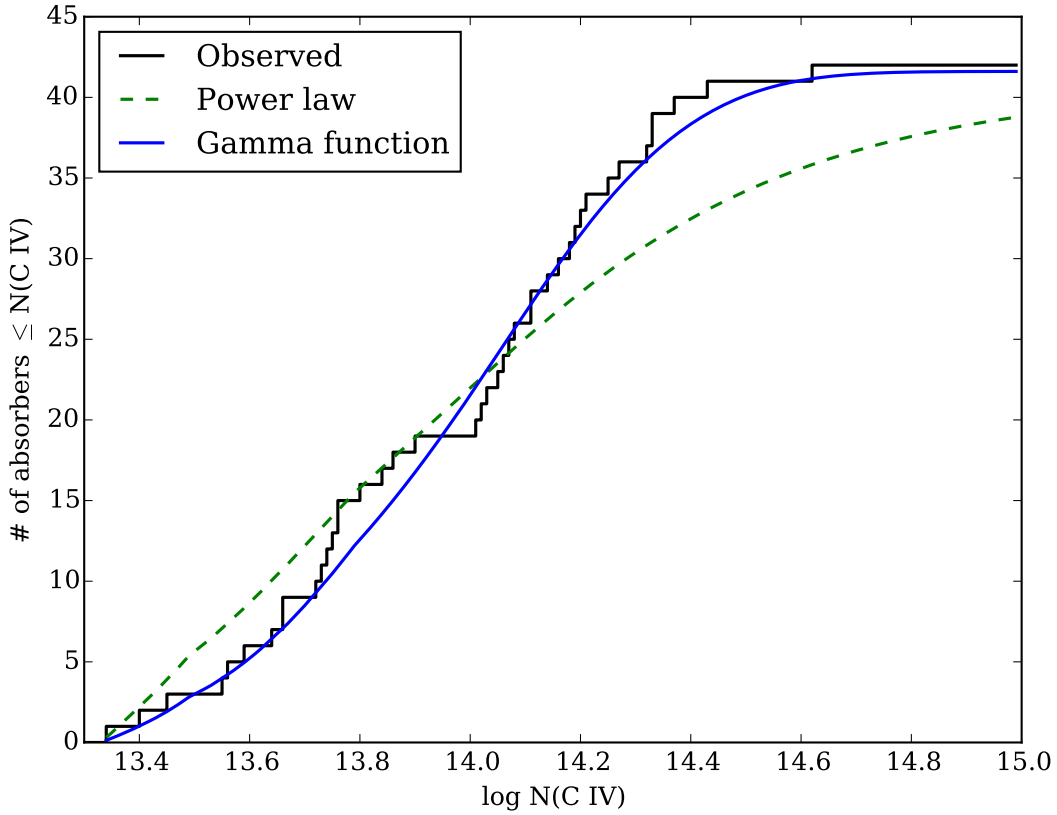

Figure 2.6 Cumulative distribution as a function of $N(\mathrm{C\ IV})$ of our C IV absorber sample compared with those resulting from the best-fit Γ- and power law column density distribution functions. Note that the Γ functional form of $f(N(\mathrm{C\ IV}))$ closely reproduces our absorber sample cumulative distribution, while the power-law distribution appears to deviate from the observed distribution at $14.1 < \log N(\mathrm{C\ IV}) < 14.7$

trials are overplotted in gray on Figure 2.7. We caution, however, that this bootstrap analysis may not sufficiently capture the sample variance in the highest $N(\mathrm{C\ IV})$ systems that contribute $\approx 20\%$ to $\Omega_{\mathrm{C\ IV}}$. Furthermore, this summed evaluation does not correct for line-saturation unlike our maximum likelihood analysis of $f(N)$. On the other hand, we find excellent agreement between the $\Omega_{\mathrm{C\ IV}}$ evaluations and have confidence that the effects of line-saturation are small. We adopt a 15% uncertainty from systematic error and report a final estimate of $\Omega_{\mathrm{C\ IV}} = 10.0 \pm 1.5 \times 10^{-8}$.

Previous analysis of *HST* spectral datasets have presented estimates for $\Omega_{\rm C\ IV}$ at $z \approx 0$. Cooksey et al. (2010) reported $\Omega_{\rm C\ IV} = 7.0 \times 10^{-8}$ ($\approx 30\%$ error) from a sample of 19 absorbers at $z < 0.6$ discovered in STIS and GHRS observations. Tilton et al. (2012) analyzed a larger set of STIS spectra and reported an $\Omega_{\rm C\ IV}$ value over twice as large from 29 absorbers at $z < 0.12$. That estimation was revised downward by Shull et al. (2014), who adopted a different approach to estimating $\Omega_{\rm C\ IV}$ using binned evaluations of $f(N)$. From their analysis of the COS linelist posted to HST/MAST by Danforth et al. (2014), they report $\Omega_{\rm C\ IV} = 10.1^{+5.2}_{-2.4} \times 10^{-8}$ (the methodology for their error estimation was not specified). Aside from the original Tilton et al. (2012) estimate, which was later revised, these various $\Omega_{\rm C\ IV}$ evaluations are in good agreement with our new analysis.

To place our result in an evolutionary context with previous authors' findings, we convert their $\Omega_{\rm C\ IV}$ values to our adopted integration limits and cosmology per Appendix C of Cooksey et al. (2010) where necessary. Figure 2.8 shows $\Omega_{\rm C\ IV}$ values spanning z$\sim$6 to the present. The present ($z = 0$) value of $\Omega_{\rm C\ IV}$ shows a clear increase over that of earlier cosmic time ($z > 4$), but the evolution since $z \sim 2$ is modest and not statistically significant.

2.4.3 Comparison with simulations

As we have alluded to above, the measurements we report are key observables that can be predicted by cosmological hydrodynamic simulations, which must reproduce not only key properties of galaxies themselves, such as the stellar mass function and evolution of the star formation density (Madau et al., 1998) but also observed properties of the CGM and IGM. In fact, galaxies, the CGM, and the IGM are intimately related in the simulations, as gas infall and outflows are required to produce the observed global properties of the galaxy population; these processes in turn produce observational signatures in the CGM and IGM (Bordoloi et al., 2011; Fumagalli et al.,

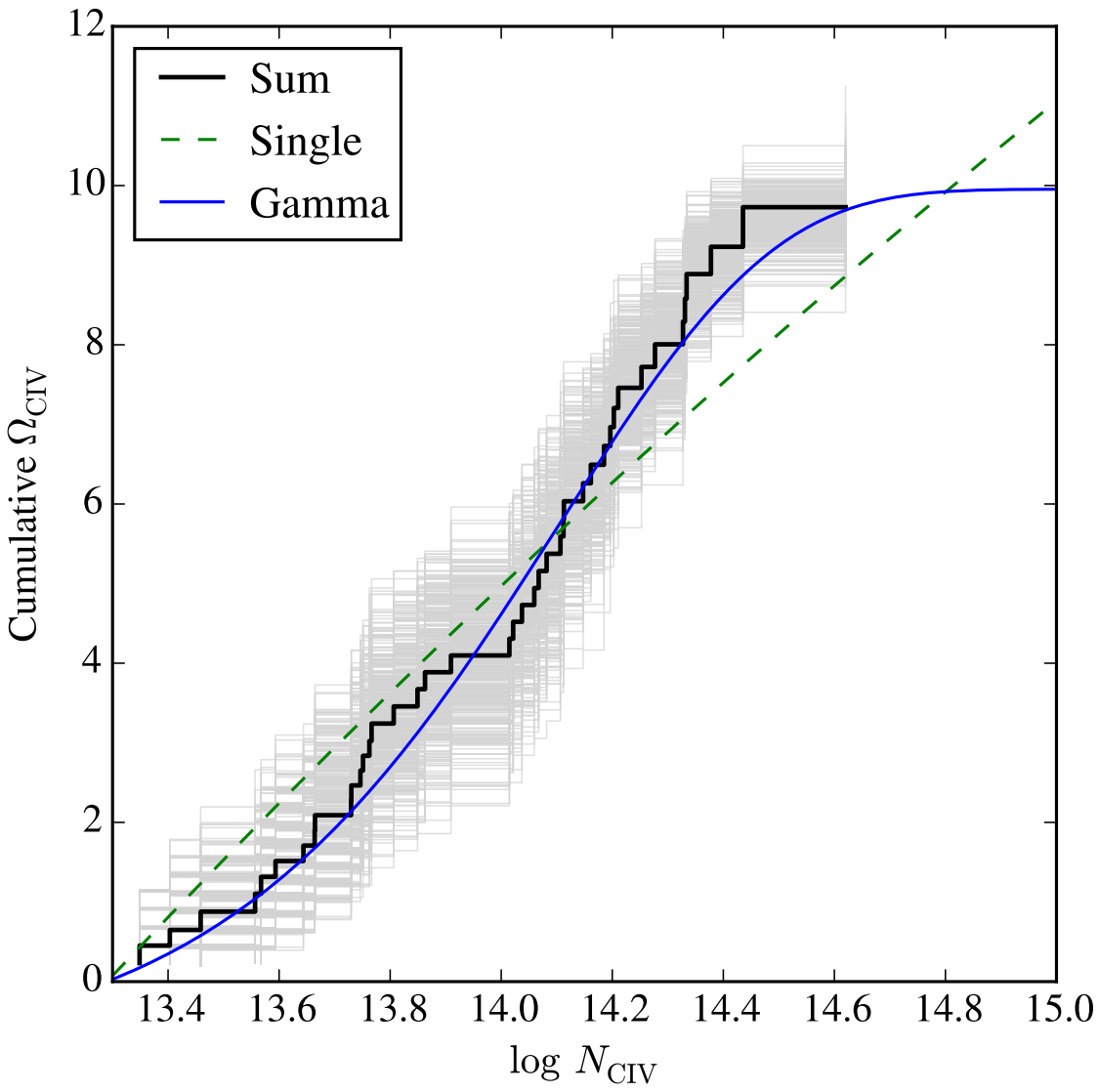

Figure 2.7 Cumulative evaluation of $\Omega_{\rm C\ IV}$ from a direct summation of our N(C IV) measurements (black histogram; Eq. 2.12). Overplotted is the integration of our best-fit $f(N)$ model (solid blue curve) from $N_{\rm min} = 10^{13.3}\,{\rm cm}^{-2}$. These lie in excellent agreement. For an estimate of sample variance we have performed a bootstrap analysis of the summed evaluation; 500 of these trials are shown in light gray on the figure. Lastly, for comparison we show the results for the best-fit power-law model (dashed green curve), which systematically overestimates the $\Omega_{\rm C\ IV}$ value at low and high column densities.

2011; Bouché et al., 2012) only probed by absorption line spectroscopy. As the scale and sophistication of cosmological simulations have progressed, the key factors driving their ability to reproduce actual observations are often encapsulated in 'sub-grid'

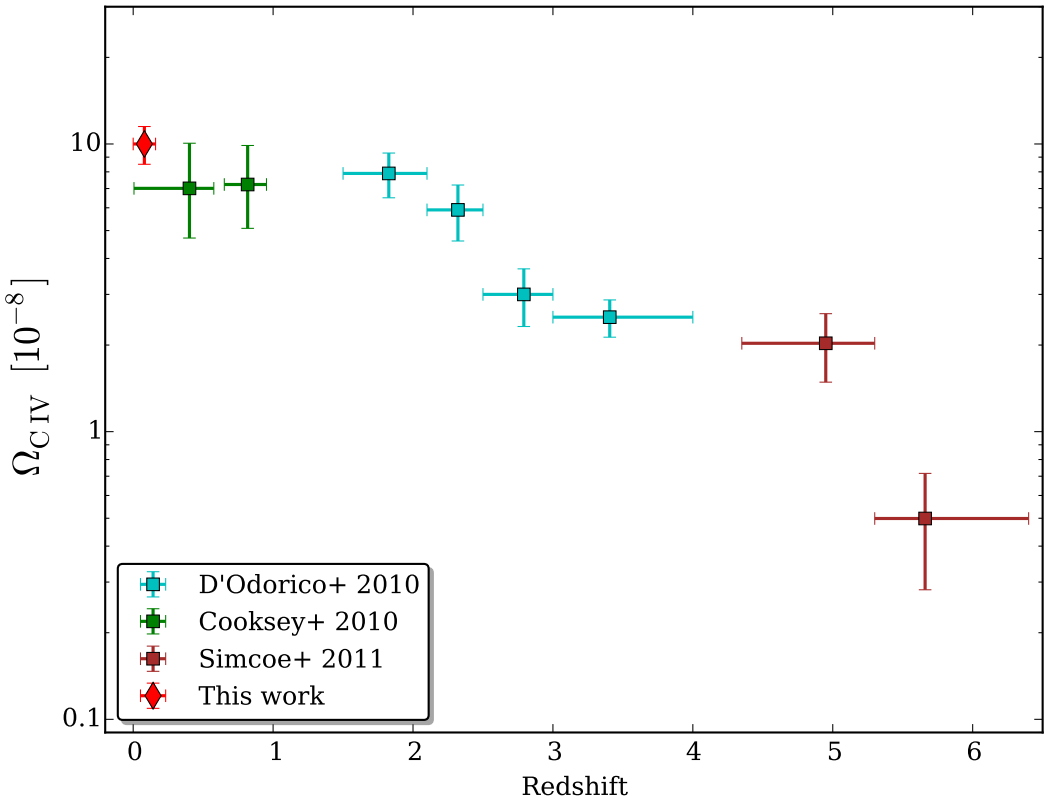

Figure 2.8 Our result for $\Omega_{\rm C\ IV}$ (red diamond) plotted along with those from Cooksey et al. (2010), D'Odorico et al. (2010), and Simcoe et al. (2011). For visual clarity, we have included only our measurement at $z \sim 0$, but the other studies in this redshift regime are discussed in the main text. Our results suggest that only a marginal evolutionary increase in $\Omega_{\rm C\ IV}$ has occurred since $z \sim 2$, but the C IV mass density in the present epoch marks a significant increase over that at $z \gtrsim 4$.

physics, prescriptions for processes such as supernova feedback and galactic winds that are not directly resolved. We attempt to use the preferred sub-grid variants of the simulations compared below, e.g., the *vzw* wind model of Oppenheimer et al. (2012), which is a momentum conserving wind prescription where the velocity of the outflowing particles scale as the internal velocity dispersion of the galaxy and which produces galaxies that more closely match observations than a constant-velocity wind model.

As the C IV doublet is among the most prominent metal-line spectral features, the $\Omega_{\rm C\ IV}$ and $f(N(\rm C\ IV))$ derived from simulation data are routinely used as metrics of the self-consistency of sub-grid processes invoked to reproduce observations of galaxies and the IGM. In Figure 2.9, we show our measured column density distribution function alongside predictions from three cosmological simulations. Cosmological hydrodynamical simulations largely use yields from stellar population synthesis models to establish global metallicities, and the uncertainties from these models can introduce uncertainties of ± 0.3 dex in the column density distribution function. Given this uncertainty, both the Schaye et al. (2015) and Oppenheimer et al. (2012) models are largely consistent with our observations over the column density range probed, yet it is quite striking how well the Oppenheimer et al. (2012) predictions seem to follow our measured distribution function. Most importantly, both simulations predict downturns relative to a single power law at low and high column densities, corroborating both the results of Cooksey et al. (2013) that $f(N(\rm C\ IV))$ deviates from a power law and our adoption of a Γ-function form. The Cen & Chisari (2011) results do not extend to to the highest column density regime covered by our observations and the other simulations, but they predict a smooth downturn (relative to a power law) at the lowest column densities. The greatest dispersion among the models occurs at log $N(\rm C\ IV) \lesssim 13.0$ cm^{-2}, but much higher S/N spectroscopy is required to constrain the behavior of $f(N(\rm C\ IV))$ in this regime.

Figure 2.10 shows the predicted evolution of $\Omega_{\rm C\ IV}$ by Oppenheimer et al. (2012) and Cen & Chisari (2011) from $z = 2.5$ to the present alongside observational measurements. The Oppenheimer et al. (2012) simulations predict minimal evolution in $\Omega_{\rm C\ IV}$, but the uncertainties dwarf any differences between the observational constraints. However, Cen & Chisari (2011) predict a steady upward evolution in $\Omega_{\rm C\ IV}$. The behaviors of these predictions differ most significantly between $z \sim 1.5$ and $z \sim 0.5$, where the observational constraints are insufficient to favor one model over

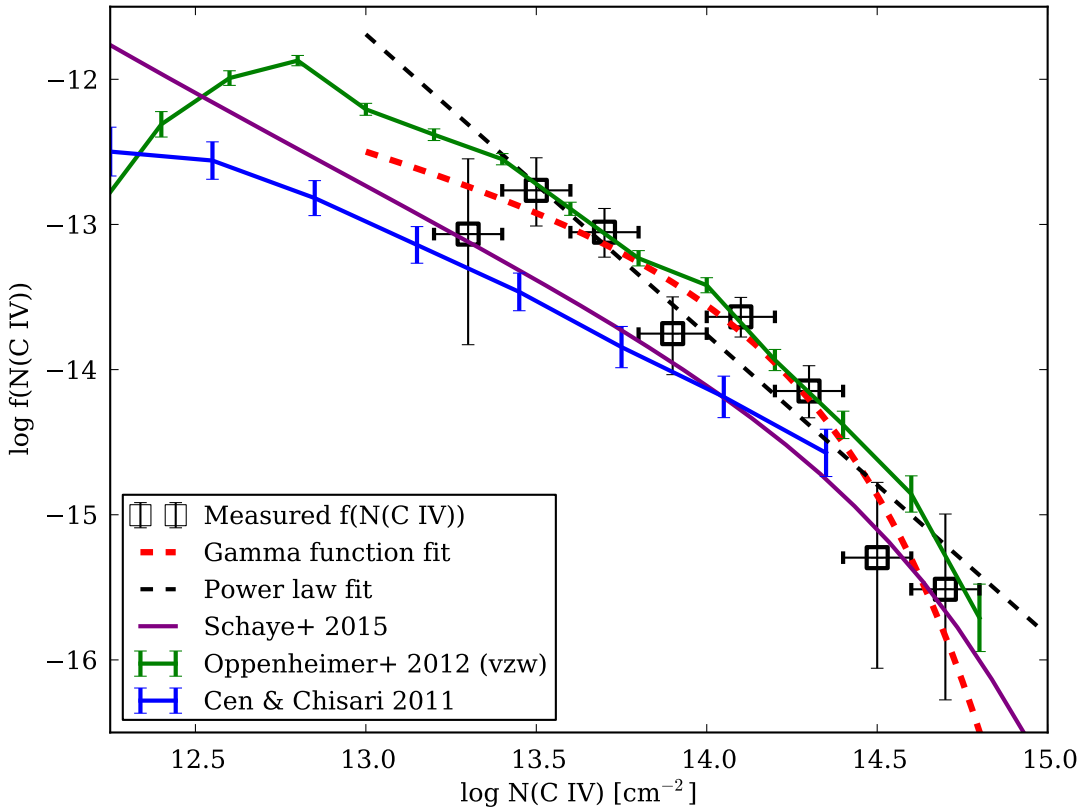

Figure 2.9 Predictions of the column density distribution function from three cosmological hydrodynamic simulations [Oppenheimer et al. (2012, green), Schaye et al. (2015, purple), and Cen & Chisari (2011, blue)] alongside our observational results. The black dashed line shows a single power law fit for f(N), while the red dashed line shows the preferred Γ-function fit. All theoretical predictions exhibit qualitatively similar forms to the Γ-function we have adopted, while the single power law form overestimates both the measurements and predictions at low and high column densities.

the other. Regardless, the predicted $\Omega_{\mathrm{C\ IV}}$ values at $z \sim 0$ are consistent with our reported measurement.

As an indicator of the physical conditions in the gas, the Doppler b value provides another observable in the absorption line data by way of Voigt profile fitting. As Cen & Chisari (2011) remark, directly comparing the b values from any simulation versus those measured in observed absorbers is complicated by differences in measurement procedures (we derive b(C IV) from Voigt profile fitting); the problem is exacerbated

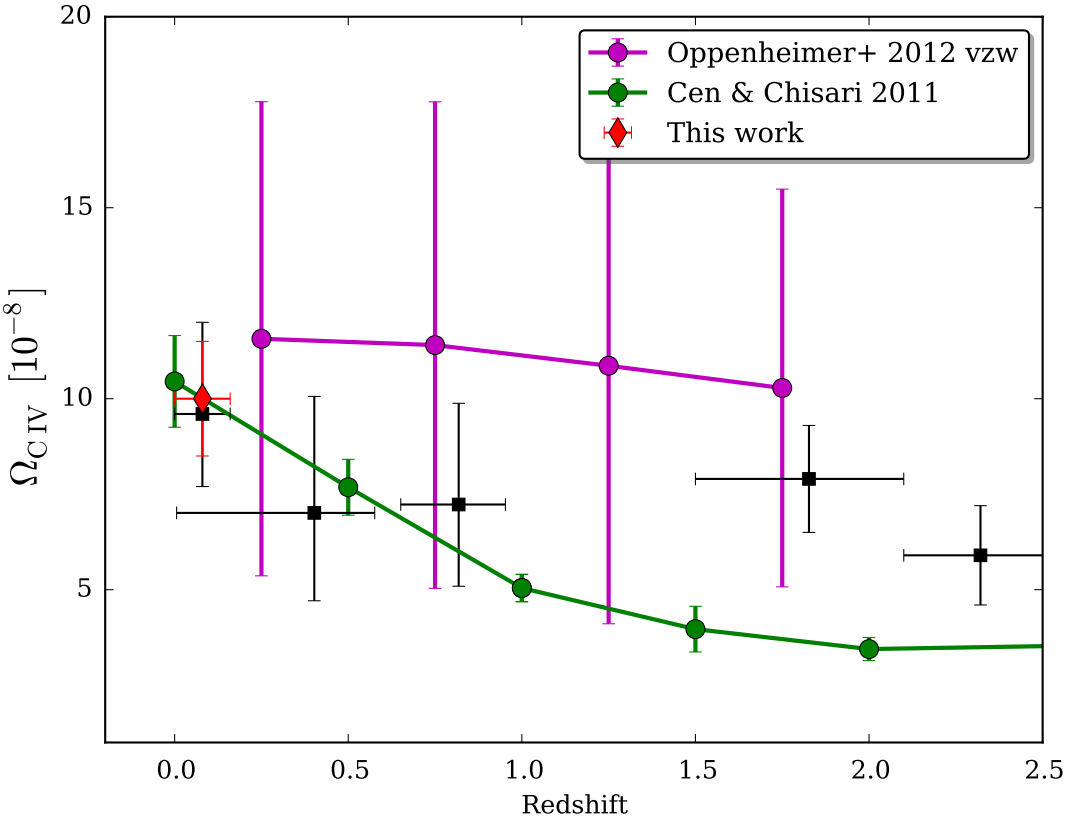

Figure 2.10 The evolution of $\Omega_{\rm C\ IV}$ since $z = 2.5$ as observed (black squares; Cooksey et al., 2010; D'Odorico et al., 2010; Shull et al., 2014) and as predicted by the cosmological hydrodynamical simulations of Oppenheimer et al. (2012) and Cen & Chisari (2011) (purple and green lines and circles, respectively). Our measurement is shown with a red diamond and is consistent with either theoretical result, although the evolutionary behaviors of these simulations differ from $z \sim 2$ to $z \sim 0.5$.

in systems with many components spread over a wide velocity range. However, our sample is primarily composed of systems with simple velocity structures (one or two components spread over < 100 km/s), so our data often provide reliable b-values that can be compared with simulation predictions. We compare our sample with the predicted b(C IV) distributions from Oppenheimer et al. (2012), who produced mock spectra for direct comparison with COS observations, in Figure 2.11. The distributions shown here from Oppenheimer et al. (2012) employ their preferred feedback prescription including and excluding a model for turbulence. While their turbulence

model improves the reproduction of O VI absorber observations, the model overpredicts the line widths of observed C IV absorbers. Our data suggest that the media probed by C IV absorption at $z \sim 0$ may not be highly turbulent or that the turbulence model does not properly treat the media where C IV is observed. We return to the discussion of these predictions in Section 2.5.2.

Also shown in Figure 2.11 are the predicted b(C IV) distributions from Cen & Chisari (2011) for two column density bins: log N(C IV) = 13 − 15 cm^{-2} and log N(C IV) = 14 − 15 cm^{-2}, ranges over which our survey is sensitive. Their data are not intended for direct comparison with observations, and we only present them here for discussion. They report an increasing mean b(C IV) with increasing N(C IV), and as seen in Figure 2.11, the b-value distribution for their log N(C IV) = 14 − 15 cm^{-2} bin (cyan circles in Fig. 2.11) shows a higher mean b(C IV) than that of the wider N(C IV) range (blue circles). Cen & Chisari (2011) physically explain this trend by lower column C IV absorbers residing in 'quiescent' environments. If this interpretation is valid, the dearth of low-N(C IV), high-b(C IV) absorbers in our sample (see Section 2.6) may in fact be of physical origin rather than observational bias.

2.5 Ion-ion Correlations

We now explore relationships between the various metal species accessed by the COS data in addition to C IV. While C IV provides the most distinctive absorption-line tracer of metals within the COS G130M/G160M bandpass at very low redshift ($z_{\rm abs} \lesssim 0.1$), other metal-line transitions also fall within this bandpass and redshift range. As summarized in Table 1, we have identified and measured these additional lines occurring within our sample of C IV absorbers.

The additional metal-line species, Si II, Si III, C II, etc., can probe gas that is less ionized than C IV (and possibly in different phases altogether), as the ionization

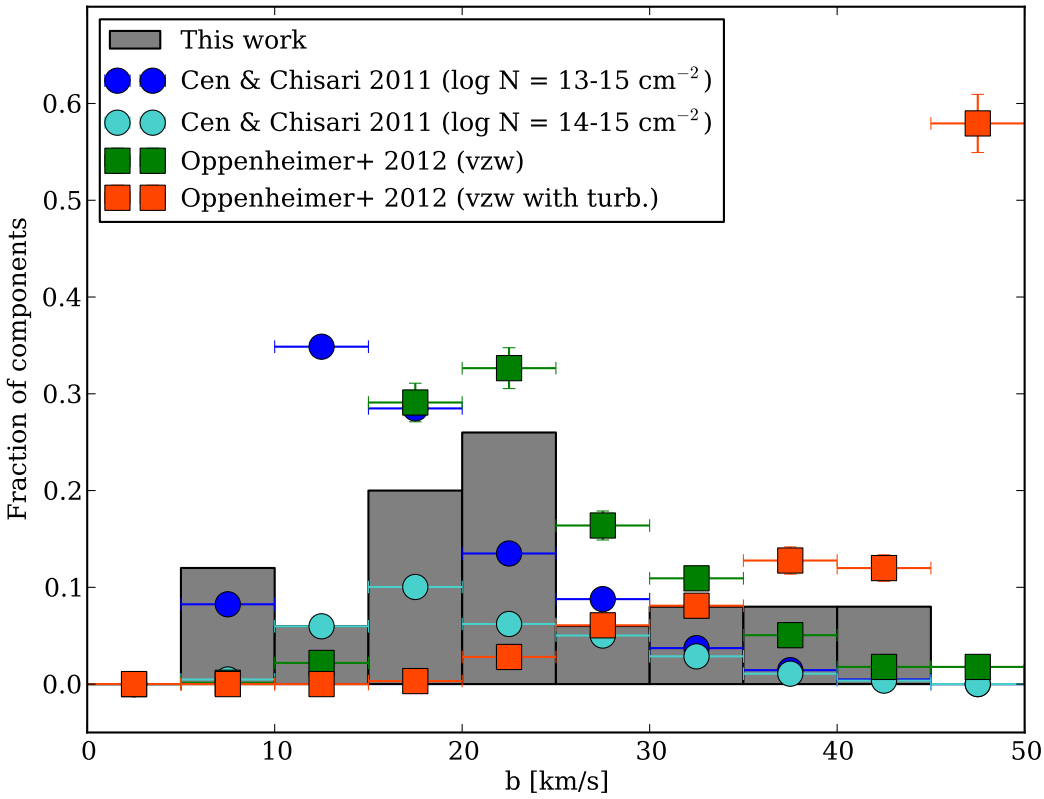

Figure 2.11 The distribution of Doppler b parameters measured from our C IV absorber sample and from cosmological simulations. The orange and green squares show predictions from the Oppenheimer et al. (2012) simulations run with and without added turbulence, respectively. Note the pronounced overprediction of b(C IV) when including the turbulence model. The blue and cyan circles show the b-value distributions from Cen & Chisari (2011) for absorbers with log N(C IV) $= 13 - 15$ cm^{-2} and log N(C IV) $= 14 - 15$ cm^{-2}, respectively. Their measurement methods produce data that may not be compared with observations, and we present them here only for comparison between their two samples (see discussion).

potentials vary widely among them. For example, the ionization energy from Si II to Si III is 16.35 eV, but the energy required to ionize C III to C IV is 47.9 eV (Kramida et al., 2014). Consequently, species such as Si II and C IV are expected to exist in very different physical conditions, and one might intuitively anticipate that these ions would be located in entirely different locations with different kinematics (i.e., Si II and C IV should exhibit different velocity centroids, line widths, etc.). Indeed,

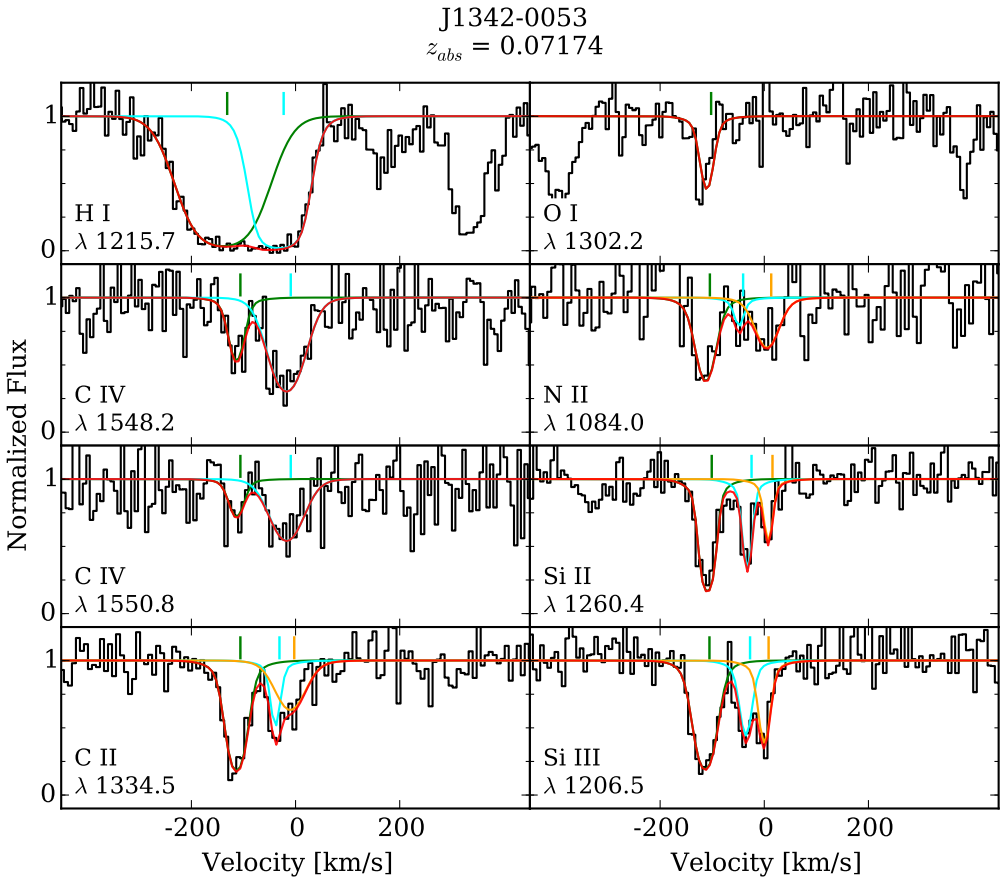

Figure 2.12 A C IV absorber at z_{abs}=0.07174 towards J1342-0053 that shows several other metal lines as labeled at the bottom of each panel. For each line, the individual component Voigt profile fits are colored green, cyan, and orange, while the composite profile resulting from a simultaneous fit of all components is shown in red. Interestingly, this system shows a neutral oxygen line well-aligned with a C IV component, which is typically associated with more highly-ionized gas.

this is predicted by cosmological simulations, which indicate that high ionization stages originate in large, low-density halos surrounding galaxies while lower ionization species such as C II, Si II, and Mg II are located in much smaller clumps embedded within the large hot halos (e.g., Shen et al., 2012; Ford et al., 2013).

However, QSO absorber observations do not entirely conform to this expectation. Many QSO absorbers show absorption lines of high-ionization species such as C IV, O VI and Ne VIII that have velocity centroids and line widths that are remarkably similar to those of low-ionizations stages such as H I, C II, Si II, and Mg II or

intermediate ionization stages including C III, O III, or Si III (Tripp et al., 2008, 2011; Meiring et al., 2013; Savage et al., 2014), even in multicomponent systems spread over large velocity ranges. Some absorbers are found to have O VI profiles that clearly differ in detail from the profiles of low ions (e.g., Werk et al., 2013), but even in these systems broad similarities in the shapes of the low-ion and high-ion profiles are evident. This kinematical alignment of low- and high-ionization species suggests that the high ions could be located in a configuration such as the surface of a cool (low-ionization) cloud instead of the large gaseous halo origin predicted by simulations.

As illustrated in Figure 2.12 and the Appendix, many of the blindly selected C IV absorbers in this paper also display clear velocity alignment of lines of lower ionization species and higher ionization C IV lines. To explore the relationship between C IV and lower ionization gas, we now consider the suite of additional metal lines covered in our blind survey. Also, if future observations of the same QSOs cover shorter wavelengths and access unsaturated higher Lyman series H I lines, the lower ionization species may be employed to study abundances in these absorbers.

2.5.1 Velocity alignment

The spectral resolution of the G130M and G160M gratings coupled with Voigt profile fitting enable the velocity centroids of unsaturated individual lines to be localized within < 10 km/s, although the COS wavelength calibration introduces additional uncertainties. Even where lines are blended, fitting the individual profiles can attempt to 'deblend' the constituents, albeit with increased uncertainty. All of the analyses in this section (this velocity comparison and the column density relationships to follow) utilize the individual components resulting from Voigt profile fitting. Thus, we begin by examining the velocity differences between fitted components of various species identified within the same system.

We examined the component structure of all species in each system and grouped together components of different species with the smallest velocity separation without yet imposing a maximum velocity offset. For example, in the absorber shown in Figure 2.12 (the $z_{abs} = 0.07174$ system in the spectrum of J1342-0053), we identified three components in the absorption profiles of Si II, C II, N II, and Si III, two components in the profiles of C IV and H I, and only one component in O I. For this absorber, we grouped together the Si II, C II, N II, and Si III components at δv= 8, -10, 5, and 0 km/s, respectively. The C II, C IV, H I, Si II, N II, O I, and Si III components at δv= -114, -114, -139, -123, -110, -110, and -113 km/s, respectively, were placed in a second group. We proceeded in this manner until all apparently related lines in the 42 absorbers in our sample had been assigned to a group. We note that in certain instances, the data are inadequate for this exercise; for example, we see that the H I Lyα line in Figure 2.12 is strongly saturated, thus precluding reliable measurements of the quantities required for this analysis.

Figure 2.13 shows distributions of velocity offsets between C IV and a variety of ions as grouped by the above procedure; the species detected in our data cover a range of ionization stages, from C II and O I (low ions) to Si III and Si IV (intermediate ions) to O VI and N V (high ions). In some instances, Figure 2.13 confirms expected outcomes, i.e., species that should be aligned (e.g., C IV and Si IV) are aligned. However, Figure 2.13 also reveals some surprising alignments. For example, the only 3 detections of O I in our sample show close alignments with components of C IV, even though the ionization potentials greatly differ: E(O I $\rightarrow$ II) = 13.6 eV and E(C III $\rightarrow$ C IV) = 47.9 eV (Kramida et al., 2014). Likewise, the majority of the C II absorption lines are well aligned with the C IV lines. For C II, we have a larger sample, and we find that the distribution of velocity differences is centered on 0 km s^{-1}, and 79% of the C II lines are aligned with C IV to within $\pm$ 20 km s^{-1}. Furthermore, our limited sample of O VI detections show decent alignment with C IV components; in contrast,

Table 2.4 Correlation Statistics of Ion Column Densities

Ion 1	Ion 2	τ_{ss}[a]	$P_{\tau ss}$[b]	τ_{sd}[c]	$P_{\tau sd}$[d]	$\Phi_I(1)$ (eV)[e]	$\Phi_I(2)$ (eV)[f]	$\lvert\Delta\Phi\rvert$ (eV)
C IV	C II	0.4286	0.0559	0.3744	0.1314	47.8	11.3	36.5
C IV	O I	0.0585	0.7698	0.0	1.0	47.8	0.0	47.8
C IV	Si III	0.4729	0.0242	0.3744	0.1353	47.8	16.3	31.5
C IV	Si IV	0.5867	0.0091	0.4933	0.0483	47.8	33.5	14.3
C IV	O VI	1.1667	0.0154	1.2778	0.0159	47.8	113.9	66.1
C IV	N V	0.3922	0.0244	0.4052	0.0224	47.8	77.5	29.7
C II	Si III	1.0292	0.0014	1.076	0.0009	11.3	16.3	5.0
C II	Si IV	0.8182	0.0172	0.8182	0.0172	11.3	33.5	22.2
Si II	Si IV	0.2821	0.4017	0.2821	0.4017	8.1	33.5	25.4
Si III	Si IV	0.8382	0.0057	0.8971	0.0034	16.3	33.5	17.2
C II	Si II	1.1048	0.0041	1.1048	0.0041	11.3	8.1	3.2
Si II	Si III	0.8235	0.014	0.8235	0.0145	8.1	16.3	8.2
C IV	Si II	0.2333	0.2427	0.1267	0.5993	47.8	8.1	39.7

[a] The Kendall tau correlation coefficient between the column densities of Ion 1 and Ion 2, assuming that lines flagged as saturated yield lower limits for their column densities.

[b] Probablility that a correlation does not exist between the column densities of Ion 1 and Ion 2, assuming that lines flagged as saturated yield lower limits for their column densities.

[c] The Kendall tau correlation coefficient between the column densities of Ion 1 and Ion 2, assuming that lines flagged as saturated yield reliable column densities.

[d] Probablility that a correlation does not exist between the column densities of Ion 1 and Ion 2, assuming that lines flagged as saturated yield reliable column densities.

[e] Energy to attain ionization state of Ion 1

[f] Energy to attain ionization state of Ion 2

Lehner et al. (2014) find that O VI and C IV components often show quite distinct kinematics from one another in their $z \sim 3$ sample of Lyman limit and damped Lyα systems. Larger low-redshift samples at higher resolution would enable a further investigation of possibly evolving kinematic relationships between these species over the age of the Universe.

It is clear from Figure 2.13 that not all component pairs classified in the above manner are well aligned. However, it is important to recognize that the spectral resolution, line-spread function, and well-known wavelength calibration problems of COS (Wakker et al., 2015) limit our ability to accurately measure velocity centroids.

Therefore, we impose the following requirement for individual component pairs in order to include them in our subsequent analyses of aligned absorption lines:

$$\delta v_{XY} \leq \sqrt{\sigma_v^2(\mathrm{X}) + \sigma_v^2(\mathrm{Y}) + \sigma_v^2(\mathrm{COS})} \tag{2.13}$$

where δv_{XY} is the velocity offset between components of species X and Y, and σ_v(X) and σ_v(Y) are the uncertainties in the component velocity centroids of species X and Y, respectively, from Voigt profile fitting. The final term, σ_v(COS), accounts for known (but poorly understood) errors in the COS wavelength solution that well exceed the 15 km/s resolution of the instrument (Wakker et al., 2015). Efforts by several teams are underway to solve for corrections to these errors, but the effects appear to be highly wavelength dependent and nonlinear. We have adopted σ_v(COS) = 25 km/s, commensurate with offsets we have measured in our spectra between multiple transitions of the same ion that should be perfectly aligned but are not (Tripp et al., in preparation).

2.5.2 Correlations of column densities between ions

Using the components grouped in accord with Eq. 2.13, we next examine the correlations in column density of one species with another. The aforementioned limitations in our H I measurements (due to strong saturation of the only available H I lines) inhibit our ability to analyze the absorbers with the usual photoionization or collisional ionization models, but we can nevertheless gain insights on the nature of these systems by comparing unsaturated species. For example, if two given species generally are located in the same (cospatial) gas phase, then one might expect their column densities to be strongly correlated if the various clouds have the same relative abundance patterns. Conversely, if two species have a physical relationship but are not necessarily cospatial (e.g., if the C IV arises in an interface layer on the surface of a low-ionization phase), then the column densities of those species might be poorly

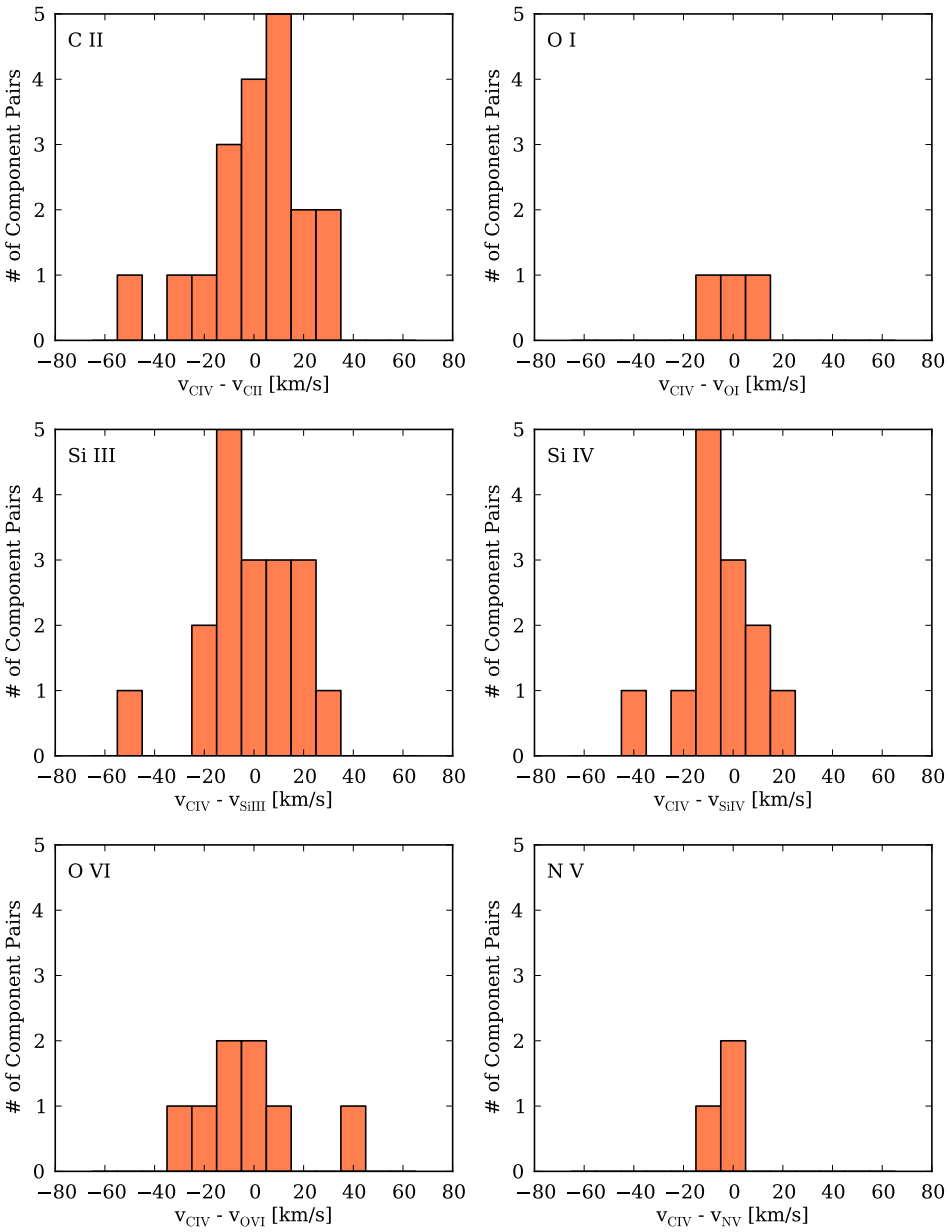

Figure 2.13 Offsets in velocity between components of C IV and other ions detected in the data. The plots are roughly arranged to show the C IV offsets from low, intermediate, and high ions in the top, middle, and bottom rows, respectively. Close alignments in velocity space among components are typically interpreted as indicators of physical association, such as the species arising in the same kinematically connected structure (e.g., isolated gas cloud in a galaxy halo) or even in the same gas phase. The many instances of offsets similar to the nominal resolution of 15 km/s indicate closely associated C IV components with a variety of ionization stages.

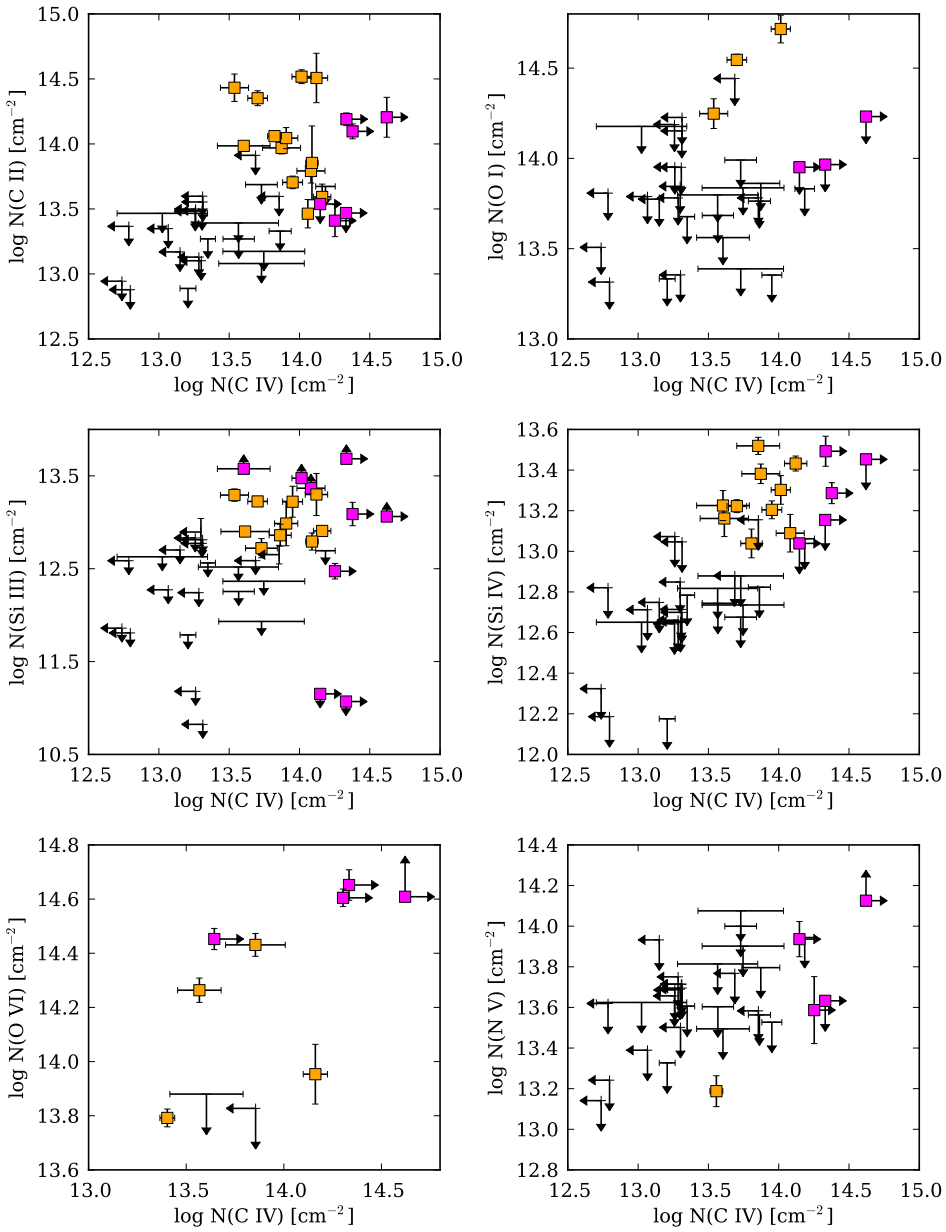

Figure 2.14 Column densities of various species as a function of C IV column density. Yellow squares represent unsaturated detections in both species plotted while magenta squares denote saturation in one or both species. Nondetections are shown with 3-σ upper limits.

correlated despite being kinematically well aligned. We note that it has already been shown that the population of O VI absorbers that are well aligned with H I exhibit

very weak correlation between N(O VI) and N(H I) (Tripp et al., 2008), and we might anticipate a similar situation with C IV.

Figures 2.14, 2.15, and 2.16 show the column density measurements of individual species components associated in velocity as described above. The points marked by yellow squares indicate unsaturated detections of both species, and magenta squares indicate that one of the two species is saturated. Here, we have flagged a line as saturated if $\geq$10% of the pixels in the line profile have flux values that are less than their noise values. Upper limits are indicated where one or both species was not detected at a coincident velocity to components identified in one or more other species. Certain points in the ion-ion plot reflect only upper limits for both species, and we have excluded these cases from the statistical analysis below.

To quantitatively assess whether the species shown in Figures 2.14, 2.15, and 2.16 are correlated, Table 2.4 shows the ion-ion column density correlation statistics calculated using the Kendall Tau rank correlation method, which incorporates censored data (upper/lower limits) to calculate the probability of the null hypothesis that no correlation exists between the two variables (smaller values of P_{tau} in Table 2 correspond to *greater* confidence of rejecting the null hypothesis that the quantities are not correlated). We have imposed a criterion for saturation upon the column density measurements as described above. However, these column densities may be better constrained than merely assigning lower limits, as Voigt profile fitting (used to measure column densities) is able to measure mildly saturated lines with adequate accuracy. Therefore, we calculate the Kendall tau correlation statistics flagging the measurements of the 'saturated' lines as both lower limits and detections, which are reflected in $P_{\tau ss}$ and $P_{\tau sd}$, respectively.

With the exception of cases in which our sample is very small (e.g., O I, N V), most of the Kendall-Tau tests in Table 2.4 suggest that the column densities of most of these species are correlated, albeit in some cases weakly. However, we find that

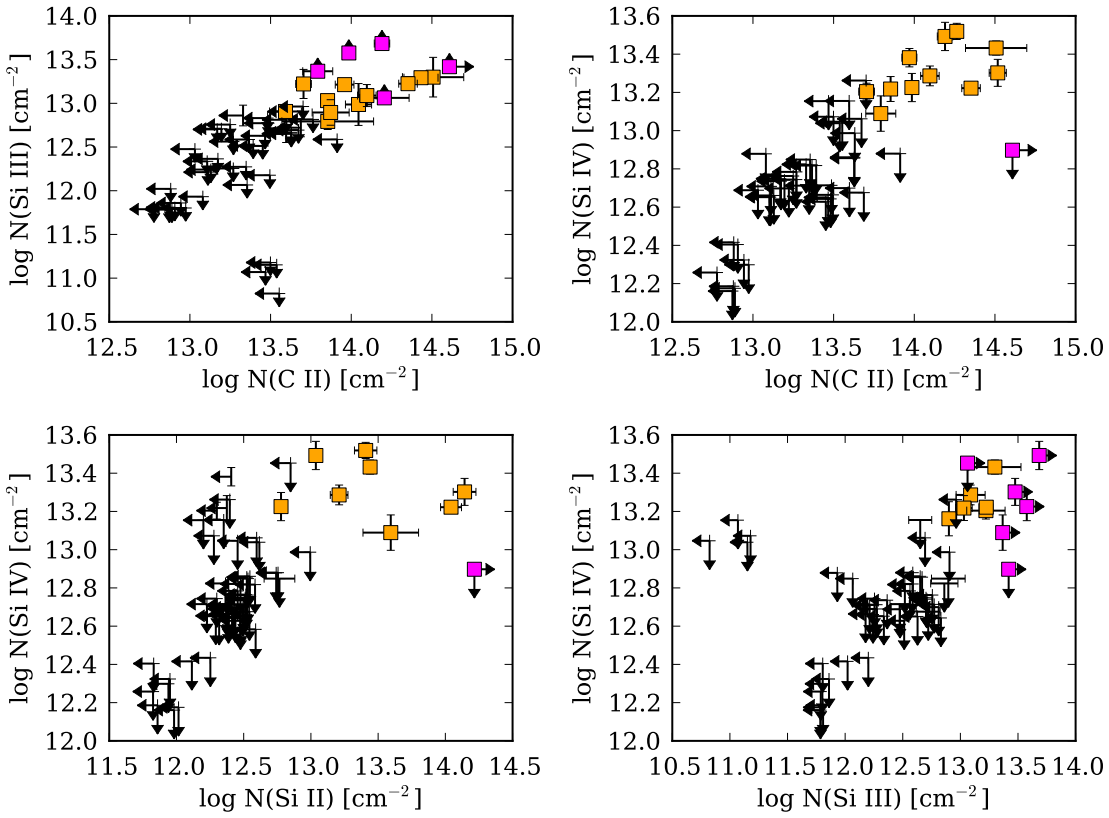

Figure 2.15 Column densities of low- and mid-ionization species versus one another. Yellow squares represent unsaturated detections in both species plotted while magenta squares denote saturation in one or both species. Nondetections are shown with 3-σ upper limits.

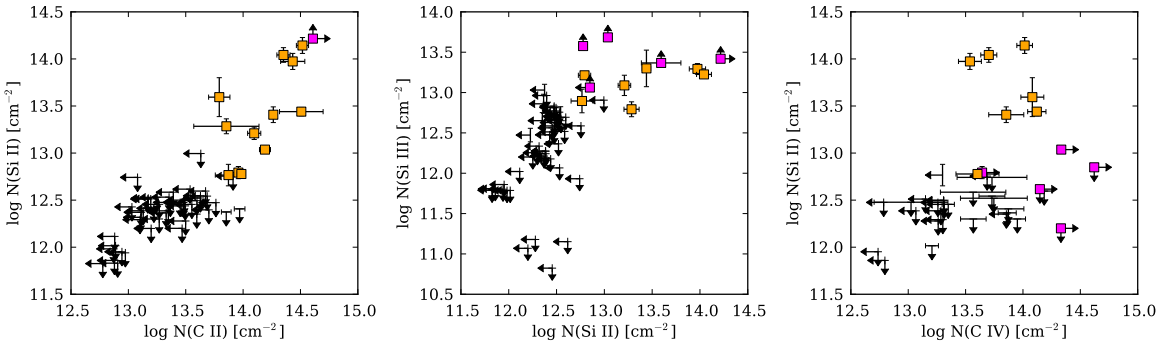

Figure 2.16 Column densities of low-ionization species Si II and O I as a function of C II, another low ion. Yellow squares represent unsaturated detections in both species plotted while magenta squares denote saturation in one or both species. Nondetections are shown with 3-σ upper limits.

the likelihood of a correlation is generally very strong (i.e., small P_τ) between species with small ionization energy differences ($|\Delta\Phi| < 20$ eV). The most notable exception occurs for the C IV-O VI pair, which shows a $\sim 98\%$ probability for the existence of a correlation even though these species have the greatest separation in ionization potential ($|\Delta\Phi| = 66.1$ eV). This result should be interpreted cautiously as we only have a small sample of O VI lines, but this could occur if the C IV and O VI arise in a collisionally ionized hot phase. We note that our survey is C IV selected and therefore includes, by design, gaseous systems with ionization conditions conducive to maintaining sufficient quantities of C IV ions for detection. Given the small sample sizes of certain ion pairs, we caution against overinterpreting these correlation results; some peculiarities clearly arise in Table 2.4, such as the apparent correlations for C II-Si II and C II-Si IV but the lack thereof for Si II-Si IV.

The decreasing likelihood of correlation with increasing differences in ionization potential may indicate that C IV has some type of physical relationship with lower ionization stages but nevertheless arises in a phase that is distinct from the low ions. This would help to explain the poor agreement between the observed C IV $b-$values and the predicted $b-$values from Oppenheimer et al. (2012) when turbulence is included (purple points in Figure 2.11): Oppenheimer et al. (2012) were motivated to add turbulence to their model based on the nonthermal broadening required by aligned O VI and H I absorbers under the assumption that the $b-$values of O VI and H I can be jointly used to solve for the temperature and nonthermal broadening. If the O VI and H I lines arise in physically distinct phases, then the nonthermal broadening found this way may not be valid. Indeed, the addition of this "turbulence" is not supported by the measured C IV b-values in our sample (see Figure 2.11). More sophisticated modeling of multiphase absorbers may be required for these CGM absorbers. It would also be helpful to expand the sample of C IV absorbers to improve the statistical significance of these analyses.

2.6 N(C IV)-b relationship and physical origin of C IV absorbers

The larger aim of our survey is to place the gas traced by C IV absorption in context with the galaxies that may host the gas or have some past or present association. While we may, in general, expect the gas to arise from a variety of astrophysical configurations, we may inquire whether the absorption data themselves suggest that the gas arises under some characteristic set of physical conditions.

Heckman et al. (2002) found that O VI absorbers observed in the Galactic disk, Galactic halo, Magellanic Clouds, and IGM all fall on a common N(O VI) vs. b-value relation. They further interpreted this result to suggest that the gas is tracing radiatively cooling gas that is passing through the 'warm-hot' regime at $T = 10^5 - 10^6$ K. Tripp et al. (2008) find that their large sample of O VI absorbers do not follow the Heckman et al. (2002) relation as closely, but their subsample of 'intervening' absorbers (those with a greater velocity separation from the QSO itself) do show a marginal correlation between N(O VI) and b(O VI).

We present the N(C IV)-b(C IV) relationship for our absorber sample in Figure 2.17. To assess whether a correlation exists between the two variables, we employ a nonparametric Spearman rank-order correlation test. For the entire sample, we obtain a p-value for the null hypothesis (that no correlation exists) of 0.022, suggesting that a correlation exists at the 97.8% confidence level. However, the apparent envelope separating the region devoid of low-N(C IV), high-b points in Figure 2.17 (the lower-right corner) is at least partly due to an observational bias. Very broad, low-column density absorbers produce shallow line profiles, which are difficult to detect above the noise. To account for this bias, we also consider only systems that have log N(C IV) > 13.5 cm^{-2}, approximately above which we measure the full range of b-values. A Spearman test for the correlation among these points yields a likelihood of 86.8%, i.e., when we account for our inability to detect C IV absorbers with large b-values

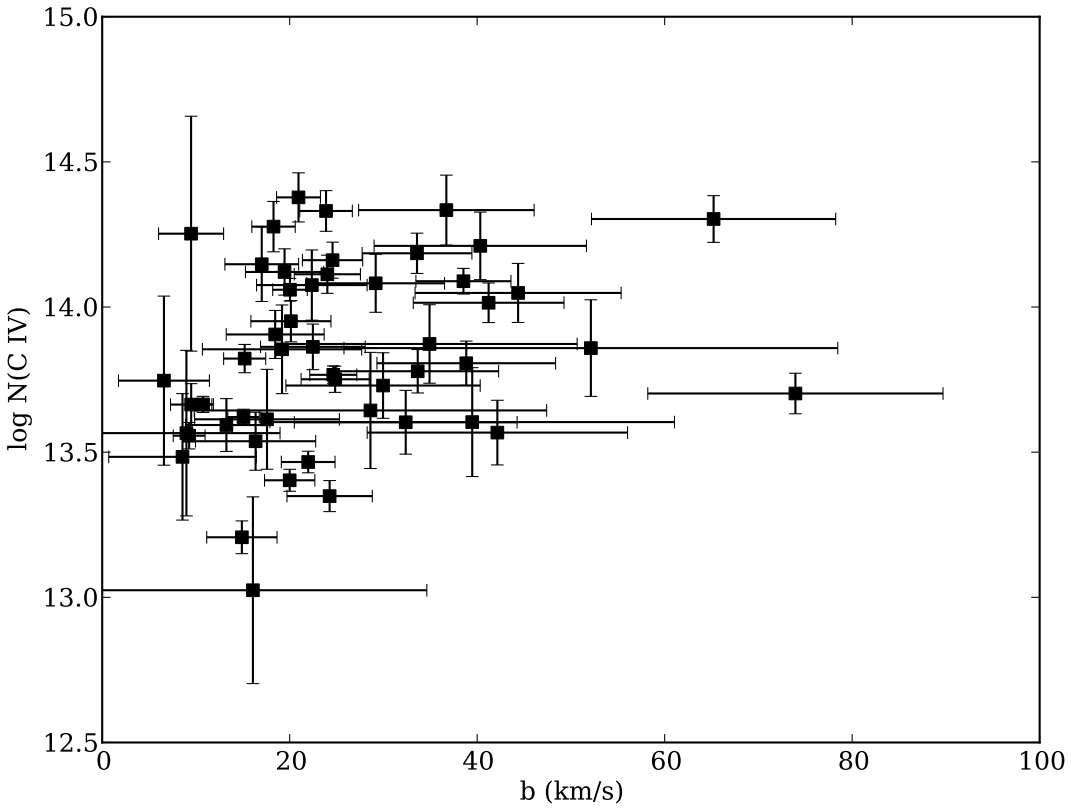

Figure 2.17 Column densities of C IV as a function of the b-value for individual absorption components. Both quantities and their errors are measured from Voigt profile fitting.

and low column densities, we find that there is no compelling evidence that b(C IV) and N(C IV) are correlated in our CIV sample.

2.7 Summary and Conclusions

From a blind survey utilizing HST/COS spectra of 89 QSOs, we have presented our sample of 42 $z < 0.16$ C IV absorbers, their measurements, statistics, and correlations between the ions detected. These absorbers compose the parent sample for a larger program that aims to study the state of cosmic heavy-element enrichment in the most recent epoch (as in this paper) and characterize the CGM with unprecedented

sensitivity to faint dwarf galaxies (Papers I, III, and subsequent works), the latter enabled by the low redshift regime of our sample.

We summarize our primary findings as follows:

1. At $z < 0.16$, we measure $\Omega_{\rm C\ IV} = 10.0 \pm 1.5 \times 10^{-8}$ for $\log N({\rm C\ IV}) > 13.0$ cm^{-2}; therefore, the C IV cosmic mass density has indeed increased over cosmic time, but marginally so since $z \sim 1.5$.

2. At $z \leq 0.16$, the frequency of C IV absorbers per comoving path length $d\mathcal{N}/dX = 7.5 \pm 1.1$, representing an increase relative to the value measured over the full $z < 1$ epoch (4.9; Cooksey et al., 2010).

3. Various cosmological hydrodynamic simulations that include galactic outflows qualitatively produce increased $d\mathcal{N}/dz$, $d\mathcal{N}/dX$, and $\Omega_{\rm C\ IV}$ since $z \sim 4$, and their predictions are indeed consistent with our measurement of $\Omega_{\rm C\ IV}$ at $z \sim 0$. However, discrepancies arise among the evolutionary tracks of these theoretical predictions, likely due to 'sub-grid' physics prescriptions that handle processes such as feedback and star formation. Our results are consistent with $\Omega_{\rm C\ IV}$ remaining relatively constant at $z = 0$ from $z = 1$.

4. Close alignments in velocity occur between species of varying ionization potential, but evidence for correlations between the column densities of several of these well-aligned ion pairs appears to weaken as the differences in their ionization potentials increase. This comparative analysis would benefit from larger samples of systems that show components of multiple ions; however, the close velocity alignments of certain species that show a decreased likelihood of a correlation suggests that many absorbers in our sample reside in multiphase material.

5. Some evidence exists for a correlation between N(C IV) and b(C IV) but the evidence is not strong over the entire sample when considering incompleteness to high-b, low-N(C IV) absorbers.

Acknowledgements

The authors would like to thank George Becker for sharing software; Valentina D'Odorico, Hsiao-Wen Chen, and Charles Danforth for helpful discussions; and Ben Oppenheimer, Renyue Cen, Elisa Chisari, and Ali Rahmati for sharing their simulation results to include in this study. We also thank Kathy Cooksey for providing software and assistance with statistics calculations. Support for this research was provided by NASA through grants HST-GO-11741, HST-GO-11598, HST-GO-12248, and HST-AR-13894 from the Space Telescope Science Institute, which is operated by the Association of Universities for Research in Astronomy, Incorporated, under NASA contract NAS5-26555.

CHAPTER 3

A DEEP SEARCH FOR FAINT GALAXIES ASSOCIATED WITH VERY LOW-REDSHIFT C IV ABSORBERS: III. THE MASS- AND ENVIRONMENT-DEPENDENT CIRCUMGALACTIC MEDIUM

Joseph N. Burchett[1], Todd M. Tripp[1], Rongmon Bordoloi[2], J. Xavier Prochaska[3], Jessica K. Werk[3], Jason Tumlinson[2], C. N. A. Willmer[4], John M. O'Meara[5], and Neal Katz[1]

Using Hubble Space Telescope Cosmic Origins Spectrograph observations of 89 QSO sightlines through the Sloan Digital Sky Survey footprint, we study the relationships between C IV absorption systems and the properties of nearby galaxies as well as large-scale environment. To maintain sensitivity to very faint galaxies, we restrict our sample to $0.0015 < z < 0.015$, which defines a complete galaxy survey to $L \gtrsim 0.01\ L*$ or stellar mass $M_* \gtrsim 10^8\ M_\odot$. We report two principal findings. First, for galaxies with impact parameter $\rho < 1\ r_{vir}$, C IV detection strongly depends on the luminosity/stellar mass of the nearby galaxy. C IV is preferentially associated with galaxies with $M_* > 10^{9.5}\ M_\odot$; lower mass galaxies rarely exhibit significant C IV absorption (covering fraction $f_C = 9^{+12}_{-6}\%$ for 11 galaxies with $M_* < 10^{9.5}\ M_\odot$). Sec-

[1]Department of Astronomy, University of Massachusetts, 710 North Pleasant Street, Amherst, MA 01003-9305

[2]Space Telescope Science Institute, Baltimore, MD 21218

[3]UCO/Lick Observatory, University of California, Santa Cruz, CA

[4]Steward Observatory, University of Arizona, Tucson, AZ, 85721

[5]Department of Chemistry and Physics, Saint Michaels College, One Winooski Park, Colchester, VT 05439

ond, C IV detection within the $M_* > 10^{9.5}$ $M_\odot$ population depends on environment. Using a fixed-aperture environmental density metric for galaxies with $\rho < 160$ kpc at $z < 0.055$, we find that 57^{+12}_{-13}% (8/14) of galaxies in low-density regions (regions with fewer than seven $L > 0.15$ $L*$ galaxies within 1.5 Mpc) have affiliated C IV absorption; however, none (0/7) of the galaxies in denser regions show C IV. Similarly, the C IV detection rate is lower for galaxies residing in groups with dark-matter halo masses of $M_{\rm halo} > 10^{12.5}$ $M_\odot$. In contrast to C IV, H I is pervasive in the CGM without regard to mass or environment. These results indicate that C IV absorbers with log N(C IV) $\gtrsim 13.5$ cm^{-2} trace the halos of $M_* > 10^{9.5}$ $M_\odot$ galaxies but also reflect larger scale environmental conditions.

3.1 Introduction

The interactions of galaxies over their lifetimes – with their ambient gaseous surroundings as well as with other galaxies – is currently a subject of intensive scrutiny. Galaxies' gaseous halos, or circumgalactic media (CGM), serve as the mediators of processes believed to enable ongoing star-formation and galaxies' eventual quenching and/or transformation. For example, *feedback*, the combined mechanisms that inject energy and momentum into the interstellar medium (ISM) of galaxies and transport metal-enriched gas expelled by stars or active galactic nuclei (AGN) into their CGM and beyond (e.g., Oppenheimer & Davé, 2008; Springel & Hernquist, 2003; Martin, 2005; Tremonti et al., 2007; Bordoloi et al., 2011), is central to the galaxy formation and evolution paradigm. Galaxy formation models that do not include outflows produce galaxies with much higher stellar masses and star-formation rates (SFRs) than those observed (Davé et al., 2011; Vogelsberger et al., 2013). Furthermore, these processes are required to enrich the intergalactic medium (IGM) with metals to the observed levels (Cen & Chisari, 2011; Oppenheimer et al., 2012; Rahmati et al., 2015), and this metal-enriched gas directly traces the products of these feedback processes

(Ford et al., 2013; Oppenheimer & Davé, 2006; Rubin et al., 2014; Veilleux et al., 2005b).

A galaxy's reservoir for star formation is likely to be fed by infalling gas from the IGM (Kereš et al., 2005; Dekel & Birnboim, 2006). This material, which is metal poor relative to the gas in the disk, has been fervently sought by observers over nearly all wavelengths (e.g., Kacprzak et al., 2012b; Ribaudo et al., 2011; Rubin et al., 2012; Martin et al., 2015), but it is still unclear how galaxies acquire gas and how the physical conditions in the CGM mediate the fueling. Nevertheless, this diffuse medium is most sensitively probed by absorption line spectroscopy of quasi-stellar objects (QSOs; Fumagalli et al., 2011), revealing the imprint of neutral hydrogen (H I) as well as heavy elements in a variety of ionic states. While H I has been shown to trace the halos of galaxies out to great distances of ∼300 kpc and beyond (Morris et al., 1993; Tripp et al., 1998; Chen et al., 2005; Prochaska et al., 2011), the various metal-line transitions probe the physical conditions and enrichment of the gas (Meiring et al., 2013; Lehner et al., 2013; Werk et al., 2014).

Besides the internal processes mentioned above, galaxy evolution critically depends on the galaxy environment. For over half a century, galaxy clusters have been known to be largely composed of red, early-type galaxies (e.g., Abell, 1965) and to be deficient in neutral hydrogen (H I) (Davies & Lewis, 1973). As for a physical mechanism relating the cluster environment to the dearth of H I, Gunn & Gott (1972) detailed the process known as 'ram-pressure stripping' whereby the hot intracluster medium can remove the gas from an infalling galaxy. Dressler (1980) showed that the presence of elliptical and S0 galaxies increases with local galaxy density, indicating that the degree by which the corresponding processes impact galaxy morphology increases continuously for denser environments. Furthermore, Butcher & Oemler (1984) found that the fraction of blue galaxies in clusters decreases from $z \sim 0.45$ to the present and that the spiral galaxies in $z \sim 0$ clusters are redder in color than field

spirals. More recently, phenomenology in much less dense regimes has revealed relationships between satellites and central galaxies in groups such that passive satellites preferentially reside around passive centrals and star-forming satellites tend to reside in groups with star-forming centrals (Weinmann et al., 2006; Knobel et al., 2015), an effect known as 'galactic conformity'. This phenomenon suggests a deeper, underlying causal relationship between group galaxies and the larger dark matter halos in which they reside. While the question naturally arises whether environmental effects manifest in the CGM, research on the matter (Finn et al., 2016; Johnson et al., 2015, 2014; Yoon & Putman, 2013; Wakker et al., 2015; Tejos et al., 2012) is in its infancy.

Both theory and observations suggest that C IV absorbers are closely tied to galaxies. Based on a sample of 14 absorbers at z<0.9, Chen et al. (2001) found that strong C IV absorbers ($W_{1548} \gtrsim 200$ mÅ) tend to be found within ∼180 kpc of galaxies, regardless of morphology or luminosity. Stocke et al. (2013) found that the C IV systems in their 9-absorber sample lie within ~ 250 kpc of galaxies at similar redshifts. In their simulations, Ford et al. (2013) find that nearly all detectable C IV absorption at $z = 0.25$ occurs within 300 kpc of galaxies, dropping precipitously at impact parameters $\rho \gtrsim$250 kpc for $M_{\rm halo}$=10^{11} $M_\odot$ galaxies. The COS-Dwarfs survey (Bordoloi et al., 2014) systematically characterized the C IV-enriched CGM by targeting a sample of QSO sightline-galaxy pairs with a range of carefully chosen galaxy characteristics, including stellar mass $10^8 M_\odot \lesssim M_* \lesssim 10^{10} M_\odot$, $\rho < 150$ kpc, and specific star formation rate (sSFR) spanning both star-forming and quiescent galaxies. Among the key COS-Dwarfs results are the following: an anticorrelation between N(C IV) and impact parameter, with no C IV absorbers detected beyond 0.5 virial radii (r_{vir}), and a tentative correlation between N(C IV) and sSFR. Liang & Chen (2014) also report a dearth of C IV absorbers beyond 0.7 r_{vir}. However, both the Bordoloi et al. (2014) and Liang & Chen (2014) samples were selected to favor of isolated galaxies, a key difference from this work.

The work presented here leverages a blind survey of low-redshift C IV absorbers as described in Burchett et al. (2015, hereafter Paper II) to investigate the distribution of ionized metal-enriched gas around galaxies down to $M_* \sim 10^8 M_\odot$, how this distribution changes with host galaxy mass, and whether the halos traced by C IV show effects of the large-scale environment. The low redshifts of our sample presented in Paper II cover the most recent two billion years of cosmic time and enable deep, high-resolution, multiwavelength studies of the galaxy environments near the absorbers. At the lowest-redshift end of our distribution ($z \lesssim 0.01$), the Sloan Digital Sky Survey[6] (SDSS) is complete down to very faint galaxies ($L \sim 0.01L*$). In previous studies, this completeness issue has been perpetually problematic for associating the detected gas with a host galaxy. At even moderate redshifts of z$\sim$0.2, the angular size scale of modest impact parameters becomes very small and drastically complicates resolving individual galaxies from one another and from the QSO. By focusing on the lowest redshifts, we exploit the rich galaxy survey data provided by the SDSS and the literature to achieve completeness to faint dwarf galaxies and to begin to assess the relationship between these objects and the absorbing clouds that are readily detectable at all redshifts.

The paper is organized as follows: The sources of our absorber and galaxy data as well as the methods of deriving measurements from them are described in Section 3.2. We present our analyses and results in Section 3.3 and discuss the implications of our study in Section 4.5. Section 4.6 summarizes the paper. For the reader interested in more information about the large-scale environments analyzed in this work, we offer sightline-centric maps of the galaxies composing them in the Appendix.

[6]http://skyserver.sdss3.org

3.2 Data and Measurements

The sources of our data and measurements derived from them are described below. Throughout the paper, we assume nine-year WMAP (Hinshaw et al., 2013) cosmology values, with $H_0 = 69.3$, $\Omega_m = 0.29$, and $\Omega_\Lambda = 0.71$. All stellar mass, halo mass, and star formation rate calculations assume a Chabrier (2003) initial mass function. Due to the low-redshift nature of our sample, galaxy distances obtained from a pure Hubble flow are very sensitive to the gravitational effects of the Virgo Cluster, the Shapley Supercluster, etc., on measured recession velocities. Therefore, we correct for these effects as a function of object position and redshift using the formalism of Mould et al. (2000). These corrections typically result in impact parameters and masses that are within 10% of their uncorrected values and are well within their uncertainties; however, $\sim 5\%$ of objects in our galaxy survey data require distance corrections $> 10\%$ and may affect the mass calculation by up to a factor of ~ 2, comparable to the uncertainty of our stellar mass calculations.

3.2.1 C IV Absorber Sample and Redshift Criteria

The analyses herein most heavily employ the C IV absorber sample from Paper II, which is a blind survey for C IV absorbers within QSO spectra observed with the Hubble Space Telescope Cosmic Origins Spectrograph (HST/COS) in the COS-Halos (Tumlinson et al., 2013; Werk et al., 2012), COS-Dwarfs (Bordoloi et al., 2014), and the COS Absorption Survey of Baryon Harbors (CASBaH, Tripp et al., 2011; Meiring et al., 2013) programs. Spanning redshifts $0 < z_{\rm abs} < 0.16$, the full sample comprises 42 absorbers that were discovered in 89 sightlines. Stemming from a blind survey, this absorber sample is free from any galaxy association biases inherent in targeted galaxy/absorber studies and indeed does not impose *a priori* that a given absorber is associated with any galaxy at all.

For our analyses in this paper, the existing galaxy survey data around these absorber sightlines (see Section 3.2.2) do not have sufficient spectroscopic completeness for galaxies over the full $z = 0 - 0.16$ range where C IV is covered by the high-resolution COS gratings. Therefore, the two primary but complementary analyses presented in this paper adopt redshift limits commensurate with the requirements of each:

(1) A defining objective of this series of papers is to surpass the sensitivity of previous surveys to dwarf galaxies potentially associated with C IV absorbers and assess the connection of these faint dwarfs, undetected at higher redshifts, to the absorbers. Thus, we first examine absorber/galaxy associations as a function of galaxy mass, where the mass range spans down to an order of magnitude below the lowest mass where circumgalactic C IV has been previously characterized by galaxy-selected studies (Bordoloi et al., 2014; Liang & Chen, 2014). The median galaxy masses of the COS-Dwarfs (Bordoloi et al., 2014) and Liang & Chen (2014) samples are 2×10^9 $M_\odot$ and 5×10^9 $M_\odot$, respectively. Using the M$_*$-absolute r-band magnitude ($\mathcal{M}_r$) relation derived by Liang & Chen (2014) from the NASA-Sloan Atlas[7], a stellar mass of $2{\times}10^8$ $M_\odot$ corresponds to $\mathcal{M}_r = -16.6$, approximately $L_r \sim 0.01$ $L*$ (Blanton et al., 2003). Given its apparent magnitude limit, the SDSS should be complete to galaxies of this mass at $z \lesssim 0.015$. Therefore, our absorber-galaxy mass analysis adopts a redshift limit of $z \lesssim 0.015$.

(2) Following on the results of (1) where we find an increased C IV detection rate for $M_* > 10^{9.5} M_\odot$ galaxies over less massive galaxies, we then investigate the dependence of CGM absorption on the larger environments of these galaxies. Because we select the CGM/environmental analysis sample on $M_* > 10^{9.5} M_\odot$ galaxies (corresponding to $\mathcal{M}_r \lesssim -19$), we expect spectroscopic completeness to these galaxies over the full

[7]http://www.nsatlas.org

redshift range of the NASA-Sloan Atlas. Therefore, we adopt the upper redshift limit of the atlas, $z = 0.055$, minus a small buffer to mitigate edge effects, for this analysis, including absorbers at $z < 0.052$ and their measurements from COS-Dwarfs (Bordoloi et al., 2014) and the blindly-detected sample of Paper II (Burchett et al., 2015).

The column densities of detected absorbers were obtained via Voigt profile fitting. The upper and lower limits reported here were measured by the apparent optical depth method (Savage & Sembach, 1991) using the error vector output from the COS data reduction pipeline and assuming a velocity window of $\pm$ 50 km/s of the corresponding galaxy redshifts. Covering fractions reported for galaxies/absorbers from this work assume 3-σ detection thresholds of log N(C IV) > 13.5 cm^{-2} and log N(H I) > 13.0 cm^{-2}.

3.2.2 Optical Galaxy Surveys

As all but one of the QSOs observed in our dataset (Paper II) fall within the SDSS footprint, this study employs the SDSS extensively, specifically SDSS Data Release 12 (Alam et al., 2015) and the NASA-Sloan Atlas, for both spectroscopy and photometry. We also exploit the NASA/IPAC Extragalactic Database[8], which houses catalogs from several large galaxy surveys, such as the Third Reference Catalogue of Bright Galaxies (RC3; de Vaucouleurs et al., 1991; Corwin et al., 1994) and the Two-degree-Field Galaxy Redshift Survey (2dFGRS; Colless et al., 2001). The NASA-Sloan Atlas is a catalog compiling newly remeasured SDSS and GALEX photometry along with spectral line measurements using an improved calibration of the SDSS spectra. The core sample for this catalog stems from SDSS DR8 and adds objects missed or excluded by SDSS but spectroscopically measured by the CfA Redshift Survey (Huchra et al., 1995), 2dFGRS, etc. According to Strauss et al. (2002), the

[8]http://ned.ipac.caltech.edu; The NASA/IPAC Extragalactic Database (NED) is operated by the Jet Propulsion Laboratory, California Institute of Technology, under contract with the National Aeronautics and Space Administration.

SDSS spectroscopic survey is complete down to $m_r \sim 17.7$. All magnitudes expressed herein are derived from the model-fit magnitudes from the NASA-Sloan Atlas, which calculate total magnitudes of galaxies by Sersic profile fits, or the 'modelMag' values, those deemed the better fit between de Vaucoleurs and exponential profiles, directly from the SDSS database for objects not provided by NASA-Sloan.

At the low redshifts ($z < 0.015$) primarily targeted in this work, even low-mass galaxies appear quite extended on the sky and a number of issues occur within the SDSS databases. For the analyses herein, we primarily employ the NASA-Sloan Atlas instead of the 'stock' SDSS databases. However, we also produced our own SDSS catalog to corroborate results obtained using the NASA-Sloan Atlas and specifically address certain linking issues within SDSS: First, extended objects may have received multiple spectroscopic measurements and thus may be duplicated in the spectroscopic object ('SpecObj') tables. Second, we found numerous cases of galaxy spectra linked to incorrect galaxy photometric objects, thus yielding clearly incorrect redshifts retrieved through queries to the 'Galaxy' table of the SDSS database. Third, spectroscopic data are primarily keyed to photometric objects via the 'FluxObjID' field in the 'SpecObj' table, and these linked photometric objects are sometimes 'Child' objects that do not reflect the full integrated photometry of the galaxy. Finally, certain nearby galaxies were not targeted by the SDSS. Therefore, we produced a new spectroscopic galaxy catalog by (1) querying the SDSS 'SpecObj' table for all galaxies within 7 degrees of the QSO sightlines (corresponding to 1 Mpc projected on the sky at $z = 0.002$), (2) running an internal crossmatch using the STILTS software package (Taylor, 2006) to find duplicate objects, (3) identifying objects with suspected incorrectly linked photometry ($m_r > 19$ when the nominal SDSS completeness limit is $m_r = 17.7$) and requerying the SDSS 'PhotoObj' table for brighter objects that may be the true 'parent' photometric object within 10 arcsec, and (4) incorporat-

ing galaxies from RC3, which complements the SDSS by including the bright objects SDSS may not have targeted (approximately 650 galaxies over our full sample).

The analysis presented in Section 3.3.2 utilizes the group halo catalog of Yang et al. (2007) (specifically their version updated for SDSS DR7), which includes the results of a group finding algorithm to identify galaxy groups within the SDSS at $z > 0.01$. The data products[9] include group centroids, halo masses, and the identified galaxy members of each group, which we use to assign halo masses and virial radii to the larger dark matter halos in which our absorbers/galaxies reside.

3.2.3 Stellar Masses, Halo Masses, and Virial Radii

Our galaxy stellar masses (M_*) are calculated using SDSS photometry and the KCORRECT software, which fits galaxy spectral templates to broadband photometric data (Blanton & Roweis, 2007). The NASA-Sloan Atlas provides stellar masses output from KCORRECT using the improved photometry, and we used the software to also calculate stellar masses for galaxies not included in the atlas.

Our analyses consider galaxy halos on two scales: individual galaxies and groups/clusters. Our first objective is to characterize the galaxies associated with C IV absorbers at low redshift, and the extent of a galaxy's dark matter halo provides a natural scale for associating an absorbing gas cloud with the galaxy. We adopt r_{200}, the radius within which the average mass density is 200 times the critical density of the Universe, as the virial radius (r_{vir}) of a galaxy halo. To estimate the total halo masses ($M_{\rm halo}$) and virial radii of the galaxies around QSO sightlines, we primarily employ the redshift-dependent stellar mass/halo mass relation of Moster et al. (2013) and the calculation described by Burchett et al. (2013). However, similar to Prochaska et al. (2011) and Stocke et al. (2013), both of whom analyzed galaxy/absorber associations with respect to r_{vir}, we employ an M_*-$M_{\rm halo}$relation that diverges from that obtained

[9]http://gax.shao.ac.cn/data/Group.html

through pure halo abundance matching for massive galaxies. Moster et al. (2013) parameterize the $M_*/M_{\rm halo}$ ratio using a double power-law form with slopes above and below a characteristic mass:

$$\frac{M_*}{M_{\rm halo}} = 2N \left[\left(\frac{M_{\rm halo}}{M_1} \right)^{-\beta} + \left(\frac{M_{\rm halo}}{M_1} \right)^{\gamma} \right]^{-1} \tag{3.1}$$

where N is the normalization and M_1 is the characteristic mass above and below which the behavior of $M_*/M_{\rm halo}$ follows the slopes β and γ. This form is motivated by the deviation of the galaxy luminosity function from the halo mass function at low and high masses (Yang et al., 2003), and it is assumed that the galaxy populations within halos below a certain $M_{\rm halo}$, on average, are dominated by the central galaxy. Higher-mass halos will be increasingly populated by satellite galaxies in number, and by comparing the conditional mass function of centrals with the full stellar mass function of halos at varying $M_{\rm halo}$, Moster et al. (2010) find that the satellite contribution becomes increasingly important above log $M_{\rm halo} = 12.0\ M_\odot$. Therefore, a stellar-to-halo mass conversion from halo abundance matching for $L > L_*$ galaxies (assuming the galaxy is a central) provides $M_{\rm halo}$ values appropriate for group and cluster scales; we employ this conversion, using the Equation 3.1 parameter values from Moster et al. (2013), for $M_{\rm halo}$ and r_{vir} in the galaxy environment/absorber analysis.

Aiming to produce a scaling more suited to individual galaxies across a wide dynamic range in stellar mass, we modify the M_*-$M_{\rm halo}$ conversion as follows. In the $M_{\rm halo} > M_1$ regime (log $M_1 = 11.590$ at $z = 0$), the $M_*/M_{\rm halo}$ ratio decreases with increasing $M_{\rm halo}$, and halos become dominated by satellite galaxies at log $M_{\rm halo} > 12.0\ M_\odot$. Thus, we effectively truncate the contribution of the second term by fixing it at $M_{\rm halo} = M_1$, which is firmly within the central-dominated regime but where the contribution of this term is non-negligible. Equation 3.1 becomes

$$\frac{M_*}{M^s_{\rm halo}}(z=0) = 0.0702 \left[\left(\frac{M^s_{\rm halo}}{10^{11.590}} \right)^{-1.376} + 1 \right]^{-1} \tag{3.2}$$

where we have also substituted the $z = 0$ values for M_1, β, and γ. The halo masses used to associate individual galaxies with absorbers via the virial radius were then obtained by numerically solving the analog of Equation 3.2 at the redshift and stellar mass of each galaxy in the database using the appropriate parameters from Moster et al. (2013).

3.2.4 Star Formation Rates

Throughout the paper, figures are color coded to reflect whether the galaxies plotted are star forming (blue) or quiescent (red). This distinction was made based on star formation rates (SFRs) calculated from either the GALEX FUV and NUV photometry provided by the NASA-Sloan Atlas or the Hα and Hβ spectral line measurements from SDSS spectroscopy. Because good quality GALEX data were not available for many galaxies, mostly due to problems with the FUV band, the Balmer line measurements provided a secondary means to measure or place limits on the SFRs. The primary disadvantage for these spectroscopically derived values is the need for flux correction due to the small angular size of the SDSS spectrograph fibers compared to the full projected size of the galaxies targeted.

SFRs using the GALEX data were calculated using Equations (5), (7), and (8) of Salim et al. (2007). The SFRs from Balmer line measurements were calculated using Equation (4) of Brinchmann et al. (2004), where the Hα luminosity was corrected for dust attenuation using the intrinsic Hα-to-Hβ luminosity assuming Case B recombination and 10^4 K gas from Osterbrock & Ferland (2006), and k(Hα)-k(Hβ) was calculated from the extinction law of Cardelli et al. (1989). The Balmer line-derived SFRs were fiber corrected by scaling the flux of each line by the ratio of the total 'model' NUV flux, resulting from the photometric fit of the entire galaxy, to the 'fiber' flux, which has an aperture equal to the size of the SDSS fiber. If the NUV data were not available, we used the u-band fluxes in an attempt to capture, as much

as possible, stellar continuum from the youngest populations. A comparison of the total-to-fiber flux ratios between the NUV and SDSS u-band, where the NUV data were available, revealed that the u-band ratios were systematically lower than the NUV ratios. This difference in flux ratios is likely driven by two effects: (1) GALEX better captures more diffuse star formation occurring in the outer regions of galaxies and (2) the u-band flux has a greater contribution from older stars and is more centrally concentrated. For comparison, the r-band in turn yields lower total-to-fiber flux ratios than the u-band, supporting this second point. We thus considered the Balmer-line SFRs using u-band flux corrections as lower limits. In cases where the FUV and NUV data were not available and the Hα line was not detected at 3σ significance, we adopted a 3-σ upper limit from the Hα line measurement uncertainty scaled for the fiber correction.

With these SFRs in hand, we set a threshold separating passive and star-forming galaxies based on the the bimodality in the locus of specific star formation rate (sSSFR=SFR/M_*) vs. M_* for the entire NASA-Sloan Atlas at log (sSFR/yr^{-1}) = -10.75. Galaxies with sSFR above and below this threshold are represented in blue and red, respectively, in figures throughout the paper.

3.3 Analysis and Results

We now investigate the connections between C IV absorbers and nearby galaxies. In particular, we pose two overarching questions: 1) How is the material traced by C IV absorption distributed relative to nearby galaxies in terms of proximity to the associated galaxies and as a function of galaxy mass? 2) How, if at all, is the CGM affected by the environment in which a host galaxy resides?

3.3.1 Absorption profiles and the dependence of C IV absorption on galaxy mass

Here, we complement the galaxy-selected approach of COS-Dwarfs with a blindly detected sample of C IV absorbers (Paper II) for which we search the SDSS for galaxy counterparts. As stated in section 3.2.1, these analyses employ a $z \leq 0.015$ galaxy/absorber subsample that includes detected C IV absorbers as well as upper limits on the C IV absorption at redshifts where galaxies fall within 500 kpc of a QSO sightline. For comparison, we also include similar relations for H I Lyα . As employed by COS-Halos (Tumlinson et al., 2013) and COS-Dwarfs, we adopt a search window of $|\Delta v| < 600$ km/s for velocity separations between galaxies and absorbers.

First, we describe our selection methods for associating galaxies to absorbers; then, we present the resulting column density-impact parameter profiles and C IV detection statistics as a function of associated galaxy mass.

3.3.1.1 Selecting Absorber-associated Galaxies

Nine C IV absorbers from our sample meet the $z < 0.015$ criterion, and we consider associated galaxies based on two selection methods: we identify the galaxy with the smallest projected separation from the sightline in terms of (1) proper distance (kpc) and 2) galaxy virial radius (ρ/r_{vir}). We present maps of the galaxy fields within proper distances of 500 kpc surrounding each $0.0015 < z_{abs} < 0.015$ absorber in Figure 3.1. Note that these maps contain *all* galaxies with available spectroscopic redshifts and have no imposed minimum luminosity. Each galaxy's virial radius is represented by a red circle. As shown in the maps, the C IV systems largely occur in galaxy environments that are sufficiently populated to preclude unambiguous selection of a 'host galaxy', and we proceed by selecting as 'associated' the most proximal galaxies to each sightline using the two metrics mentioned above and examining the resulting distributions of absorption (or lack thereof) with respect to these two selections. With

the exception of one absorber ($z_{\rm abs} = 0.00261$ in the sightline of QSO J0925+4004, but see the discussion below), we find galaxies within impact parameters of 200 kpc for all absorbers in this subsample. Certain C IV absorbers are located outside of the virial radii of all nearby galaxies, but only moderately beyond the virial radii.

These maps underscore the difficulty of associating absorbers with individual galaxies. Only the field of J0155-0857 presents a fairly unambiguous association between an absorber and galaxy regardless of selection method. The J0242-0759, J1059+1441, J1122+5755, and J1445+3428 fields contain absorbers that appear to fall within the virial radii of multiple galaxies. J0925+4004, J0928+6025, and PG1148+549 contain absorbers outside the virial radius of any galaxy at the same redshift. Although several fields depicted in Figure 3.1 show an abundance of galaxies near the QSO sightline (due to the high completeness to faint galaxies), the two selection schemes we have employed capture the essential absorber/galaxy trends and enable comparison to previous studies.

The absorber in J0925+4004 does not appear to have a galaxy within 300 kpc or 1.7 r_{vir} even if we expand the velocity search window to $|\Delta v| < 800$ km/s (note that the galaxies depicted in Figure 3.1 for this absorber all exceed velocity differences of 600 km/s). Another galaxy, SDSS J092422.92+400527.1, occurs at 141 kpc and 1.2 r_{vir} if the velocity window is widened to 850 km/s. However, this low-surface brightness galaxy's SDSS spectrum is quite noisy, and if its redshift is equal to that of the absorber, the impact parameter decreases to 56 kpc. If the SDSS redshift is accurate, this last absorber presents a similar issue to that presented by Burchett et al. (2013), where a candidate host galaxy may have a smaller impact parameter if the gas is moving at a very high velocity relative to the galaxy, e.g., a high-velocity outflow. Such outflow speeds are certainly plausible and have in fact been observed unambiguously in 'down-the-barrel' studies where the ejecting galaxy itself was used as a background source to study the outflowing gas in absorption (e.g., Rubin et al.,

2014; Tremonti et al., 2007). However, using distant QSOs as the background continuum source probes circumgalactic gas that is transversely separated in projection from possible host galaxies and introduces ambiguity in cases where large velocity offsets may not indicate large line-of-sight Hubble flow distances. We defer a deeper analysis of the velocity offset/impact parameter degeneracy to future galaxy surveys that will improve statistics while maintaining a sensitivity to faint dwarfs (Burchett et al., in preparation).

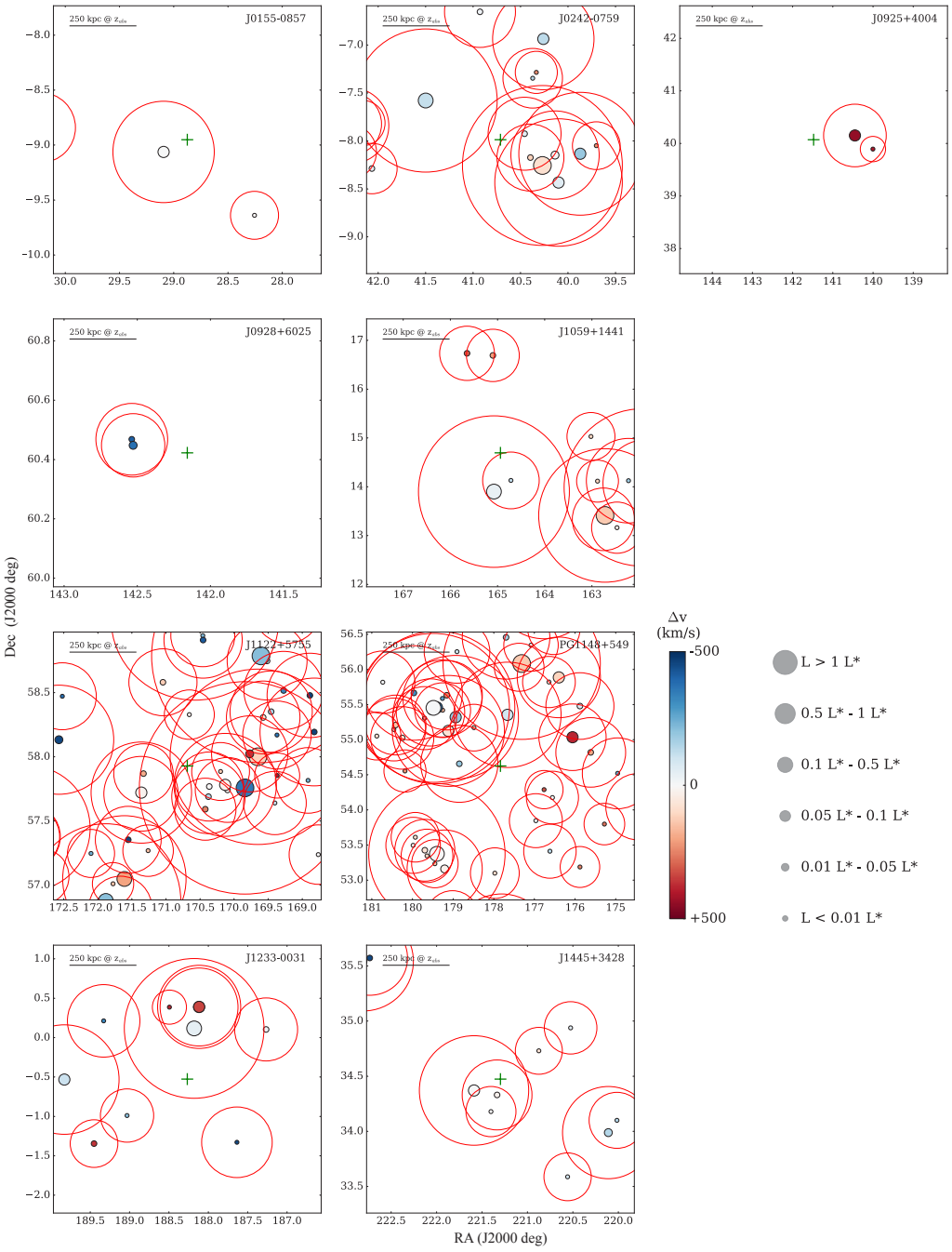

Figure 3.1 Galaxies around QSO sightlines within ± 500 km/s of the $z < 0.015$ absorber subsample. Following the legend and scalebar on the right side, the marker size indicates galaxy $r-$band luminosity, the marker color indicates the separation in radial velocity from each absorber, and the red circles mark the virial radius of each galaxy. The abbreviated field name is printed in the upper-right corner of each panel. A physical scale is given in each panel. Note that all galaxies in the J0925+4004 frame have $v_{\rm gal} - v_{\rm abs} > 700$ km/s and thus lie at much larger impact parameters than that indicated by the reference scale.

Table 3.1. Closest SDSS galaxies to z<0.015 C IV absorption systems, selected by proper distance.

QSO	z_{abs}	Galaxy	α_{gal} (J2000) (degrees)	δ_{gal} (J2000) (degrees)	z_{gal}	ρ (kpc)	δv (km/s)	log M_* ($M_\odot$)	ρ/r_{vir}
J0155-0857	0.00547	NGC 0755	29.09370	-9.06231	0.00547	98	0	9.67	0.53
J0242-0759	0.00477	SDSS J024149.95-075530.0	40.45766	-7.92484	0.00458	88	57	8.65	0.69
J0925+4004	0.00261	NGC 2844	140.45005	40.15125	0.00496	369	-701	10.26	1.50
J0928+6025	0.01494	SBS 0926+606A	142.52826	60.44781	0.01366	201	378	8.18	1.83
J1059+1441	0.00242	SDSS J105851.95+140748.2	164.71646	14.13006	0.00199	65	128	7.15	0.83
J1122+5755	0.00640	UGC 06369	170.36413	57.76851	0.00640	139	0	8.81	1.02
J1233-0031	0.00392	SDSS J123718.74+001248.0	189.32907	0.21289	0.00282	137	326	7.18	1.72
J1445+3428	0.00549	SDSS J144520.23+341948.1	221.33415	34.33011	0.00556	80	-20	8.93	0.56
PG1148+549	0.00349	UGC 06894	178.84798	54.65728	0.00284	185	193	8.67	1.42

Table 3.2. Closest SDSS galaxies to z<0.015 C IV absorption systems, selected by virial radius.

QSO	z_{abs}	Galaxy	α_{gal} (J2000) (degrees)	δ_{gal} (J2000) (degrees)	z_{gal}	ρ (kpc)	δv (km/s)	log M_* ($M_\odot$)	ρ/r_{vir}
J0155-0857	0.00547	NGC 0755	29.09370	-9.06231	0.00547	98	0	9.67	0.53
J0242-0759	0.00477	NGC 1052	40.27000	-8.25578	0.00504	192	-79	10.74	0.45
J0925+4004	0.00261	NGC 2844	140.45005	40.15125	0.00496	369	-701	10.26	1.50
J0928+6025	0.01494	SBS 0926+607	142.53767	60.46827	0.01355	209	411	8.53	1.70
J1059+1441	0.00242	NGC 3489	165.07691	13.90107	0.00230	106	35	10.23	0.44
J1122+5755	0.00640	NGC 3613	169.65041	58.00007	0.00678	343	-115	11.09	0.42
J1233-0031	0.00392	NGC 4517	188.17980	0.11716	0.00376	206	45	10.43	0.73
J1445+3428	0.00549	SDSS J144520.23+341948.1	221.33415	34.33011	0.00556	80	-20	8.93	0.56
PG1148+549	0.00349	NGC 3913	177.66224	55.35397	0.00317	255	96	9.86	1.27

Selecting a galaxy to be associated with an absorber based on the closest transverse proper distance is the scheme employed by most comparable surveys to date. In many ways, this criterion is the most intuitive and captures a natural suspect for the source of the gas based on pure proximity. Also, this scheme is relatively free of the assumptions inherent in an assignment based on galaxy properties, such as the virial radius. However, as a survey becomes sensitive to fainter galaxies, the luminosity function (Schechter, 1976) indicates that the number density of galaxies will increase as $\phi \propto L^{\alpha}$, where recent estimates place $\alpha \sim -1.3$ for the full star-forming and quiescent population (Loveday et al., 2012; Willmer et al., 2006). While this increases the likelihood of detecting a galaxy closer to the sightline, the question remains whether the fainter galaxy is the true source of the gas.

Galaxies potentially associated with absorbers may also be selected based on galaxy virial radii. The galaxy's virial radius provides an estimate of a galaxy halo's extent, insomuch as gas within the virial radius is consistent with being bound to the galaxy provided its velocity separation is also less than the galaxy's escape velocity. Indeed, previous studies have reported that the column density of C IV absorbers anticorrelates with impact parameter relative to the host galaxy virial radius ($\rho/r_{\rm vir}$; Bordoloi et al., 2014; Liang & Chen, 2014).

To verify the advertised completeness of our galaxy data, we investigated what galaxies down to the desired luminosity limit may have been missed by the publicly available redshift surveys between the QSO sightlines and the associated galaxies we identified. We scaled the galaxies around each sightline from the SDSS photometry that did not have SDSS spectroscopic redshifts to their hypothetical absolute r-band magnitudes, assuming they were all at the redshift of the absorber. We then estimated the galaxy luminosities relative to L* using the r-band absolute magnitude $M*_r = -20.44 - 5 \log h$ (Blanton et al., 2003) and the SDSS dereddened r-band model-derived magnitudes, which use extinction values from the Schlegel et al. (1998) dust maps.

As a result, we find that our galaxy redshift data (SDSS, etc.) are 100% complete to 0.01 $L*$ in the region of interest around 8 sightlines in this subsample and 100% complete to 0.025 $L*$ in the one remaining sightline ($z = 0.01494$ in the J0928+6025 sightline). These luminosities are commensurate with the survey goals outlined in Section 3.2.1.

The absorber-galaxy associations were then drawn as follows: (1) We used the traditional method of assigning an absorber to the galaxy with the smallest impact parameter and velocity separation from the absorber. We refer to the sample selected in this way as *proper-distance selected*. (2) Alternatively, we assigned the absorber to the galaxy at the absorber redshift that is closest in terms of the fraction of its virial radius (ρ/r_{vir}). This alternative selection produces our *virial-radius selected* sample. The resulting galaxies selected by these two methods are shown in Tables 1 and 2, respectively. SDSS composite images of the selected galaxies are shown in Figure 3.2, where a pair of panels is shown for each absorber in the 6/9 cases where the two selection methods choose different galaxies, and single panels are shown for the three cases where the selection methods choose the same galaxy (marked with red borders).

In addition to searching for galaxies associated with detected absorbers, to quantify the cases where no absorption was detected but galaxies lie near the sightline, we also searched the SDSS for $z_{gal} < 0.015$ galaxies at impact parameters within 500 kpc of *any* of the 89 QSO sightlines described in Section 3.2.1. We further filtered the galaxies found in this search by iterating through each galaxy to identify the galaxy with the smallest impact parameter, both in proper distance and virial radius, of any galaxy within a redshift range of $\delta z_{gal} < 0.003$, or ~ 900 km/s. This velocity range was chosen to exceed that for which we matched *detected* absorbers and galaxies (600 km/s) and mitigate confusion between galaxies that may lie at similar redshifts to one another due to peculiar motion but fall at similar line-of-sight cosmological distances. Also, galaxies targeted by the COS-Dwarfs survey were rejected for this stage

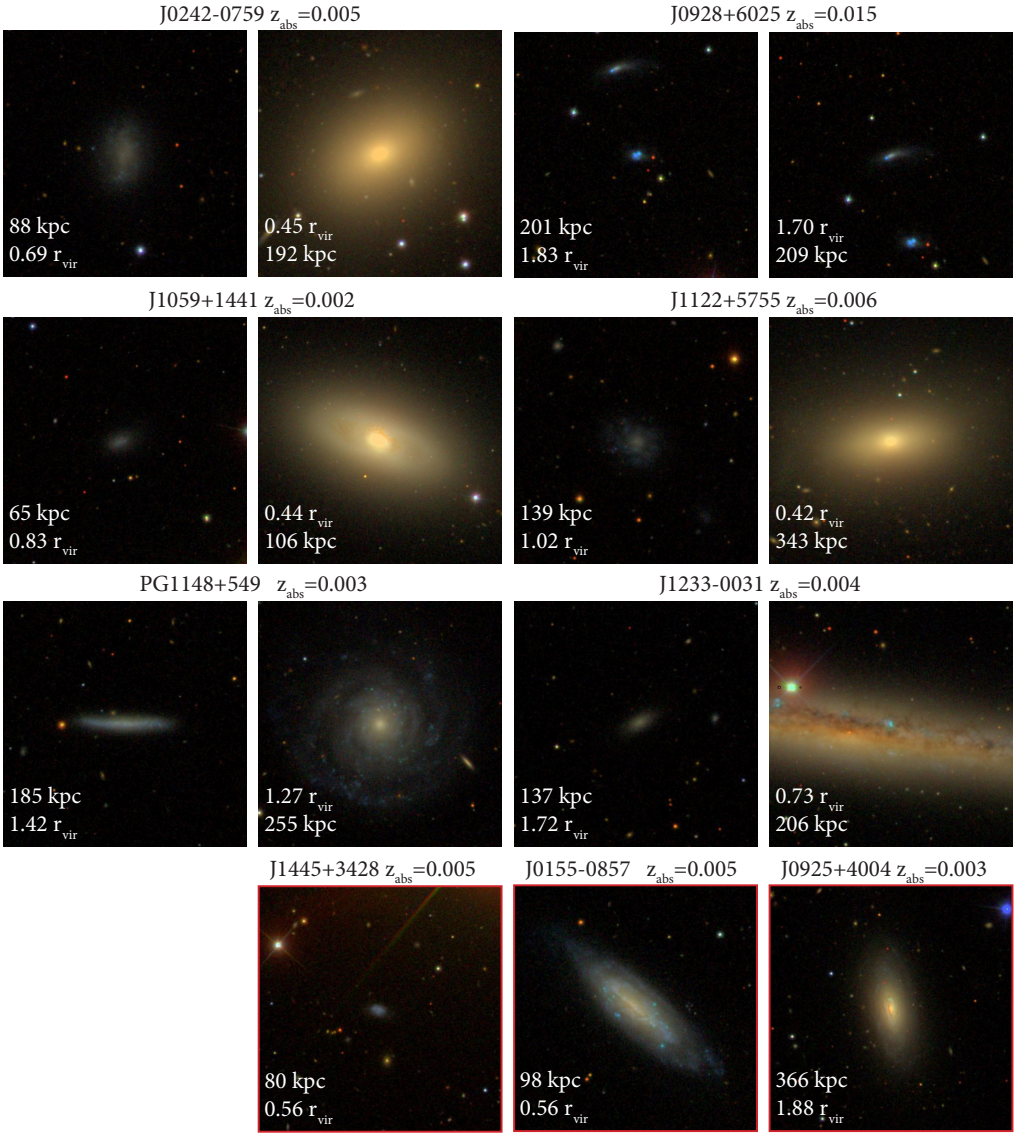

Figure 3.2 SDSS false color images (from g, r, and i bands; Lupton et al., 2004) of galaxies selected to be associated with our $z < 0.015$ C IV absorber subsample. We selected associated galaxies by both the smallest proper distance impact parameter and impact parameter relative to the virial radii of the galaxies in the field. Except for the three bottom panels marked with red boxes, panels are paired for each absorber (labeled above) where the left panel shows the galaxy selected by proper distance and the right shows the galaxy selected by virial radius. Each panel depicts a projected area on the sky approximately 3.5 arcminutes per side.

of the analysis to further ensure that our sample is blind in both absorber and galaxy selection (although we include them later for the environmental analysis where their inclusion does not introduce bias).

3.3.1.2 C IV column density and galaxy impact parameter

Using the selection procedures described above, we produced samples of galaxy/absorber pairs imposing a galaxy luminosity cut of $\mathcal{M}_r \leq -16.4$, corresponding to the completeness limit of SDSS (see Section 3.2.2). Figures 3.3 and 3.4 show the absorber C IV and H I column densities (including 3-σ upper limits) as a function of impact parameter; Figure 3.3 presents the proper-distance selected sample, and Figure 3.4 shows the virial-radius selected sample. In these figures, we differentiate between passive and star-forming galaxies using the sSFR separation described in Section 3.2.4. For the detected absorbers in our sample, the column densities shown represent the total column densities summed over all velocity components in each absorber. The C IV column density upper limits shown were measured by integrating the C IV λ 1548 apparent column density profiles (Savage & Sembach, 1991) within $\pm$50 km/s at the redshifts where no C IV absorber was detected. The largest impact parameters in these plots correspond to the absorber at $z_{abs} = 0.00261$ in the sightine of QSO J0925+4004, for which no galaxy was found closer than $|\delta v| = 700$ km/s. For comparison, we show in the top panels of Figs. 3.3 and 3.4 the C IV absorber-galaxy pairs from the COS-Dwarfs survey (faint circles; Bordoloi et al., 2014) alongside our blindly selected dataset.

For the proper distance-selected sample from our blind survey, we detect C IV absorption within 160 kpc of 6 out of 19 galaxies (32^{+11}_{-10}%). Within the measurement uncertainties, this detection rate agrees with the COS-Dwarfs result of 17 detections out of 43 galaxies targeted (39^{+8}_{-7}%). For our virial radius-selected sample, we obtain 7 detections around 21 galaxies (33^{+11}_{-9}%) probed within 1 virial radius; COS-Dwarfs

yielded 17 detections within 1 virial radius of 41 galaxies targeted (41^{+8}_{-7}%). Our blind survey also extends the CGM probed by C IV absorption out to impact parameters of 400 kpc and beyond, and we find absorbers out to $\sim$ 350 kpc and > 1.5 $r_{\rm vir}$ from the nearest galaxy. However, beyond 160 kpc and 1 r_{vir}, the detection rate dramatically decreases for the proper distance- and virial radius-selected samples, respectively: two detections out of a possible 19 (10^{+10}_{-5}%) occur in the 160-250 kpc region; we report 0/16 detections (0^{+6}_{-0}%) at 1-1.5 r_{vir} and 1/12 (8^{+11}_{-5}%) at 1.5-2 r_{vir}. Covering fractions under certain selection criteria for both the proper distance selection and the virial radius selection are shown in the top two sections of Table 3.

The detection at the largest impact parameter in the proper distance-selected sample (368 kpc) occurs for the absorber at $z_{abs} = 0.00261$ in the J0925+4004 sightline, and this absorber is associated with the same galaxy, NGC 2844, in both selection methods (but note the caveat in Section 3.3.1.1 regarding this association). NGC 2844 also has a very large velocity separation with the absorber (-701 km/s) but serves as the closest in impact parameter with the smallest velocity offset.

Two notable points are immediately apparent. First, as seen in Figure 3.3, the detections of C IV absorption are predominantly associated with galaxies, most often within 200 kpc of a galaxy. This result was in essence first demonstrated for strong absorbers ($W_{1548} \gtrsim 200$ mÅ) by Chen et al. (2001) using data from the *Faint Object Spectrograph* on HST (Bahcall et al., 1993). Our survey enables sensitivity to much weaker absorbers ($W_{1548} \lesssim 100$ mÅ) and fainter galaxies, and we indeed find that this close association persists. However, the nearest luminous galaxies to the absorbers, such as those selected by virial radius, have much larger impact parameters for 3/9 absorbers ($\rho > 250$ kpc; Tables 1 and 2).

Second, some metal-enriched gas may arise well beyond the virial radius of a galaxy. Absorbers at large distances have been previously reported (Stocke et al., 2013; Tripp et al., 2006; Johnson et al., 2013); however, the COS-Dwarfs sample

showed no C IV detections beyond approximately 0.5 r_{vir} (Bordoloi et al., 2014), corresponding to 0.66 r_{vir} using the cosmology and velocity corrected distances adopted here and reflected in Figs. 3.3 and 3.4. We further compare these results with previous studies in Section 3.4.2.

3.3.1.3 H I column density

The bottom panels of Figs. 3.3 and 3.4 show the corresponding H I column density measurements for the same galaxies appearing in the C IV profiles in the top panels. The H I identifications and measurements suffer from two complications that do not arise for C IV: (1) At the redshifts we are probing in this analysis, only the Lyα line, which is typically saturated and only yields a lower limit on N(H I), falls in the COS bandpass. (2) The Lyα lines at the redshifts of these $z < 0.015$ galaxies often fall within the Galactic Lyα profile where the Milky Way damping wings reduce the S/N or the flux disappears altogether. H I detections are shown in Figs. 3.3 and 3.4 where Lyα absorption was identified within 600 km/s of a galaxy's redshift. We attempted to corroborate Lyα detections with other metal lines where possible to ensure that the line in question was not associated with another known system in the spectrum. If the flux values in the core of line profile were greater than the corresponding errors, we fitted the line with a Voigt profile to obtain a column density. Otherwise, a lower limit on the column density was measured using the apparent optical depth method (AODM) (Savage & Sembach, 1991). For nondetections, we measured upper limits using the AODM with the error vector over a velocity range of $\pm$ 50 km/s centered on the rest frame of the detected galaxy. H I data for the COS-Dwarfs galaxy/absorber pairs are adopted from Bordoloi et al. (2016, in preparation).

Figures 3.3 and 3.4 show a markedly higher detection rate for Lyα than for C IV, at all impact parameters. Higher detection rates of H I over metal ions have been reported in many absorber/galaxy studies (e.g., Wakker & Savage, 2009; Prochaska

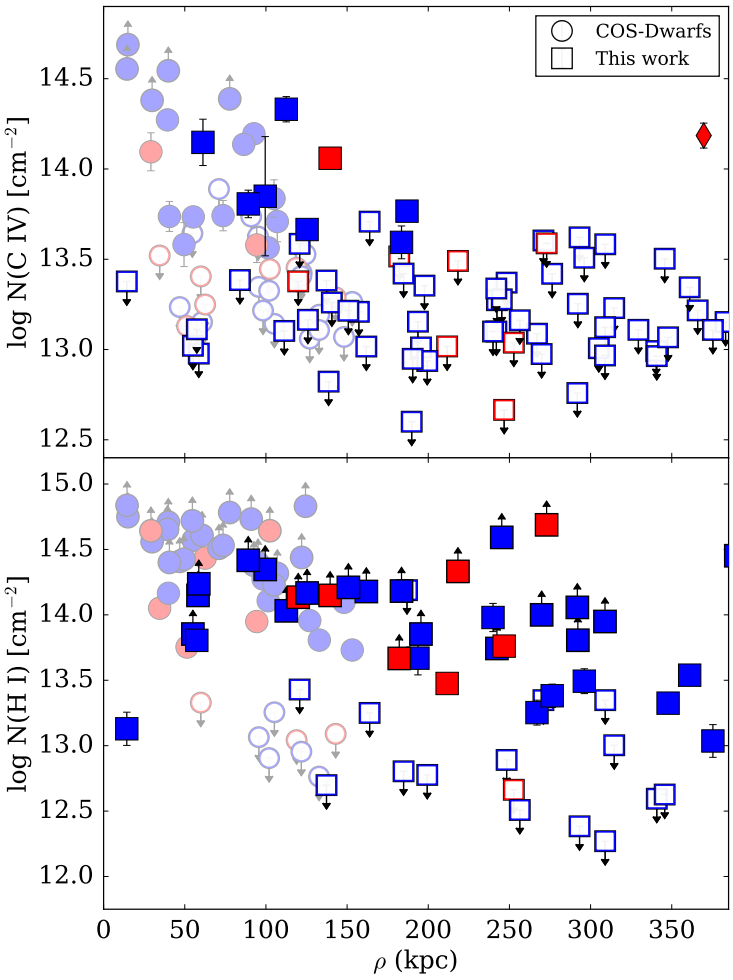

Figure 3.3 The C IV (top) and H I (bottom) column density profiles for our low-z absorber/galaxy sample (squares). Associated galaxies were selected by proper distance proximity using a galaxy magnitude limit of $\mathcal{M}_r \leq -16.4$. The galaxy/absorber pair indicated with a diamond in the top panel has the greatest velocity separation of all pairs plotted, with $\delta v > 600$ km/s. Red and blue symbols denote passive and star-forming galaxies, respectively. The open symbols with downward arrows correspond to 3-σ upper limits on the absorption; filled symbols with upward arrows indicate lower limits measured using the apparent optical depth on saturated lines.

et al., 2011; Stocke et al., 2013), and we briefly contrast the emerging views of the CGM traced by C IV and H I.

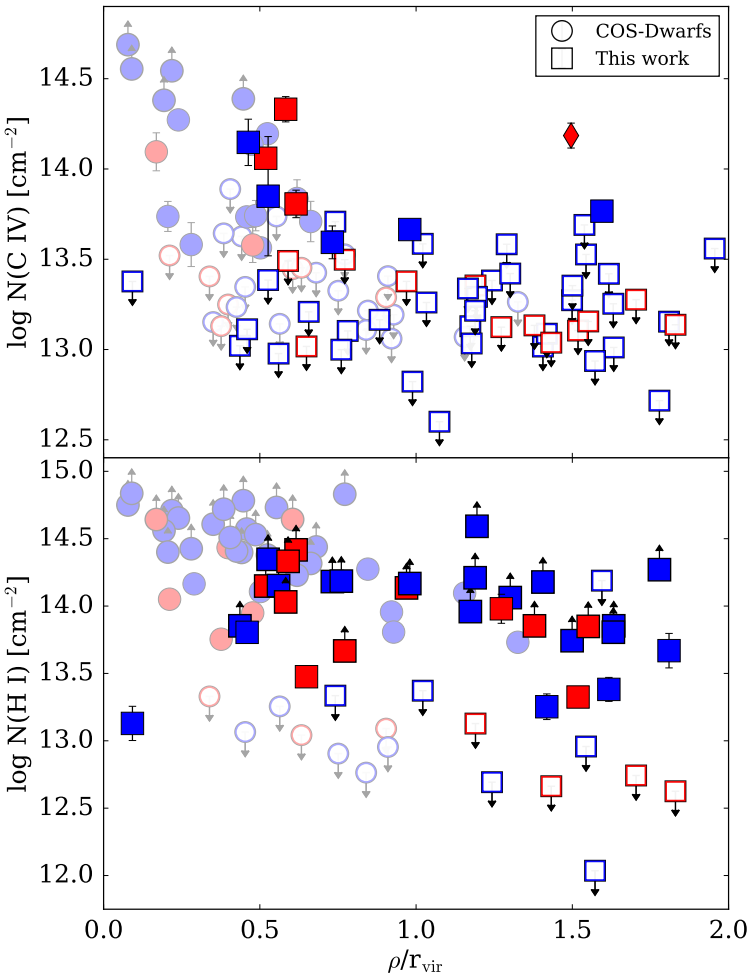

Figure 3.4 The C IV (top) and H I (bottom) column densities of our low-z absorber sample (squares) as functions of impact parameter of the associated galaxies selected by fraction of the galaxy virial radius using a galaxy magnitude limit of $\mathcal{M}_r \leq -16.4$. The COS-Dwarfs sample (fainter circles; Bordoloi et al., 2014) is also plotted for comparison. The galaxy/absorber pair indicated with a diamond in the top panel has the greatest velocity separation of all pairs plotted, with $\delta v > 600$ km/s. Red and blue symbols denote passive and star-forming galaxies, respectively. The open symbols with downward arrows correspond to 3-σ upper limits on the absorption; filled symbols with upward arrows indicate lower limits measured using the apparent optical depth on saturated lines.

First, we underscore that while the CGM is quite patchy to C IV, H I is nearly ubiquitous. If nearly all galaxies have gaseous halos, as indicated by the very high covering fraction within 1 $r_{\rm vir}$ ($0.94^{+0.04}_{-0.10}$ for N(H I) $> 10^{13.5}$ cm^{-2}), the gas traced by C IV may therefore possess a 'special' set of ionizing conditions sufficient for a detectable fraction of the carbon to be triply ionized. Another possibility is that the clouds traced by C IV represent a more metal-enriched sample of the larger population of halo clouds; however, as also pointed out by Stocke et al. (2013), the C IV clouds may simply comprise clouds of similar metallicity as the H I-only detections but are simply more massive. Lastly, many of the H I-only detections might be metal-poor intergalactic gas, while the C IV absorbers tend to trace metal-enriched circumgalactic gas.

Second, among the 26 H I clouds we detect within 2 $r_{\rm vir}$ of a galaxy, only 5 have well constrained H I column densities that are less than log N(H I) $= 10^{13.5}$ cm^{-2}. Chen et al. (2005) conducted a cross-correlation analysis between H I absorbers and galaxies at $z < 0.5$ and report that N(H I) $> 10^{14}$ cm^{-2} absorbers have a significant cross-correlation signal with emission line galaxies that rivals the autocorrelation of galaxies with themselves. However, they find that N(H I)$< 10^{13.6}$ cm^{-2} absorbers have a random distribution with galaxies relative to galaxies with themselves. Therefore, the weaker H I absorbers that we detect are similar (at least in H I column density) to those that statistically bear the mark of run-of-the-mill IGM clouds. Figure 3.3 shows several H I detections at $\rho \gtrsim 300$ kpc but only 1 C IV detection at $\rho \gtrsim 300$ kpc. Half of these H I detections have N(H I)$\lesssim 10^{13.7}$cm^{-2}, which coupled with the decreased C IV detection rate suggests that the conditions giving rise to the characteristic differences between the CGM and IGM have generally transitioned to IGM by $\rho \sim 300$ kpc.

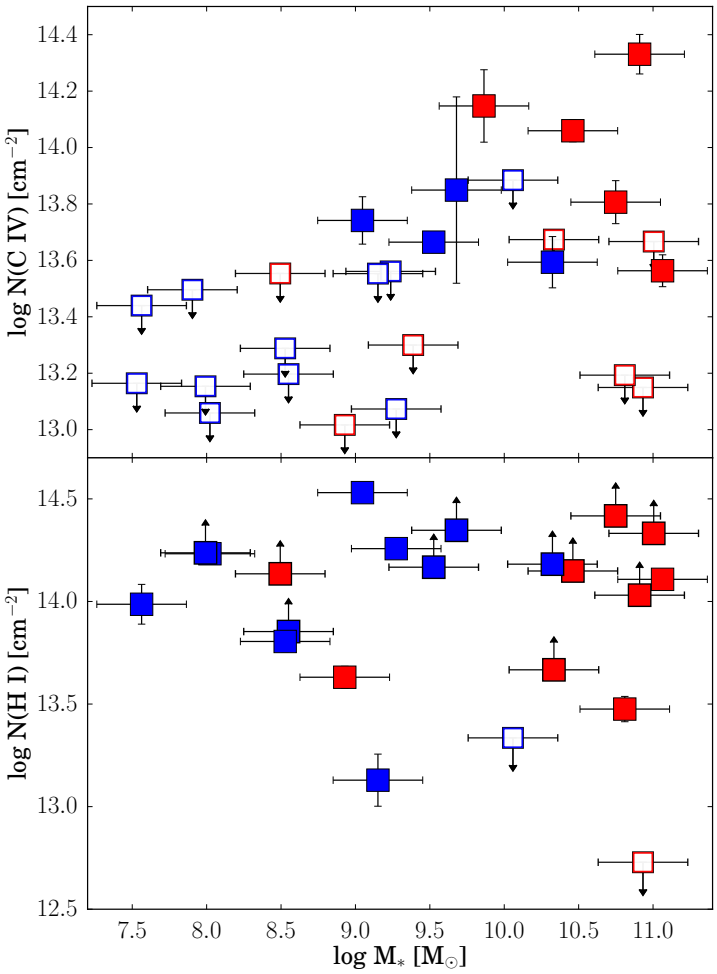

Figure 3.5 The C IV (top) and H I (bottom) column density as a function of stellar mass of the highest-mass galaxy within 1 virial radius. Red and blue symbols correspond to passive and star-forming galaxies, respectively. The downward arrows correspond to 3-σ upper limits on the absorption. We note a dramatically increased detection rate of C IV within 1 r_{vir} of galaxies with log $M* > 9.5$ $M_\odot$. The open symbols with downward arrows correspond to 3-σ upper limits on the absorption; filled symbols with upward arrows indicate lower limits measured using the apparent optical depth on saturated lines.

3.3.1.4 The CGM as a function of stellar mass

Our blind survey provides a galaxy sample independent of any mass selection criteria and that spans a wide dynamic range in mass. We now investigate whether

the CGM absorption, in terms of C IV and H I, depends on galaxy stellar mass. For this analysis, we selected galaxies in a similar manner to the virial-radius selection described in Section 3.3.1.1 but with one key difference. When multiple galaxies were probed within 1 r_{vir} by a QSO sightline and those galaxies had redshifts within $\sim$ 600 km/s of one another, we selected the most massive of those galaxies. As shown in Figure 3.1, low-mass galaxies probed within 1 r_{vir} are frequently satellite galaxies within 1 r_{vir} of a more massive galaxy. By choosing the most massive galaxies within 1 r_{vir}, we ensure a fair comparison between the halos of low-mass and higher-mass galaxies because the halo properties of these low-mass galaxies are less likely to be dominated by a massive counterpart, i.e., the low-mass galaxies should be centrals of their halos. Because their targeting procedure does not introduce bias into this analysis, we include the COS-Dwarfs data here; however, we subjected those galaxies/absorbers to the same procedure as the rest of the data. In certain cases, a more massive galaxy than that targeted by COS-Dwarfs was present at a similar redshift, and we included the more massive galaxy in our sample. We note that the results of this section are qualitatively insensitive to small changes in the 1 r_{vir} selection criterion, although increasing the selection beyond 1 r_{vir} produces more non-detections in the both the low- and high-mass regimes (consistent with the previous section's results). As in the previous section, this analysis is limited to $z < 0.015$ for survey completeness.

Figure 3.5 shows the C IV and H I column densities as a functions of galaxy stellar mass according to the above selection procedure. We note that the detection rate of C IV sharply increases for $M_* > 10^{9.5}$ $M_\odot$ galaxies. Using a detection threshold of log N(C IV) > 13.5 cm^{-2}, we detect C IV within 1 virial radius of 8 out of 10 galaxies (80^{+10}_{-15}%) and 1 out of 11 galaxies (9^{+12}_{-5}%) in the $M_* > 10^{9.5}$ $M_\odot$ and $M_* < 10^{9.5}$ $M_\odot$ bins, respectively. This result is qualitatively consistent with the O VI dependence observed by Prochaska et al. (2011), although our mass bins are

substantially less populated. To test the significance of this difference, we employ a Fisher's exact test, which is well suited to small sample sizes, assuming that the variables are categorical with galaxy mass categories of $> 10^{9.5}$ and $< 10^{9.5}$ $M_{\odot}$ and categories for the detection and nondetection of C IV. As a result, we reject the null hypothesis that the difference in the fraction of detections between galaxy masses is purely random with confidence $> 99.7\%$. We also estimated the significance of this result by taking the same distribution of galaxy masses as shown in Figure 3.5, randomly assigning C IV detection or nondetection status to each each galaxy based on the covering fraction of $\sim 40\%$ reported by Bordoloi et al. (2014), and producing 10^6 Monte Carlo resamples. Based on the probability of reproducing the observed distribution of C IV detections and nondetections, we reject the null hypothesis that the rates observed between the $> 10^{9.5}$ and $< 10^{9.5}$ $M_{\odot}$ galaxies occur at random with $> 99.9\%$ confidence.

For comparison, the bottom panel of Figure 3.5 shows the same mass-column density relationship for neutral hydrogen within 1 r_{vir} of the same $z < 0.015$ galaxies. The issues with H I measurements discussed in Section 3.3.1.3 also arise here and result in a smaller sample being represented in the bottom panel than the top panel (for C IV). However, H I *is* detected even in the halos where we do not detect C IV. Assuming a detection threshold of $\log N(\text{C IV}) > 13.5$ cm^{-2}, the $< 10^{9.5}$ $M_{\odot}$ bin has an H I detection rate within 1 r_{vir} of $100^{+0}_{-10}\%$, not statistically different from that for more massive galaxies, $82^{+9}_{-14}\%$ of which yield H I detections. As for the previous sections' analysis, these covering fractions are summarized in Table 3. Nevertheless, Lyα is a much stronger transition than the C IV lines and is predominately saturated in our data; thus, an H I-mass dependence may still be present but could be obscured by our inability to precisely constrain the column densities in the strong H I lines.

A number of scenarios may be invoked to explain the difference in C IV detection between the galaxy mass bins. These include, but are certainly not limited to, the

following: 1) The gas in the CGM of dwarfs is sufficiently less dense or less self-shielded as to allow more energetic photons to ionize the C IV to a higher ionization state(s). In this hypothesis, the H I would be more ionized as well, but H I remains detectable even when the H I ionization fraction is quite small, so the C IV absorption could disappear while the H I persists. Better constrained H I column densities may provide insight here as whether a significant difference exists in the H I column densities of Figure 3.5 between the two mass bins. 2) Because of their shallower potential wells, the lowest mass dwarf galaxies are better able to expel their metal-enriched gas into IGM regions where the gas is further ionized and/or falls below the column density detection threshold. 3) The gas in a lower ionization stage due to a lower virial temperature of the low-mass halo, and the carbon is better traced by C III (not covered in our data) than C IV. 4) Less massive galaxies have less mass in their CGM and shorter sightline paths through their halos; therefore, given similar underlying physical conditions and feedback behavior as in more massive galaxies, the column density (and detectability) of any species will be lower. This would affect both C IV and H I, but because the H I lines are predominately saturated, it could be difficult to see this effect in the H I data.

3.3.2 Galaxy environments of C IV absorbers

As shown in our work and in the previous studies discussed, C IV absorbers are typically found to be coincident with nearby galaxies (with a few exceptions, e.g., Tripp et al., 2006). As shown in Figure 3.1, the C IV absorbers clearly occupy a variety of environments, from one or two nearby galaxies to relatively well-populated groups, and many absorbers occur within the virial radii of multiple galaxies. Our small galaxy/absorber subsample might represent a wide diversity in the physical nature of the gas detected. While environmental effects are conspicuous in galaxy disks and central regions, the mechanisms involved must also be felt in the interme-

diary CGM and, therefore, impact the feeding and outflow processes occurring there. For instance, if galaxies reside in a larger group halo, would-be cold-mode infalling gas could be shock heated even when the individual galaxies' subhalo is below the threshold mass ($M_{halo} = 10^{11.4}\ M_{\odot}$) at which an individual halo would dynamically shock-heat accreting intergalactic gas. Furthermore, tidal forces may assist the mass transfer of metal-enriched outflows to leave the CGM. Thus, we now leverage our low-z absorber sample, for which we have rich galaxy survey data from SDSS, to investigate the role of environment on the gas traced by C IV.

The analyses herein leverage the full NASA-Sloan atlas and all C IV absorbers at $z < 0.055$ within our QSO sightline sample. As in Section 3.3.1.4, the COS-Dwarfs sample introduces no inherent bias to the current environmental analysis, and these galaxies/absorbers are included.

3.3.2.1 Fixed-aperture Galaxy Density

To investigate how the detection of C IV depends on the local galaxy environment, we first employ a straightforward, sightline-centric fixed-aperture number density, i.e., how does the observed C IV column density (or upper limit for nondetections) depend on the number of nearby galaxies within some projected distance and velocity tolerance? Muldrew et al. (2012) employed a large volume of simulated dark matter halos to compare several metrics commonly used to quantify environment. In general, fixed-aperture methods and nearest-neighbor distances are found to probe different scales of environment (individual halos to large-scale structure), and these dependencies are sensitive to the parameters chosen. Both Muldrew et al. (2012) and Haas et al. (2012) find that fixed-aperture densities correlate well with halo mass on scales of rich groups to clusters using apertures of $\sim 1h^{-1}$ Mpc and $\delta v = \pm 1000$ km/s. However, smaller halos ($M_{\rm halo} < 10^{13} M_{\odot}$) are not well differentiated by this metric.

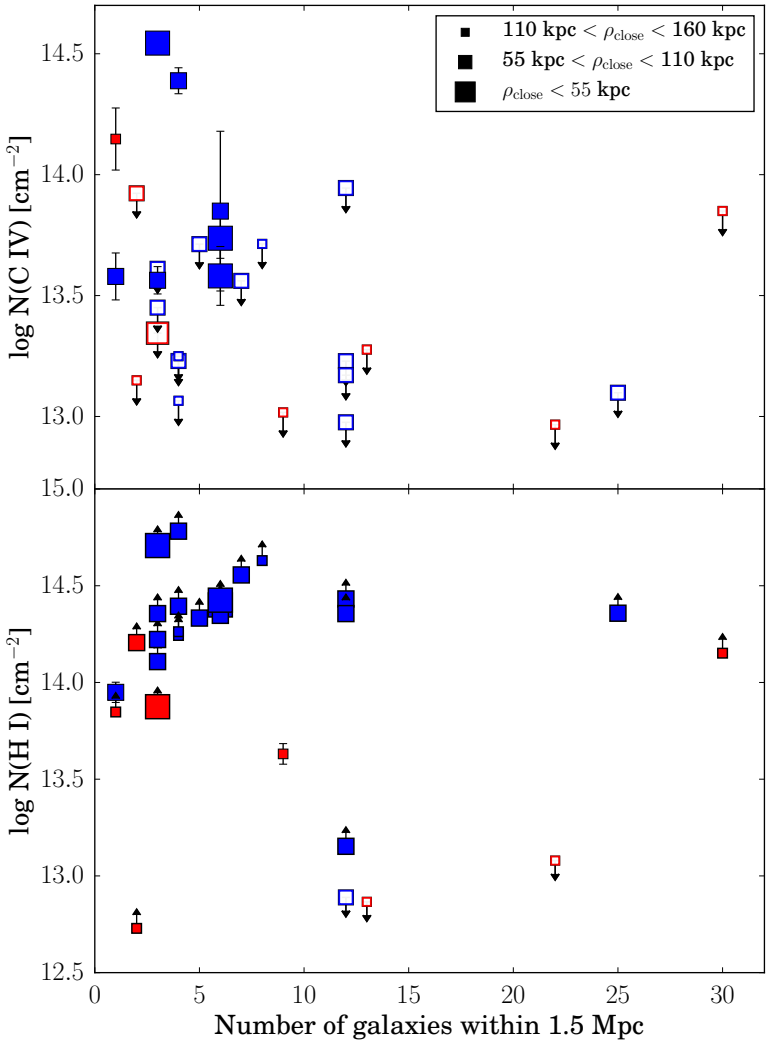

Figure 3.6 (Top) C IV column density as a function of the number of galaxies within 1.5 Mpc of the QSO sightline, where filled squares represent detections of C IV and open squares represent nondetections; red and blue squares correspond to the passive and star-forming galaxies, respectively. Shown are the systems where at least one $\mathcal{M}_r < -19$ ($M_* \gtrsim 10^{9.5}\ M_\odot$) galaxy falls within an impact parameter $\rho < 160$ kpc. The x-axis represents the number of galaxies (once again with $\mathcal{M}_r < -19$) within a 1.5 Mpc projected aperture centered on the sightline and $\Delta z = 0.0033$ of the nearest galaxy to the sightline. Upper limits shown on the column density are 3-σ. Note the lack of C IV detections where the number of galaxies within 1.5 Mpc exceeds 7. Symbol sizes are scaled according to impact parameter (larger symbols have smaller impact parameters) of the closest galaxy (≤ 160 kpc) to show that impact parameter effects alone do not account for the detection or nondetection of C IV. (Bottom) H I column density as a function of the same environmental metric. Unlike C IV, H I is detected at even the highest densities probed, although the only H I nondetections do at occur at relatively high density.

As stated in Section 3.2.1, we use galaxies with k-corrected absolute r-band magnitudes of $\mathcal{M}_r \leq -19$ as tracers of the local density. As shown in Section 3.3.1.4, C IV absorption undergoes an increase in detection within the virial radius at $M_* > 10^{9-9.5} M_\odot$. The distribution of galaxies at $M_* \sim 10^{9.5}$ peaks at $\mathcal{M}_r \sim -19$, which is conveniently 0.1 mag brighter than the expected spectroscopic completeness limit at $z \sim 0.055$, the upper redshift limit of the NASA-Sloan Atlas. Therefore, we select from our entire dataset the sightlines and redshifts where galaxies more luminous than $\mathcal{M}_r < -19$ occur within impact parameters of $\rho \leq 160$ kpc. This distance is approximately the virial radius of a $M_* = 10^{9.5} M_\odot$ galaxy; furthermore, C IV detection declines at larger impact parameters (Bordoloi et al., 2014; Liang & Chen, 2014). Finally, we counted the number of $\mathcal{M}_r < -19$ galaxies, N_{1500}, within $\rho < 1500$ kpc (approx. 1 h^{-1} Mpc in the adopted cosmology) and $|\delta z| < 0.0033$ (approx. 1000 km/s) in accordance with the results of Muldrew et al. (2012) and Haas et al. (2012). Our results do not qualitatively change under small deviations ($\sim 10\%$) of these parameters. Maps of the galaxy environments included in this analysis are provided in the Appendix; also included are plots showing overdensities at various redshifts along the QSO sightline.

Figure 3.6 shows detections and non-detections of C IV at redshifts $z < 0.055$ where at least one $M_* \gtrsim 10^{9.5} M_\odot$ galaxy has $\rho \leq 160$ kpc. A density threshold is apparent, as the regions of highest density with $N_{1500} \gtrsim 7$ do not contain *any* C IV absorbers above the detection limits imposed by the COS spectra. In contrast with C IV, but as observed with the mass dependence discussed in Section 3.3.1.4, the bottom panel of Figure 3.6 shows that H I is detected at the highest densities where C IV is not. However, the only 3 nondetections of H I do occur at $N_{1500} > 10$, which may hint at a density dependence, but larger samples with more precise H I column densities are required to test this trend.

To quantify the statistical significance of this result, we compared the N(C IV) measurements for galaxies in environments above and below the apparent $N_{1500} = 7$ density threshold seen in Figure 3.6. The log-rank nonparametric test, which accepts censored data, with 3-sigma upper limits on the column density for nondetections, indicates that we may reject the null hypothesis that the two samples are drawn from the same distribution with >98% confidence. Alternatively, we compared the two detection rates adopting a detection threshold of log N(C IV) = 13.5 cm^{-2} using the Newcombe-Wilson method for the difference between two proportions; the test yields a 99% confidence that we may reject the null hypothesis that the detection rate is equal above and below the threshold value. For reference, Table 3 includes the covering fractions for C IV and H I in the two N_{1500} density bins.

We qualify that we have assessed the statistical significance adopting an apparent threshold value of N_{1500}. The apparent threshold value depends on, e.g., increasing or decreasing the outer impact parameter from 1500 kpc. Smaller choices of outer impact parameter decrease the apparent threshold value by one or two galaxies, bringing more nondetections to lower densities. However, a threshold density remains apparent unless the chosen outer impact parameter is much smaller than 1000 kpc, at which scales the fixed-aperture density may not be probing the full extent of more massive halos. Conversely, larger choices of outer impact parameter aperture probe scales beyond individual halos, and the detections at low density in Figure 3.6 would move to higher density because of contamination from other halos in the density metric.

Figures 3.3 and 3.4 show that the metal-enriched gas traced by C IV absorption preferentially resides within projected distances of $\sim$ 200 kpc from nearby galaxies. However, the dearth of C IV detections in dense environments as shown in Figure 3.6 suggests that the presence of many galaxies near a sightline does not have an additive effect on the presence of C IV-traced gas, as these environments should provide more potential sources for the metals. Therefore, the absorption line data may be reflecting

changing physical conditions of the CGM influenced by the larger scale environment. We return to this assertion for further discussion in Section 3.4.3.

3.3.2.2 Group Dark Matter Halo Mass

While Figure 3.6 suggests a C IV detection threshold in terms of the local galaxy density quantified by simply counting galaxies, the question remains whether the galaxies whose CGM is probed falls within the same larger dark matter halo as the surrounding galaxies counted. Therefore, we have cross-matched the galaxies initially selected in our fixed-aperture analysis, i.e., those with $\rho < 160$ kpc, with the group catalog of Yang et al. (2007) (using their version updated for SDSS DR7) to obtain the halo masses ($M_{\rm halo}$) of the groups in which these galaxies reside. We assigned halo masses as follows: (1) For the galaxies that were directly classified as group members by Yang et al. (2007), we assigned group halo masses from the catalog. (2) If the galaxies were not identified as group members and were not projected within 1 r_{vir} of any group in the catalog, we assigned the halo mass from abundance matching as described in 3.2.3. (3) Galaxies that were not identified as group members but were at projected distances within 1 r_{vir} of a group were assigned the mass of that group.

The resulting N(C IV)-$M_{\rm halo}$ relation is shown in Figure 3.7; as for the most populated local regions depicted in Figure 3.6, we do not detect C IV in the CGM of galaxies residing in the largest-$M_{\rm halo}$ groups ($M_{\rm halo}\sim 10^{12.7}$ $M_{\odot}$). The group catalog only includes galaxies at $z \geq 0.01$, so any non-isolated galaxies at $z < 0.01$ shown in Figure 3.6 are omitted from this figure. The only $z < 0.01$ galaxy included here contains no other galaxies within the 1500-kpc aperture, and we have assigned its halo mass through abundance matching as with the other isolated galaxies.

The gas traced by C IV in the low-z, inner CGM is likely subject to a number of influences, evidenced by (1) trends of decreasing column densities for several ions with increasing impact parameter and increasing column density ratios of higher to

Table 3.3. Covering fractions of C IV and H I absorption with respect to impact parameter, galaxy mass, and environment.

Ion	Detection Threshold (log N(X) [cm^{-2}])	Redshift range	Selection Criteria	N_{det}	N_{tot}	f_c (%)
Impact parameter distributions for galaxies with $\mathcal{M}_r \leq -16.4$ (proper distance-selected)						
C IV	13.5	$z \leq 0.015$	$\rho < 160$ kpc	6	19	32^{+11}_{-10}
C IV	13.5	$z \leq 0.015$	$\rho < 100$ kpc	3	8	38^{+18}_{-15}
C IV	13.5	$z \leq 0.015$	100 kpc $\leq \rho <$ 200 kpc	5	21	24^{+10}_{-8}
C IV	13.5	$z \leq 0.015$	200 kpc $\leq \rho <$ 300 kpc	0	16	0^{+6}_{--0}
C IV	13.5	$z \leq 0.015$	300 kpc $\leq \rho <$ 400 kpc	0	12	0^{+8}_{--0}
H I	13.0	$z \leq 0.015$	$\rho < 160$ kpc	12	13	92^{+5}_{-11}
H I	13.0	$z \leq 0.015$	$\rho < 100$ kpc	7	7	100^{+0}_{-13}
H I	13.0	$z \leq 0.015$	100 kpc $\leq \rho <$ 200 kpc	10	13	77^{+10}_{-13}
H I	13.0	$z \leq 0.015$	200 kpc $\leq \rho <$ 300 kpc	13	17	76^{+9}_{-12}
H I	13.0	$z \leq 0.015$	300 kpc $\leq \rho <$ 400 kpc	5	8	62^{+15}_{-18}
Impact parameter distributions for galaxies with $\mathcal{M}_r \leq -16.4$ (virial radius-selected)						
C IV	13.5	$z \leq 0.015$	$\rho < 1\ r_{vir}$	7	21	33^{+11}_{-9}
C IV	13.5	$z \leq 0.015$	$1\ r_{vir} \leq \rho < 2\ r_{vir}$	1	28	4^{+5}_{-2}
H I	13.0	$z \leq 0.015$	$\rho < 1\ r_{vir}$	13	14	93^{+4}_{-10}
H I	13.0	$z \leq 0.015$	$1\ r_{vir} \leq \rho < 2\ r_{vir}$	13	22	59^{+10}_{-11}
Dependence on galaxy mass within $\rho = 1\ r_{vir}$						
C IV	13.5	$z \leq 0.015$	$M_* < 9.5\ M_\odot$	1	11	9^{+12}_{-6}
C IV	13.5	$z \leq 0.015$	$M_* \geq 9.5\ M_\odot$	8	10	80^{+10}_{-15}
H I	13.0	$z \leq 0.015$	$M_* < 9.5\ M_\odot$	9	9	100^{+0}_{-10}
H I	13.0	$z \leq 0.015$	$M_* \geq 9.5\ M_\odot$	9	11	82^{+9}_{-14}
Dependence on galaxy environment given an $\mathcal{M}_r \leq -19$ galaxy within $\rho = 160$ kpc						
C IV	13.5	$z \leq 0.055$	$\mathcal{N}_{1500} \leq 7$	8	14	57^{+12}_{-13}
C IV	13.5	$z \leq 0.055$	$\mathcal{N}_{1500} > 7$	0	7	0^{+13}_{-0}
H I	13.0	$z \leq 0.055$	$\mathcal{N}_{1500} \leq 7$	16	16	100^{+0}_{-6}
H I	13.0	$z \leq 0.055$	$\mathcal{N}_{1500} > 7$	7	10	70^{+12}_{-16}
Dependence on group dark halo mass given an $\mathcal{M}_r \leq -19$ galaxy within $\rho = 160$ kpc						
C IV	13.5	$z \leq 0.055$	$M_{\rm halo} < 12.5 M_\odot$	7	14	50^{+13}_{-13}
C IV	13.5	$z \leq 0.055$	$M_{\rm halo} \geq 12.5 M_\odot$	0	5	0^{+17}_{-0}
H I	13.0	$z \leq 0.055$	$M_{\rm halo} < 12.5 M_\odot$	16	17	94^{+4}_{-9}
H I	13.0	$z \leq 0.055$	$M_{\rm halo} \geq 12.5 M_\odot$	5	6	83^{+10}_{-20}

lower ions with increasing impact parameter (Bordoloi et al., 2014; Liang & Chen, 2014) and (2) the galaxy mass dependence reported in Section 3.3.1.4. The results presented in this section suggest that a third environmental influence must be added as well. We have attempted to control for impact parameter- and mass-dependent effects to some degree by requiring that at least one $\mathcal{M}_r \leq -19$ galaxy fall within $\rho = 160$ kpc of the QSO sightline, but much larger galaxy/absorber samples are required to separate these effects while simultaneously controlling for galaxy density, mass, etc.

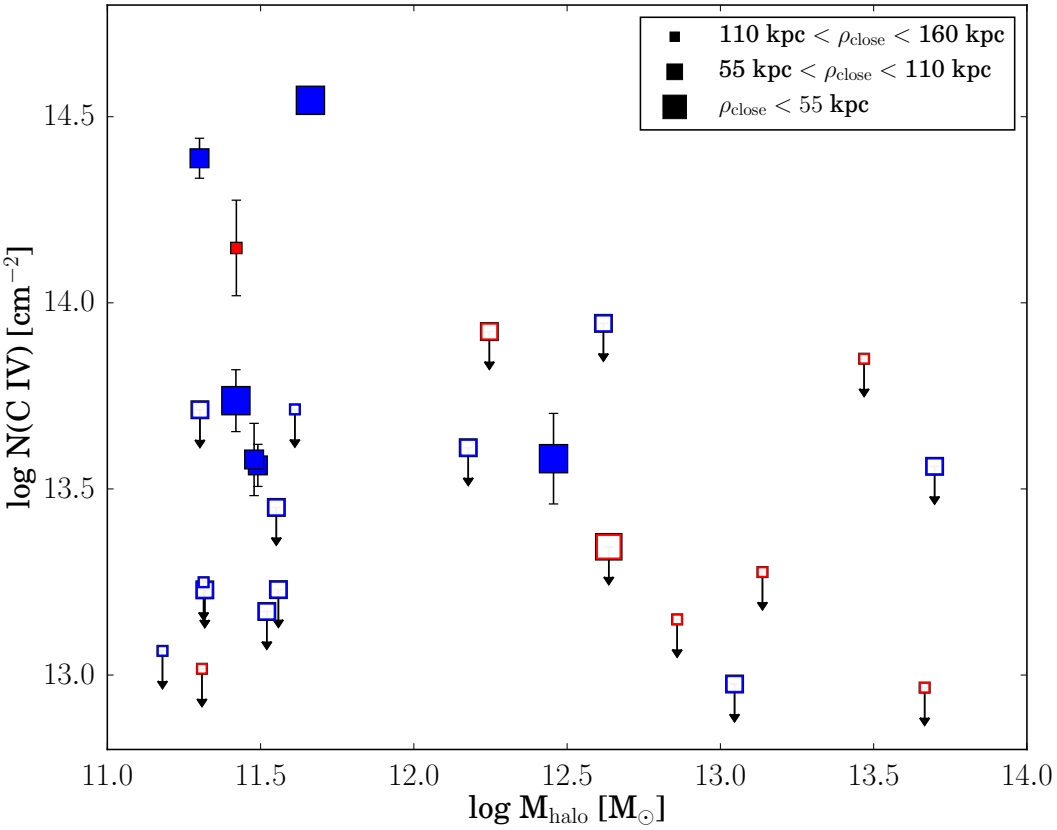

Figure 3.7 The C IV column density as a function of dark matter group halo mass for the CGM absorbers and nondetections plotted in Fig. 3.6. The halo masses were adopted from the Yang et al. (2007) group catalog for the galaxies within 160 kpc of the QSO sightlines or from halo abundance matching for galaxies not in groups. As in Figure 3.6, the larger symbols indicate smaller impact parameters to the closest galaxy. The open symbols with downward arrows correspond to 3-σ upper limits on the absorption; filled symbols with upward arrows indicate lower limits measured using the apparent optical depth on saturated lines. Consistent with the galaxy counts plotted in Fig. 3.6, the galaxies residing in halos of $M_h \gtrsim 10^{12.7} M_\odot$ do not show C IV absorption in their CGM.

3.4 Discussion

3.4.1 Faint dwarf galaxies as underrepresented sources of C IV absorbers

As shown in Figure 3.2, for 5/9 absorbers, the galaxies with the smallest impact parameters (in proper distance) are low-surface brightness objects. The proper distance selection method yields lower mass galaxies than the virial radius selection, as

the larger virial radii of more massive galaxies in the field bring them closer in terms of $r/r_{\rm vir}$. Indeed, 6/9 absorbers yield larger impact parameters to their associated galaxies under the virial-radius selection method than those chosen by proper distance (by factors of $\gtrsim 2$ in some cases). This result accentuates the dilemma in attributing absorbers to individual nearby galaxies: selecting by virial radius may provide a physically motivated connection but may overlook important processes plausibly occurring, such as outflows or mass loss from dwarf galaxies. On the other hand, galaxies increase in density with decreasing mass, and the mere proximity of a low-mass dwarf does not necessarily implicate it as the source of the gas, especially if both the absorber *and* the dwarf galaxy may reside within the dark matter halo of a more massive galaxy. In fact, for all six absorbers that have two different galaxies associated according to the two selection methods, *the less massive galaxy falls within 1 projected r_{vir} of the more massive galaxy.*

Even given the ubiquity of dwarf galaxies in close proximity to QSO sightlines, the mass dependence of C IV detections exhibited in Figure 3.5 calls into question the relative importance of the fainter dwarfs when proceeding to cross-correlate the CGM gas and galaxy properties. For example, correlating the CGM absorption with the star formation activity of the massive galaxies selected by virial radius may mask the effects of the fainter star-forming galaxies within the same halo, such as if the massive galaxies' CGM are partly enriched by the dwarf galaxies residing therein. In fact, it may be an important clue that the C IV absorbers typically lie outside the putative virial radii of the nearest dwarf galaxy as the gas can more easily escape the dwarf's shallower potential well than that of the central galaxy, and the transfer of the metal-enriched gas outside the dwarf may even be aided by the presence of the counterpart (Johnson et al., 2015).

Two important points arise from the result presented in Section 3.3.1.4: (1) Isolated galaxies with $M_* < 9.5\ M_\odot$ ($L \sim 0.1L*$) have a low covering fraction for

$\mathcal{N}_{\rm abs}(N(\text{C IV})) > 10^{13.5}\text{cm}^{-2}$ absorbers. (2) Dwarf galaxies, however, are frequently found at small impact parameters to sightlines/redshifts where C IV is detected. While this second point is itself not surprising, we now ask if our blind C IV absorption has picked out special configurations of satellites and centrals such that the absorbers are tracing halos that are not only sufficiently massive but that also contain dwarf satellites at especially small impact parameters. To address this question, we ran a simple Monte Carlo experiment to assess the typical distribution of impact parameters to faint dwarf galaxies given the presence of more massive galaxies within $\sim 1\ r_{vir}$. Within the SDSS footprint, we chose random coordinates to represent QSO sightlines and then a redshift at $z \leq 0.015$ to localize simulated absorbers.. Then, we recorded the impact parameters and r-band magnitudes of all galaxies around the sightline within $|\delta z| < 0.002$. After repeating this 50,000 times, we identified cases where sightlines passed within 180 kpc, 250 kpc, and 350 kpc of an $L > 0.1\ L*$ galaxy, the approximate onset of C IV absorption as a function of galaxy mass. These impact parameters were chosen to represent the approximate virial radii of $L \sim 0.1\ L*$, $L \sim L*$, and $L > L*$. Then, in each of these cases, the impact parameter to the nearest $L < 0.1\ L*$ galaxy was tabulated.

Figure 3.8 shows the resulting impact parameter distributions; the color of each histogram signifies the impact parameter selection criterion for the more massive galaxy. If our C IV absorber-selected galaxy environments differed from those probed at random sightlines/redshifts, we might expect our distribution of proper-distance selected impact parameters to peak at smaller values than those from the Monte Carlo experiment. While some scenarios yield $L < 0.1\ L*$ at much larger impact parameters than the $L > 0.1\ L*$ galaxies, the less massive galaxies are overwhelmingly found nearer the sightline. Figure 3.9 shows the cumulative distribution of impact parameters to faint dwarfs $L < 0.1\ L*$ given each impact parameter selection for $L > 0.1L*$ galaxies. While our low-z absorber sample is small, the Monte Carlo experiment

reveals no strong evidence that the combination of faint dwarfs at small impact parameters with more massive galaxies at small r/r_{vir} are unique to the presence of C IV absorbers.

To conclude this discussion, we emphasize the following: (1) Galaxy surveys around QSO sightlines that are complete down to even $L \sim 0.1\ L*$ are in general missing fainter galaxies at small impact parameters $\rho \leq 100$ kpc. (2) However, these $L \lesssim 0.1\ L*$ galaxies in isolation do not give rise to $\mathcal{N}_{\rm abs}(N(\text{C IV})) > 10^{13.5}\text{cm}^{-2}$ absorbers. The same is not true for H I absorption, as seen in Figure 3.5. While the dwarf galaxies are believed to be effective at enriching the CGM/IGM on large scales (Shen et al., 2014), the properties of C IV absorption exhibited here may be more indicative of physical/dynamical conditions in moderately populated halos ($M_{\rm halo} \gtrsim 10^{11.5} M_{\odot}$).

3.4.2 Comparing absorber statistics with previous surveys

As remarked in Section 3.3.1.2, our C IV column density profiles show some differences from those previously reported, such as the incidence of C IV absorbers out to and beyond 1 r_{vir}. Between the maximum impact parameter for a COS-Dwarfs C IV detection ($\rho = 0.66\ r_{vir}$) and the maximum they probed ($\rho = 1.33\ r_{vir}$), we report 2 of out of a possible 19 C IV detections ($10^{+9}_{-5}\%$) compared to 0/11 in COS-Dwarfs ($0^{+8}_{-0}\%$), not a statistically significant difference. However, our covering fraction is statistically nonzero with $> 99.7\%$ confidence. We also note the differences in galaxy masses between this work and COS-Dwarfs: our two detections in this impact parameter range occur at 0.73 r_{vir} from a $10^{10.4}\ M_*$ galaxy,which exceeds the COS-Dwarfs target mass range, and at 1.27 r_{vir} from a $10^{9.9}\ M_*$ galaxy, similar to the highest-mass COS-Dwarfs galaxies. A similar result to that of COS-Dwarfs was reported by Liang & Chen (2014), who detect no C IV absorption at $\rho > 0.7\ r_{vir}$, but their galaxy sample has no imposed upper mass limit. Our detection fractions at $\rho < 0.6\ r_{vir}$ and that of Liang & Chen (2014) are within the uncertainties of each other, but our

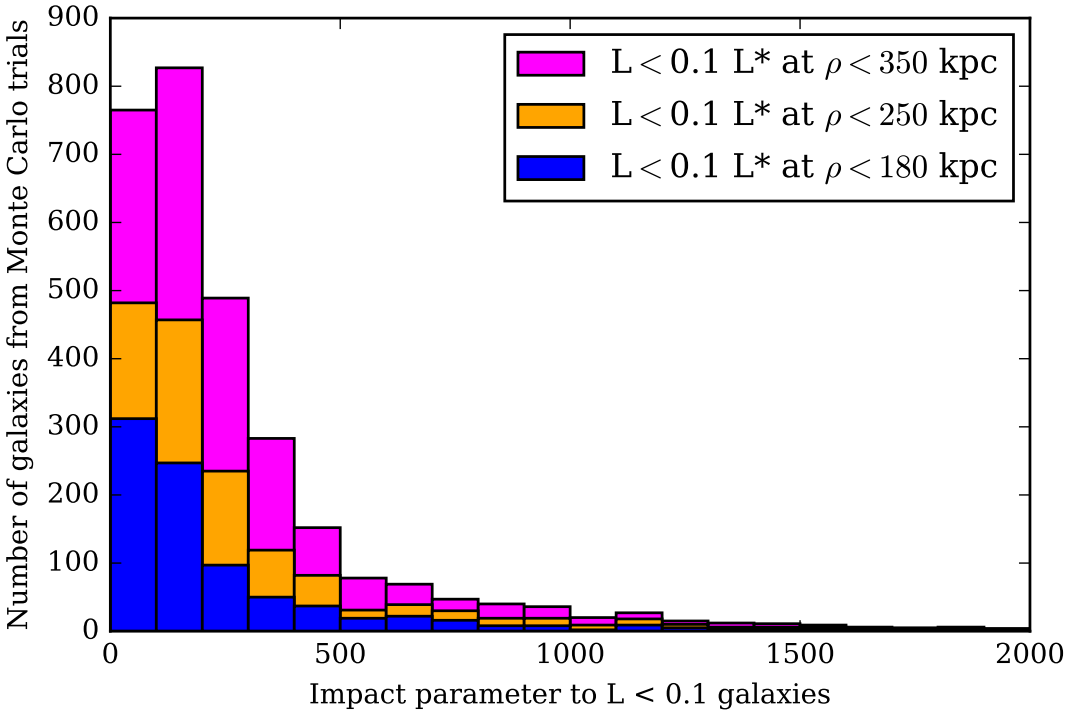

Figure 3.8 Monte Carlo simulation results of the distribution of impact parameters of random 'sightlines' and redshifts to faint dwarf galaxies $L < 0.1L*$ when a more massive galaxy lies within three different impact parameters as indicated in the legend. The three selections of impact parameters roughly correspond to the virial radii of $L \sim 0.1L*$, $L \sim L*$, and $L > L*$ galaxies.

detections at $\rho \geq 1\ r_{vir}$ are somewhat surprising given their lack of detections beyond $\rho > 0.7\ r_{vir}$; this could be a result of small-number statistics and differences in our halo radius/r_{vir} definitions. This rarer high-ρ/r_{vir} population of absorbers may offer key insights to outflow and stripping mechanisms that transport enriched gas out of galaxies and into the IGM.

Strong C IV absorption is patchy in the CGM, as shown above and also reported by Bordoloi et al. (2014), Borthakur et al. (2013), and others. For star-forming galaxies alone, we only detect C IV within 150 kpc of 5/17 galaxies. With a larger sample, COS-Dwarfs finds a C IV covering fraction that is ~ 0.8 in the inner 50 kpc of star-forming galaxies, but decreases to < 0.2 in the outer 50 kpc of star-forming galaxies.

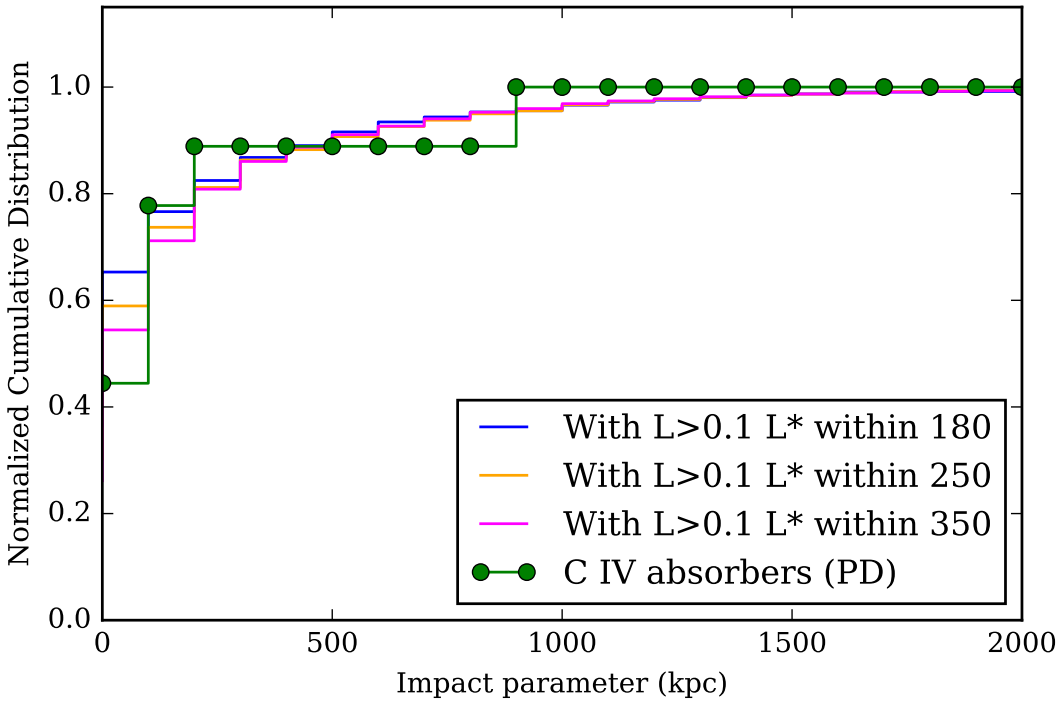

Figure 3.9 The cumulative distribution of impact parameters to $L < 0.1L*$ galaxies for the three scenarios presented in Figure 3.8 (in blue, orange, and magenta) alongside the observed impact parameter distribution from our proper distance-selected galaxy/absorber associations (green). The Monte Carlo experiment suggests that configurations of galaxies and faint dwarf satellites associated with our blindly detected C IV absorbers are similar to those that would be obtained given random sightlines and absorber redshifts.

This characteristic of C IV absorption contrasts with the behavior seen in another strong-transition metal ion: O VI. The COS-Halos team finds strong O VI to be nearly ubiquitous in the CGM of their star-forming galaxy sample (Tumlinson et al., 2011). Their survey targeted QSO sightlines out to 150 kpc of $\sim L*$ galaxies with a redshift distribution chosen to provide coverage of the O VI $\lambda\lambda$ 1032,1028 doublet in the COS G130M grating.

We emphasize that O VI and C IV are generally not simultaneously covered by our observations except for a narrow swath of redshift space, $0.11 < z_{abs} < 0.16$. The lower-redshift end of O VI coverage lies well beyond the cutoff for our low-z

galaxy/absorber sample chosen for completeness to faint dwarf galaxies. Therefore, we are prevented from directly comparing the C IV and O VI characteristics within our galaxy/absorber pairs. We must thus rely on O VI studies for this analysis. Bordoloi et al. (2014) suggest that the differences between observations of C IV and O VI may be attributable to the masses of the target galaxies (sub-$L*$ and $\sim L*$ for COS-Dwarfs and COS-Halos, respectively). This conjecture appears to be supported by Prochaska et al. (2011), who find that the O VI covering fraction is higher within the virialized halos of $L > 0.1\ L*$ galaxies than for their dwarf galaxy counterparts ($L < 0.1\ L*$). This explanation is also consistent with results from blind O VI surveys (e.g, Tripp et al., 2008), which typically find much lower O VI column densities than those measured in the COS-Halos survey. It is also possible that the COS-Halos sample probes more rare luminous galaxies that have unusually high quantities of O VI in their halos. This as-yet unexplored C IV-O VI overlap region at $z > 0.11$ (at least in terms of HST/COS capability) holds great promise for investigating the apparent discrepancy between the profiles of these two ions around galaxies.

3.4.3 Group/cluster environments and the CGM

A novel facet of this work is the investigation of environmental effects on the metal-enriched gas traced by C IV. We have found an apparent suppression of circumgalactic C IV absorbers within halos of $\log M_{\rm halo} = 12 \sim 13\ M_{\odot}$, or approximately the transition region where halos that typically host isolated galaxies transition to hosting groups (Yang et al., 2003). Oppenheimer et al. (2016) contend that the prevalence of O VI and the correlation between sSFR and N(O VI) found by COS-Halos can be attributed to the similarity between the virial temperature corresponding to dark matter halos hosting $L*$ galaxies and the peak temperature for O VI abundances under collisional ionization.

The peak temperature for C IV due to collisional ionization equilibrium occurs at $\sim 10^{5.1}$ K (Gnat & Sternberg, 2007; Verner et al., 1994). Using the expression given by Oppenheimer et al. (2016) for the virial temperature of a dark matter halo, which they find follows the typical gas temperature for halos in their simulations, the peak temperature for C IV corresponds to log $M_{\rm halo} = 11.1 M_{\odot}$. We find that the CGM C IV detection rate increases sharply at log $M_* = 9.0 - 9.5$ $M_{\odot}$ (cf., Figure 3.5), which corresponds to halo masses of log $M_{\rm halo} = 11.0 - 11.2$ $M_{\odot}$ from halo abundance matching. Thus, the gas we observe via C IV may in part be collisionally ionized. The simulations of Cen & Chisari (2011) indicate that C IV absorbers are dominated by photoionization after $z = 3$, but some contribution of absorbers with N(C IV)= 10^{12-14} cm^{-2} does arise from gas at temperatures near $\sim 10^{5.1}$ K.

However, it is also clear from Figure 3.5 that C IV absorption persists when $M_* > 10.0$ $M_{\odot}$, which corresponds to $M_{\rm halo} > 11.5$ $M_{\odot}$ from halo abundance matching. The virial temperatures of these halos well exceed the peak of the triply ionized state of carbon, and this simple picture does not quite reconcile the results of Sections 3.3.1.4 and 3.3.2. Section 3.3.2 shows that the C IV detection rate indeed declines just beyond this halo mass, and H I persists beyond the halo mass range where C IV is deficient. The overdense region may simply contain more gas, compensating for the lowered abundance of the C IV ionization state when the dominant state has transitioned to C V. Schaye et al. (2003) found that the observed C IV at $1.8 < z < 4.1$ must arise from photoionization based on C III/C IV ratios. Unfortunately, we do not cover C III ($\lambda_r = 977$Å) for any of the galaxy/group-absorber pairs in this study to use this diagnostic.

Lastly, we suggest that a galaxy's CGM may well be affected by its relationship to the encompassing group. The galaxy associated with the one detection of C IV shown in Figure 3.7 where $M_{\rm halo} > 12$ $M_{\odot}$ lies at $r > 0.5$ r_{vir} relative to the *group* virial radius. No detection occurs for galaxies within $r = 0.5$ r_{vir}(group) of halos with

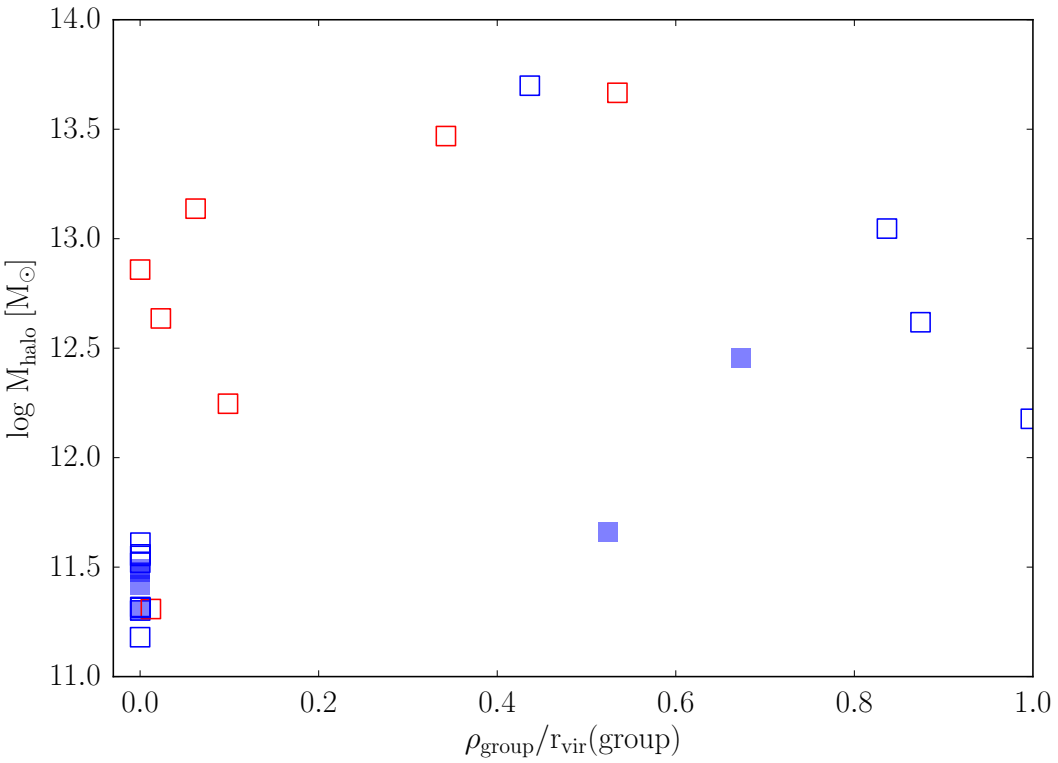

Figure 3.10 The halo masses of our C IV galaxy/absorber environment sample versus impact parameter relative to the group virial radius. Open squares represent C IV nondetections, and filled squares denote detections. We note that the lone detection of C IV in an $M_{\rm halo} > 10^{12}$ $M_\odot$ occurs beyond 0.5 r_{vir}in projection. Filling in this parameter space will provide insight to the effects of environment on the CGM (and presumably the host galaxies themselves).

$M_{\rm halo} > 12$ $M_\odot$. In Figure 3.10, we plot the halo mass of each galaxy/absorber from Figure 3.7 against the projected distance of the galaxy relative to the associated group virial radius; the solid squares correspond to C IV detections and the open squares nondetections. This representation of our data underscores that large regions of parameter space pertaining to the CGM/environment connection remain unexplored. Many points are clustered in the lower-left of this plot, and these largely correspond to isolated galaxies. If larger samples filling in the large $\rho_{\rm group}$/r$_{\rm vir}$(group) but high-$M_{\rm halo}$ regime reveal little C IV absorption, these galaxies' CGM may indeed be undergoing ram-pressure or tidal stripping.

3.5 Summary and Conclusions

This work, Paper III of an ongoing program, presents initial survey results employing public archival galaxy survey data (SDSS, RC3, etc.), including spectroscopy and imaging, covering fields around the QSO sightlines employed in our blind C IV survey presented in Paper II. To achieve high completeness to faint dwarf galaxies ($L \sim 0.01L*$), we limit our analyses of individual galaxy-absorber associations (Section 3.3.1) to $z \leq 0.015$ based on the magnitude limit of the SDSS spectroscopic data. Our C IV-environment analysis (Section 3.3.2) includes galaxies and absorbers to $z < 0.055$ building on the increased detection rate of C IV in the CGM of $M_* \gtrsim 10^{9.5} M_\odot$ host galaxies.

We summarize our main results below:

1. Selecting individual galaxies that are associated with C IV absorbers is generally ambiguous. We have selected associated galaxies based both on their proper distance separations and in terms of their virial radii. For 6/9 of our blindly detected C IV absorbers at $z \leq 0.015$, these differing criteria yield associations with different galaxies: the galaxies with the smallest proper distance impact parameters are dwarf galaxies, most with low surface brightnesses.

2. When selecting galaxy/absorber associations by proper distance, we find galaxies at impact parameters $\rho < 200$ kpc with the exception of one galaxy/absorber pair with $\rho > 350$ kpc. This large-ρ absorber also has a velocity separation $\delta v > 700$ km/s. In addition, we observe a prevalence of H I out to 350 kpc; however, at least half of the $\rho > 300$ kpc Lyα absorbers have low column densities that are similar to those statistically unassociated with galaxies. When selecting by virial radius, 3/9 C IV absorbers fall $\gtrsim 1\ r_{vir}$ of any galaxy detected.

3. We find that galaxies with $M_* > 10^{9.5} M_\odot$ show a significantly greater C IV detection rate within 1 r_{vir} than galaxies of lower mass. This mass dependence

does not extend to H I, as high detection rates occur for H I within 1 r_{vir} of galaxies with masses $M_* < 10^8 M_\odot$.

4. At $z < 0.055$, we do not detect C IV within 160 kpc of any galaxy residing in an environment containing more than seven $\mathcal{M}_r \leq -19$ galaxies within 1.5 Mpc but find a 57% detection rate within 160 kpc of galaxies when six or fewer galaxies of this luminosity reside within 1.5 Mpc. It is unclear what mechanisms lead to the dearth of C IV absorbers in the inner CGM in dense environments, but these regions are not devoid of gas, as we detect H I independent of environment. When using group halo masses rather than galaxy counts to quantify the environments of these same galaxies, the C IV detection rate falls to 0% at $M_h > 10^{12.7} M_\odot$.

The data presented here highlight the close association between galaxies and metal-enriched gas using a novel combination of sensitivity to low-luminosity galaxies and blindly discovered C IV absorbers. These findings emphasize that the CGM is a key constituent in galaxy ecosystems, reflecting the buildup of enriched material through mass assembly while signifying the dependence of physical conditions on large-scale environment.

Acknowledgements

We thank John Stocke, Hsiao-Wen Chen, Houjun Mo, Kate Rubin, Romeel Davé, Martin Weinberg, Andrew Battisti, Brice Ménard, and Sandy Faber for helpful discussions at various stages of survey design and analysis. Support for this research was provided by NASA through grants HST-GO-11741, HST-GO-11598, HST-GO-12248, and HST-AR-13894 from the Space Telescope Science Institute, which is operated by the Association of Universities for Research in Astronomy, Incorporated, under NASA contract NAS5-26555. Funding for SDSS-III has been provided by the Alfred

P. Sloan Foundation, the Participating Institutions, the National Science Foundation, and the U.S. Department of Energy Office of Science. The SDSS-III web site is http://www.sdss3.org/.

SDSS-III is managed by the Astrophysical Research Consortium for the Participating Institutions of the SDSS-III Collaboration including the University of Arizona, the Brazilian Participation Group, Brookhaven National Laboratory, Carnegie Mellon University, University of Florida, the French Participation Group, the German Participation Group, Harvard University, the Instituto de Astrofisica de Canarias, the Michigan State/Notre Dame/JINA Participation Group, Johns Hopkins University, Lawrence Berkeley National Laboratory, Max Planck Institute for Astrophysics, Max Planck Institute for Extraterrestrial Physics, New Mexico State University, New York University, Ohio State University, Pennsylvania State University, University of Portsmouth, Princeton University, the Spanish Participation Group, University of Tokyo, University of Utah, Vanderbilt University, University of Virginia, University of Washington, and Yale University.

CHAPTER 4

WARM-HOT GAS IN X-RAY BRIGHT GALAXY CLUSTERS AND THE H I-DEFICIENT CIRCUMGALACTIC MEDIUM IN DENSE ENVIRONMENTS

Joseph N. Burchett[1], Todd M. Tripp[1], Q. Daniel Wang[1], Christopher N.A. Willmer[2], David V. Bowen[3], Edward B. Jenkins[3]

We analyze the intracluster medium (ICM) and circumgalactic medium (CGM) in 7 X-ray detected galaxy clusters using spectra of background QSOs from the Hubble Space Telescope (HST) Cosmic Origins Spectrograph (COS) and Space Telescope Imaging Spectrograph (STIS), optical spectroscopy of the cluster galaxies from MMT/Hectospec and the Sloan Digital Sky Survey (SDSS), and X-ray imaging/spectroscopy from XMM-Newton and Chandra. First, the optical spectroscopy reveals many galaxies at small impact parameters (< 300 kpc) to the QSO sightlines and within ~ 1000 km s^{-1} of the cluster redshifts; we report a very low covering fraction of H I absorption in the CGM of these cluster galaxies, $f_c = 18^{+14}_{-9}\%$, to stringent detection limits (N(H I) $< 10^{13}$ cm^{-2}) in most cases. As field galaxies have an H I covering fraction of $\sim 100\%$ at similar radii, the dearth of CGM H I in our data indicates that the cluster environment has effectively stripped or gravitationally heated and overionized the gaseous halos of these member galaxies. Second, we assess the contribution of warm-hot ($10^5 - 10^6$ K) gas to the ICM as traced by O VI and broad Lyα (BLA)

[1]University of Massachusetts - Amherst

[2]Steward Observatory, University of Arizona

[3]Princeton University Observatory

absorption, which would potentially bring the cluster baryon content closer to the universal baryon mass fraction ($\sim 17\%$). Despite the high signal-to-noise of our data, we do not detect O VI in any cluster, and we only detect BLA features in the QSO spectrum probing one cluster. We estimate that the total column density of material in the warm-hot phase along this line of sight totals to $\sim 3\%$ of that contained in the hot $T > 10^7$ K X-ray emitting phase. The features fall at high velocities relative to the cluster redshift and may trace pre-shocked material outside the cluster. Comparing the properties of gaseous galaxy halos in regions ranging from the low-density 'field' to galaxy groups and high-density clusters, we find that the CGM is progressively depleted of H I with increasing environmental density, where galaxy clusters are extreme sites where the CGM is most severely transformed. This transformation may play a key role in environmental galaxy quenching.

4.1 Introduction

Galaxy clusters represent the largest collapsed structures in the Universe. In the Λ Cold Dark Matter paradigm, these regions occur when strong density perturbations in the early Universe grow through structure formation as dark matter and baryonic matter accrete via gravitational collapse. As a result, we observe galaxy clusters in the present epoch to be rather extreme environments, comprising highly evolved galaxy populations, gravitationally heated gas with $T \gtrsim 10^7$ K, and prodigious galaxy-galaxy mergers and interactions. Therefore, clusters represent vital laboratories for studying how the largest structures are still forming from the cosmic web, how galaxy evolution is impacted by environment, and for testing the consistency of cosmological models and their measured parameters.

Since the early cataloging of galaxy clusters (Abell, 1965), the galaxy populations they host have been shown to possess quite different properties from galaxies in less dense environments. Cluster galaxies are more likely to have quenched star

formation, have elliptical morphologies, and be deficient in cold gas (e.g. Davies & Lewis, 1973; Oemler, 1974; Dressler, 1980; Sandage et al., 1985). Within clusters, the distributions of galaxies with varying morphologies, star formation rate (SFR), and gas content have motivated much investigation into the mechanisms that transform galaxies. To explain the proclivity of S0 and elliptical galaxies to reside cluster centers, Spitzer & Baade (1951) concluded that galaxy-galaxy collisions could remove the interstellar gas from normal spiral galaxies to leave behind S0s. Gunn & Gott (1972) found that the cluster galaxies' gas reservoirs, out of which stars could form, should be removed by interactions with the hot intracluster medium (ICM) itself by ram pressure stripping. Indeed, both galaxy-galaxy and galaxy-ICM interactions have been shown to be important transformation mechanisms in modern hydrodynamical simulations. As an example of the former, Moore et al. (1996) have argued that the cumulative effect of many high-speed galaxy-galaxy encounters can profoundly alter the gas distributions and morphologies of galaxies in the cluster environment, a process they refer to as 'galaxy harassment' (Moore et al., 1996, 1998; Marasco et al., 2016). Ram pressure stripping has been shown theoretically to be effective at removing a galaxy's halo gas well beyond the cluster virial radius (e.g., Bahé et al., 2013; Zinger et al., 2016) as well as gas in the disk once the galaxy falls within the cluster virial radius (Tonnesen et al., 2007). The shock-heated ICM may also quench galaxies by halting the accretion of fresh fuel for star formation ('strangulation'; Larson et al., 1980; van de Voort et al., 2017). Despite all of this work, the effectiveness of these processes has yet to be constrained observationally.

Observationally, 21 cm emission mapping of neutral hydrogen (H I) reveals the evidence of ram pressure stripping, harassment, and tidal stripping due to the cluster itself acting on galaxies' disk gas (Warmels, 1988; Chung et al., 2009). However, the effects of the cluster environment on the circumgalactic medium (CGM) – massive gaseous reservoirs enveloping galaxies – are considerably more difficult to observe

due to the low densities and likely temperatures of the CGM. Currently absorption-line spectroscopy using background quasi-stellar objects (QSOs) provides the most practical means to investigate how the cluster environment affects the low-density CGM. Most resonance transitions must be observed in the ultraviolet (UV) at the lower redshifts of mature galaxy clusters, and the relative scarcity of UV-bright background sources that are well positioned to probe foreground galaxies in clusters has resulted in limited data appropriate for such investigation. In contrast, the H I in the CGM of field galaxies has been characterized for two decades (e.g., Lanzetta et al., 1995b; Tripp et al., 1998; Chen et al., 2005; Wakker & Savage, 2009; Prochaska et al., 2011; Tumlinson et al., 2013; Burchett et al., 2016). Preliminary results have recently suggested that the properties of circumgalactic H I in denser environments differ significantly from the circumgalactic H I of field galaxies. Yoon & Putman (2013) show that the CGM in their sample of Virgo cluster galaxies exhibit a decreased covering fraction of H I relative to galaxies in the field. Moreover, Burchett et al. (2016) have found that environmental effects on the CGM may be evident even on group scales.

While the cooler, low-density phases of the CGM are most easily probed in absorption with current facilities, the hot $> 10^6$ K phase of the ICM is readily observed in X-rays via bremsstrahlung and line emission, particularly in the central cluster regions. In addition to the galaxy quenching/transformation phenomena discussed above, the X-ray emitting ICM provides key insight into other major astrophysical questions. Among these is the so-called "missing baryons" problem (Persic & Salucci, 1992; Fukugita et al., 1998), whereby an accounting of the observed baryon mass relative to the dark matter mass at present times does not match the cosmological baryon fraction measured via, e.g., Big Bang nucleosynthesis as constrained by deuterium abundances (Riemer-Sørensen et al., 2017; O'Meara et al., 2006) or fluctuations in the cosmic microwave background (Planck Collaboration et al., 2016). Indeed, the baryon fractions in galaxy clusters, where the baryons should be parti-

tioned primarily between the stars and X-ray emitting gas, have been shown to be deficient relative to the universal fraction (Vikhlinin et al., 2006; Andreon, 2010; Laganá et al., 2013). However, Gonzalez et al. (2013), identifying a mass-dependent contribution of the intracluster light, argue that the baryon content indeed appears to be closed for clusters $M_{500} > 3 \times 10^{14}\ M_{\odot}$, but much scatter exists below these masses[4]. Also, towards even lower masses ($\mathrm{M_{halo}} = 10^{13-14} M_{\odot}$), dynamically relaxed groups may have baryon fractions calculated from simply stars and hot gas consistent with the universal value (Mathews et al., 2005; Buote et al., 2016), although groups of similar masses may not exist in the same dynamical state and/or emit in X-rays at detectable surface brightness. In any case, such conclusions only apply to the inner regions (e.g., $< r_{500}$). Inference of the baryon content at larger radii, i.e., at $> r_{200}$, from X-ray observations depends sensitively on such assumptions as the clumpiness and thermal state of the hot gas.

Cosmological hydrodynamical simulations suggest that the missing baryon contribution should arise from 'warm-hot' gas at $T \sim 10^{5-6}$ K (Cen & Ostriker, 1999), which would elude detection by most observational techniques. The primary means by which observers can search for this warm-hot material with current facilities involve absorption line spectroscopy in the UV and X-ray regimes. Detections of the warm-hot intergalactic medium[5] have been reported using X-ray absorption (e.g., Fang et al., 2002; Nicastro et al., 2005; Buote et al., 2009; Bonamente et al., 2016); however, many of these marginal detections have been controversial owing to the lack of high spectral resolution and sensitivity combined with systematic issues in X-ray

[4]Throughout this paper, r_{500} refers to the radius within which the average mass density is 500 times the mean matter density of the Universe. $\mathrm{M_{500}}$ is the mass enclosed within r_{500}. Similarly, $\mathrm{M_{200}}$ and r_{200} correspond to overdensities by a factor of 200.

[5]The term 'WHIM' refers to intergalactic material residing in large-scale structures such as filaments and down to very low overdensities ($\delta < 50$; Davé et al., 2001); we are focused on the regions within galaxy clusters and on the outskirts of galaxy clusters and will simply refer to gas with temperatures $T \sim 10^{5-6}$ K as 'warm-hot'.

spectra. Gas in the $T \sim 10^{5-6}$ K regime has been readily detected with less ambiguity in UV absorption lines, namely the O VI $\lambda\lambda$1032, 1038 Å doublet (Tripp et al., 2000; Danforth & Shull, 2005; Tripp et al., 2008; Savage et al., 2014) and broadened H I Lyα features (Tripp et al., 2001; Richter et al., 2006; Lehner et al., 2007; Tejos et al., 2016). All of these studies have provided evidence that O VI and broad Lya absorbers could be important baryon reservoirs, but the physical conditions and origins of these absorption systems remain open topics of debate. Likewise, UV absorption line spectroscopy can be employed to measure the warm-hot gas contribution to the baryon budget on galaxy cluster scales provided the sightlines are appropriately positioned.

In this paper, we present analyses combining optical galaxy spectroscopy, UV QSO spectroscopy, and X-ray imaging and spectroscopy of five galaxy cluster systems (two of which are merging cluster pairs) to characterize the circumgalactic medium in the cluster environment as well as quantify the contribution of $T = 10^{5-6}$ K gas to the baryon content in the outer regions of galaxy clusters. In Section 4.2, we describe our observations and data. Section 4.3 presents the cluster galaxy data and analysis, and Section 4.4 contains the results gleaned from the full dataset. Section 4.5 discusses the implications of our results, and we summarize our findings and conclude the paper in Section 4.6.

4.2 Data and Observations

4.2.1 Sample Selection and X-ray imaging/spectroscopy

The key feature of our study is that we jointly probe a sample of galaxy clusters with X-rays and QSO absorption line spectroscopy. Our core galaxy cluster/QSO sample was selected such that UV-bright background QSOs fall within 1.5 r_{200} of optically-selected, rich clusters at $z_c > 0.10$. This redshift lower limit was imposed to place the O VI λ1032, 1038 doublet at the cluster redshift within the bandpass of spectrographs aboard the Hubble Space Telescope (HST).

Two of these clusters (Abell 1095 and Abell 1926), were targeted in our HST/XMM-Newton joint program, HST GO 13342 (PI: Wang). The two QSO/cluster pairs observed in this program were selected such that the diffuse outer regions of clusters would be bright enough to observe with $XMM-Newton$ efficiently and that the QSOs had sufficient UV brightness to be observed with the Cosmic Origins Spectrograph (COS) in a reasonable number of HST orbits. The third targeted cluster field, Abell 2246, was observed with the Chandra X-ray Telescope, and its observations were compiled from the Chandra archive. The A1095 and A1926 fields were observed with the $XMM-Newton$ European Photon Imaging Cameras (EPIC) for 47 ks and 47.5 ks, respectively. The A2246 field was observed with the $Chandra$ X-ray telescope Advanced CCD Imaging Spectrometer (ACIS) for 240 ks. Further details regarding the program design/target selection as well as the X-ray imaging and spectroscopy observations, data reduction, and measurements are provided by Wang & Walker (2014) and Ge et al. (2016) (hereafter WW14 and G16, respectively).

The X-ray imaging for A1095 and A1926 (Figure 4.1) reveal rich substructure, most importantly, dual concentrations of emission suggesting that each 'cluster' is actually a pair of merging clusters. G16 derive the physical properties (mass, temperature, etc.) of each individual subcluster, labeling them A1095W, A1095E, A1926S, and A1926N. These X-ray measurements lead to substantially more reliable estimates of the cluster masses and hence their r_{200} radii than the optical catalogs from which they were selected. They are significantly smaller than the original estimates based on the optical richnesses, largely due to the subcluster pairing. We adopt the same nomenclature when referring to these smaller clusters individually but simply refer to 'A1095' and 'A1926' when treating the merging system or targeted field as a whole. In addition to the targeted clusters, other previously identified clusters from various optical catalogs were also detected in X-ray emission in our target fields. We include two of these, GMBCG J255.34805+64.23661 (WW14) and MaxBCG J217.84740+24.68382

(G16), in our analysis and will refer to them as GMBCG J255.55+64.23 and MaxBCG J217.55+24.68, respectively.

Certain salient characteristics of the galaxy clusters featured in this study are summarized in Table 4.1.

Table 4.1 Selected properties of galaxy clusters and their QSO probes

Cluster	z_c [a]	log M_{200} [log $M_\odot$]	r_{200} [kpc]	ρ_{cl} [b] [kpc]	QSO
Abell 1095E	0.213	14.4	1240	865	SDSS J104741.75+151332.2
Abell 1095W	0.210	14.4	1190	1046	
Abell 1926S	0.136	14.1	990	2411	2MASS J1431258+244220
Abell 1926N	0.136	14.0	940	1921	
Abell 2246	0.229	14.5	1300	491	HS1700+6416
MaxBCG J217.84740+24.68382[c]	0.097	13.9	1240	156	2MASS J1431258+244220
GMBCG J255.34805+64.23661	0.452	14.7	1400	1132	HS1700+6416

[a] Adopted cluster redshifts based on spectroscopic redshifts of BCGs.

[b] Impact parameter defined as projected distance between QSO sightline and X-ray centroid assuming Hubble flow distance at redshift of BCG.

[c] Values for r_{200} and M_{200} extracted from optical catalog (Rykoff et al., 2014)

Table 4.2 Summary of QSO observations

QSO	RA (J2000)	Dec (J2000)	z_{QSO}	T_{exp}	Instrument/Grating	Dataset IDs
SDSS J104741.75+151332.2	10 47 41.751	+15 13 32.30	0.4069	24881.2	COS G130M	LC8901010,LC8901020,LCKU09010
				18819.4	COS G160M	LCKU10010,LCKU11010
2MASS J1431258+244220	14 31 25.880	+24 42 20.68	0.3858	14523.9	COS G130M	LC8903010,LC8903020
						LBS314010,LBS314020
HS1700+6416	17 01 00.620	+64 12 09.04	2.7407	175443.7	COS G130M	LC8301010-LC8312010
				101968.0	STIS E140M	O4SI02010-O4SI050A0

4.2.2 QSO spectroscopy

The three QSOs included in this study were observed with HST using COS (Green et al., 2012) and STIS (Woodgate et al., 1998). We obtained COS observations of SDSS J104741.75+151332.2 and 2MASS J1431258+244220 through the joint XMM-Newton/HST program described above. Additionally, SDSS J104741.75+151332.2 was observed with the G160M grating as part of HST GO program 13833 (PI: Tejos), and 2MASS J1431258+244220 was observed in program 12603. HS1700+6416 was observed with the COS G130M grating for the HST program 13491 (PI: Tripp) and with the STIS E140M grating for program 7778 (PI: Jenkins).

COS far-ultraviolet spectra are recorded with two abutted cross-delay line microchannel-plate detectors (Fox et al., 2017), and the physical gap between the two segments leads to an appreciable gap (≈15 Å) in spectral coverage. To fill in this gap in our programs, we observed the targets with two or three different grating tilts (for program 13342, we used central wavelengths = 1309 and 1327 Å; for program 13491 we employed CENWAVE = 1309, 1318, and 1327 Å). In addition, to mitigate the effects of COS fixed-pattern noise, we obtained multiple exposures at different focal-plane split positions with each grating tilt. As noted above, J104741.75+151332.2 was also observed for program 13833, which used CENWAVE = 1291 Å for G130M and CENWAVEs = 1577 and 1600 Å for G160M. The G130M observations of J1431258+244220 for program 12603 used CENWAVEs = 1300 and 1327 Å. The STIS observations of HS1700+6416 used the E140M echelle mode with the 0.2 × 0.2 aperture. To produce our final, fully combined spectra, we retrieved the data from the Mikulsky Archive for Space Telescopes and carried out the standard processing steps and 1-d spectrum extraction using CALCOS (v3.1.7) and CALSTIS (v2.22). We then checked and (if necessary) adjusted the wavelength alignment of exposures by comparing appropriate absorption lines (e.g., Milky Way interstellar lines of comparable strength), and finally we coadded the spectra using the weighting scheme described

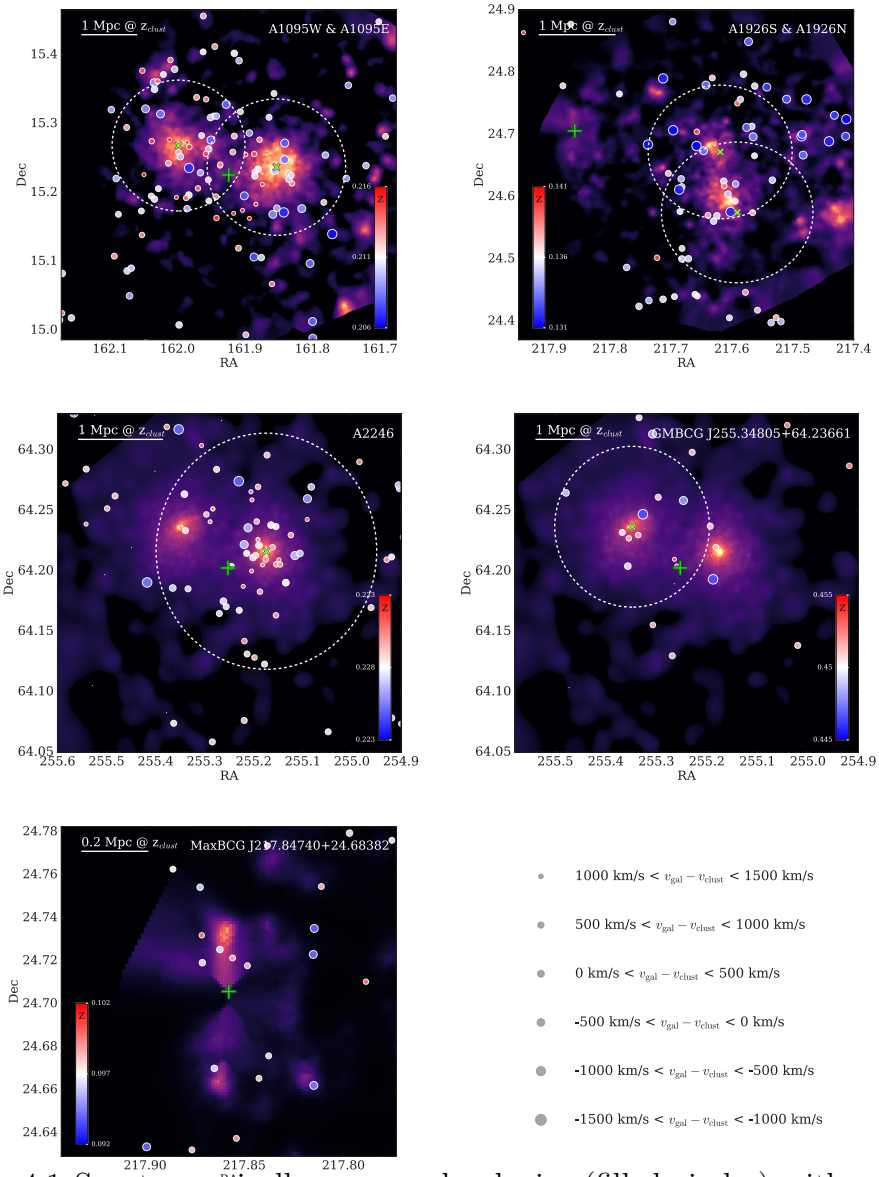

Figure 4.1 Spectroscopically measured galaxies (filled circles) with redshifts within $\delta z = 0.01$ of the cluster brightest cluster galaxies plotted on sky. The X-ray intensity is plotted in color and is scaled to maximize visibility of low surface brightness emission; the X-ray centroids of each subcluster are marked with green crosses. The large dashed circles mark r_{200} derived from each X-ray derived cluster/subcluster centroid (Lying at the edge of the FOV, the X-ray data for MaxBCG J217.55+24.68 are insufficient to derive masses, etc., so r_{200} is not marked for this cluster.). The green plus signs denote the location of each QSO sightline (see Table 4.1). Corresponding to the colorbar in each panel, the filled circles are colored according to galaxy redshift relative to each cluster redshift (marked at the center of each colorbar). Note: Even though both clusters fall within the same FOV, A2246 and GMBCG J255.55+64.23 as well as A1926N/S and MaxBCG J217.55+24.68 are plotted separately due to their widely separated redshifts.

by Tripp et al. (2001) including coaddition of the overlapping regions of adjacent echelle orders in the STIS data. The fully coadded COS data cover wavelength ranges of 1133−1778 Å (J104741.75+151332.2), 1150−1470 Å (J1431258+244220) and 1152−1472 Å (HS1700+6416) with spectral resolving power of 16000−21000 (Fox et al., 2017). The STIS E140M echelle spectrum of HS1700+6416 covers 1150−1710 Å with a resolving power of 45800 (Riley et al., 2017). While the COS G130M and STIS echelle spectra of HS1700+6416 overlap at observed wavelengths $\lambda_{obs} < 1472$ Å, the signal-to-noise (S/N) of the COS G130M spectrum is much higher in this region, and we primarily use the STIS data for constraints on lines with $\lambda_{obs} > 1472$ Å.

The COS G130M spectra of SDSS J104741.75+151332.2 and 2MASS J1431258+244220 have S/N of approximately 24 and 14, respectively, per resolution element at the observed wavelength of the O VI doublet at the redshifts of our targeted clusters. The G130M spectrum of 2MASS J1431258+244220 also covers Lyα at S/N = 17. The G130M spectrum of HS1700+6416 reaches a S/N of 40 near the expected wavelength of O VI arising from A2246. The G160M spectrum of SDSS J104741.75+151332.2 and the STIS spectrum of HS1700+6416 are included here to cover Lyα at the redshifts of A1095 and A2246, with S/N = 18 and 4, respectively. The COS spectra and the STIS spectrum have spectral resolution ∼15 km s^{-1} and ∼7 km s^{-1}, respectively. A summary of our QSO observations and their corresponding archival datasets is presented in Table 4.2.

4.2.3 Galaxy Spectroscopy

Given the redshifts of our target QSO-cluster pairs (WW14 & G16), we required a deeper spectroscopic galaxy survey than the publicly available data in order to investigate CGM properties in the clusters. Therefore, in addition to data from SDSS, we obtained new observations at the MMT with the Hectospec Multifiber Spectrograph (Fabricant et al., 2005; Mink et al., 2007). Hectospec is a 300 fiber

spectrometer with a 1° diameter field of view (FOV) and covers a wavelength range of 3650-9200 Å with a 6 Å resolution (1.2 Å pixel^{-1}, R = 600 − 1500).

We selected galaxies in the cluster/QSO fields to receive fibers using SDSS photometry according to the following procedure. First, we queried the SDSS for all objects identified as galaxies within 30 arcmin of each QSO sightline and that would have r-band absolute magnitudes corresponding to at least 0.1 $L*$ ($\mathcal{M}_r \lesssim -18.6$; Blanton et al., 2003) if at the redshift-indicated distances of the targeted clusters. We then removed objects with photometrically measured properties that suggested problematic SDSS data. These included making a cut on the r-band 'fiberMag' ($r_{\rm fib} \leq 22.8$) to remove objects with magnitudes far fainter than are reliable for SDSS photometry; such faint magnitudes are symptomatic of image artifacts being classified as galaxies. Also, we found that image artifacts and other clearly misclassified or problematically measured objects in the SDSS also contain unusually large r-band Petrosian radius measurements ('petroRad_r' > 100 arcmin). Lastly, following Strauss et al. (2002), we rejected objects with r-band 'psfMag' values within 0.1 mag of their 'modelMag' values to mitigate confused star/galaxy classifications. To further reject objects that were likely stars or extremely distant galaxies ($z_{\rm gal} >> z_{\rm QSO}$), we placed a conservative $z_{\rm QSO}$-dependent cut in g-r — r-i color-color space based on archival spectroscopic galaxy surveys (Geha et al., 2017). We placed color thresholds such that galaxies in these surveys with g-r and r-i colors redder than the threshold values were highly likely to have $z_{\rm gal} > z_{\rm QSO}$. For fiber targeting, we then selected all remaining galaxies without SDSS spectra and with r-band absolute magnitudes corresponding to 0.2 $L*$ or brighter if at the redshifts of the targeted clusters.

The assignment of objects to fibers was done using XFITFIBS [6], which takes into account the number of configurations, the object priorities, and the number

[6]http://www.harvard.edu/john/xfitfibs

Table 4.3 Summary of MMT/Hectospec Observations

Field	R.A. (J2000)	Dec. (J2000)	Exposure	Date
A1095	10:47:41.33	+15:13:44.30	780s	2016-02-08
A1095	10:47:41.33	+15:13:44.30	720s	2016-03-12
A1926	14:31:21.92	+24:42:02.68	600s	2016-02-04
A1926	14:31:21.92	+24:42:02.68	600s	2016-03-15
A2246	17:00:58.80	+64:12:55.33	600s	2014-06-24
A2246	17:00:57.31	+64:13:09.67	4500s	2014-06-25
A2246	17:01:00.27	+64:13:14.49	3600s	2014-06-25
A2246	17:01:05.22	+64:12:57.12	960s	2016-03-02
A2246	17:01:05.22	+64:12:57.12	960s	2016-03-03

of sky positions. For the observations here, we assigned a minimum of 40 fibers to measure the sky background and 10 to place on stars for flux calibration (Cool et al., 2008), leaving typically 250 fibers that could be assigned to program objects. XFITFIBS enables the survey designer to assign priorities for objects to receive fibers in the generated configurations, and we prioritized galaxies based on their QSO-centric impact parameters (ρ), impact parameters relative to the cluster X-ray centroids measured by WW14 and G16, and color consistency with belonging to a 'red sequence' (e.g., Faber, 1973) with other cluster galaxies. The color criteria for red sequence candidates were set according to visually identified overdensities in $g - r$ color for each cluster field. We assigned priorities for each targeted galaxy in the following order: 1) impact parameters $\rho < 300$ kpc from the QSO sightline, 2) red sequence candidates with cluster-centric $\rho < 3$ Mpc, 3) non-red sequence candidates with cluster-centric $\rho < 3$ Mpc, 4) red sequence candidates and cluster-centric $\rho > 3$ Mpc, and 5) non-red sequence candidates with cluster-centric $\rho > 3$ Mpc.

The Hectospec observations were taken in queue mode, which enables targeting the field when optimally placed on the sky. A total of 9 configurations were obtained, 3 during Spring 2014 and 6 during Spring 2016. A log of the observations is shown

in Table 4.3, which contains the field identification (named for the targeted cluster), the J2000.0 coordinates, total exposure time and date of observation.

The Hectospec data were reduced using the *HSRED 2.0* pipeline (Cool et al., 2008), which is an ensemble of IDL scripts based on the SDSS pipeline. *HSRED* performs bias, flatfield, illumination, and wavelength calibrations, subtracts the sky background, and extracts one-dimensional spectra. The flux calibration was done using the spectra of 610 stars selected to have SDSS colors consistent with F stars and that are observed simultaneously with the main galaxy sample. The flux calibration correction was obtained combining the extinction-corrected SDSS photometry of these stars with Kurucz (1993) model fits (Cool et al., 2008). These stellar spectra were also used to remove the telluric lines. The spectral range covered by Hectospec allows for the detection of one or more typical emission lines present in the spectra of galaxies ([O II], Hβ, [O III], Hα), for galaxies to $z \sim 1$. The redshifts measured by HSRED also use a code adapted from SDSS and the same templates as SDSS (Stoughton et al., 2002). All spectra were visually inspected for validation as described below.

A redshift quality flag is assigned to each spectrum, following the same procedure used for the DEEP2 survey (Willmer et al., 2006; Newman et al., 2013), where redshift qualities range from Q = 4 (probability P >95% of being correct), 3 (90% < P <95%), 2 (P <90%), and 1 (no features recognized). Q = 2 spectra are assigned to objects for which only a single feature is detected, but cannot be identified without ambiguity. The Q = 3 spectra have more than one spectral feature identified, but tend to have low S/N. The typical confidence levels for these objects is 90% for the DEEP2 galaxies. Finally, Q = 4 objects have two or more spectral features with reasonable to high S/N. The confidence level of these redshifts is typically >95%. Because of the larger spectral range covered by Hectospec (3800-9500 Å) relative to DEEP2 (5000-9500 Å), we expect that the quoted confidence levels are the conservative limits for our spectra. HSRED returns typical redshift measurement errors of $\sigma_z \sim 0.0001$. However, upon

evaluating the dispersion in redshift measurements for several objects with duplicated Hectospec observations, we adopt a more conservative $\sigma_z \sim 0.00055$ ($\sigma_v \sim 165$ km s^{-1}) as our minimum uncertainty.

For the A2246 field, we also include galaxies measured using LDSS-2 on the William Herschel Telescope at the Observatorio del Roque de Los Muchachos. Details regarding the observations and redshift measurement techniques are provided by Bowen et al. (2001).

In the Appendix, we provide all galaxy redshifts obtained through our spectroscopic efforts as well as those included in our analysis from SDSS.

4.3 Cluster Member Galaxies

The optical galaxy spectroscopy obtained in these QSO/fields dramatically expands the breadth and depth of analyses enabled by the X-ray and UV data. The advantages of spectroscopically measured redshifts are many for studies of this kind. First, photometric redshifts provided by the SDSS have typical uncertainties on the order of $z \pm 0.01$, corresponding to velocity uncertainties of thousands of km s^{-1} and cosmological distance uncertainties of $\sim$50 Mpc at $z = 0.2$. In contrast, our spectroscopic redshifts have uncertainties $\delta z \sim 0.0001$, resulting in galaxy velocity uncertainties similar to those of the UV QSO spectra and enabling localization in velocity between individual galaxies and absorption features. Tumlinson et al. (2013) showed that H I absorption systems associated with $\sim L*$ galaxy halos are typically found within $\pm$ 200 km s^{-1} of the galaxy systemic velocities, setting an expected galaxy-absorber velocity separation scale. We note that this velocity scale is smaller than typical cluster velocity dispersions by a factor of a few, and broadband photometric redshifts do not provide sufficient precision. Second, the spectroscopic redshift precision mitigates confusion between legitimate cluster members and distant galax-

ies in the foreground and background. Therefore, the velocity structure of the cluster can be more accurately characterized.

Figure 4.2 shows the distributions of galaxies local to the targeted clusters. WW14 and G16 measured X-ray centroids of these clusters (except for MaxBCG J217.55+24.68), and the cluster redshifts they provide correspond to spectroscopic redshifts for the brightest cluster galaxies (BCGs) identified in cluster catalogs from the literature. Shown in Figure 4.2 are the spectroscopic redshifts from our survey plotted as a function of projected angular separation from the QSO sightlines probing our cluster sample. The red solid horizontal lines mark the cluster redshifts given by WW14 and G16 and the red dashed lines mark the range in redshift of galaxies plotted in Figure 4.1. Histograms of galaxy redshifts in bins of $\Delta z = 0.005$ are also given for each cluster field. Our follow-up survey has dramatically increased the available spectroscopic measurements in these fields; by comparison, all of these clusters are contained within the SDSS footprint, but fewer than 1/8 of the spectra indicated in Figure 4.2 for any field are provided by SDSS. The galaxy overdensities are quite conspicuous about the cluster redshifts and as shown by the histograms on the right of each panel, our survey reveals > 50 cluster member candidates for most fields.

Figure 4.1 shows the spectroscopically measured galaxies from our surveys and the SDSS within $\Delta z = 0.005$ of the BCG cluster redshifts along with the imaged X-ray emission. The green cross in each panel denotes the position of the observed QSO sightline, and the dashed circles demarcate r_{200} from each cluster X-ray centroid as reported by WW14 and G16. Note that A2246 and GMBCG J255.55+64.23 lie at quite different redshifts and are thus shown in separate panels though they fall within the same *Chandra* FOV. Likewise, A1926S/A1926N and MaxBCG J217.55+24.68 are plotted separately due to their widely separated redshifts, and the color scaling for the X-ray emission has been scaled separately to bring out low surface brightness features in each panel.

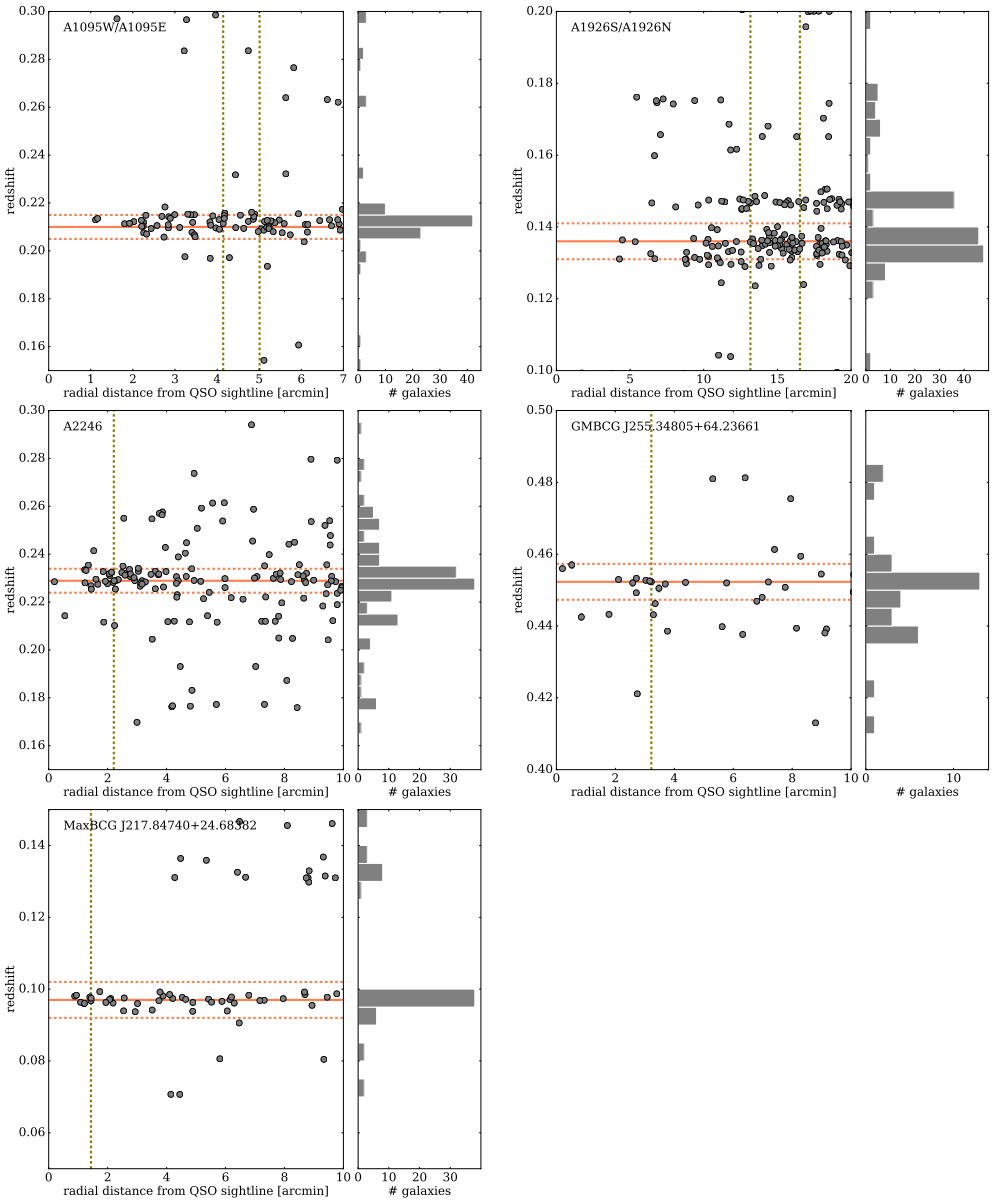

Figure 4.2 Redshifts of spectroscopically measured galaxies as a function of angular separations from the QSO sightlines probing each galaxy cluster. The solid red horizontal lines mark the cluster redshifts as reported by Wang & Walker (2014) and Ge et al. (2016) and are derived from the optically identified BCGs; the only exception is A2246, for which our optical survey measured the redshift of the likely true BCG coinciding with the X-ray centroid. The red dashed horizontal lines mark the redshift range of galaxies plotted in Figure 4.1. The vertical dashed lines mark the projected separations of each X-ray centroid from the QSO sightline. To the right of each redshift map, histograms in bins of $\Delta z = 0.005$ show the redshift distributions of galaxies in each cluster region. Our optical surveys in these regions have increased the number of galaxies with spectroscopic redshifts by more than a factor of 8 in each field.

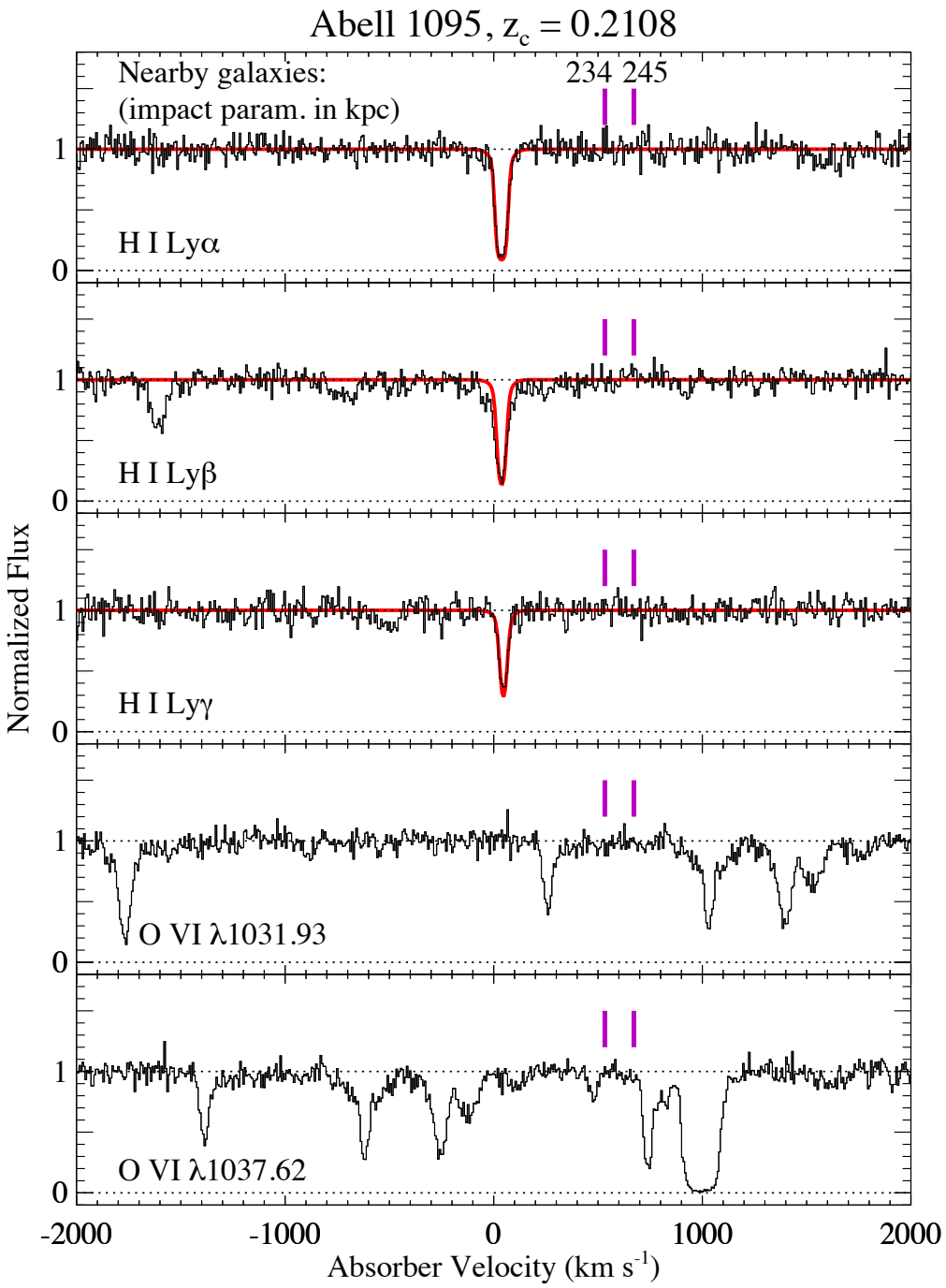

Figure 4.3 The continuum-normalized COS spectrum of SDSS J104741.75+151332.2 showing the H I and O VI transitions covered. The velocity zero point is fixed to the optically derived redshift, z_c, of A1095 given by G16. Voigt profiles fitted to the absorption lines identified within the velocity range shown are plotted in red. Purple hashes mark the velocity offsets of galaxies within 300 kpc of the QSO sightline.

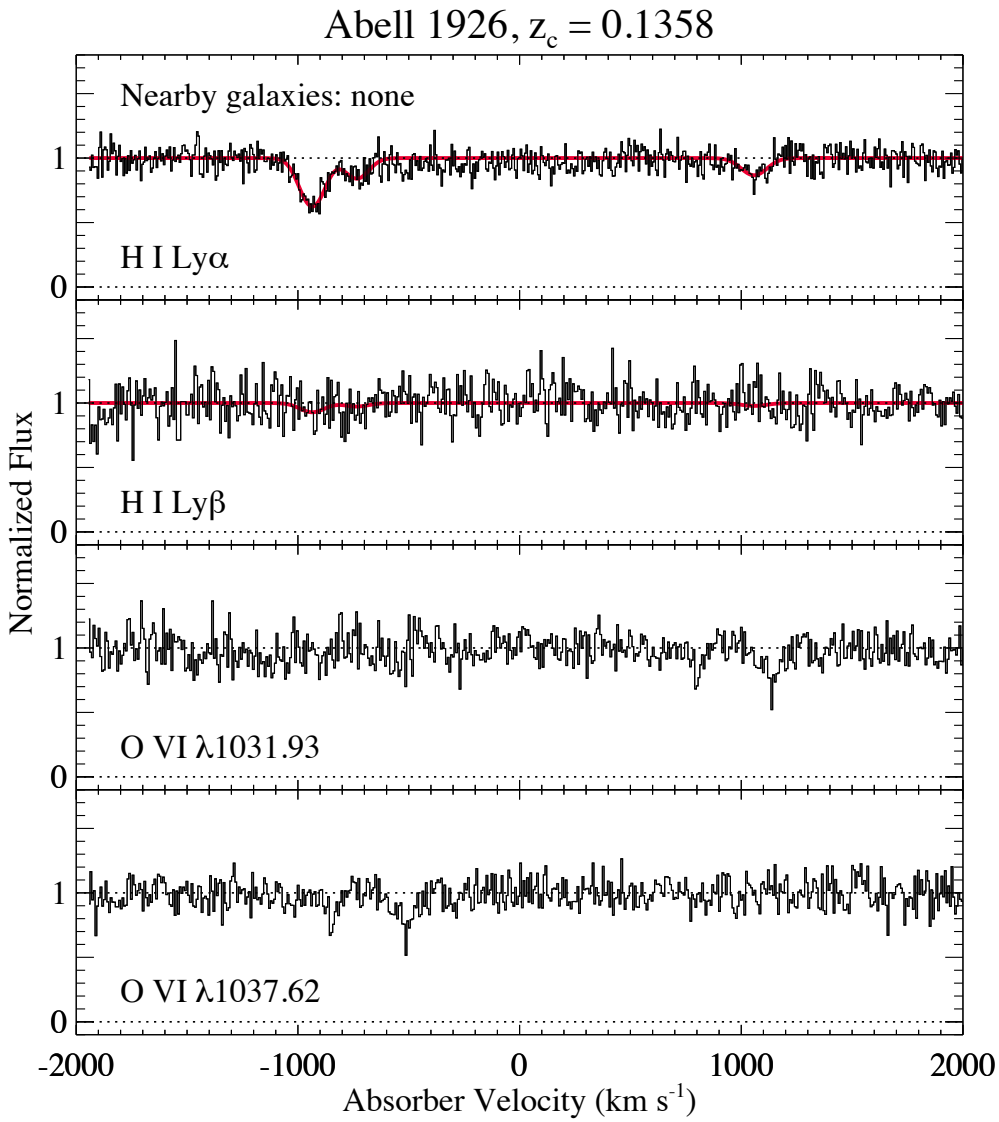

Figure 4.4 The continuum-normalized COS spectrum of 2MASS J1431258+244220 showing the H I and O VI transitions covered. The velocity zero point is fixed to the optically derived redshift, z_c, of A1926 given by G16. Voigt profiles fitted to the absorption lines identified within the velocity range shown are plotted in red.

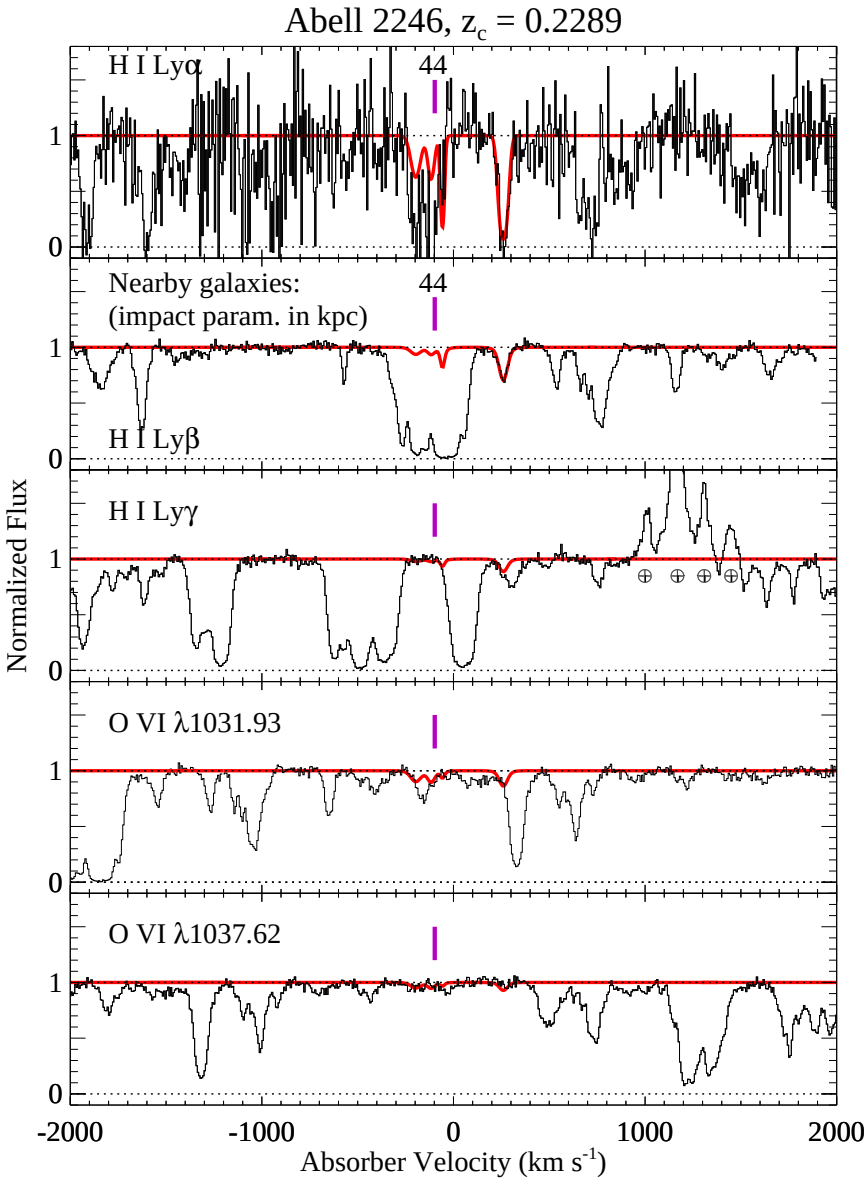

Figure 4.5 The continuum-normalized COS and STIS spectra of HS1700+6416 showing the H I and O VI transitions covered. The velocity zero point is fixed to the optically derived redshift, z_c, of A2246 given by WW14. Voigt profiles fitted to the absorption lines identified within the velocity range shown are plotted in red. Purple hashes mark the velocity offsets of galaxies within 300 kpc of the QSO sightline. Note that the profiles shown between -200 and 100 km s^{-1} were fitted to provide upper limits for the corresponding species; the H I component at approx. +260 km s^{-1} serves as the only unambiguous detection plotted here. Geocoronal emission features in the center panel are labeled with $\oplus$.

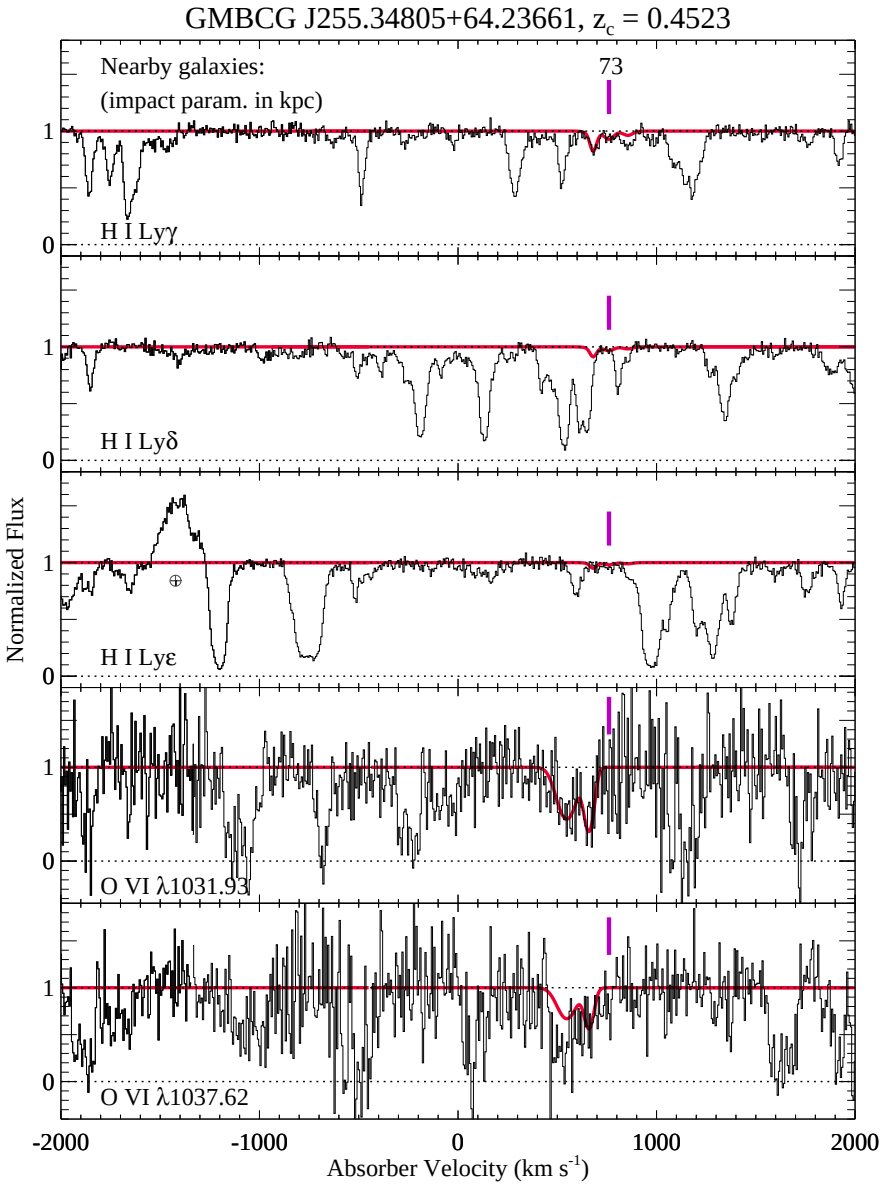

Figure 4.6 The continuum-normalized COS and STIS spectra of HS1700+6416 showing the H I and O VI transitions covered. The velocity zero point is fixed to the optically derived redshift, z_c, of GMBCG J255.55+64.23 given by WW14. Purple hashes mark the velocity offsets of galaxies within 300 kpc of the QSO sightline. Note that the profiles shown in red were fitted to provide upper limits for the corresponding species only. No absorption associated with this cluster was unambiguously detected. A geocoronal emission feature in the center panel is labeled with $\oplus$.

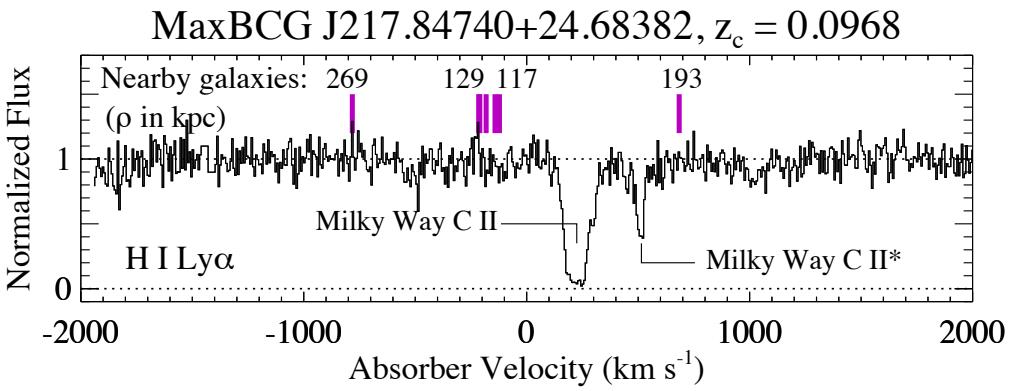

Figure 4.7 The continuum-normalized COS and STIS spectra of 2MASS J1431258+244220 showing the H I Lyα transition. The velocity zero point is fixed to the optically derived redshift, z_c, of MaxBCG J217.55+24.68 given by G16. Purple hashes mark the velocity offsets of galaxies within 300 kpc of the QSO sightline.

We defer to a subsequent publication several in-depth analyses involving the cluster member sample, including inferring the velocity and spatial substructure to compare with the X-ray morphology as well as analyzing the star formation activity in and around the clusters, and primarily focus on the UV absorption herein.

4.4 Results

We now leverage the QSO absorption spectra along with the optical and X-ray data presented above to characterize the CGM in the cluster environment and investigate the warm-hot phase contribution to the ICM. Figures 4.3 - 4.7 show continuum-normalized absorption profiles of H I and O VI transitions covered in our QSO spectra centered about each cluster's redshift (corresponding to $v = 0$). In particular, the redshifts adopted here for $v = 0$ are those spectroscopically measured for the BCG of the corresponding cluster or subcluster with the smallest impact parameter. The red curves show Voigt profiles fitted to species that we report as either detections or upper limits. For the latter cases, possible absorption arises from the species named but is heavily blended with interloping lines from other redshifts (heavy blending precludes secure identification and measurement of H I and O VI, so we conservatively derive

Table 4.4 Voigt profile fitting results for absorbers and limits on potential absorbers within ±600 km/s of cluster galaxy redshifts

Cluster	z_c	log N(H I) [cm^{-2}]	b [km/s]	v [km/s]	Detected lines
A1095	0.2108	14.93 ± 0.03	16 ± 1	36 ± 1	Lyα,Lyβ,Lyγ,Lyδ,Lyϵ
A1926	0.1358	13.66 ± 0.04	69 ± 9	-937 ± 6	Lyα,Lyβ
A1926	0.1358	13.12 ± 0.12	61 ± 24	-736 ± 15	Lyα,Lyβ
A1926	0.1358	13.18 ± 0.11	71 ± 23	1061 ± 16	Lyα,Lyβ
A2246	0.2289	13.97 ± 0.02	25 ± 1	260 ± 1	Lyα,Lyβ,Lyγ
A2246	0.2289	<13.30[1]	-	-197	-
A2246	0.2289	<13.18[1]	-	-116	-
A2246	0.2289	<13.50[1]	-	-57	-
GMBCG J255.55+64.23	0.4523	<14.08[1]	-	681	-
GMBCG J255.55+64.23	0.4523	<13.78[1]	-	761	-
GMBCG J255.55+64.23	0.4523	<13.50[1]	-	856	-

[1] Upper limit on column density derived by fitting Voigt profiles to potentially blended absorption. See Figures 4.5 and 4.6.

upper limits on the maximum H I/O VI absorption allowed by the data). The purple ticks mark relative velocities of galaxies found at small impact parameters to the sightline (see the appendix for additional information on the galaxy-redshift survey).

In Table 4.4, we present the measurements for the H I absorbers we detect and limits where absorption at the cluster redshift is blended with absorption lines from other redshifts. For these possible blends, we fit Voigt profiles to all lines confidently identified in the relevant spectral region and then add components of H I (using as many Lyman series lines as covered) until all of the optical depth was accounted for; in many cases, the absorption is predominantly due to lines from other redshifts, and by using the full set of available lines, we can set useful upper limits on H I and O VI absorption despite the presence of these blends.. We report no unambiguous detections of O VI associated with any of the clusters.

4.4.1 The CGM of Cluster Galaxies

As shown in Figures 4.1 and 4.2, our galaxy surveys in the cluster fields reveal several galaxies at similar redshifts to the galaxy clusters and at small impact parameters. Therefore, we exploit our QSO spectroscopy and galaxy survey data to

produce a sample of galaxy/sightline pairs, for which we can measure the absorption at each galaxy redshift, enabling us to constrain the circumgalactic gas of galaxies residing in the cluster environment.

We begin by searching each sightline's spectroscopic galaxy database for objects with redshifts within $\Delta v < 1200$ km s^{-1} of the redshifts of the clusters probed by that sightline. As all of the clusters probed are expected to have velocity dispersions > 1200 km s^{-1}, we chose our redshift separation criterion to conservatively select galaxies at redshifts consistent with being cluster members. This search produces an initial sample of several galaxies, whose velocities relative their host clusters are labelled in Figures 4.3 - 4.7 by magenta tick marks. In most cases, the impact parameters of the galaxies are listed above the purple tick marks (except in the MaxBCG J217.84740+24.68382 plot, where many galaxies are close to the sightline; in this case, we only indicate the impact parameters of the closest galaxies). Then, we search for absorption associated with these galaxies in the HST/COS spectrum of the background QSO. As we will compare our galaxy cluster CGM sample with the field sample of Prochaska et al. (2011), we adopt a similar galaxy/absorber velocity separation criterion: $|v_{\rm gal} - v_{\rm abs}| \leq 400$ km s^{-1}. We note that the velocity window used by COS-Halos to draw galaxy-absorber associations is larger ($|\Delta v| \leq 600$ km s^{-1}); however, for all of their galaxies with associated absorption at $|\Delta v| \geq 400$ km s^{-1}, they also detect absorption components at $|\Delta v| \leq 400$ km s^{-1}. Unfortunately, line blending with interloping absorption systems from different redshifts hampers stringently imposing these criteria. We therefore detail the galaxy/absorber sample selection for each cluster individually below. Our analysis will focus on galaxy/absorber associations with impact parameters $\rho < 300$ kpc; A1926 is the only cluster without spectroscopically confirmed galaxies within this impact parameter range. We adopt $W/\sigma_W > 3$, where W and σ_W denote the equivalent width and its error, respectively, as our criterion for statistically significant absorption detections. Our CGM absorber

measurements are collected in Table 4.5.

A1095: We detect galaxies with impact parameters 234 and 245 kpc. No H I or O VI absorption features arise in the QSO spectrum within 400 km s^{-1} of these galaxies' redshifts (see Figure 4.3, although a narrow H I component does lie at $\Delta v \sim 500$ km s^{-1} from the galaxy at $\rho = 234$ kpc. Due to the large velocity separation, we do not consider this absorber to be associated with either of the two galaxies, although we do offer an alternative explanation for it's origin in Section 4.5.2. As no absorption was associated with these galaxies, we measured 3σ upper limits on the column density using the apparent optical depth method (AODM; Savage & Sembach, 1991) at their redshifts.

A2246: A galaxy is detected with $\rho = 43$ kpc as is one unambiguous H I component at $\delta v \sim 350$ km s^{-1}. As the sightline probing A2246 and GMBCG J255.55+64.23 is that of a relatively high redshift QSO, many interloping systems appear in the spectral regions of interest. To place upper limits on H I affiliated with the galaxy at $\rho = 43$ kpc, we used our Voigt-profile fitting software to determine the maximum amount of H I absorption that is *jointly* allowed by the Lyα , Lyβ, Lyγ, Lyδ, and Lyϵ profiles. Comparison of these profiles revealed a clear detection of H I at $v =$ 460 km s^{-1} (indicated by fully consistent absorption lines of Lyα and Lyβ, which are not blended at this velocity, and corroborated by consistent optical depth in the higher Lyman series lines) with log N(H I) $= 13.97 \pm 0.02$ cm^{-2}. The rest of the absorption within $\pm$600 km s^{-1} of this galaxy is *not* consistently present in the various Lyman series lines and therefore is at least partially due to absorption lines at other redshifts, but some affiliated H I could be hidden in these nearby absorption blends. To determine how much H I could be hidden in these blends, we iteratively explored models with one to several additional components, and we found that we obtained a

maximal increase in H I with three additional components that would contribute an additional H I column density of log N(H I) = 13.83 cm^{-2}. We emphasize that due to blending, the three additional components cannot be securely attributed to H I but are not ruled out by the data. Thus, we conservatively state that the H I column is at least log N(H I) = 13.97 cm^{-2} and could be as high as log N(H I) = 14.20 cm^{-2}. For O VI, none of the absorption shows the velocity spacing and relative strengths of the O VI doublet. There are several features near the expected wavelength of the O VI 1031.92 line, but the the O VI 1037.62 line falls in a relatively clean region. Assuming that the O VI has a similar component structure to the H I (as is often observed in O VI absorbers, Tripp et al., 2008), we derive log N(O VI) $<$ 13.80 cm^{-2} from the joint constraints provided by both lines of this doublet.

GMBCG J255.55+64.23: We detect one galaxy at 73 kpc. Like A2246, this cluster is probed by the HS1700+6416 sightline, and similar line blending issues arise. Unlike, A2246, no unambiguous H I is identified near the redshift of GMBCG J255.55+64.23. Some very weak components may be present near the redshift of the detected galaxy, but these cannot be verified and we use a similar Voigt profile fitting procedure as that for A2246 above to place upper limits for H I and O VI.

MaxBCG J217.55+24.68: This cluster provides several galaxies within our impact parameter selection range but introduces complications due to line blending as well. Unfortunately, Lyα is the only H I line covered in the COS bandpass due to the lower redshift of this cluster, and O VI is also not covered. Also, the strong C II and C II* profiles from our own Galaxy fall very near the would-be location of Lyα at the cluster redshift. The redshifts of several galaxies close to the sight line would place their Lyα lines directly on top of the MW ISM C II/C II* lines if the Lyα lines are exactly at the galaxies systemic velocities. Since the Galactic C II is saturated, it

would be difficult to recognize the Lyα lines if this were the case. Of course, affiliated absorption is not necessary exactly at the a galaxy's systemic redshift, and we would detect Lyα from these galaxies at other velocities, but to be conservative we omit these galaxies from the CGM/absorber sample CGM galaxy/absorber sample, keeping only those shown at $v_{\rm abs} < 0$ km s^{-1} at $v_{\rm abs} > 600$ km s^{-1} in Figure 4.7. We have identified the weak absorption feature seen at $v_{\rm abs} \sim -600$ km s^{-1} in Figure 4.7 as Lyδ at $z = 0.3686$ (the corresponding Lyβ is also covered and detected with a proportionately strong profile). Although we concede that Lyα absorption could arise at $v_{\rm abs} - v_{\rm gal} \leq 400$ km s^{-1} from those galaxies we have kept in our sample, this absorption would be blended with the Milky Way lines and have have likelier associations with those galaxies we have omitted. Again, 3σ upper limits are derived by AODM at the redshifts of each galaxy remaining in our sample. One galaxy at $z \sim 0.0963$ yielded $W/\sigma_W \sim 3.25$ when integrating over $v \pm 50$ km s^{-1} about its redshift, and the H I measurement for this galaxy in Table 4.5 reflects the integrated apparent column density and its error.

Figure 4.8 shows the resulting N(H I) as a function of QSO-galaxy impact parameter constructed from our cluster CGM sample and two surveys from the literature, COS-Halos (Tumlinson et al., 2013) and Prochaska et al. (2011). The H I absorption appears to be highly suppressed in the CGM of our cluster galaxies relative to the literature data. For the eleven galaxies shown here, we detect H I absorption with $\rho < 300$ kpc of only two. For our detection limits $W_{\rm lim} > 30$ mÅ, we report a covering fraction of f(H I) $= 18^{+14}_{-9}$% at $\rho < 300$ kpc of our cluster galaxies.

We also searched for O VI absorption in the CGM of these same galaxies for which the $\lambda\lambda$ 1032, 1038 Å O VI transitions fall within the COS bandpass at the galaxy redshifts. While H I is covered for all five cluster systems considered in this

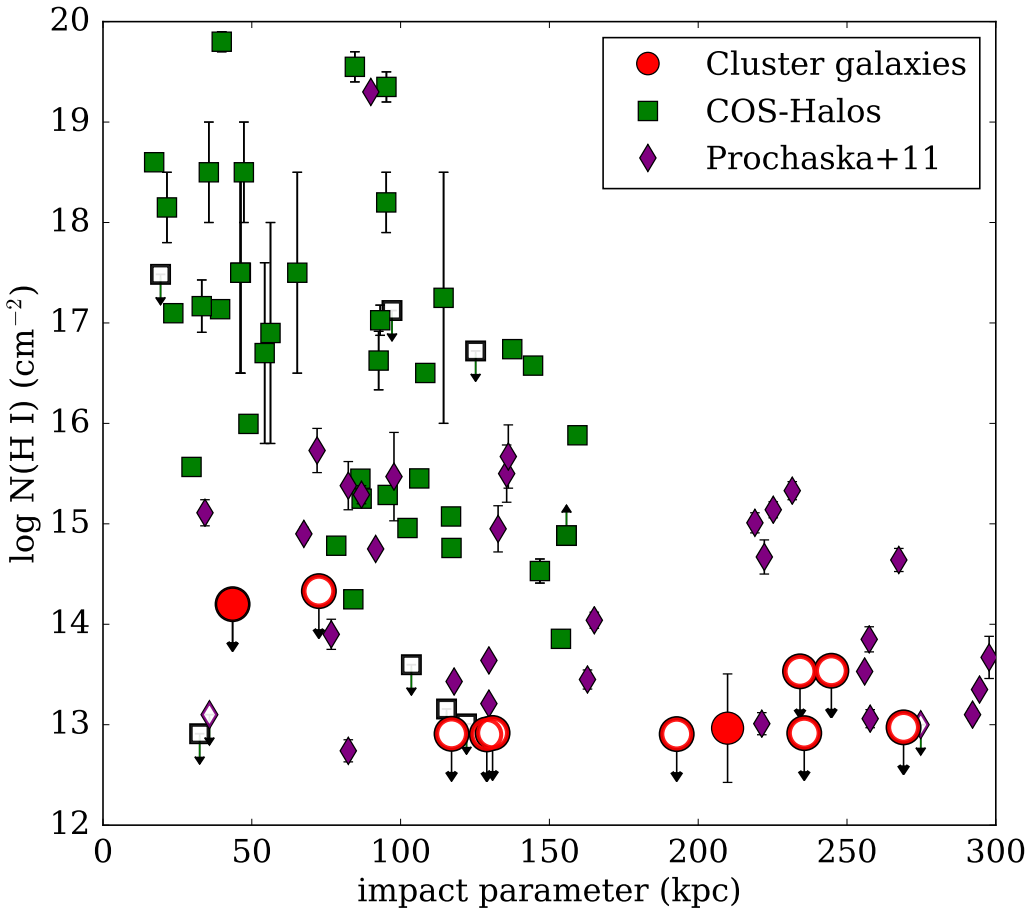

Figure 4.8 The H I column densities measured in our cluster galaxies' CGM compared with field galaxy CGM measurements from the literature. The red circles denote cluster galaxies from our sample, while the green and purple points correspond to CGM measurements of field galaxies. All upper limits (open symbols) are 3σ. The filled symbol with a downward arrow corresponds to the unambiguous plus possibly blended H I absorption for the galaxy in A2246. The column densities and galaxy information for our cluster galaxy sample may be found in Table 4.5.

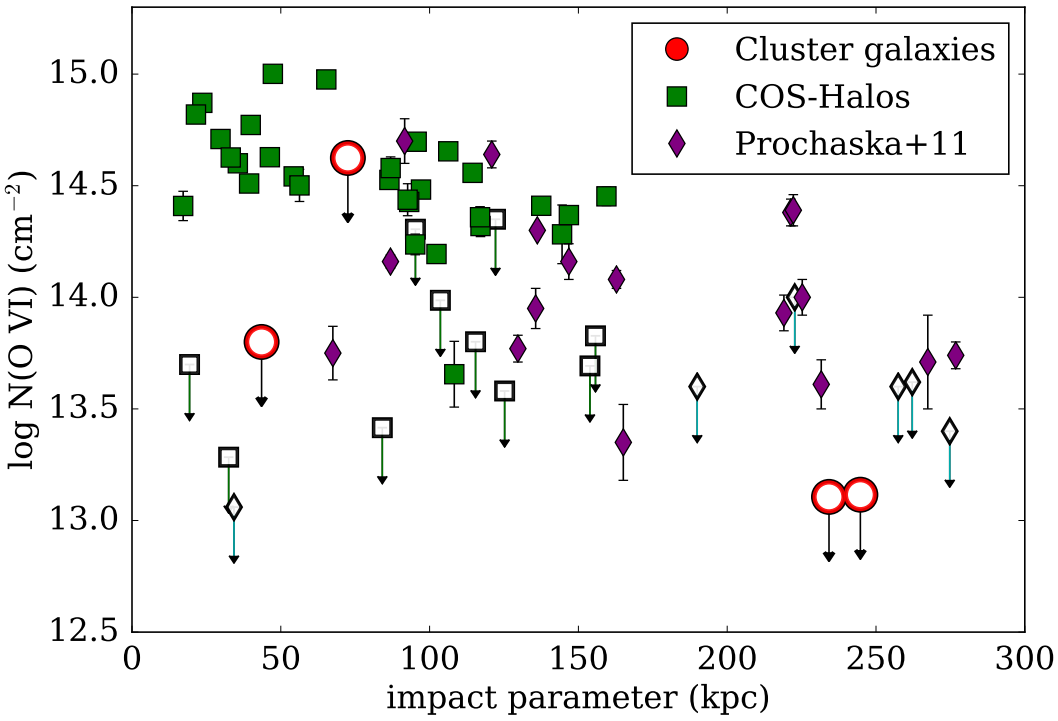

Figure 4.9 The O VI column densities measured in our cluster galaxies' CGM compared with field galaxy CGM measurements from the literature. The red circles denote cluster galaxies from our sample, while the green and purple points correspond to CGM measurements of field galaxies. All upper limits (open symbols) are 3σ. The column densities and galaxy information for our cluster galaxy sample may be found in Table 4.5.

Table 4.5 Column densities of H I and O VI associated with individual cluster galaxies

Cluster	$z_{\rm gal}$	ρ [kpc]	log N(H I) [cm^{-2}]	log N(O VI)
MaxBCG J217.55+24.68	0.0939	269	<12.97	-
MaxBCG J217.55+24.68	0.0960	129	<12.90	-
MaxBCG J217.55+24.68	0.0993	193	<12.91	-
MaxBCG J217.55+24.68	0.0964	117	<12.91	-
MaxBCG J217.55+24.68	0.0961	236	<12.92	-
MaxBCG J217.55+24.68	0.0960	131	<12.92	-
MaxBCG J217.55+24.68	0.0963	210	12.97 ± 0.54	-
A1095	0.2130	234	<13.53	<13.11
A1095	0.2135	245	<13.54	<13.12
A2246	0.2285	44	<14.20[1]	<13.80
GMBCG J255.55+64.23	0.4560	73	<14.33	<14.62

[1] Upper limit includes the column density of unambiguously detected H I and any possible contribution of H I to nearby blended absorption features

work, O VI is only redshifted into the bandpass for four of them, producing a CGM O VI sample of only four galaxies. A2246 contains a galaxy at $z = 0.22849$ and impact parameter of $\rho = 43$ kpc; GMBCG J255.55+64.23 contains one at $z = 0.45599$ and $\rho = 72$ kpc. The QSO spectrum corresponding to A2246 and GMBCG J255.55+64.23 (HS1700+6416; Figures 4.5 and 4.6), being of a high-redshift QSO sightline that is heavily populated with absorption features, shows several interloping lines from different redshifts but no unambiguous O VI features within ±400 km s^{-1} of the galaxy redshifts. The combined constraints from both lines of the doublet only allow very weak O VI lines near the redshift of the A2246 galaxy, and none of the data provide compelling evidence of any O VI. We establish an upper limit on N(O VI) for the A2246 galaxy by fitting Voigt profiles to the complexes of absorption at the would-be locations of O VI assuming that the O VI and H I components potentially associated with this galaxy have the same velocity structure. For the GMBCG J255.55+64.23 galaxy, we find that a substantial amount of O VI could be hidden in nearby blended features, but there is no H I at the velocities of those features. To derive a conservative upper limit, we allowed the possibility that the O VI and H I are decoupled in this

environment, and we used component fitting to determine the maximal amount of O VI that could be hidden in those blends. The resulting Voigt profile model that provides this upper limit is indicated by the red line in the lower two panels of Figure 4.6, and we report the sum of column densities from these models as the upper limit. A1095 is the remaining cluster with galaxies $\rho < 300$ kpc from the sightline and also contains no unambiguous components of O VI. These data are plotted alongside the COS-Halos (Tumlinson et al., 2011) and Prochaska et al. (2011) samples in Figure 4.9.

4.4.2 The Warm-hot Gas Content of Galaxy Clusters

As found by G16, the baryonic mass within r_{500} accounted for by stars and X-ray emitting gas is approximately 9% and 10% of M_{500} in the subclusters of A1926 and A1095, respectively. These measurements fall short of the Universal baryon fraction, 16.6% (Bennett et al., 2013), potentially signaling that the clusters may contain some fraction of their gas in some other phase. Most of our QSO sightlines piercing the ICM of these clusters fall beyond r_{500}, but the impact parameter of A1095W is approximately equal to r_{500}. The spatial coincidence of our detected X-ray emission and the QSO spectra enable a unique opportunity to directly constrain the relative contributions of gas in the hot phase from X-rays and in the warm-hot phase from the QSO data, particularly in the poorly constrained regions beyond r_{500}.

4.4.2.1 Diagnostic: O VI

The $\lambda\lambda$ 1032,1038 Å O VI doublet is the most frequently used tracer of 10^{5-6} K gas, and we designed our experiment such that the COS G130M grating would cover the O VI doublet at the redshifts of A1095, A1926, and A2246. O VI shifts into the COS/G130M bandpass at approximately $z \sim 0.1$ and is therefore covered by our data at the redshift of GMBCG J255.55+64.23 but not for MaxBCG J217.55+24.68.

As seen in Figures 4.3 - 4.7, no significant, unambiguous O VI features are detected within 1500 km s^{-1} of the cluster redshifts.

4.4.2.2 Diagnostic: Broad H I

In addition to O VI, warm-hot gas may also be detected as thermally broadened spectral features, most notably H I Lyα (broad Lyα or BLA; e.g., Lehner et al., 2007). The line broadening of the Voigt profile is parameterized by the Doppler b value. In general, the b value contains both thermal and nonthermal contributions. The thermal contribution is simply related to the gas temperature through the kinetic energy of the gas particles:

$$b_{th} = \sqrt{\frac{2kT}{m}} = 0.129\sqrt{\frac{T}{A}} \text{ km s}^{-1} \tag{4.1}$$

where k is the Boltzmann constant, T is the gas temperature, and m and A are the particle mass and atomic mass number, respectively, of the species responsible for the absorption. The rightmost expression corresponds to temperatures measured in Kelvin and yields units of km s^{-1}. Therefore, gas at the temperatures of interest ($10^5 - 10^6$ K) has corresponding b values of 40-150 km s^{-1} for hydrogen. Non-thermal contributions may arise from turbulence or bulk motions; furthermore, unresolved blends of narrow components can mimic broad features. For our conversions between Doppler b and temperature, we assume a nonthermal contribution of 30% to the line width from turbulence as measured by Hitomi Collaboration et al. (2016) in the Perseus cluster[7]. Despite the intrinsic strength of Lyα , line broadening will make gas

[7]The *Hitomi* satellite obtained a high-resolution spectrum in the Perseus cluster ICM, enabling simultaneous measurements of the plasma temperature and widths of emission lines from Fe. From these Fe lines, they measure a line of sight velocity dispersion due to turbulence of 164 ± 10 km s^{-1}, having removed a thermal contribution of 80 km s^{-1}. Scaling this thermal velocity to that expected for hydrogen nuclei (the dominant species) via the atomic masses of Fe and H (cf. Equation 1) yields a thermal velocity of ~ 600 km s^{-1}, of which the turbulent contribution $\sim 30\%$.

of a given column density more difficult to detect, hampered by both the decreased optical depth per resolution element and uncertainty of the continuum placement.

Our COS data cover Lyα for A1095 and A1926 and Lyβ for A2246. For A2246, Lyα is covered by the archival STIS spectrum of HS1700+6416, albeit at much lower S/N than the COS data for the other sightlines. We detect BLA features in the QSO spectrum probing one cluster: A1926 (Figure 4.4). The features are well-fit by Voigt profiles at velocities $v = -937$, -736, and 1061 km s^{-1} relative to the adopted cluster redshift. The resulting b values for these components are 69 ± 9, 61 ± 24, and 71 ± 23 km s^{-1}, which correspond to temperatures of log T = 5.1, 5.0, and 5.2 K, respectively.

Because the line broadening can be significant at the temperatures we are interested in probing with the QSO spectroscopy, we wish to constrain, as a function of temperature, the absorbers to which our study is sensitive. In practice, determining the statistical significance of a spectral feature involves fitting a continuum, measuring the equivalent width of the feature and the uncertainty in this measurement, and taking the ratio of the equivalent width and its uncertainty. Statistical uncertainties arise from both the optical depth of the line relative to the noise of the data and the shape of the fitted continuum. Fitting a continuum requires choosing line-free segments of the spectrum blueward and redward of the desired feature to be measured, introducing considerable systematic uncertainty given the combination of low-frequency undulations that are empirically known to exist in QSO spectra and the possible presence of substantially broadened absorption lines. While the uncertainty in the continuum can be characterized given sufficient knowledge of line-free regions (Sembach & Savage, 1992), the systematic uncertainty from the probably false assumption that these regions are free of lines is extremely difficult to quantify.

However, the parameter space of detectable absorbers can be somewhat constrained using the idealized scenario where a) the continuum is well behaved (i.e., free of undulations in the region of the spectrum where the BLA is to be measured)

and b) the line-free regions are clearly selected on either side of the BLA. Indeed, calculating the detection significance of BLAs as a function of column density and b value under these idealized circumstances will identify a class of absorbers that are completely undetectable at a given S/N level. To do so, we conduct a simulation experiment as follows: First, we generate Voigt profiles over a grid of column densities, log N(H I) = $11 - 16$ cm^{-2}, and b values that correspond to temperatures log T $\sim 4 - 6$ K. Then, we inject each absorber onto a flat continuum, convolve with the COS line spread function, and add Gaussian noise commensurate with the S/N levels in our data at the locations of Lyα lines with redshifts equal to the galaxy clusters they probe. Using the formalism of Sembach & Savage (1992), we fit a continuum declaring two line-free regions on either side of the injected absorption line (with centroid λ_O): between the blue edge of the simulated 'spectrum' (λ_O -10 Å) and $\lambda_O - \frac{2b}{c}$ and between $\lambda_O + \frac{2b}{c}$ and the red edge of the spectrum, where c is the speed of light. Finally, we measure the equivalent width of the line (W) and the uncertainties from both the noise in the flux (σ_{W_f}) and that due to the uncertainty from the continuum placement (σ_{W_c}; Sembach & Savage, 1992). For each simulated absorber, the detection significance is then

$$S = \frac{W}{\sqrt{\sigma_{W_f}^2 + \sigma_{W_c}^2}} \tag{4.2}$$

where W, σ_{W_f}, and σ_{W_c} are all measured over velocity widths of $dv \in [-b/2, +b/2]$.

Figure 4.10 shows the detection significance of simulated absorbers across the full grid of N(H I) and b values. In absorption line studies, typical thresholds for detection are $3 - 5\sigma$, and Figure 4.10 shows that the absorber column densities that may be detected *even given the idealized continuum placement conditions* increases by ~ 0.5 dex across the range of b values (corresponding to log T $\sim 4 - 6$ K assuming purely thermal line broadening). Thus, in terms of column density, the *maximum* sensitivity drops by more than half across this temperature range. Furthermore, the

uncertainty in continuum placement will only exacerbate the decreased sensitivity to higher temperature gas. Lastly, we assessed the likelihood of noise features mimicking BLA absorption through a similar experiment but without injecting synthetic line profiles. We confirm that the false positive rate of purely Gaussian noise producing significant BLA-like features is $< 0.01\%$; therefore, the dominant source of error is most likely the continuum placement uncertainty.

4.4.2.3 The relative baryon contributions of the hot and warm-hot phases

We now quantify the amount of gas in the 10^{5-6} K warm-hot phase along the line of sight probing A1926 to place in context with that derived by G16 for the $> 10^7$ K hot phase. Using the column densities of H I measured by Voigt profile fitting, we convert to total H column density (N(H^+) + N(H I)) using an ionization correction. We employ here the Oppenheimer & Schaye (2013) ionization models evaluated at a metallicity of Z = 0.3 $Z_\odot$ and total hydrogen density of $n_H = 10^{-4}\mathrm{cm}^{-3}$. These models feature photoionization equilibrium (although we also experimented with their nonequilibrium photoionization models and find that this added effect did not change our results) and assume that the gas is cooling from an initial temperature of 10^7 K. We adopt the models run with a Haardt & Madau (2012) ionizing photon background evaluated at $z = 0.2$. The ionization corrections we derived were insensitive to these model parameter choices, deviating by ~ 0.05 dex.

The Oppenheimer & Schaye (2013) models provide ion fractions as function of temperature for the ionization states of several species. We calculate N(H) as

$$N(H) = \frac{\mathrm{N(H\ I)}}{\chi_{H\ \mathrm{I}}(T, n_H, Z, z)} \tag{4.3}$$

where $\chi_{H\ \mathrm{I}}$ is the ionization ratio $\mathrm{n}_{H\ \mathrm{I}}/\mathrm{n}_H$ and the other parameters are set as above.

In Figure 4.11, we present the total column density of hydrogen resulting from this calculation for the three broad Lyα components associated with A1926 and

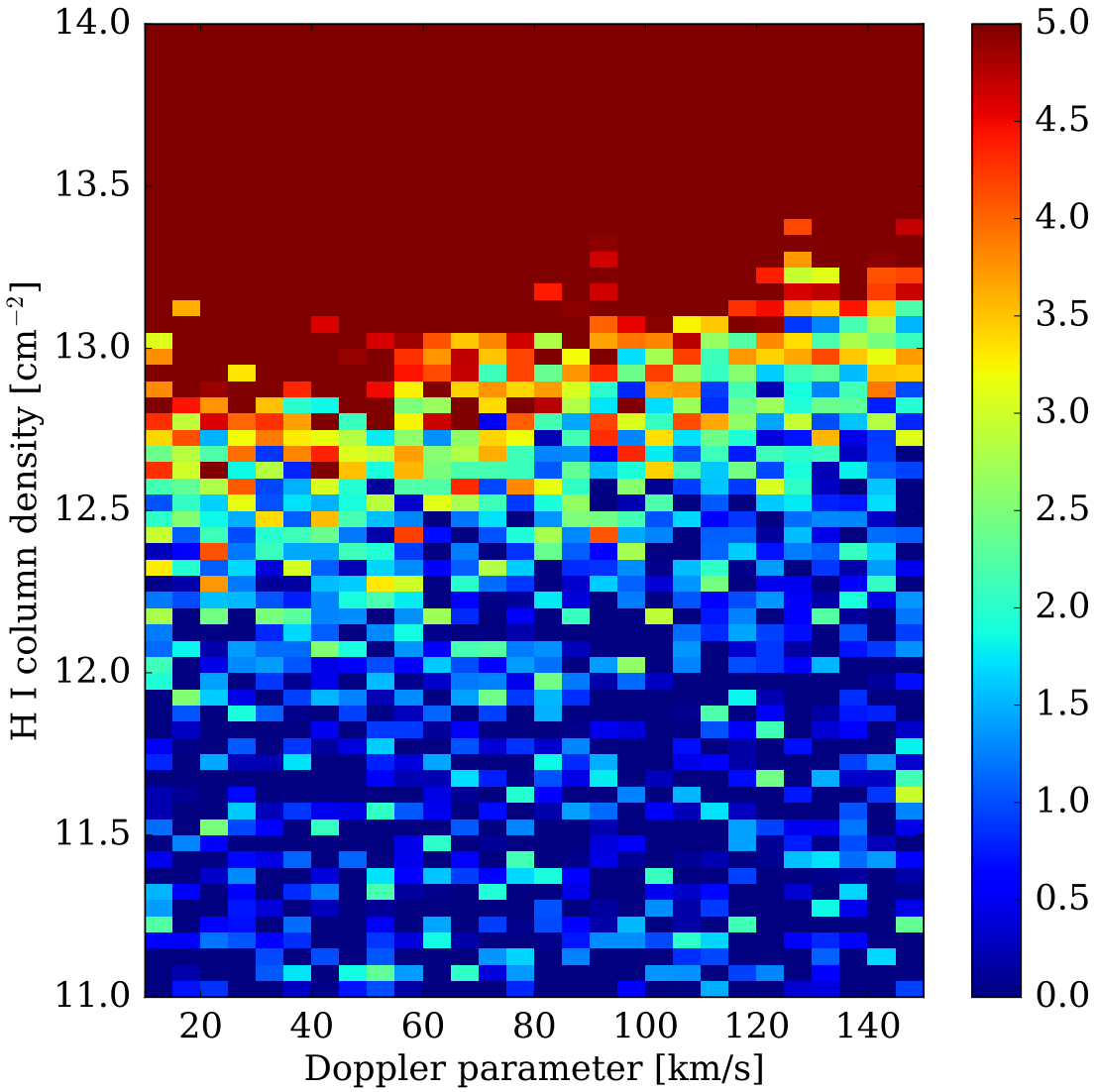

Figure 4.10 Detection significance of idealized simulated Lyα absorbers (see color bar on right) as a function of N(H I) and b value where the noise of the simulated spectrum is commensurate with those probing A1095 and A1926 in our sample. For a given column density N(H I) $> 10^{12.5}$ cm^{-2}, absorption features become less detectable with increasing Doppler parameters. Adopting a significance threshold of $3-5\sigma$, the column density sensitivity decreases by 0.5 dex over the range of Doppler parameters shown, which correspond to temperatures log T $\sim 4-6$ K assuming pure thermal broadening.

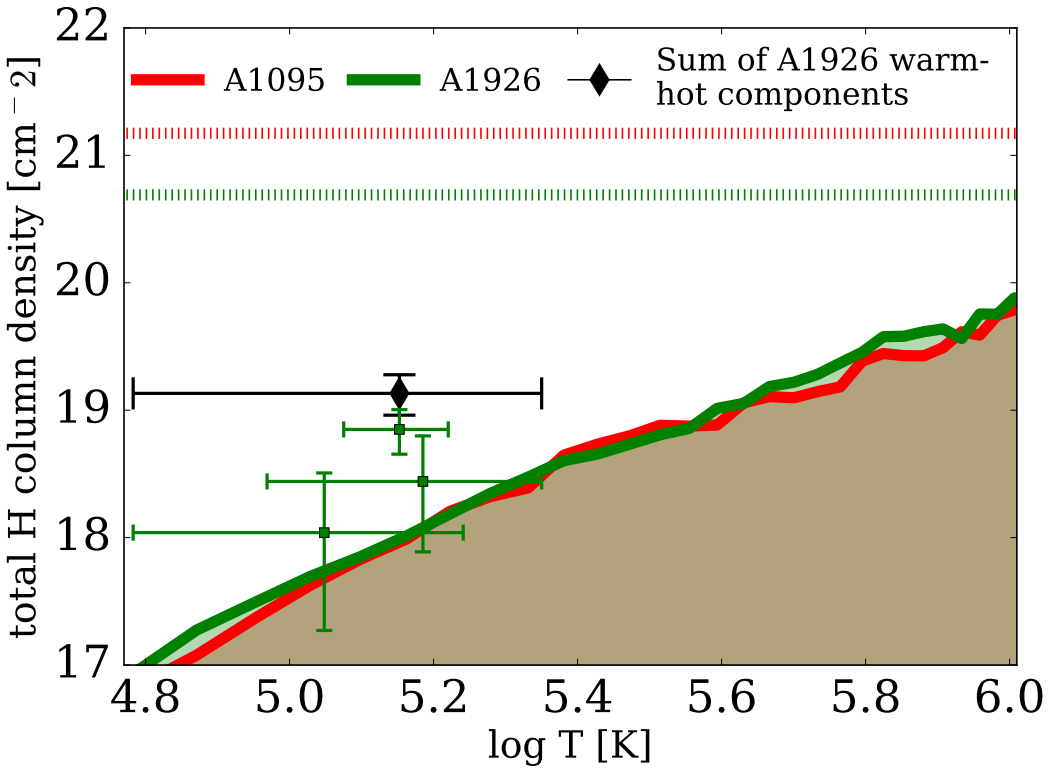

Figure 4.11 The contributions of the warm-hot and hot gas phases to the total hydrogen column density (N(H) = N(H I+ H II)) along the QSO sightlines probing A1095 and A1926 as a function of temperature. The red and green dashed lines mark the $> 10^7$ K hot gas contributions to N(H) for A1095 and A1926, respectively, measured at the locations of the QSO sightlines by G16. The green points with error bars correspond to the 3 Lyα components detected near the redshift of A1926 in the UV spectrum of 2MASS J1431258+244220. The red and green lines and shaded regions below them depict the limits on N(H) from potentially detectable (but undetected in the actual data) BLA absorbers given the idealized conditions described in Section 4.4.2.2. Given the idealized nature of our experiment, the true upper limits would be higher (see Section 4.4.2.2), thus potentially hiding significant columns of warm-hot gas. The black diamond with error bars shows the summed contribution from the BLAs detected near A1926 with derived temperatures $T = 10^{5-6}$ K.

reported in Section 4.4.2.2 (green points with error bars), the contribution measured from the X-ray emitting gas in G16 (dashed lines), and the limits placed on the total H column using the idealized simulated absorption (green and red solid lines and shaded regions) as described in the previous section. The bold, black diamond and error bars represent the sum of the three components whose Doppler b-values suggest gas temperatures of 10^{5-6} K, N(H) $\sim 10^{19}$ cm^{-2}.

By comparison, the total warm-hot gas detected in the BLA absorbers associated with A1926 (black marker in Figure 4.11) amounts to approximately 3% of that in the hotter phase traced by X-rays. We note that the warm-hot material may also additionally photoionized by the radiation emitted by the nearby 10^7 K gas, which would further decrease $\chi_{H\ \textsc{i}}$ and increase the derived N(H) in the warm-hot phase, but these photon contributions are not included in our modeling. Because of the continuum and flux uncertainties described in Section 4.4.2.2, more warm-hot material may reside in undetectable lower-column density clouds. In fact, we caution that the limits represented by shaded regions in the Figure 4.11 underestimate the true limits due to the idealized nature of our absorption experiment. Particularly with the systematic continuum placement uncertainty involved in choosing line-free regions to fit continuua, the detectability of weaker BLAs in actual QSO spectra can also depend on the spectral region of interest being fortuitously flat.

These uncertainties notwithstanding, the warm-hot phase may only represent a significant contribution to the baryon budget in the outer regions of A1926 if a large mass of the material is actually at log $T > 5.5$ K, with broad lines that are extremely difficult to detect. We emphasize that the BLA features we detect lie at velocities $\Delta v \sim \pm 1000$ km s^{-1} relative to the cluster redshift. While these velocities are consistent with the velocity dispersion of an $M_{200} > 10^{14}\ M_\odot$ cluster, they would correspond to distances of > 14 Mpc if due to pure Hubble flow. Assuming that these absorbers are associated with A1926, the velocities may be an important clue that

the absorbing gas is falling into the cluster. We return to this point in Section 4.5.2 for further discussion.

4.5 Discussion

4.5.1 A continuum of environmental impacts on the CGM

In Section 4.4.1, we have presented evidence that the CGM of galaxies in our cluster sample has been stripped or has become sufficiently heated and ionized such that the column densities of neutral hydrogen fall well below measurements reported for galaxies in less dense environments. Previous studies have also reported environmental effects on the CGM, and we now place our results in context with their findings.

Yoon et al. (2012) and Yoon & Putman (2013) employed a sample of QSO sightlines that pierce the nearby Virgo cluster and are perhaps the most directly comparable studies to ours. Yoon et al. (2012) reported statistics of Lyα absorbers relative to the cluster as a whole and find that the covering fractions of strong Lyα absorbers ($>$ 100 mÅ) are lower within 1 r_{vir} of the cluster (60^{+16}_{-13}%) than from 1-2 r_{vir} (100_{-14}%), suggesting that the physical conditions inside the cluster virial radius are such that the neutral gas content is suppressed, likely shock-heated and ionized. Yoon & Putman (2013) studied associations between Lyα absorbers and individual cluster galaxies and report significantly lower covering fractions of Lyα around individual galaxies within 1 r_{vir} of Virgo than galaxies in the field. Using a similar velocity cut as we used in Section 4.4.1 and that of Prochaska et al. (2011), they find $f_c = 39^{+14}_{-12}$% for their cluster galaxies within 1 r_{vir} of Virgo. Their result is within the errors of the covering fraction we report in Section 4.4.1 ($f(\mathrm{H\ I}) = 18^{+14}_{-9}$%). In Figure 4.12, we show the covering fractions both from our sample (orange) and as a result of combining the Yoon & Putman (2013) sample with ours (red) in two bins of impact parameter. Here, we have imposed the same 100 mÅ equivalent width limit as Yoon

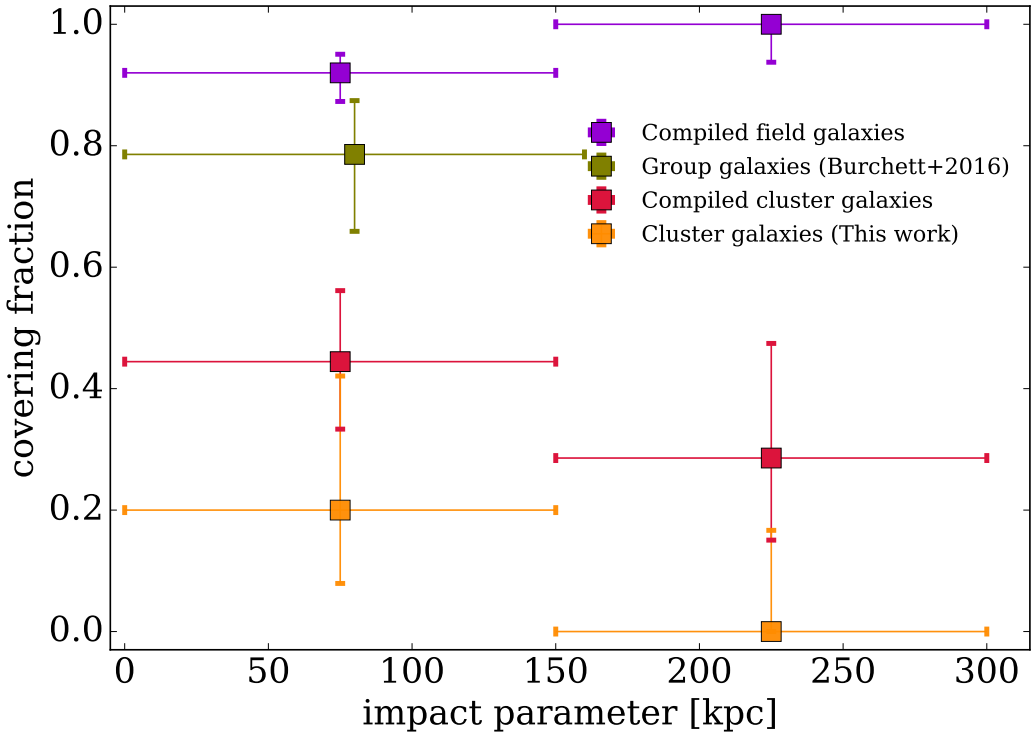

Figure 4.12 Covering fractions of H I in the CGM, calculated in bins of impact parameter indicated by the horizontal lines, of galaxies across various environments. Shown are a field galaxy sample (purple) combining those of Tumlinson et al. (2013), and Prochaska et al. (2011), galaxies in group environments (green) from Burchett et al. (2016), a cluster sample (red) combining this work and that of Yoon & Putman (2013), and the data from this work alone (orange). For comparison, we have imposed the same 100 mÅ detection threshold as Yoon & Putman (2013) for our covering fraction measurement. The cluster galaxies show markedly lower covering fractions than those of field galaxies. However, galaxies in groups may lie between these two populations, perhaps having undergone intermediary levels of the stripping/heating processes that remove the H I from cluster galaxy halos.

& Putman (2013); their galaxy-absorber velocity association criterion ($|\Delta v| < 400$ km s^{-1}) matches that employed here and by Prochaska et al. (2011). While our measurements are not discrepant with Yoon & Putman (2013) at any statistical significance, one may expect their sample to have an intrinsically higher covering fraction due partly to sample selection: they adopt R_{100} as r_{vir} and include galaxies within this projected boundary. All of our associated galaxy/sightline associations lie projected within r_{200}.

However, another intriguing comparison arises with the CGM of galaxies in groups. Figure 4.12 shows the covering fraction of *H* I associated with a sample of group galaxies from Burchett et al. (2016, plotted in green). The group galaxies exhibit an H I covering fraction intermediate to the cluster and field samples, suggesting that the processes removing the CGM H I from cluster galaxies set in with progressively higher efficiency as the environmental density increases. Burchett et al. (2016) used a fixed-aperture density metric to quantify galaxy environment (see their Figure 6), and we are including the galaxies from their sample with 5 or more $L > 0.1\ L*$ neighbors within 1.5 Mpc and 1000 km s^{-1} as 'group galaxies'. According to the assessment by Muldrew et al. (2012) of several environmental metrics, this parameter choice should conservatively select group-sized halos ($M_{\rm halo} > 10^{13}\ M_{\odot}$) in the sense that many lower-mass halos are also likely to be included. Given that more isolated galaxies have near-unity H I covering fractions, the inclusion of galaxies in less-massive halos should increase the covering fraction; indeed the non-detections of H I in the Burchett et al. (2016) sample all occur at densities > 10 galaxies per 1.5 Mpc aperture, and cutting at higher densities than we have chosen would yield an even lower H I covering fraction and thus all the more discrepant with that of the field galaxies. At impact parameters < 350 kpc, Wakker & Savage (2009) also found a lower covering fraction of Lyα absorbers around group galaxies than field galaxies, $61 \pm 17\%$ and $100_{-37}\%$, respectively. In addition to the differences in absorber-galaxy impact pa-

rameters, their group identification/membership scheme differs from that employed by Burchett et al. (2016) and we caution against direct quantitative comparison of the two results. However, the Wakker & Savage (2009) result qualitatively agrees that the Lyα covering fraction lies between that of clusters and field galaxies.

Few instances of ram pressure acting in groups have been observed directly (e.g., Rasmussen et al., 2006; Freeland & Wilcots, 2011). Several studies, observational and theoretical, have examined galaxy quenching in groups to better constrain the quenching mechanisms (e.g., Fillingham et al., 2016; Rasmussen et al., 2012; Kawata & Mulchaey, 2008). The efficiency and relative importance of ram-pressure stripping to directly remove galaxies' cold disk gas within galaxy groups remains unclear. The question of what disturbs and even quenches group galaxies is further complicated by the variety in dynamical states of the groups and merger/harassment history of the galaxies therein. However, as suggested by Figure 4.12, the CGM is increasingly stripped and/or heated as the environmental density increases, which may quench the host galaxies on longer timescales (i.e., strangulation) even if the cold gas in the disk is not directly stripped. The unparalleled sensitivity and kinematic information provided by QSO absorption line spectroscopy can and should be leveraged to further diagnose these physical processes across the full environmental spectrum. However, substantially larger samples and uniformly identifying and quantifying mass, richness, etc., for groups and clusters will be critical.

4.5.2 The nature of the detected absorption

The QSO sightline probing A1926 reveals three Lyα components, all of which have line widths that indicate gas temperatures that could be as high as 10^{5-6} K. This sightline lies on the outskirts of a cluster merger system, projected at 2 R_{200} from A1926N, and shows an intriguingly symmetric arrangement of the Lyα components (one component at $v = -937$ km s^{-1} and another at $v = 1061$ km s^{-1}). Furthermore,

no absorption is detected between these two velocity extremes. This is consistent with the findings of Yoon et al. (2012), who report a deficiency of Lyα absorbers within a virial radius of Virgo and at similar velocities; however, the very-low redshift of Virgo hampers examining the absorption properties blueshifted relative to the cluster to look for such symmetry.

In their hydrodynamical galaxy cluster simulations, Emerick et al. (2015) find a bimodality in the velocities of Lyα absorbers centered on the rest-frame velocities of their simulated clusters. This effect arises because a significant fraction of their absorbers trace infalling filamentary material. The BLAs we detect near A1926 are quite consistent with this behavior, suggesting that the absorbers may trace material accreting onto the cluster from the intergalactic medium and is either preheated to the warm-hot phase within the filament itself or at the accretion shock of the cluster environment ($2-3\ r_{vir}$; Molnar et al., 2009). It is notable that these BLA components have no associated O VI absorption and, indeed, infalling material from the IGM should have relatively low metallicity (e.g., Hafen et al., 2016; Fumagalli et al., 2011). Unfortunately, the temperatures implied by the BLAs ($T \lesssim 10^{5.4}$ K) lie in a regime where non-equilibrium effects set in, which are in turn highly dependent on the gas metallicity Gnat & Sternberg (2007). Therefore, we are unable to constrain the metallicities of these absorbers.

The A1095 complex presents an interesting configuration where the X-ray data reveal the system to be an early-stage merger of two subclusters. Furthermore, the QSO sightline pierces the interface region directly between the merging subclusters. In contrast to the absorbers detected near A1926, we detect single narrow H I component with $b = 16$ km s^{-1}, implying $T = 10^{4.2}$ K under purely thermal broadening. The curious presence of cool gas in this region that also shines in X-rays may be a result of the merger process. For example, passing shocks can act to compress as well as strip gas, as seen in examples such as ESO 137-001 (Sun et al., 2007; Fumagalli et al., 2014),

which displays prominent tails of star formation extending downstream as the galaxy passes through the ICM of the Norma cluster. This phenomenon has been reproduced in hydrodynamic simulations (Tonnesen & Bryan, 2012), where substantial gas density enhancements occur in the wake of stripping events and then cool. Tonnesen & Bryan (2012) find that the level of star formation occurring within these dense pockets is sensitive to the pressure in the ICM, while Roediger et al. (2014) showed that shocks propagating through the ICM due to a merger with another cluster can induce both thermal and ram pressure/density enhancements to levels sufficient to induce star formation. The absorber we detect in this cluster merger interface region, which contains no galaxy in our survey data with $\rho < 300$ kpc and $\delta v < 400$ km s^{-1} and thus does not appear in Figure 4.8, has log N(H I) = 14.93 cm^{-2}, clearly well below what we might expect for a region where star formation might occur. Possibilities for the nature of these absorber include the following: (1) The QSO sightline is probing a density enhancement produced by a merger shockwave out of detritus from a stripping event or, alternatively, from warm-hot gas located in the outer gas regions of a cluster. (2) The absorption arises from cool gas that has been stripped from a galaxy near the merger interface and has remained cool at large distance from its source galaxy because of a large boost in the gas-galaxy relative velocity induced by the relative velocities of the merging clusters. We note that a preliminary analysis of the galaxy spectra suggests that star formation activity is indeed enhanced along this merger interface, reminiscent of the "Sausage" and "Toothbrush" clusters (Stroe et al., 2015), but we reserve a full analysis of those data for a subsequent paper.

4.6 Summary and Conclusion

We have presented HST/COS and optical spectroscopic observations to accompany our previously published X-ray imaging/spectroscopy of a sample of galaxy clusters selected for having background QSOs probing their ICM. We leverage this

combined dataset to study the CGM of the cluster galaxies as well as the warm and warm-hot phases of the ICM not detected in X-rays. Our main results are summarized as follows:

1. The covering fraction, f_c, of H I in the CGM of our cluster galaxies is $18^{+14}_{-9}\%$, much lower than the near-unity CGM f_c measured for field galaxies. Furthermore, f_c for the for the cluster galaxies is significantly lower than that observed for group galaxies, which has in turn been measured to be lower than the field value.

2. In total, we detect three broad Lyα (BLA) components at $\rho > r_{200}$ on the outskirts of one cluster (A1926) and two narrower components at $\rho < r_{200}$ of two clusters (A1095 and A2246) The region of A1095 probed by our QSO sightline appears to be the interface of a subcluster merger.

3. We detect no unambiguous O VI absorption in any our sightlines within $\Delta v = 2000$ km s^{-1} of the cluster redshifts.

4. For the BLA components detected on the outskirts of A1926, we compare the mass of warm-hot 10^{5-6} K gas traced by BLA with the mass of X-ray traced gas. We estimate that the warm-hot gas mass $\sim 3\%$ of the hot gas mass, although much more could remain hidden if $T > 10^{5.5}$ K. Thus, at cluster-centric radii beyond r_{200}, such gas may comprise a significant contribution to the baryon content.

5. To enable follow-up studies of the clusters, we also publish our optical galaxy redshift surveys in these QSO fields in the Appendix. As the QSO spectra are also now public, these galaxy data should greatly increase the legacy value of the HST/COS data.

Our study represents a burgeoning body of work using QSOs as absorption line probes of the densest regions in the low-redshift Universe, largely enabled by the sensitivity of the Cosmic Origins Spectrograph on the *Hubble Space Telescope*. Larger sample sizes are certainly required to place these intriguing findings of our work and other authors on firm statistical footing. In particular, more sightlines systematically probing cluster-centric impact parameters from within to beyond r_{200} could illuminate the ionization and chemical states of the ICM as well as the transformation of the constituent galaxies' CGM relative to less dense regions of the Universe.

4.7 Acknowledgements

The authors would like to thank Mary Putman and Joo Heon Yoon for insightful discussion and sharing their data. Also, Benjamin Weiner provided extremely helpful advice for the Hectospec target selection strategy. The observations in this paper were obtained for HST programs 7778, 13833, 13342, and 13491, with financial support through NASA grants HST-GO-13342.002-A and HST-GO-13491.001-A from the Space Telescope Science Institute, which is operated by the Association of Universities for Research in Astronomy, Incorporated, under NASA contract NAS5-26555. This work is partly based on observations taken at the MMT Observatory, a joint facility of the University of Arizona and the Smithsonian Institution.

APPENDIX A

SPECTRAL PLOTS OF C IV SAMPLE FROM PAPER II

This section contains plots showing the spectra and Voigt profile fits of all species in our C IV absorber sample. The individual components are color coded, with the composite profile marked in dark red, and the error vector is plotted in light red. In cases where a line was deemed too saturated to yield reliable column density measurements from profile fitting, no fit is plotted. Components marked with magenta crosses denote interloping lines blended with components attributed to the species labeled in each panel. Certain spectral regions are affected by geocoronal emission and are marked with $\oplus$.

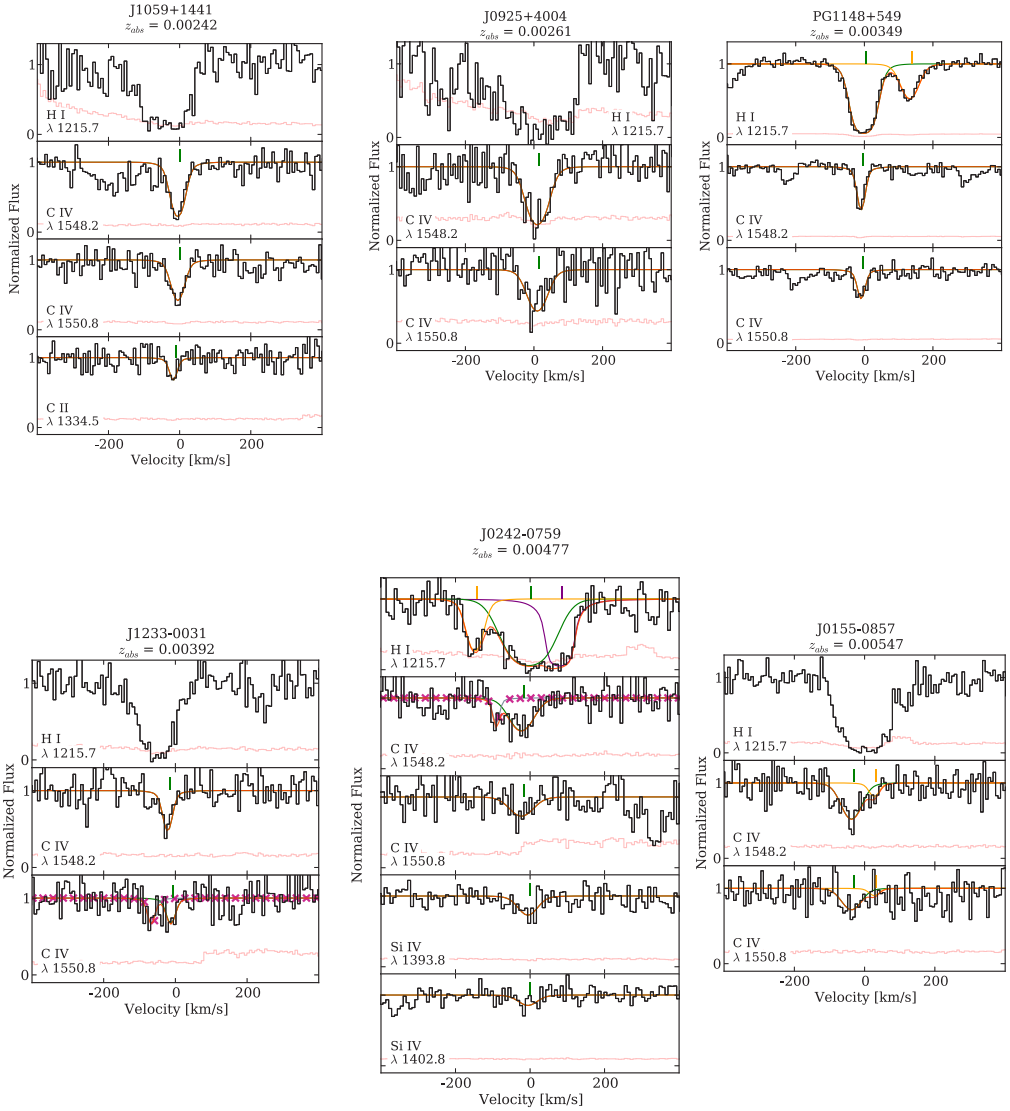

Figure A.1 Spectra and fitted Voigt profiles for our C IV absorber sample. For each system, at least one transition is shown for every ion detected, and each component is colored to match components of other species approximately aligned in velocity. Profiles of interloping lines from other systems that were included in a fit are marked with purple x's, while the overalll fit is shown in maroon. The error vector is plotted in light red.

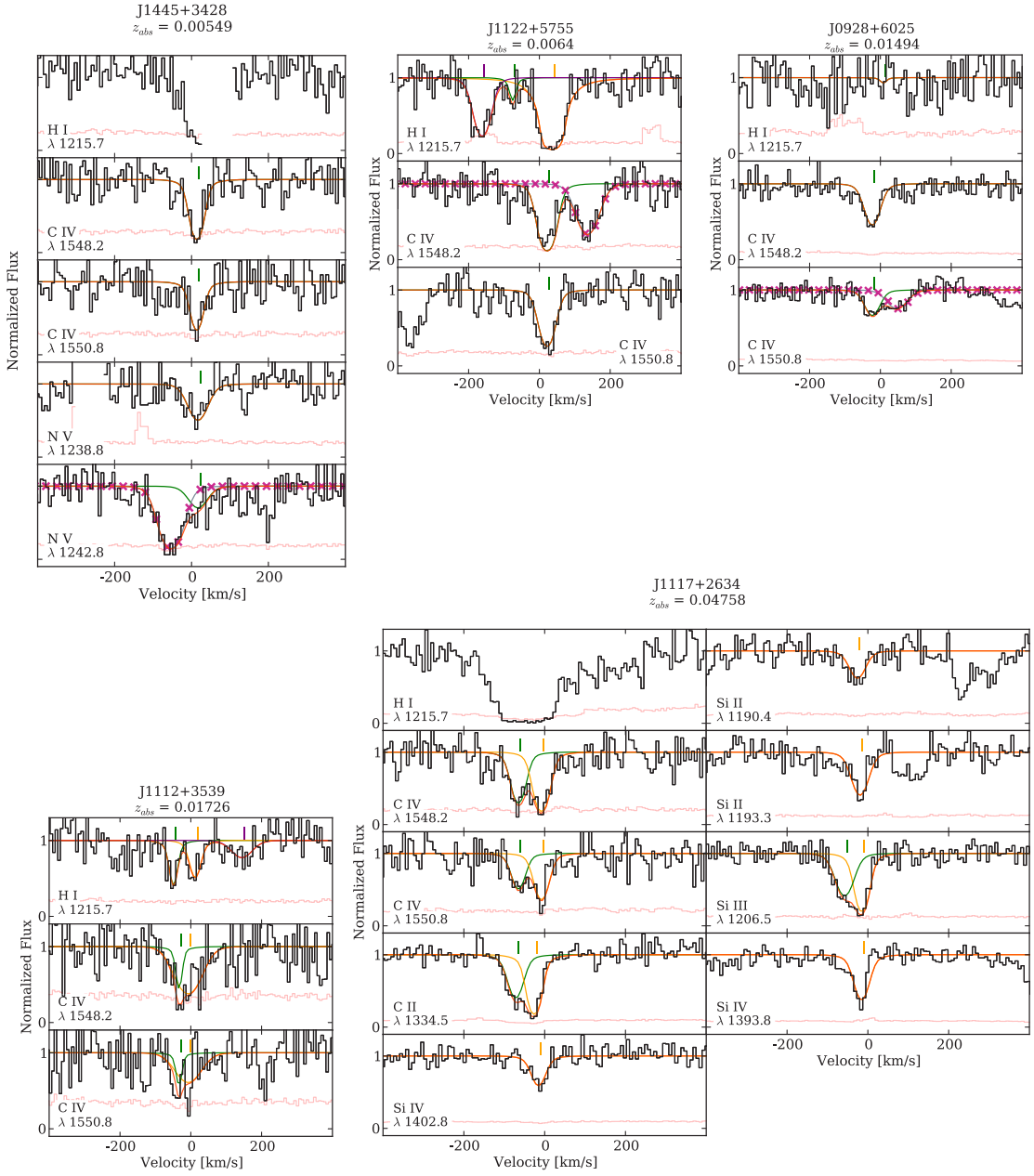

Figure A.1 continued.

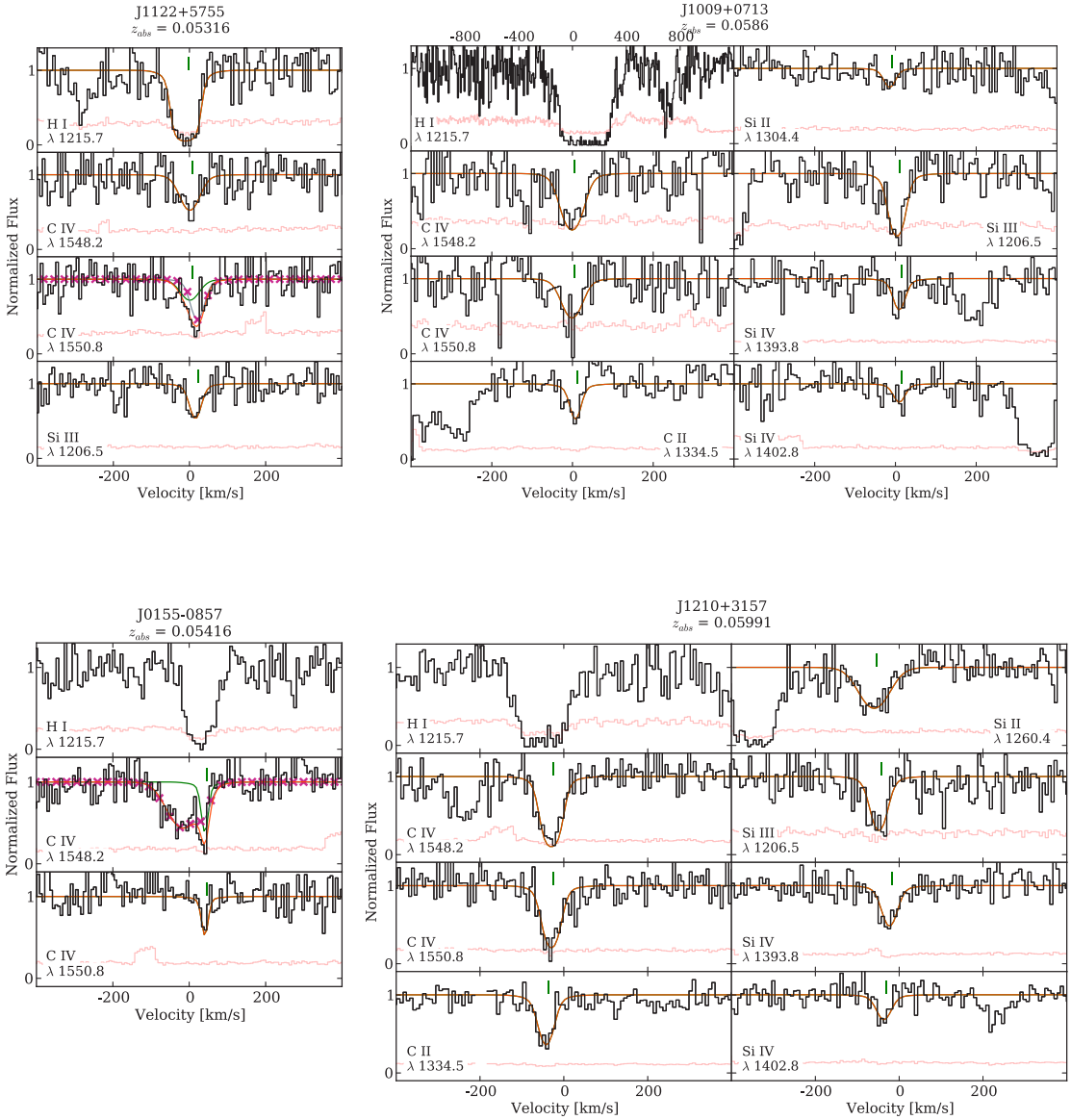

Figure A.1 continued.

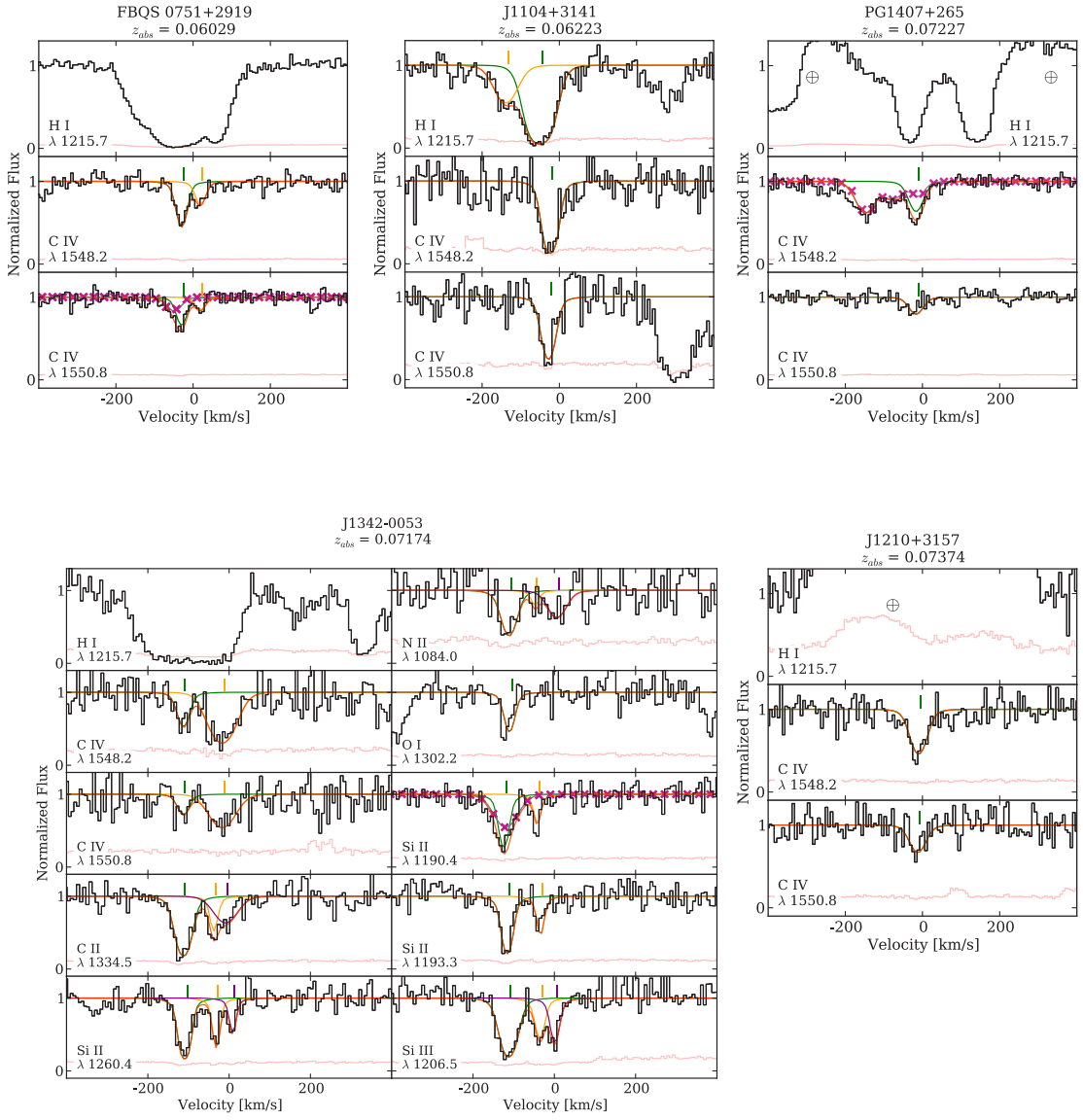

Figure A.1 continued.

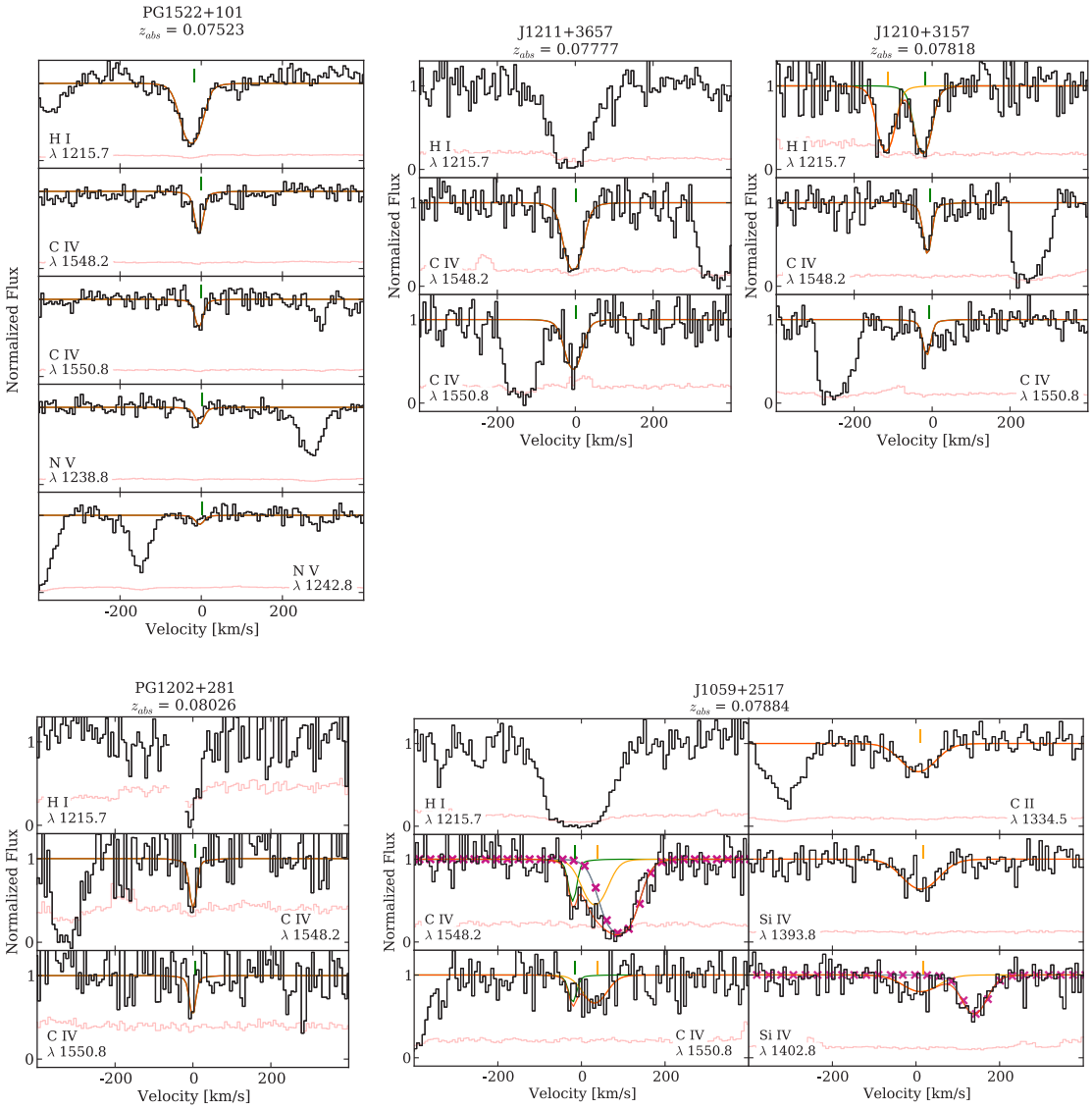

Figure A.1 continued.

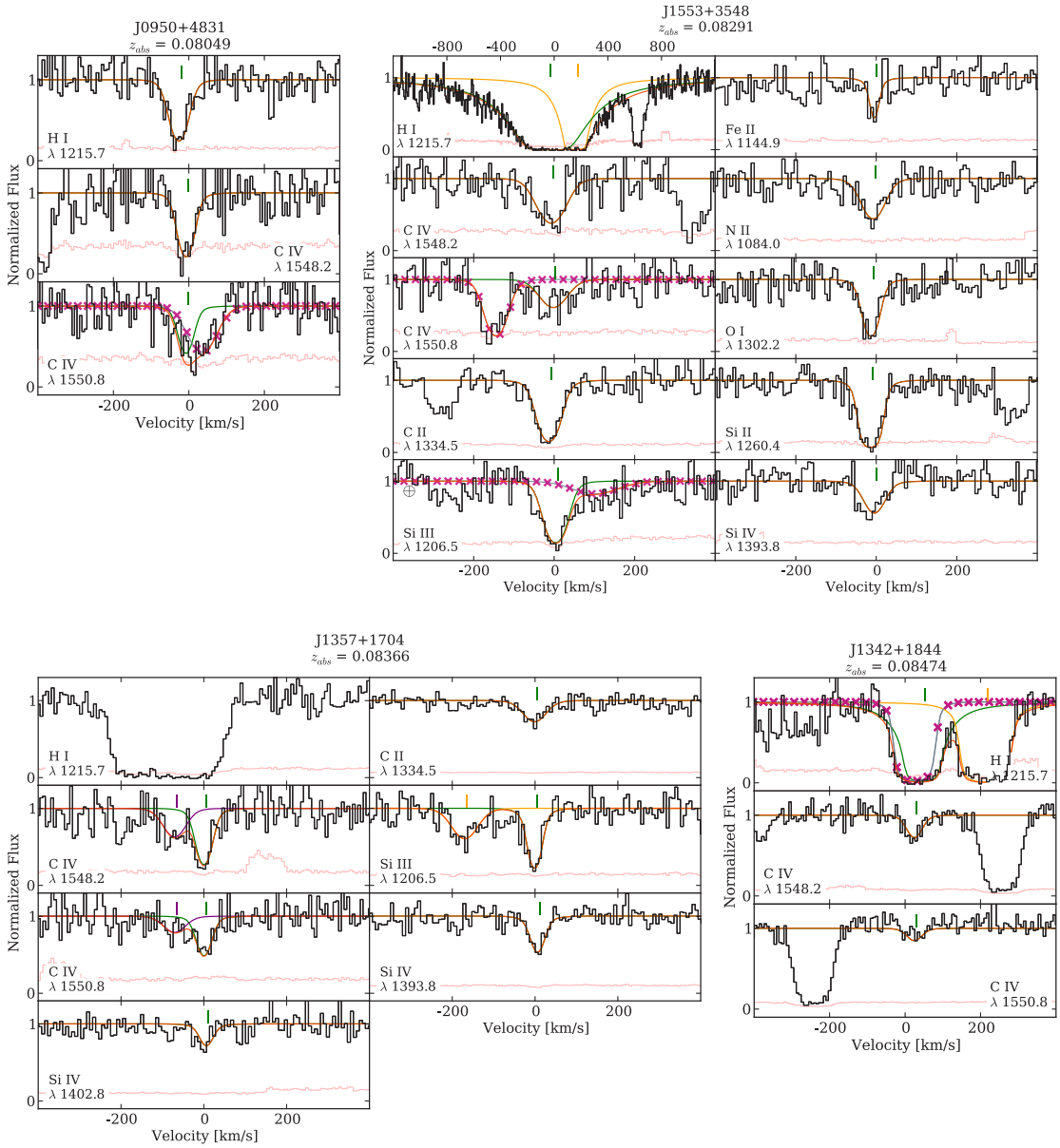

Figure A.1 continued.

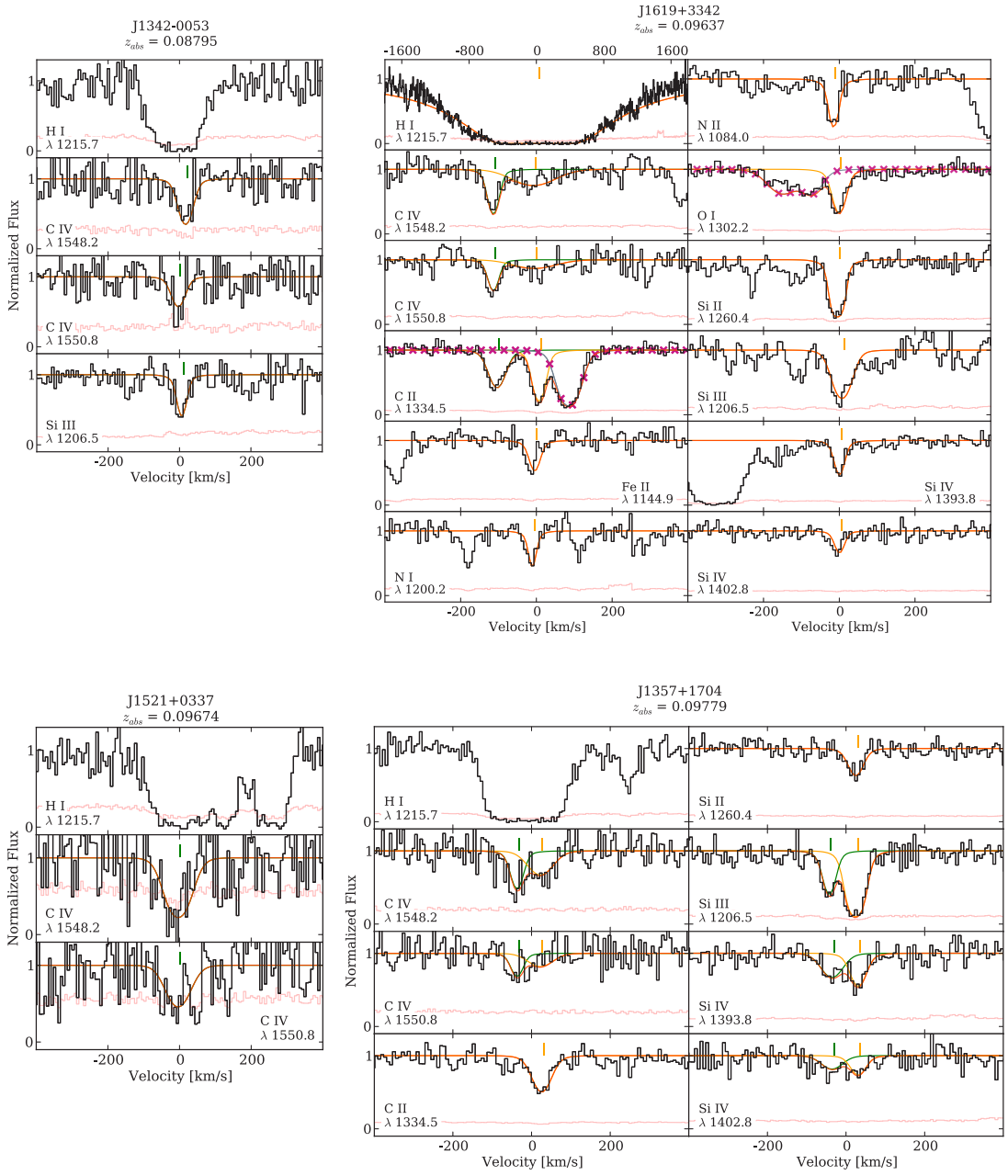

Figure A.1 continued.

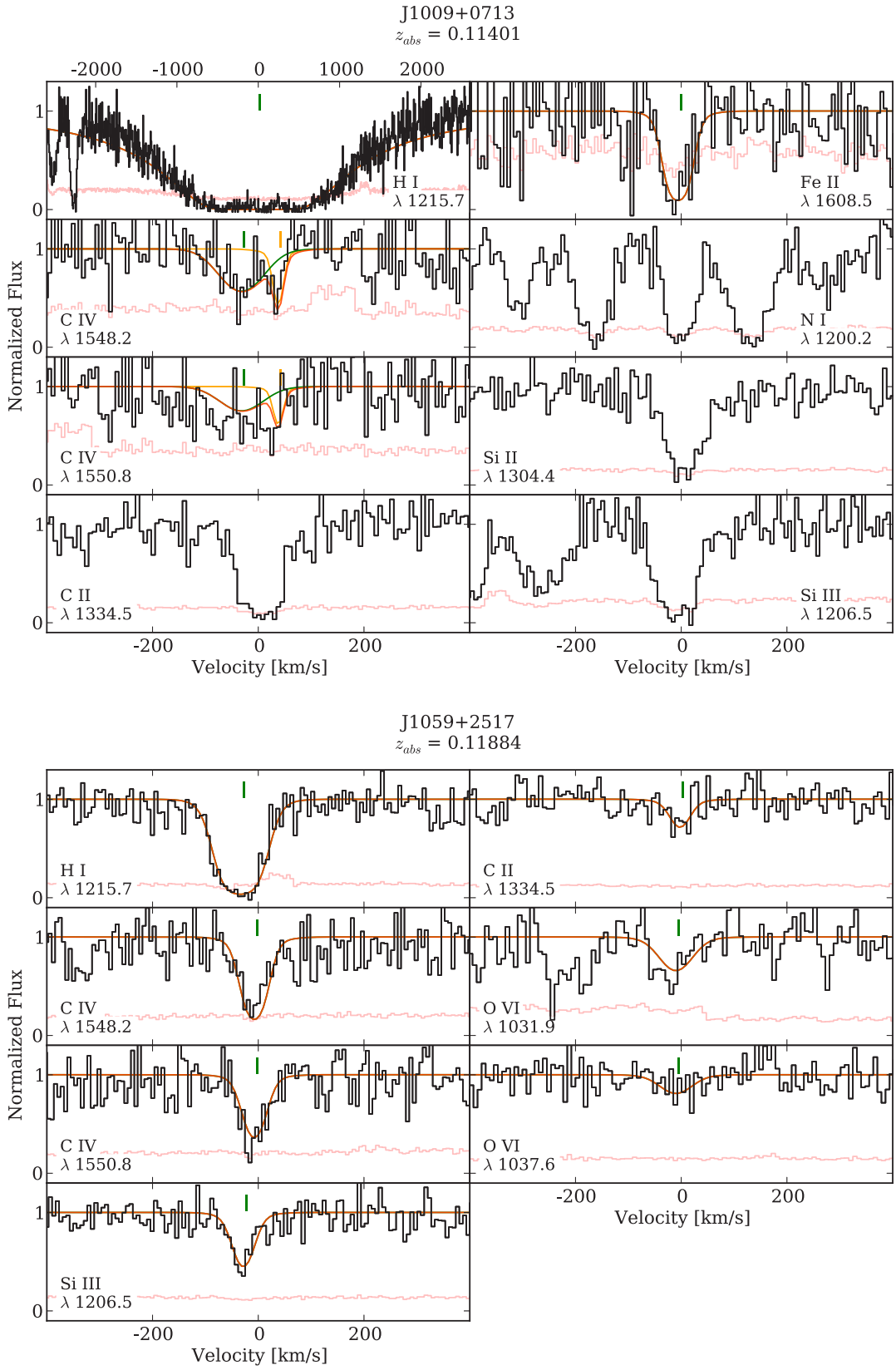

Figure A.1 continued.

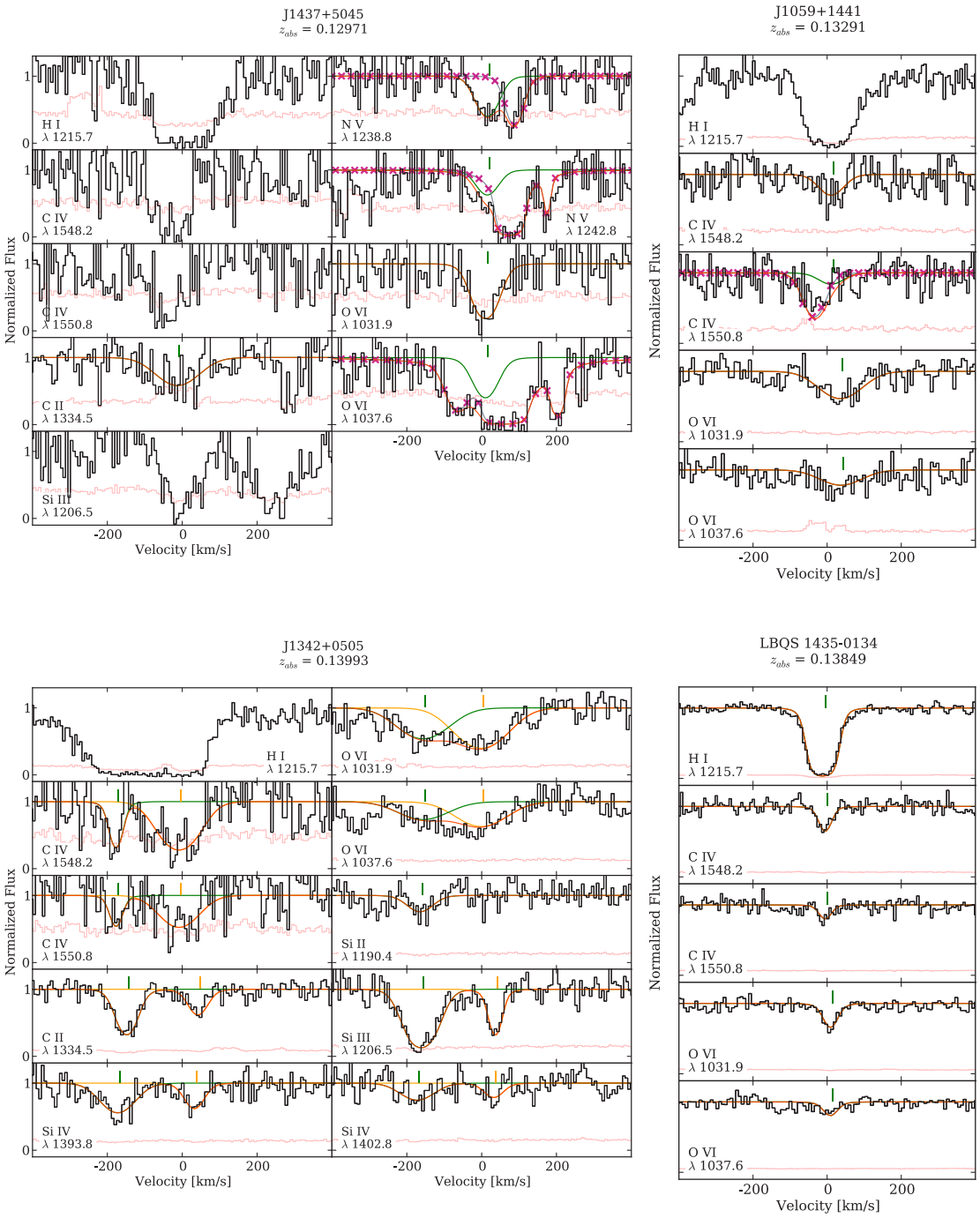

Figure A.1 continued.

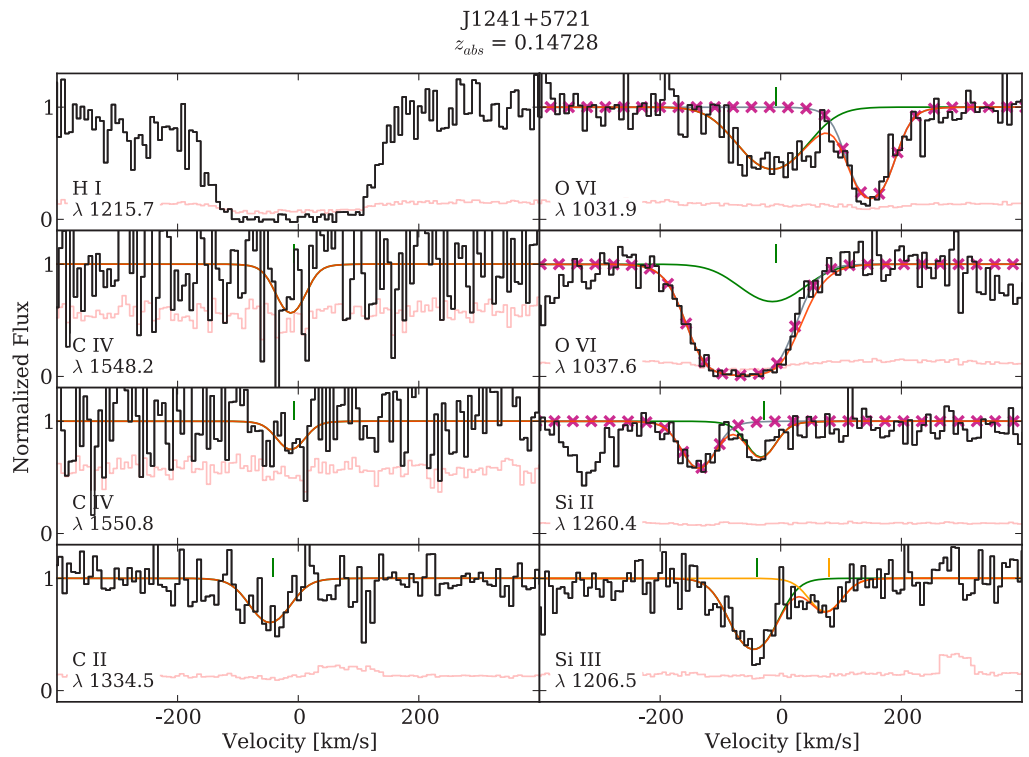

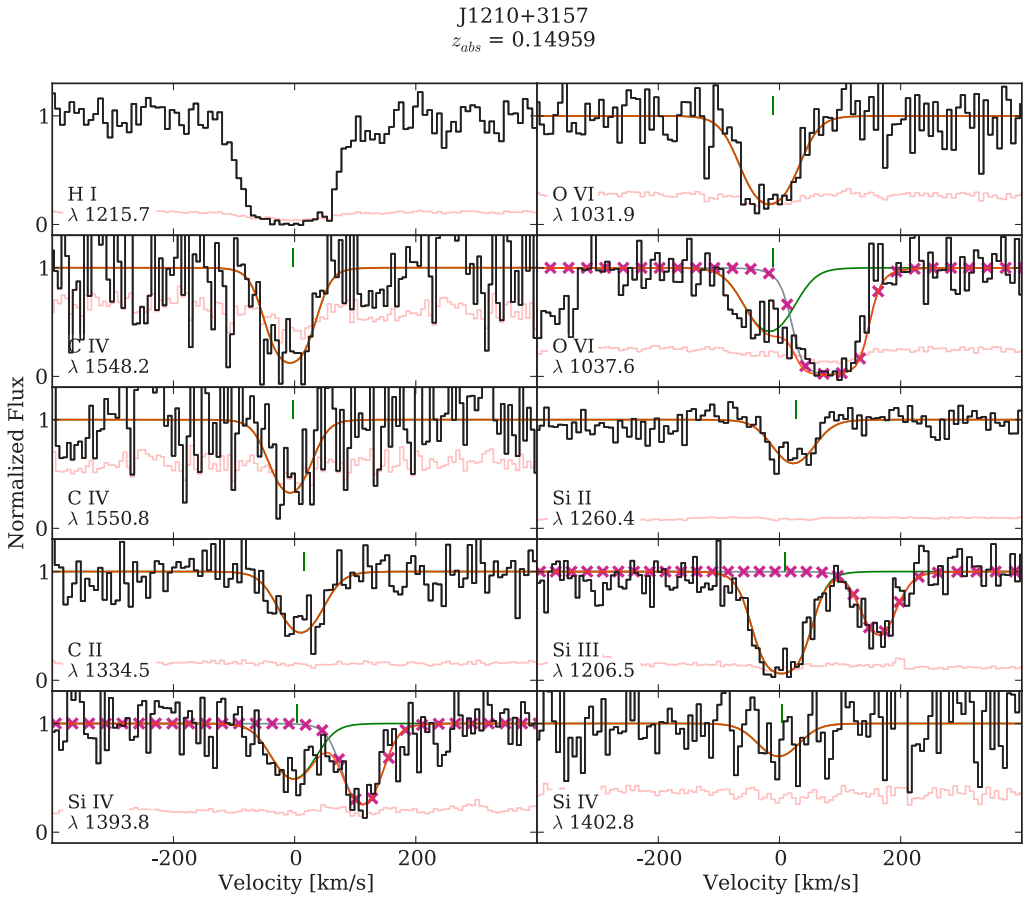

Figure A.1 continued.

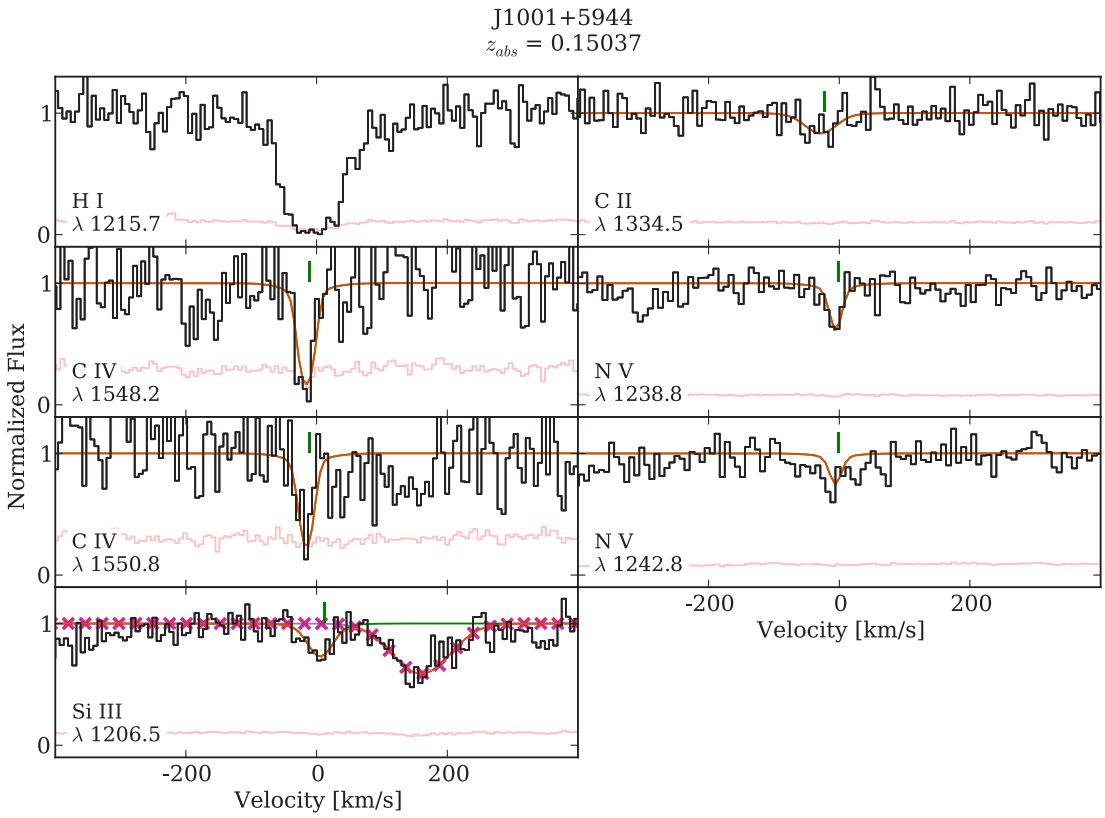

Figure A.1 continued.

APPENDIX B

GALAXY/ABSORBER ENVIRONMENT MAPS FROM PAPER III

Here, we present maps of the galaxy populations around the QSO sightlines employed in our galaxy environment/absorber analysis. Figures B.1-B.2 show the galaxies composing the environments that are plotted as individual points in Figure 3.6; these maps reveal the contrast in galaxy density that result in the differing detection rates of C IV absorption. Figures B.1-B.2 include only $\mathcal{M}_r \leq -19$ galaxies and therefore are not directly comparable to Figure 3.1, which uses no minimum luminosity. For a different perspective, Figure B.3 shows the galaxy impact parameters within 1.5 Mpc of the QSO sightlines depicted in Figure 3.6. Here, the galaxy overdensities in large-scale structures probed by the QSO sightlines are conspicuous at various redshifts. The redshifts of the $\rho \leq 160$ kpc galaxies are marked with vertical solid and dashed lines for C IV detections and non-detections, respectively.

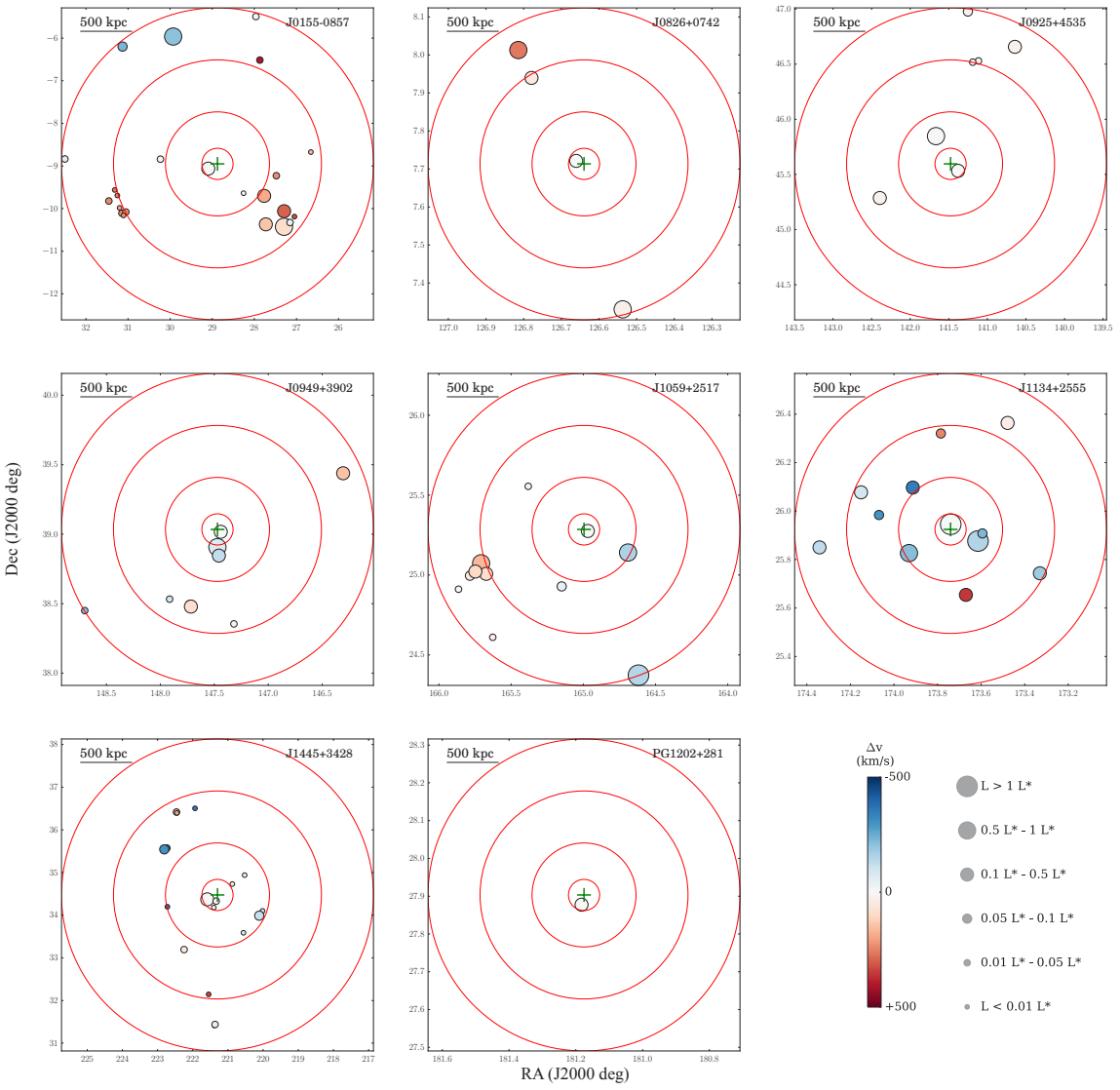

Figure B.1 The galaxy environments of the C IV detections plotted in Fig. 3.6. The crosses in the center of each map mark the QSO sightline, and the concentric circles indicate impact parameters of 150, 500, 1000, and 1500 kpc. The sizes of the symbols depict the galaxy luminosities and the color indicates the velocity offset from the detected absorber as indicated by the colorbar.

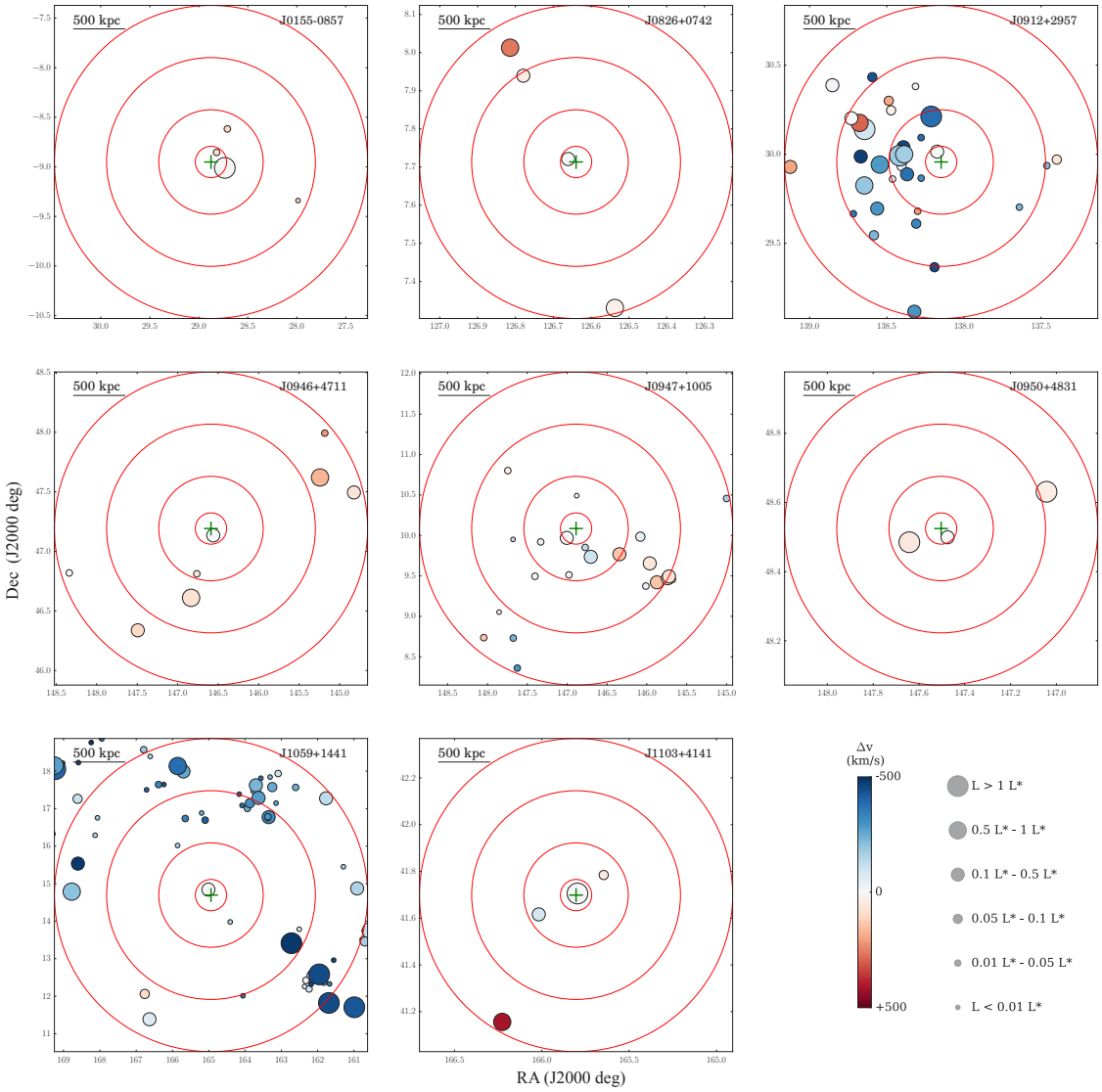

Figure B.2 Same as Fig. B.1 but for C IV *nondetections*. The velocity offsets are calculated from the innermost galaxy.

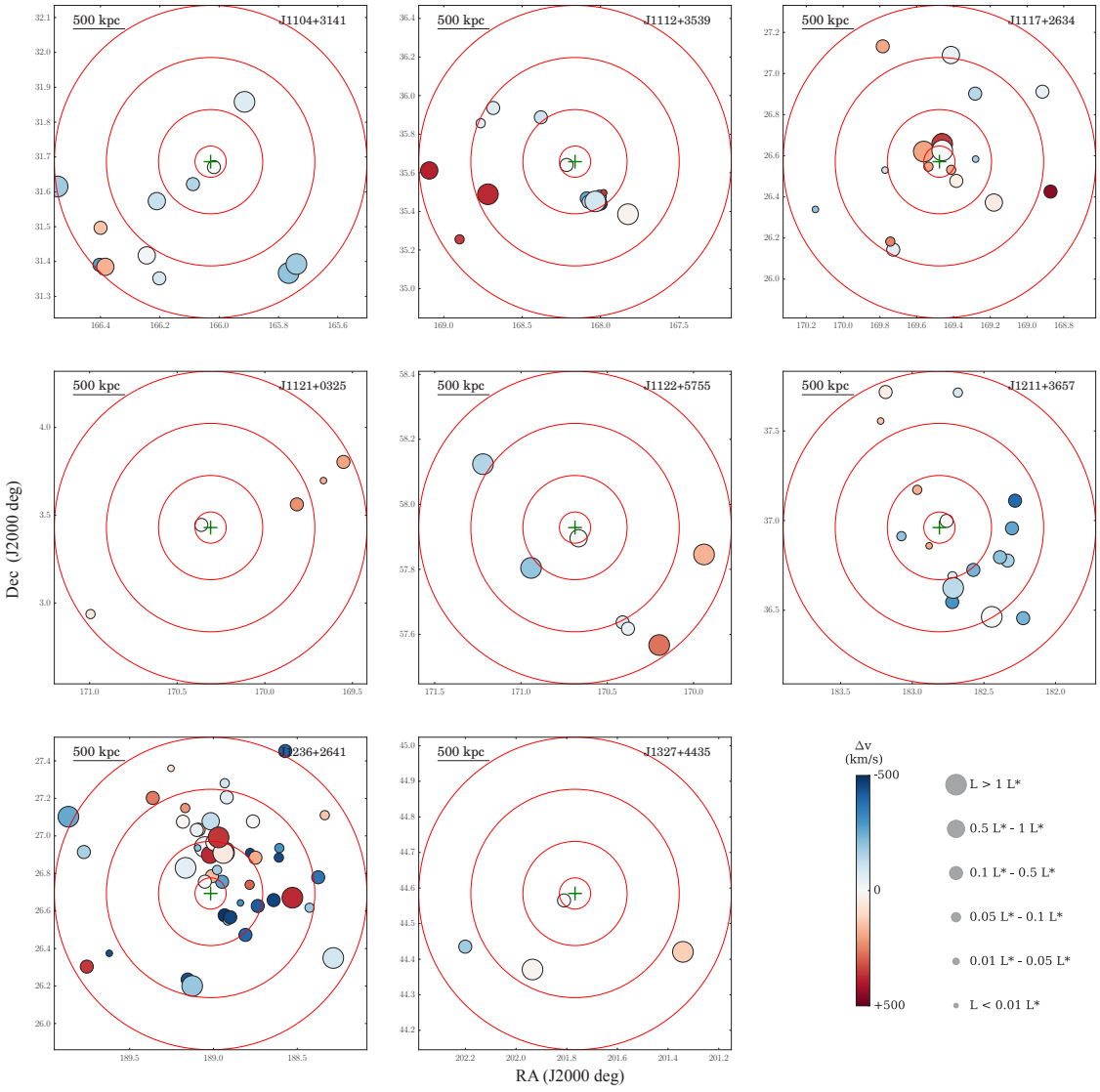

Figure B.2 Same as Fig. B.1 but for C IV *nondetections*. The velocity offsets are calculated from the innermost galaxy.

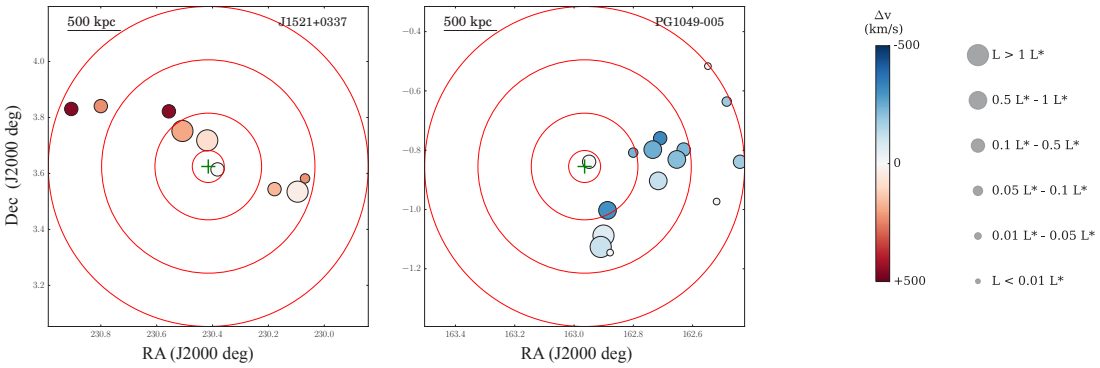

Figure B.2 continued.

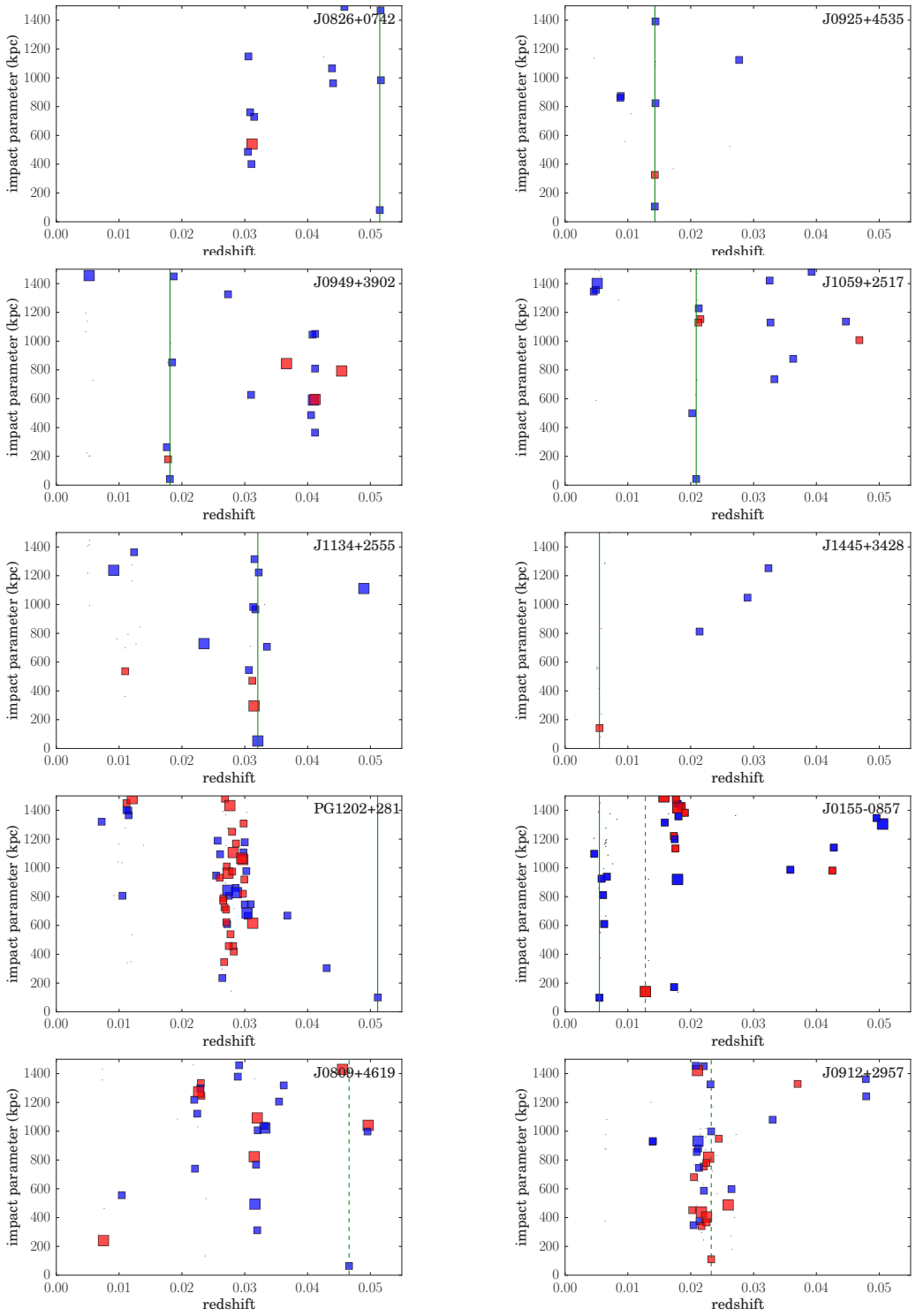

Figure B.3 Impact parameter vs. redshift for galaxies within 1500 kpc of QSO sightlines represented in Fig. 3.6 and with maps in Figs. B.1 and B.2. Vertical lines appear at redshifts where an $\mathcal{M}_r \leq -19$ galaxy falls within 160 kpc of the sightline; solid lines mark C IV detections, and dashed mark C IV nondetections.

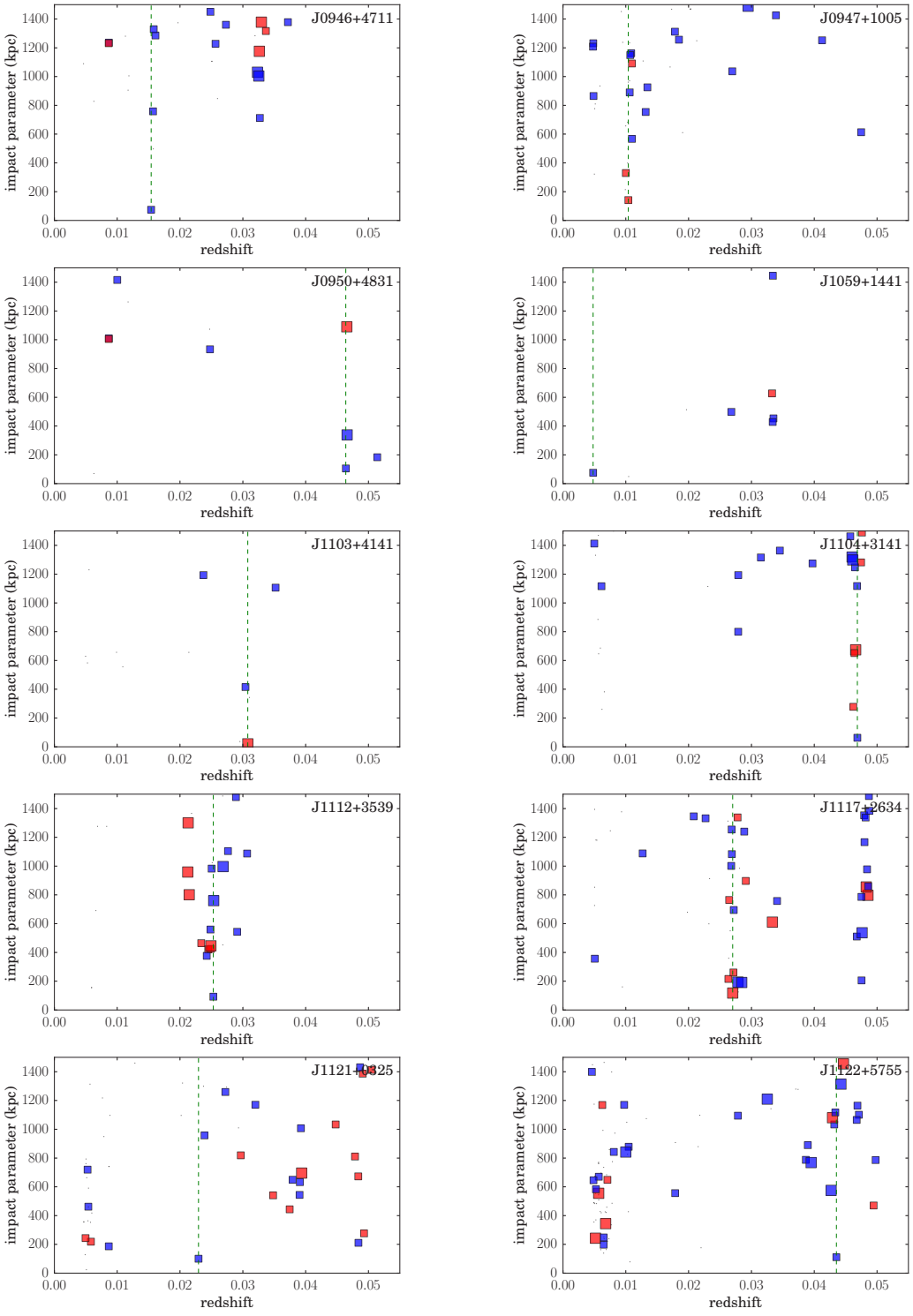

Figure B.3 continued.

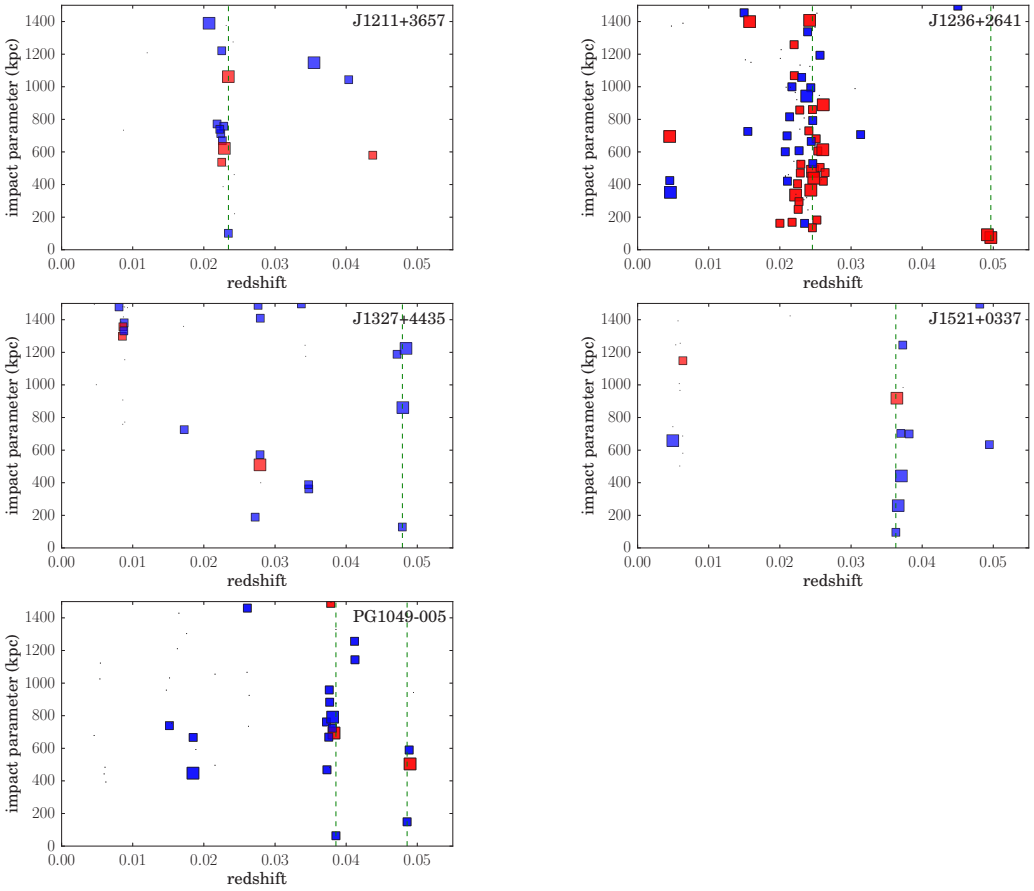

Figure B.3 continued.

APPENDIX C

SPECTROSCOPIC GALAXY SAMPLE FROM CHAPTER IV

We present the coordinates and redshifts for all galaxies spectroscopically measured, either through our own observations or those provided by the SDSS, in the QSO/cluster fields featured in this work. In the table provided, the large majority of objects are drawn from our survey with MMT/Hectospec, for which the redshift measurement software provides quality scores that reflect the confidence of the measurement (see Section 4.2.3). Although we use only objects with quality scores ≥ 3 in our analysis, we include all objects for which we obtained spectra, which will be of interest to researchers who may wish to survey these these fields further. Also for these objects measured by Hectospec, we include the object classification provided by the measurement software.

Table A1: Galaxy survey data in QSO/cluster fields.

Field	Galaxy Name	RA (J2000) (deg)	Dec (J2000) (deg)	z	σ_z	Quality	Object Class	Source
A1095	J104645.19+153230.52	161.688293	15.541811	0.1457	0.0005	4	GALAXY	Hectospec
A1095	J104835.24+151438.78	162.146820	15.244105	0.3237	0.0005	4	GALAXY	Hectospec
A1095	J104751.4+151658.04	161.964188	15.282789	0.2114	0.0005	4	GALAXY	Hectospec
A1095	J104806.03+151851.01	162.025116	15.314170	0.2082	0.0005	4	GALAXY	Hectospec
A1095	J104832.31+151223.49	162.134644	15.206525	0.1785	0.0005	4	GALAXY	Hectospec
A1095	J104835.46+151925.10	162.147781	15.323639	0.2478	0.0005	4	QSO	Hectospec
A1095	J104835.14+152359.25	162.146423	15.399792	0.0855	0.0005	4	GALAXY	Hectospec
A1095	J104818.04+151740.33	162.075180	15.294536	0.2124	0.0005	4	GALAXY	Hectospec
A1095	J104811.34+151917.88	162.047241	15.321633	0.2086	0.0005	4	GALAXY	Hectospec
A1095	J104802.8+151636.66	162.011642	15.276850	0.2155	0.0005	4	GALAXY	Hectospec
A1095	J104755.77+151558.68	161.982391	15.266300	0.2147	0.0005	4	GALAXY	Hectospec
A1095	J104838.57+152157.11	162.160706	15.365864	0.3664	0.0005	4	GALAXY	Hectospec
A1095	J104759.63+151530.77	161.998474	15.258547	0.2123	0.0005	4	GALAXY	Hectospec
A1095	J104841.98+151818.68	162.174911	15.305189	0.1562	0.0005	4	GALAXY	Hectospec
A1095	J104810.4+151429.43	162.043320	15.241508	0.2174	0.0005	4	GALAXY	Hectospec
A1095	J104829.44+151701.14	162.122681	15.283650	0.3869	0.0005	4	GALAXY	Hectospec
A1095	J104803.22+151433.37	162.013428	15.242602	0.2125	0.0005	4	GALAXY	Hectospec
A1095	J104749.01+151306.74	161.954224	15.218539	0.2113	0.0005	4	GALAXY	Hectospec
A1095	J104847.07+151654.91	162.196106	15.281919	0.1547	0.0005	4	GALAXY	Hectospec
A1095	J104912.22+151907.91	162.300903	15.318864	0.4238	0.0005	4	GALAXY	Hectospec
A1095	J104758.96+151507.34	161.995667	15.252039	0.2097	0.0005	4	GALAXY	Hectospec
A1095	J104816.24+151247.78	162.067657	15.213272	0.1325	0.0005	4	GALAXY	Hectospec
A1095	J104915.41+151551.26	162.314178	15.264239	0.4386	0.0005	4	GALAXY	Hectospec
A1095	J104823.14+151123.38	162.096405	15.189828	0.3044	0.0005	4	GALAXY	Hectospec

A full electronic version is available from the journal website.

BIBLIOGRAPHY

Abell, G. O. 1965, ARAA, 3, 1

Alam, S., Albareti, F. D., Prieto, C. A., et al. 2015, ApJS, 219, 12, arXiv: 1501.00963

Andreon, S. 2010, MNRAS, 407, 263

Bahcall, J. N., & Peebles, P. J. E. 1969, ApJL, 156, L7

Bahcall, J. N., & Spitzer, Jr., L. 1969, ApJL, 156, L63

Bahcall, J. N., Bergeron, J., Boksenberg, A., et al. 1993, ApJS, 87, 1

Bahé, Y. M., McCarthy, I. G., Balogh, M. L., & Font, A. S. 2013, MNRAS, 430, 3017

Bennett, C. L., Larson, D., Weiland, J. L., et al. 2013, ApJS, 208, 20

Bergeron, J. 1986, Astronomy and Astrophysics, 155, L8

Bergeron, J., & Boissé, P. 1991, A&A, 243, 344

Bergeron, J., Kunth, D., & D'Odorico, S. 1987, A&A, 180, 1

Bergeron, J., & Stasińska, G. 1986, A&A, 169, 1

Blanton, M. R., & Roweis, S. 2007, AJ, 133, 734

Blanton, M. R., Hogg, D. W., Bahcall, N. A., et al. 2003, ApJ, 592, 819

Boksenberg, A., & Sargent, W. L. W. 1978, ApJ, 220, 42

Bonamente, M., Nevalainen, J., Tilton, E., et al. 2016, MNRAS, 457, 4236

Booth, C. M., Schaye, J., Delgado, J. D., & Dalla Vecchia, C. 2012, MNRAS, 420, 1053

Bordoloi, R., Lilly, S. J., Knobel, C., et al. 2011, ApJ, 743, 10

Bordoloi, R., Tumlinson, J., Werk, J. K., et al. 2014, ApJ, 796, 136

Borthakur, S., Heckman, T., Strickland, D., Wild, V., & Schiminovich, D. 2013, ApJ, 768, 18

Bouché, N., Hohensee, W., Vargas, R., et al. 2012, MNRAS, 426, 801

Bowen, D. V., Blades, J. C., & Pettini, M. 1995, ApJ, 448, 634

—. 1996, ApJ, 464, 141

Bowen, D. V., Jimenez, R., Jenkins, E. B., & Pettini, M. 2001, ApJ, 547, 39

Brinchmann, J., Charlot, S., White, S. D. M., et al. 2004, MNRAS, 351, 1151

Buote, D. A., Su, Y., Gastaldello, F., & Brighenti, F. 2016, ApJ, 826, 146

Buote, D. A., Zappacosta, L., Fang, T., et al. 2009, ApJ, 695, 1351

Burbidge, E. M., Lynds, C. R., & Burbidge, G. R. 1966, ApJ, 144, 447

Burchett, J. N., Tripp, T. M., Werk, J. K., et al. 2013, ApJL, 779, L17

Burchett, J. N., Tripp, T. M., Prochaska, J. X., et al. 2015, ApJ, 815, 91

Burchett, J. N., Tripp, T. M., Bordoloi, R., et al. 2016, ApJ, 832, 124

Butcher, H., & Oemler, Jr., A. 1984, ApJ, 285, 426

Cardelli, J. A., Clayton, G. C., & Mathis, J. S. 1989, ApJ, 345, 245

Cecil, G., Bland-Hawthorn, J., Veilleux, S., & Filippenko, A. V. 2001, ApJ, 555, 338

Cen, R., & Chisari, N. E. 2011, ApJ, 731, 11

Cen, R., & Ostriker, J. P. 1999, ApJ, 514, 1

Chabrier, G. 2003, PASP, 115, 763

Chen, H.-W., Lanzetta, K. M., & Webb, J. K. 2001, ApJ, 556, 158

Chen, H.-W., & Mulchaey, J. S. 2009, ApJ, 701, 1219

Chen, H.-W., Prochaska, J. X., Weiner, B. J., Mulchaey, J. S., & Williger, G. M. 2005, ApJL, 629, L25

Chen, H.-W., Wild, V., Tinker, J. L., et al. 2010, The Astrophysical Journal Letters, 724, L176

Chung, A., van Gorkom, J. H., Kenney, J. D. P., Crowl, H., & Vollmer, B. 2009, AJ, 138, 1741

Chung, A., van Gorkom, J. H., Kenney, J. D. P., & Vollmer, B. 2007, ApJL, 659, L115

Colless, M., Dalton, G., Maddox, S., et al. 2001, MNRAS, 328, 1039

Cooksey, K. L., Kao, M. M., Simcoe, R. A., O'Meara, J. M., & Prochaska, J. X. 2013, ApJ, 763, 37

Cooksey, K. L., Prochaska, J. X., Thom, C., & Chen, H.-W. 2011, ApJ, 729, 87

Cooksey, K. L., Thom, C., Prochaska, J. X., & Chen, H.-W. 2010, ApJ, 708, 868

Cool, R. J., Eisenstein, D. J., Fan, X., et al. 2008, ApJ, 682, 919

Corwin, Jr., H. G., Buta, R. J., & de Vaucouleurs, G. 1994, AJ, 108, 2128

Cowie, L. L., & Songaila, A. 1998, Nature, 394, 44

Cowie, L. L., Songaila, A., Kim, T.-S., & Hu, E. M. 1995, AJ, 109, 1522

Danforth, C. W., & Shull, J. M. 2005, ApJ, 624, 555

Danforth, C. W., Tilton, E. M., Shull, J. M., et al. 2014, ArXiv e-prints, 1402, 2655

Davé, R., Oppenheimer, B. D., & Finlator, K. 2011, MNRAS, 415, 11

Davé, R., Oppenheimer, B. D., Katz, N., Kollmeier, J. A., & Weinberg, D. H. 2010, MNRAS, 408, 2051

Davé, R., Cen, R., Ostriker, J. P., et al. 2001, ApJ, 552, 473

Davies, R. D., & Lewis, B. M. 1973, MNRAS, 165, 231

de Vaucouleurs, G., de Vaucouleurs, A., Corwin, Jr., H. G., et al. 1991, Third Reference Catalogue of Bright Galaxies. Volume I: Explanations and references. Volume II: Data for galaxies between 0h and 12h. Volume III: Data for galaxies between 12h and 24h. No. ISBN 3-540-97552-7 (Springer)

Dekel, A., & Birnboim, Y. 2006, MNRAS, 368, 2

D'Odorico, V., Calura, F., Cristiani, S., & Viel, M. 2010, MNRAS, 401, 2715

D'Odorico, V., Cupani, G., Cristiani, S., et al. 2013, ArXiv e-prints, 1306, 4604

Dressler, A. 1980, ApJ, 236, 351

Ellison, S. L., Songaila, A., Schaye, J., & Pettini, M. 2000, AJ, 120, 1175

Emerick, A., Bryan, G., & Putman, M. E. 2015, MNRAS, 453, 4051

Faber, S. M. 1973, ApJ, 179, 731

Faber, S. M., Phillips, A. C., Kibrick, R. I., et al. 2003, in , 1657–1669

Fabricant, D., Fata, R., Roll, J., et al. 2005, PASP, 117, 1411

Fabricant, D. G., Hertz, E. N., Szentgyorgyi, A. H., et al. 1998, in , 285–296

Fang, T., Marshall, H. L., Lee, J. C., Davis, D. S., & Canizares, C. R. 2002, ApJL, 572, L127

Fillingham, S. P., Cooper, M. C., Pace, A. B., et al. 2016, Monthly Notices of the Royal Astronomical Society, 463, 1916

Finn, C. W., Morris, S. L., Tejos, N., et al. 2016, MNRAS, 460, 590

Ford, A. B., Oppenheimer, B. D., Davé, R., et al. 2013, MNRAS, 432, 89

Fox, A. J., Debes, J., Holland, S. T., & Dixon, W. V. 2017, Cosmic Origins Spectrograph Instrument Handbook, Version 9.0 (STScI)

Freeland, E., & Wilcots, E. 2011, The Astrophysical Journal, 738, 145

Fukugita, M., Hogan, C. J., & Peebles, P. J. E. 1998, ApJ, 503, 518

Fumagalli, M., Fossati, M., Hau, G. K. T., et al. 2014, MNRAS, 445, 4335

Fumagalli, M., Prochaska, J. X., Kasen, D., et al. 2011, MNRAS, 418, 1796

Ge, C., Wang, Q. D., Tripp, T. M., et al. 2016, MNRAS, 459, 366

Geha, M., Wechsler, R. H., Mao, Y.-Y., et al. 2017, ArXiv e-prints, 1705, arXiv:1705.06743

Ghavamian, P., Aloisi, A., Lennon, D., et al. 2009, Preliminary Characterization of the Post-Launch Line Spread Function of COS

Gnat, O., & Sternberg, A. 2007, ApJS, 168, 213

Gonzalez, A. H., Sivanandam, S., Zabludoff, A. I., & Zaritsky, D. 2013, ApJ, 778, 14

Green, J. C., Froning, C. S., Osterman, S., et al. 2012, ApJ, 744, 60

Gunn, J. E., & Gott, III, J. R. 1972, ApJ, 176, 1

Haardt, F., & Madau, P. 2012, ApJ, 746, 125

Haas, M. R., Schaye, J., & Jeeson-Daniel, A. 2012, MNRAS, 419, 2133

Hafen, Z., Faucher-Giguere, C.-A., Angles-Alcazar, D., et al. 2016, ArXiv e-prints, 1608, arXiv:1608.05712

Heckman, T. M., Norman, C. A., Strickland, D. K., & Sembach, K. R. 2002, ApJ, 577, 691

Heckman, T. M., Borthakur, S., Overzier, R., et al. 2011, ApJ, 730, 5

Hinshaw, G., Larson, D., Komatsu, E., et al. 2013, ApJS, 208, 19

Hitomi Collaboration, Aharonian, F., Akamatsu, H., et al. 2016, Nature, 535, 117

Holland, S. T. e. a. 2012, Cosmic Origins Spectrograph Instrument Handbook, Version 5.0, Tech. Rep. Version 5.0, STScI

Hopkins, P. F., Hernquist, L., Cox, T. J., et al. 2006, ApJS, 163, 1

Hopkins, P. F., Kereš, D., Oñorbe, J., et al. 2014, Monthly Notices of the Royal Astronomical Society, 445, 581

Huchra, J. P., Geller, M. J., & Corwin, Jr., H. G. 1995, ApJS, 99, 391

Johnson, S. D., Chen, H.-W., & Mulchaey, J. S. 2013, MNRAS, 434, 1765

—. 2015, MNRAS, 449, 3263

Johnson, S. D., Chen, H.-W., Mulchaey, J. S., et al. 2014, MNRAS, 438, 3039

Kacprzak, G. G., Churchill, C. W., & Nielsen, N. M. 2012a, ApJL, 760, L7

Kacprzak, G. G., Churchill, C. W., Steidel, C. C., Spitler, L. R., & Holtzman, J. A. 2012b, MNRAS, 427, 3029

Kant, I. 1755, Allgemeine Naturgeschichte und Theorie des Himmels

Katz, N., Weinberg, D. H., & Hernquist, L. 1996, ApJS, 105, 19

Kawata, D., & Mulchaey, J. S. 2008, The Astrophysical Journal Letters, 672, L103

Kennicutt, R. C. 1998, ARAA, 36, 189

Kereš, D., Katz, N., Weinberg, D. H., & Davé, R. 2005, MNRAS, 363, 2

Knobel, C., Lilly, S. J., Woo, J., & Kovač, K. 2015, ApJ, 800, 24

Kramida, A., Yu. Ralchenko, Reader, J., & and NIST ASD Team. 2014, NIST Atomic Spectra Database (ver. 5.2), [Online]. Available: `http://physics.nist.gov/asd` [2015, May 7]. National Institute of Standards and Technology, Gaithersburg, MD.

Kurucz, R. L. 1993, VizieR Online Data Catalog, 6039

Laganá, T. F., Martinet, N., Durret, F., et al. 2013, A&A, 555, A66

Lanzetta, K. M., Bowen, D. V., Tytler, D., & Webb, J. K. 1995a, ApJ, 442, 538

—. 1995b, ApJ, 442, 538

Larson, R. B. 1972, Nature, 236, 21

Larson, R. B., Tinsley, B. M., & Caldwell, C. N. 1980, ApJ, 237, 692

Lehner, N., O'Meara, J. M., Fox, A. J., et al. 2014, ApJ, 788, 119

Lehner, N., Savage, B. D., Richter, P., et al. 2007, ApJ, 658, 680

Lehner, N., Howk, J. C., Tripp, T. M., et al. 2013, ApJ, 770, 138

Liang, C. J., & Chen, H.-W. 2014, MNRAS, 445, 2061

Loveday, J., Norberg, P., Baldry, I. K., et al. 2012, MNRAS, 420, 1239

Lupton, R., Blanton, M. R., Fekete, G., et al. 2004, PASP, 116, 133

Lynden-Bell, D. 1975, Vistas in Astronomy, 19, 299

Lynds, C. R., Hill, S. J., Heere, K., & Stockton, A. N. 1966, ApJ, 144, 1244

Madau, P., Pozzetti, L., & Dickinson, M. 1998, ApJ, 498, 106

Marasco, A., Crain, R. A., Schaye, J., et al. 2016, MNRAS, 461, 2630

Martin, C. L. 2005, ApJ, 621, 227

Martin, D. C., Matuszewski, M., Morrissey, P., et al. 2015, Nature, 524, 192

Martínez-Delgado, D., Gabany, R. J., Crawford, K., et al. 2010, AJ, 140, 962

Mathews, W. G., Faltenbacher, A., Brighenti, F., & Buote, D. A. 2005, ApJL, 634, L137

McIntosh, D. H., Guo, Y., Hertzberg, J., et al. 2008, MNRAS, 388, 1537

Meiring, J. D., Tripp, T. M., Werk, J. K., et al. 2013, ApJ, 767, 49

Meiring, J. D., Tripp, T. M., Prochaska, J. X., et al. 2011, ApJ, 732, 35

Miller, J., & Stone, R. 1992, The Kast Double Spectrograph

Mink, D. J., Wyatt, W. F., Caldwell, N., et al. 2007, in , 249

Mo, H. J., & Miralda-Escude, J. 1996, ApJ, 469, 589

Molnar, S. M., Hearn, N., Haiman, Z., et al. 2009, ApJ, 696, 1640

Moore, B., Katz, N., Lake, G., Dressler, A., & Oemler, A. 1996, Nature, 379, 613

Moore, B., Lake, G., & Katz, N. 1998, ApJ, 495, 139

Morris, S. L., Weymann, R. J., Dressler, A., et al. 1993, ApJ, 419, 524

Moster, B. P., Naab, T., & White, S. D. M. 2013, MNRAS, 428, 3121

Moster, B. P., Somerville, R. S., Maulbetsch, C., et al. 2010, ApJ, 710, 903

Mould, J. R., Huchra, J. P., Freedman, W. L., et al. 2000, ApJ, 529, 786

Muldrew, S. I., Croton, D. J., Skibba, R. A., et al. 2012, MNRAS, 419, 2670

Murray, N., Ménard, B., & Thompson, T. A. 2011, ApJ, 735, 66

Murray, N., Quataert, E., & Thompson, T. A. 2010, ApJ, 709, 191

Newman, J. A., Cooper, M. C., Davis, M., et al. 2013, ApJS, 208, 5

Nicastro, F., Mathur, S., Elvis, M., et al. 2005, ApJ, 629, 700

Oemler, Jr., A. 1974, ApJ, 194, 1

O'Meara, J. M., Burles, S., Prochaska, J. X., et al. 2006, The Astrophysical Journal Letters, 649, L61

Oppenheimer, B. D., & Davé, R. 2006, MNRAS, 373, 1265

—. 2008, MNRAS, 387, 577

Oppenheimer, B. D., Davé, R., Katz, N., Kollmeier, J. A., & Weinberg, D. H. 2012, MNRAS, 420, 829

Oppenheimer, B. D., & Schaye, J. 2013, MNRAS, 434, 1043

Oppenheimer, B. D., Crain, R. A., Schaye, J., et al. 2016, MNRAS, 460, 2157

Osterbrock, D. E., & Ferland, G. J. 2006, Astrophysics of gaseous nebulae and active galactic nuclei (Sausalito, CA: University Science Books)

Pagel, B. E. J., & Patchett, B. E. 1975, MNRAS, 172, 13

Persic, M., & Salucci, P. 1992, Monthly Notices of the Royal Astronomical Society, 258, 14P

Pettini, M., Madau, P., Bolte, M., et al. 2003, ApJ, 594, 695

Planck Collaboration, Ade, P. A. R., Aghanim, N., et al. 2016, Astronomy and Astrophysics, 594, A13

Prochaska, J. X., Weiner, B., Chen, H.-W., Mulchaey, J., & Cooksey, K. 2011, ApJ, 740, 91

Rahmati, A., Schaye, J., Crain, R. A., et al. 2015, ArXiv e-prints, 1511, 1094

Rasmussen, J., Mulchaey, J. S., Bai, L., et al. 2012, The Astrophysical Journal, 757, 122

Rasmussen, J., Ponman, T. J., & Mulchaey, J. S. 2006, MNRAS, 370, 453

Ribaudo, J., Lehner, N., Howk, J. C., et al. 2011, ApJ, 743, 207

Richter, P., Savage, B. D., Sembach, K. R., & Tripp, T. M. 2006, A&A, 445, 827

Riemer-Sørensen, S., Kotuš, S., Webb, J. K., et al. 2017, Monthly Notices of the Royal Astronomical Society, 468, 3239

Riley, A., Biretta, J., & Hernandez, S. 2017, STIS Instrument Handbook, Version 16.0 (STScI)

Rocha-Pinto, H. J., & Maciel, W. J. 1996, Monthly Notices of the Royal Astronomical Society, 279, 447

Roediger, E., Brüggen, M., Owers, M. S., Ebeling, H., & Sun, M. 2014, MNRAS, 443, L114

Rubin, K. H. R., Prochaska, J. X., Koo, D. C., & Phillips, A. C. 2012, ApJL, 747, L26

Rubin, K. H. R., Prochaska, J. X., Koo, D. C., et al. 2014, ApJ, 794, 156

Rupke, D. S., Veilleux, S., & Sanders, D. B. 2005, ApJS, 160, 115

Rupke, D. S. N., & Veilleux, S. 2013, ApJ, 768, 75

Ryan-Weber, E. V., Pettini, M., Madau, P., & Zych, B. J. 2009, MNRAS, 395, 1476

Rykoff, E. S., Rozo, E., Busha, M. T., et al. 2014, ApJ, 785, 104

Salim, S., Rich, R. M., Charlot, S., et al. 2007, ApJS, 173, 267

Sandage, A., Binggeli, B., & Tammann, G. A. 1985, AJ, 90, 1759

Sargent, W. L. W., Boksenberg, A., & Steidel, C. C. 1988, ApJS, 68, 539

Sargent, W. L. W., Young, P. J., Boksenberg, A., Carswell, R. F., & Whelan, J. A. J. 1979, ApJ, 230, 49

Savage, B. D., Kim, T.-S., Wakker, B. P., et al. 2014, ApJS, 212, 8

Savage, B. D., & Sembach, K. R. 1991, ApJ, 379, 245

Schaye, J. 2001, ApJ, 559, 507

Schaye, J., Aguirre, A., Kim, T.-S., et al. 2003, ApJ, 596, 768

Schaye, J., Crain, R. A., Bower, R. G., et al. 2015, MNRAS, 446, 521

Schechter, P. 1976, ApJ, 203, 297

Schlegel, D. J., Finkbeiner, D. P., & Davis, M. 1998, ApJ, 500, 525

Schmidt, M. 1963, The Astrophysical Journal, 137, 758

Sembach, K. R., & Savage, B. D. 1992, ApJS, 83, 147

Shen, S., Madau, P., Aguirre, A., et al. 2012, ApJ, 760, 50

Shen, S., Madau, P., Conroy, C., Governato, F., & Mayer, L. 2014, ApJ, 792, 99

Sheth, K., Regan, M., Hinz, J. L., et al. 2010, PASP, 122, 1397

Shull, J. M., Danforth, C. W., & Tilton, E. M. 2014, ApJ, 796, 49

Simcoe, R. A. 2011, ApJ, 738, 159

Simcoe, R. A., Cooksey, K. L., Matejek, M., et al. 2011, ApJ, 743, 21

Songaila, A. 2001, ApJL, 561, L153

Spitzer, Jr., L., & Baade, W. 1951, ApJ, 113, 413

Springel, V., & Hernquist, L. 2003, MNRAS, 339, 289

Stark, D. V., Kannappan, S. J., Eckert, K. D., et al. 2016, ApJ, 832, 126

Steidel, C. C., Kollmeier, J. A., Shapley, A. E., et al. 2002, ApJ, 570, 526

Stewart, K. R., Kaufmann, T., Bullock, J. S., et al. 2011a, ApJL, 735, L1

—. 2011b, ApJ, 738, 39

Stocke, J. T., Keeney, B. A., Danforth, C. W., et al. 2013, ApJ, 763, 148

Stoughton, C., Lupton, R. H., Bernardi, M., et al. 2002, The Astronomical Journal, 123, 485

Strauss, M. A., Weinberg, D. H., Lupton, R. H., et al. 2002, AJ, 124, 1810

Stroe, A., Sobral, D., Dawson, W., et al. 2015, MNRAS, 450, 646

Sun, M., Donahue, M., & Voit, G. M. 2007, ApJ, 671, 190

Taylor, M. B. 2006, in Astronomical Data Analysis Software and Systems XV ASP Conference Series, Vol. 351, 666

Tejos, N., Morris, S. L., Crighton, N. H. M., et al. 2012, MNRAS, 425, 245

Tejos, N., Prochaska, J. X., Crighton, N. H. M., et al. 2016, MNRAS, 455, 2662

Tilton, E. M., Danforth, C. W., Shull, J. M., & Ross, T. L. 2012, ApJ, 759, 112

Tinsley, B. M. 1974, The Astrophysical Journal, 192, 629

Tonnesen, S., & Bryan, G. L. 2012, MNRAS, 422, 1609

Tonnesen, S., Bryan, G. L., & van Gorkom, J. H. 2007, ApJ, 671, 1434

Tremonti, C. A., Moustakas, J., & Diamond-Stanic, A. M. 2007, ApJL, 663, L77

Tripp, T. M., Aracil, B., Bowen, D. V., & Jenkins, E. B. 2006, ApJL, 643, L77

Tripp, T. M., Giroux, M. L., Stocke, J. T., Tumlinson, J., & Oegerle, W. R. 2001, The Astrophysical Journal, 563, 724

Tripp, T. M., Lu, L., & Savage, B. D. 1998, ApJ, 508, 200

Tripp, T. M., Savage, B. D., & Jenkins, E. B. 2000, ApJL, 534, L1

Tripp, T. M., Sembach, K. R., Bowen, D. V., et al. 2008, ApJS, 177, 39

Tripp, T. M., Meiring, J. D., Prochaska, J. X., et al. 2011, Science, 334, 952

Tully, R. B. 1987, ApJ, 321, 280

Tumlinson, J., Thom, C., Werk, J. K., et al. 2011, Science, 334, 948

—. 2013, ApJ, 777, 59

van de Voort, F., Bahé, Y. M., Bower, R. G., et al. 2017, MNRAS, 466, 3460

van den Bergh, S. 1962, The Astronomical Journal, 67, 486

Veilleux, S., Cecil, G., & Bland-Hawthorn, J. 2005a, ARAA, 43, 769

—. 2005b, ARAA, 43, 769

Verheijen, M. A. W., & Sancisi, R. 2001, A&A, 370, 765

Verner, D. A., Tytler, D., & Barthel, P. D. 1994, ApJ, 430, 186

Vikhlinin, A., Kravtsov, A., Forman, W., et al. 2006, ApJ, 640, 691

Vogelsberger, M., Genel, S., Sijacki, D., et al. 2013, MNRAS, 436, 3031

Vogelsberger, M., Genel, S., Springel, V., et al. 2014, Monthly Notices of the Royal Astronomical Society, 444, 1518

Wakker, B. P., Hernandez, A. K., French, D. M., et al. 2015, ApJ, 814, 40

Wakker, B. P., & Savage, B. D. 2009, ApJS, 182, 378

Wang, Q. D., & Walker, S. 2014, MNRAS, 439, 1796

Warmels, R. H. 1988, Astronomy and Astrophysics Supplement Series, 72, 19

Weinberg, M. D. 2014, MNRAS, 438, 3007

Weinmann, S. M., van den Bosch, F. C., Yang, X., & Mo, H. J. 2006, MNRAS, 366, 2

Werk, J. K., Prochaska, J. X., Thom, C., et al. 2012, ApJS, 198, 3

—. 2013, ApJS, 204, 17

Werk, J. K., Prochaska, J. X., Tumlinson, J., et al. 2014, ApJ, 792, 8

White, S. D. M., & Frenk, C. S. 1991, The Astrophysical Journal, 379, 52

Willmer, C. N. A., Faber, S. M., Koo, D. C., et al. 2006, ApJ, 647, 853

Woodgate, B. E., Kimble, R. A., Bowers, C. W., et al. 1998, Publications of the Astronomical Society of the Pacific, 110, 1183

Yang, X., Mo, H. J., & Bosch, F. C. v. d. 2003, MNRAS, 339, 1057

Yang, X., Mo, H. J., van den Bosch, F. C., et al. 2007, ApJ, 671, 153

Yoon, J. H., & Putman, M. E. 2013, ApJL, 772, L29

Yoon, J. H., Putman, M. E., Thom, C., Chen, H.-W., & Bryan, G. L. 2012, ApJ, 754, 84

Zinger, E., Dekel, A., Kravtsov, A. V., & Nagai, D. 2016, ArXiv e-prints, 1610, arXiv:1610.02644